Novel Cavity Design for High Power Microwave Applications

Lorna Fisher

(200661676)

Department of Physics and Applied Physics

University of Strathclyde

Thesis submitted for the degree of Doctor of Philosophy
September 2010

This thesis is the result of the author's original research. It has been composed by the author and has not been previously submitted for examination which has led to the award of a degree.

Abstract

The excitation of a novel cavity based on a two-dimensional periodic structure by an energy source, such as relativistic electrons, results in stimulated, single frequency coherent emission. A high-Q cavity has been achieved via a resonant coupling between surface waves and volume waves. The concept of a Cherenkov maser based on such a novel cavity is discussed and results of numerical studies presented. Links between the model described and the concept of a surface plasmon amplifier, which has been recently introduced are described. It is suggested that a two-dimensional periodic structure can complement devices operating at THz frequencies.

Acknowledgements

I am heartily thankful to Professor Alan Phelps, Dr. Ivan Konoplev and Dr. Adrian Cross for their time, encouragement, patience and support throughout this PhD and beyond.

A special thanks to both Dr. Kevin Ronald and Dr. Philip MacInnes for their time spent, not only in detailed explanations, but with their invaluable assistance toward experimental investigations.

I would also like to thank the Engineering and Physical Sciences Research Council in financially supporting this research.

Lastly, I offer my regards and blessings to all of those who supported me in any respect during the completion of the project.

Table of Contents

4. Experimental Analysis

5. Applications

6. Conclusions & Future Work

Appendix A

Appendix B

Appendix C

Appendix D

Publications & Conference Proceedings

List of Figures

Nomenclature

$(r, \theta, z) = Cylindrical\ coordinate\ system$

$E_r = Radial\ electric\ field\ component\ (Vm^{-1})$

$E_\theta = Azimuthal\ electric\ field\ component\ (Vm^{-1})$

$E_r = Longitudinal\ electric\ field\ component\ (Vm^{-1})$

$H_r = Radial\ magnetic\ field\ component\ (Vm^{-1})$

$H_\theta = Azimuthal\ magnetic\ field\ component\ (Vm^{-1})$

$H_z = Longitudinal\ magnetic\ field\ component\ (Vm^{-1})$

$p = Transverse\ wave\ number\ (m^{-1})$

$\beta = Longitudinal\ wave\ number\ (m^{-1})$

$\omega = Angular\ frequency\ (rads^{-1})$

$\mu = Permeability\ (Hm^{-1})$

$\mu_r = Relative\ Permeability\ (Hm^{-1})$

$\mu_0 = Permeability\ of\ free\ space\ (\cong 4\pi \times 10^{-7}\ Hm^{-1})$

$\varepsilon = Permittivity\ (Fm^{-1})$

$$\varepsilon_i = Relative\ Permittivity\left(Fm^{-1}\right)$$

$$\varepsilon_r = Relative\ Permittivity\left(=\frac{\varepsilon_i}{\varepsilon_0}\right)$$

$$\varepsilon_0 = Permittivity\ of\ \ free\ space\left(\cong 8.85\times 10^{-12}\ Fm^{-1}\right)$$

$$a_{eff} = Effective\ radius\left(mm\right)$$

$$\eta_{eff} = Effective\ refractive\ index\left(=\sqrt{\varepsilon_r \mu_r}\right)$$

$$k_z = Longitudinal\ \ Wave\ \ Number\left(m^{-1}\right)$$

$$k_{\perp} = Transverse\ \ Wave\ \ Number\left(m^{-1}\right)$$

$$\omega = Angular\ \ \ frequency\left(rad\ \sec^{-1}\right)$$

$$\omega = Angular\ \ \ frequency\left(rad\ \sec^{-1}\right)$$

$$c = Speed\ \ of\ light\ \ in\ \ vacuum\left(ms^{-1}\right)$$

1 Introduction

1.1 Historical Review

Microwave radiation sources providing high power, broadband, and frequency tuneable radiation are used for many important applications, such as plasma heating [1], particle acceleration [2], and material processing, and, in recent years the demand for high power masers operating at sub GW and GW powers in the frequency range from 30 GHz to 300 GHz and beyond has significantly increased [3-7].

At low power (tens of Watts) there exists a number of highly developed solid state sources available covering the wavelength range from centimetres to millimetres and beyond. However there exist applications which require frequency controllable radiation with high power outputs (kW to MW). The most promising method used to generate high power levels at high frequencies (>10GHz) is to use the interaction of an electron beam in a vacuum with an electromagnetic wave, and a number of discreet amplifiers and oscillators based on this principle are already in use. Problems arise however when we seek to increase the operating frequency, therefore reducing the dimensions of the

interaction region, whilst still trying to achieve high levels of power. The power density can become large this can lead to breakdown inside the interaction space. This issue may be addressed via the application of an oversized, (with respect to the wavelength of operation) electron beam [8,9]. This allows for a moderate power density inside the interaction space to be achieved whilst simultaneously avoiding the formation of beam instabilities due to the high beam charge density [10]. One might argue that this now oversized system has no apparent method for frequency selectivity or tuneability, but this issue may be addressed, and has been previously [15,16], by the application of two-dimensional distributed feedback to the interaction region [11]. This circumvents the problem by providing spatial and temporal coherence of the radiation from the large size (in comparison with the operating wavelength) active medium [12-14].

This chapter begins with an overview of microwave devices to date, before discussing the different types of microwave device available, along with the different fundamental types of interaction achievable between an electromagnetic wave and an electron beam. It then gives introduction to the method of feedback via Bragg scattering and previous successful applications to date before considering its limitations and restrictions before stating the aim of this work and layout of this thesis.

1.2 Background

High power microwaves are generated by transferring the kinetic energy of moving electrons to the electromagnetic energy of the microwave fields. This process occurs typically in a waveguide or cavity, the role of which is to tailor the frequency and spatial structure of the fields in such a way as to optimise the energy extraction from specific natural modes of oscillation of the electrons. Analysing this process always deals with the interaction between two concepts: (1) the normal electromagnetic modes of the waveguide or cavity, and (2) the natural modes of oscillation of the electron beam. These two entities exist independently of each other except for certain values of frequency and wavelength for which they can resonantly exchange energy.

1.3 Types of Microwave Device

The microwave generation process in all high power microwave sources generally always involves an interaction between an active media, such as an electron beam, with an electromagnetic wave. This corresponds to resonant interactions between the normal electromagnetic wave modes of a cavity or waveguide and the natural modes of oscillation in a beam or layer of electrons. The natural modes of oscillation in a beam of electrons are formed by either the longitudinal spatial bunching or the rotational phase bunching of the electrons in the beam. Both these cavity modes and beam modes can be described by specific dispersion relations relating angular frequency ω to axial wave number k_z.

In this section, the general dispersion relations of waveguide modes and electron beam modes are first described, followed by a general introduction into different kinds of free electron maser devices. The three generic interactions, including Cherenkov, FEL and Cyclotron interactions, are introduced. Finally the saturation mechanism in microwave generation is discussed.

1.3.1 Dispersion Relations

In this section, the dispersion relations (ω, k_z) governing both the normal waveguide modes and the natural electron beam modes are described. The conditions for their interaction are described and the mechanisms involved for microwave generation are discussed for different devices.

1.3.1.1 The Natural Waveguide Modes

The standard electromagnetic wave behaviour in a smooth wall waveguide (or cavity) having uniform cross section is generally described by the dispersion relation [15]:

$$\omega^2 = k_z^2 c^2 + \omega_{co}^2(n,p) \tag{1.1}$$

where $\omega_{co}^2(n,p)$ is the cut off frequency of the $TM_{n,p}$ and $TE_{n,p}$ modes in a given waveguide, where *n* is the number of azimuthal variations, and *p* the number of radial variations. A plot of this dispersion relation is shown in Figure 1.1 where two axial velocities are shown in this figure: one is a phase velocity in which the wave phase advances along the axis, and the gradient of a line connecting a point on the curve to the origin, denoted by $\upsilon_{ph} = \frac{\omega}{k_z}$, and the other is the group velocity of the EM wave along the axis, with the gradient of the ling at a tangent to the curve, $\upsilon_g = \frac{\partial \omega}{\partial k_z}$.

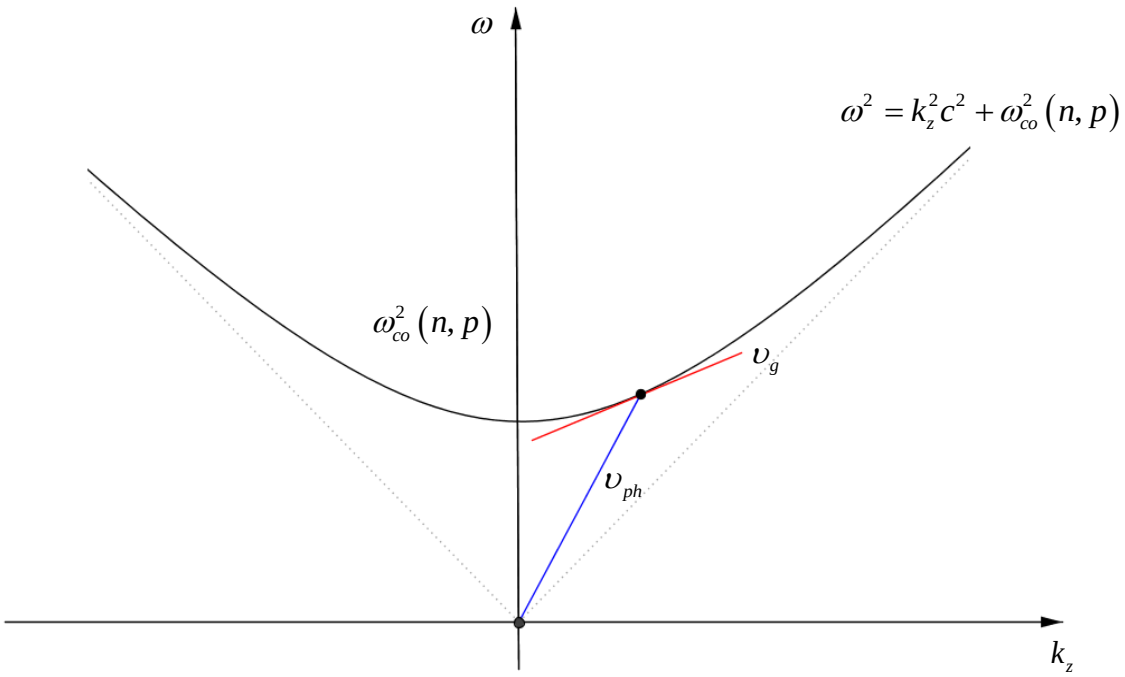

Figure 1.1: Dispersion of Electromagnetic Waves

The phase velocity must always exceed the speed of light, *c*, whilst the group velocity must always be less than *c*. By making changes to the waveguide wall, via either

structural modification such as a corrugation or by insertion of a dielectric material, the phase velocity of the waveguide modes can be reduced to less than the value *c*.

1.3.1.2 Electron Beam Modes

The dispersion curves describing the oscillation in a beam of electrons is dependent on the motion of these electrons and also their oscillating mode. The most basic oscillation mode for an electron beam is its space charge oscillation wave, which is created by the bunching of beam electrons. In its most simple situation, without any consideration for the radial boundaries, the dispersion relation describing the space charge wave for a beam propagating along the *z*-axis, is expressed via:

$$\omega = k_z \upsilon_z \pm \frac{\omega_b}{\gamma_0} \tag{1.2}$$

where $\omega_b = \left(\frac{|\rho_0| e^2}{\varepsilon_0 m \gamma_0} \right)^{\frac{1}{2}}$ is the beam plasma frequency for a beam of charge density ρ_0 and velocity υ_b $\left(\upsilon_b \equiv \upsilon_z \right)$, with $\gamma_0 = \left(1 - \frac{\upsilon_z^2}{c^2} \right)^{-\frac{1}{2}}$ the relativistic factor. The waves having frequencies denoted by this equation are known commonly as 'fast and 'slow' space charge waves, according to the use of the '+' or '-' sign respectively and are illustrated in figure 1.2. There are two distinct cases presented: 1) when no radial boundary is present, i.e. an infinite beam, and 2) when the beam is bound within a waveguide, i.e. the phase velocity of the space charge waves is always less than *c*. In either case, with or without the radial boundary taken into account, the slow space charge wave is the negative energy wave and the fast space charge wave has positive energy [17]. Microwave generation occurs at a frequency and wave number roughly given by the intersection between the dispersion curves for the slow space charge wave and an

electromagnetic mode. When this generation occurs, the electron oscillation taking part in the resonance is said to be a negative energy wave.

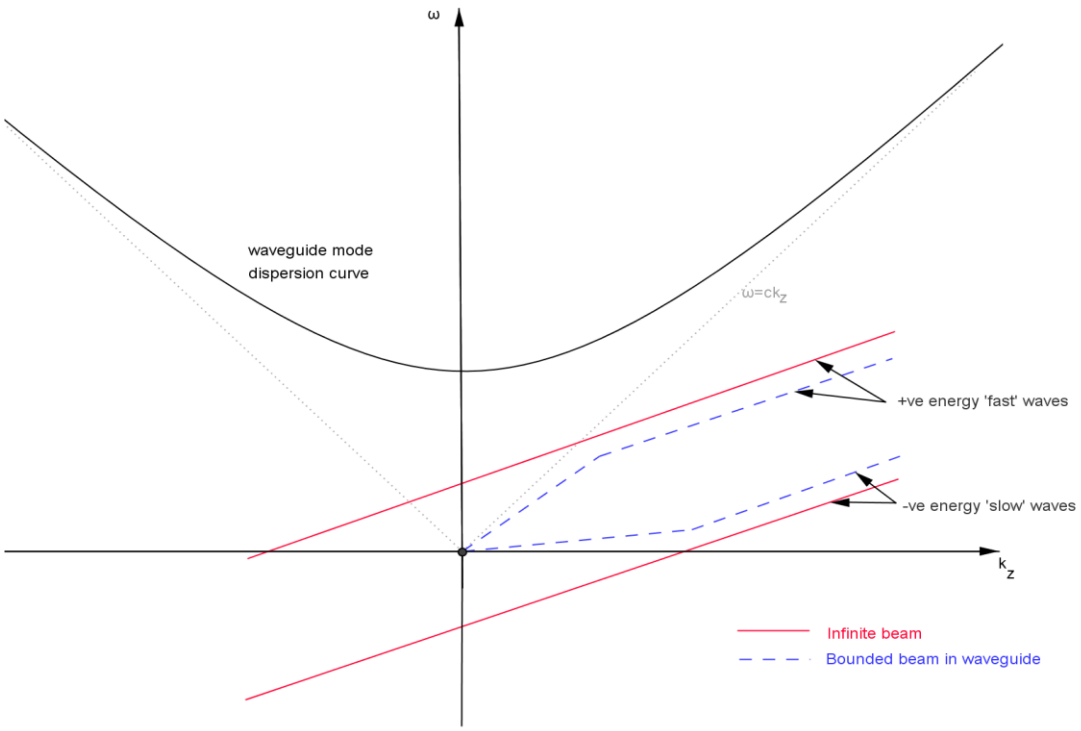

Figure 1.2: Illustration showing the space charge modes of an infinite electron beam (red) and a waveguide bounded electron beam (blue dashed).

The total energy of the coupled system, including the EM energy of the waveguide mode and the summed energy of the electrons, is positive. However, the total energy is higher in the initial equilibrium state with no electron oscillations than it is in the presence of the unstable electron oscillation. The electron oscillation has therefore reduced the total energy of the system and has a negative energy in the incremental sense. This energy reduction does not occur for some electron oscillations, which are said to have positive energy waves, and will not interact with the waveguide modes to generate microwaves.

1.3.1.3 Free Electron Maser Devices

There are several aspects to be considered in the beam-wave interaction: (1) waveguide and cavity modes, (2) electron motion and oscillation modes, (3) beam-wave interaction mechanism, (4) electron beam intensity and (5) operational effects. With respect to electromagnetic modes, microwave sources are said to be either fast-wave or slow-wave, dependant on the interaction. A fast-wave interaction involves a waveguide mode with a phase velocity greater than the speed of light, whilst a slow-wave interaction involves a waveguide mode whose phase velocity is less than the speed of light.

In terms of electron motion, devices are generally classified into three types: Type 1 are known as O-type devices, in which the electrons drift axially along an externally applied magnetic field. The field helps to guide the beams through the device, and in some cases plays an important role in the generation process (parallel field devices); Type 2 are the M-type devices in which the electrons drift perpendicular to crossed electric and magnetic fields (crossed field devices) and the third variant are known as Space charge devices, where the interaction is intrinsically traceable to an intense space charge interaction such as a virtual cathode oscillator [18].

With regard to mode of operation, microwave devices can be classed into two types: (1) Amplifier devices, which produce an output signal that is a larger amplitude version of some input signal (in the absence of an input signal there is usually no output signal other than low-level amplified noise); (2) Oscillators – these require feedback and sufficient gain to overcome the net losses per cycle, such that an output signal can be generated in the absence of an input signal.

According to the beam current density, devices are grouped into two operating regimes: (1) Compton regime, involving low beam currents. Here, collective space-charge effects are negligible and the electrons behave as a coherent ensemble of individual emitters; (2) Raman regime of operation, this involves the use of high electron densities with beam currents approaching a significant fraction of the space-charge limit. The collective modes of electron oscillation play the central role in microwave generation.

1.3.2 Beam-Wave Interaction Mechanisms

In order to realise the various types of interaction between an electron beam and an electromagnetic wave, it is necessary to satisfy the synchronism condition associated with each type of interaction. The synchronism conditions are met at the cross point between an electromagnetic (EM) wave dispersion curve, defined as:

$$\omega = \upsilon_{ph}\sqrt{k_z^2 + k_\perp^2} \tag{1.3}$$

and an electron beam line:

$$\omega - k_z\upsilon_z = s\Omega_{eff} \tag{1.4}$$

where ω is the angular frequency of the EM wave, k_z is the axial wave number, and $k_\perp$ is the transverse wavenumber, υ_{ph} is the phase velocity of the wave, υ_z the axial velocity of the electron, s is the harmonic number and Ω_{eff} is an effective frequency corresponding to oscillatory motion of the electrons, which determines the cut-off frequency of the waveguide. The interaction points are shown in Figure 1.3. Looking at the dispersion curves it is evident that the slow space-charge waves, having $\frac{\omega}{k_z} < c$, cannot couple to the normal fast-wave modes of a smooth wall waveguide, for which $\frac{\omega}{k_z} > c$.

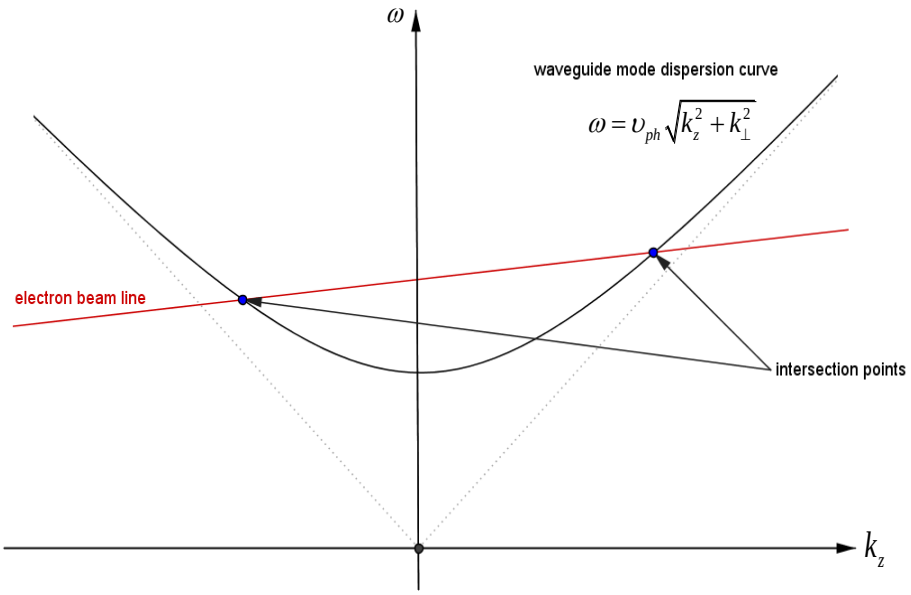

Figure 1.3: Schematic of the synchronism condition, illustrating the point(s) of intersection between an electron beam and a waveguide cavity mode.

Nevertheless, there are ways to achieve the required coupling by either reducing the phase velocity of the wave mode, or by up-shifting the electron oscillation mode. To achieve these there are three main mechanisms: Cherenkov Interactions, Free Electron Laser (FEL) interactions, and Electron Cyclotron Maser (ECM) interactions.

1.3.2.1 The Cherenkov Interaction

Cherenkov radiation occurs when electrons move in a medium whose refractive index is greater than one, $n>1$, and $\upsilon_z \geq \upsilon_{ph}$ where $\upsilon_{ph} = c/n$, and c is the speed of light in vacuum. This shows that if the refractive index is large enough it is possible to match the electron velocity and the EM phase velocity, i.e. $\upsilon_z \simeq \upsilon_{ph}$. Referring to Equation (1.4), let us note that due to $\upsilon_z \simeq \upsilon_{ph}$ there is no requirement for electrons to have transverse

momentum (i.e. $\Omega_{eff} = 0$) to ensure solutions to Equations (1.1) and (1.2). The synchronism condition therefore reduces to

$$\omega = k_z \upsilon_z \tag{1.5}$$

1.3.2.1.1 Energy Transfer in a Cherenkov Interaction

The generation of electromagnetic radiation by an electron beam requires a bunching mechanism to impart an ac component of the beam current to the EM wave. This holds true for all types of interaction, not just the Cherenkov. In order for bunches to build up, and to allow sustained energy transfer, the electrons must remain in close synchronism with the EM wave. Bunching and synchronism are two fundamental conditions for the generation of coherent radiation in vacuum-electronic devices and can be explained by considering the uniform electron beam as follows:

- In a uniform electron beam the contributions of all the individual electrons to the radiation field will be random in phase and therefore the square of the total field equals the sum of the squares the individual fields. If however the electrons are bunched within a distance comparable to the wavelength of the radiation, their fields will add up in phase, thus resulting in the emission of coherent radiation.

- The power level of the coherent radiation generated by a bunched electron beam is typically several orders of magnitude higher than the non-coherent radiation generated by a uniform electron beam.

The process of bunching itself can be thought of by considering the electron distributions, where initially, they are uniformly distributed over the distance of the waveguide wavelength λ_z; half of the electrons are accelerated and the other half decelerated by the electric field, thus allowing bunches to form as illustrated in Figure 1.4(a). If the axial velocity is allowed to equal to phase velocity, $\upsilon_z = \upsilon_{ph}$, the bunches will form in the vicinity of the field null which does not allow for transfer of energy. If

however the velocity of the electron beam is made slightly greater, i.e. $\upsilon_z > \upsilon_{ph}$, it will travel faster than the wave resulting in the bunch centre to advance into the decelerating phase of electric field and therefore resulting in a net transfer of the beam energy to the electromagnetic wave, shown in Figure 1.4(b).

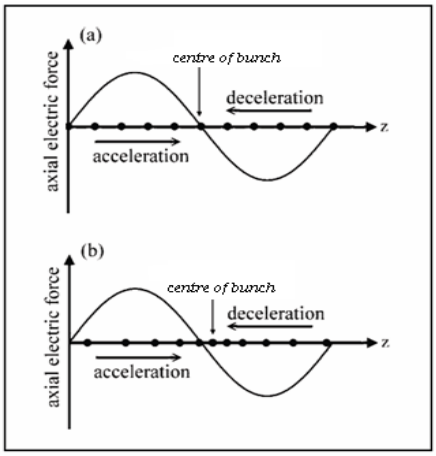

Figure 1.4: Bunching of an electron beam in a linear beam source, by the axial electric field of a synchronized travelling wave, showing (a) bunch formation due to the action of the electric field, and (b) shift of bunch into decelerating phase of electric field.

Radiation sources based on this type of interaction are the Travelling Wave Tube (TWT) and the Backward Wave Oscillator (BWO), these are linear beam devices (have no transverse momentum). The TWT is an amplifier and follows a convective instability, such that in addition to the waves growing they also convect away from the location at which they were created, shown in Figure 1.5. The BWO is an oscillator and obeys an absolute instability, i.e. the instability grows as time progresses without moving from the point of origin, shown in Figure 1.6. Alternatively, the waveguide modes can be slowed down by modifying the shape of the confining walls by some kind of 'loading'. This 'loading' effect may be achieved by introducing a periodic variation in the radius of a cylindrical waveguide.

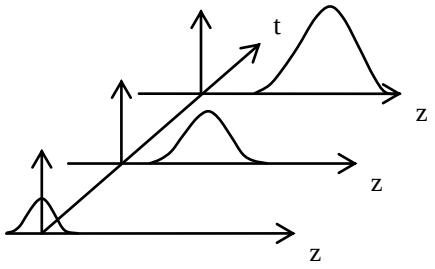

Figure 1.5: Convective instability

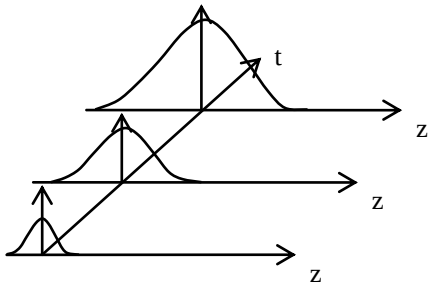

Figure 1.6: Absolute instability

This is the basis of devices such as the backward wave oscillator (BWO) and the travelling wave tube (TWT) in which the device type depends upon whether the intersection with the waveguide curve occurs at a point of negative (BWO) or positive (TWT) group velocity [19]. Traveling Wave Tubes operate in the region of the dispersion curve where the group velocity ($\upsilon_{gr} = \frac{\partial \omega}{\partial k_z}$) of the slow wave is positive ($\upsilon_{gr} > 0$) and amplify forward waves whereas Backward Wave Oscillators operate where the group velocity is negative ($\upsilon_{gr} < 0$). In Figure 1.7 the dispersion diagram for radiation sources based on the Cherenkov interaction is shown.

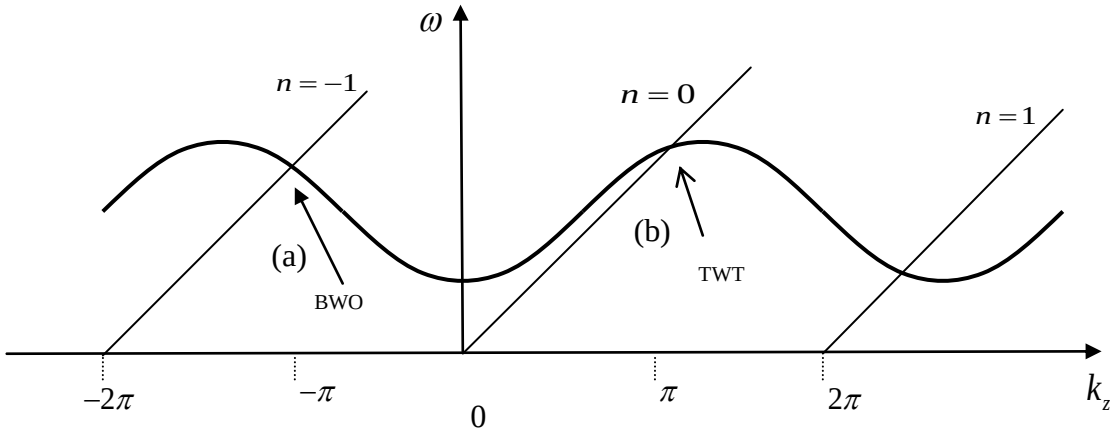

Figure 1.7: Dispersion diagram for Cherenkov devices, showing (a) the interaction between the n = -1 harmonic of the slow space charge electron beam and the EM wave, which leads to a backward wave oscillation, and (b) the interaction between the fundamental harmonic (n = 0) of the slow space charge electron beam wave with the EM wave to produce the forward wave interaction of the TWT.

1.3.2.1.2 The Smith Purcell Interaction

The electron beam can also interact with the spatial harmonics of the EM wave. The wave spatial harmonics can be observed in periodic structures, whereby Floquet's theorem [17] allows an electromagnetic wave to be represented as the superposition of an infinite number of its spatial harmonics;

$$E\left(r_{\perp},z\right)=e^{-i\omega t}\sum_{l=-\infty}^{+\infty}A_{l}\left(r_{\perp}\right)e^{ik_{zl}z} \tag{1.6}$$

with axial numbers k_{zl}; $$k_{zl}=k_{z0}+\left(2\pi l/d\right) \tag{1.7}$$

Here d is the period of the structure, l is the harmonic number, k_{z0} is the wave number of the zeroth-order spatial harmonic $\left(-\pi/d<k_{z0}<\pi/d\right)$, and A_l is the amplitude of the harmonic determined by the geometry of the structure. This type of radiation from electrons in a periodic structure is known as Smith-Purcell radiation where a spatial harmonic has an effective phase velocity, $\upsilon_{ph_l}=\omega/k_{zl}<c$ propagating in a medium with an effective refractive index, $n_l=ck_{zl}/\omega$. This allows us to understand Smith-Purcell radiation as a kind of Cherenkov radiation. Let it be noted that the transverse wave number of slow waves is imaginary, i.e. $k_{\perp l}^{2}=\left(\frac{\omega}{c}\right)^{2}-k_{zl}^{2}<0$, therefore the field of the corresponding spatial harmonic is localized near the wall of the structure therefore electrons must propagate close to the wall in order to couple to this harmonic. An example of a radiation source which utilized the Smith-Purcell effect is the Orotron [20].

1.3.2.2 The Electron Cyclotron Maser Interaction

Cyclotron Masers are high power microwave sources of coherent millimeter or sub-millimeter radiation. They take advantage of the interaction between a fast electromagnetic wave and electrons to transfer energy from electrons gyrating in a

strong guiding magnetic field to an electromagnetic wave. The use of the fast wave interaction to generate millimetre-wave power has great potential as the supporting structures can be simple smooth waveguides.

1.3.2.2.1 Energy Transfer in an Electron Cyclotron Maser

In this type of device the electron bunching can be due to the effect of the electromagnetic field on both the axial and transverse velocities of the electrons, υ_z and $\upsilon_\perp$. The Cyclotron Resonance Maser (CRM) can be designed to operate using either fast or slow waves.

In the case of fast wave CRM's, we consider a beam of electrons travelling along a reasonably strong guide field, B_0 and imagine that the individual electrons have a velocity component perpendicular to B_0 such that they execute a small orbit Larmour rotation about their guiding centres at the cyclotron frequency $\omega_c = \frac{eB_0}{m\gamma}$ where γ is the relativistic factor of the moving electrons. The scaling of ω_c allows for external tuning of the output frequency through an adjustment of either the magnetic field or the beam voltage, thus allowing the individual electrons to spontaneously emit Doppler shifted cyclotron radiation:

$$\omega = k_z \upsilon_z + s\omega_c \tag{1.8}$$

where *s* takes the value of any integer not equal to zero. Electrons emitting this radiation can interact resonantly with the fast waveguide modes, and, as the cyclotron frequency is beam energy dependent, the rotating electrons will become bunched in their rotational phase (which is different from the spatial bunching of space-charge waves), illustrated Figure 1.8. The generation in ECM devices is therefore based upon the extraction of the electrons rotational energy in a magnetic field.

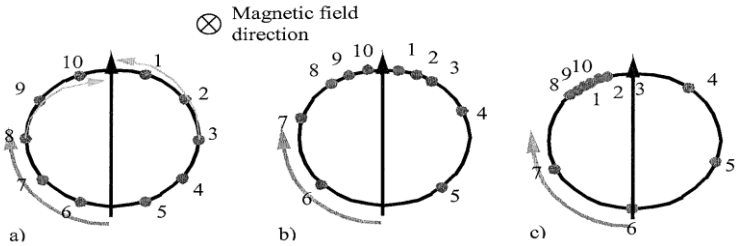

Figure 1.8: Schematic of orbital bunching in CRM devices showing, a) the initial position of the uniformly distributed electrons, b) interaction between the electron beam and the wave and c) the phase slippage between the formed electric bunch and the electric field.

a) At time $t = 0$ (the start time), electrons gyrating in a circular orbit are evenly distributed in azimuthal position and they interact with an electric field, either absorbing or radiating an EM wave.

b) The action of the electromagnetic field on the electrons causes them to bunch due to the dependence of the electron gyration frequency on the relativistic mass (electron energy). After several rotations, a phase bunch is formed. Electrons that are decelerated increase in gyro frequency therefore advance in phase, and electrons that are accelerated decrease in gyro frequency and retard in phase.

c) If the electron cyclotron frequency is less than the frequency of the electromagnetic field, the position of the bunches are delayed with respect to the phase of the electric field, this is known as phase slippage and as a result the net kinetic energy of the particles will decrease.

In the case of slow-wave CRMs the dominant effect is axial bunching due to the change in Doppler term, this is achieved if the magnetic forces ($\upsilon_{\perp} \times B_{\perp}$) of the wave dominate. This is a non-relativistic effect and is known as the Weibel instability. A device which utilizes this instability is the Slow Wave Cyclotron Amplifier [21].

Radiation sources based on the Cyclotron interaction include; the Gyrotron [22,23], the CARM [24], the gyro-BWO [25,26] and the gyro-TWT [27]. These are all gyro-devices driven by annular beams. The most widely known and used ECM is the Gyrotron and further details are given in Appendix A.

1.3.2.3 The Free Electron Maser Interaction

The Free Electron Maser (FEM) uses an electron beam passing through a periodic magnetic field of an undulator to produce electromagnetic radiation. They do not require slow wave structures and can operate at very short wavelengths/high frequencies. The interaction is achieved by a modification, not of the waveguide dispersion, but of the space-charge wave dispersion. If a periodic transverse magnetostatic field of alternating polarity (known as an undulator or wiggler) is applied inside the waveguide, the result is that the dispersion curves for the space-charge waves will be Doppler 'up-shifted' in frequency by an amount equal to the wiggle frequency of the electrons, $\omega_w \cong k_w \upsilon_z$, where $k_w = \frac{2\pi}{\lambda_w}$ with λ_w the periodicity of the magnetic field. This can be understood as: in the frame moving with electrons, the wiggler field is an electromagnetic wave moving towards the electrons; hence the space-charge waves become fast waves capable of interacting with the fast waveguide modes. The FEM is therefore a fast-wave device.

The synchronism condition is similar to a Cherenkov type instability but in this case the interaction of electromagnetic waves occurs with a pondermotive wave of the electron beam. The operating frequency of an FEM is determined by the condition that the electron in its rest frame, observes the radiation and the periodic external force at the same frequency. If the beam is highly relativistic the radiation will have a much shorter wavelength, determined by the relativistic Doppler Effect. Fast frequency tuning is possible by variation of the relativistic factor. The bunching of electrons in the FEM is due to the perturbation of beam electrons by the pondermotive well which is caused by "beating" of the electromagnetic wave with the spatially periodic undulator field. The

essential feature of the FEM mechanism is that the beam electrons undergo axial bunching in the combined wiggler and radiation fields -it is the axial bunching that is responsible for the generation of coherent radiation. The operating frequency of the FEM is dependent on beam energy and undulator period therefore the FEM can be tuned over a broad range of frequencies.

Free Electron Lasers differ from other microwave sources in that they have demonstrated output over a range of frequencies extending far beyond the microwave spectrum, well in to the visible and ultraviolet range by adjusting the 'wiggler' frequency via the electron energy. These devices are best known for their applications outside of the microwave range, using high energy, low current accelerators. Nevertheless, a substantial effort had been devoted to development of FELs as a source of mm-waver radiation sources, driven by intense pulsed electron beams [28 - 30].

1.3.2.4 Experimental Observations at Strathclyde

A Free Electron Maser experiment using two dimensional distributed feedback was successfully carried out at Strathclyde [31-35]. The device is capable of producing up to 60MW of pulsed output power at a frequency of 37.2GHz. In the experiment an oversized ($\frac{D}{\lambda} > 10$, where D represents the diameter of the waveguide) annular electron beam was used to drive the maser. The design comprised of a coaxial cavity with two individual 2D corrugated inner conductors separated by a region of plane conductor. A heterodyne frequency diagnostic was used to measure an operating frequency of 37.2GHz and the efficiency of the Free Electron Maser was found to equal approximately 10%.

1.3.3 Saturation Mechanism

In most sources, wave growth is accompanied by a bunching of the electrons in some form or another. In some devices electrons form spatial bunches, in others, they will bunch the phase of their rotation about the magnetic field lines. In any event, bunching is an important phenomenon as it enforces the coherence of the electromagnetic waves that are generated. Bunching makes the difference between the incoherent spontaneous emission of the initial state, and the coherent stimulated emission of the later state. When the beam is strongly bunched, the microwave output power is proportional to the number of bunches, N_b, and the square of the number density of electrons within the bunches, n_b:

$$P \propto N_b n_b^2 \tag{1.9}$$

Of course, the process of wave growth and bunching cannot continue infinitely - eventually, given enough time the instability will proceed to saturation and wave growth ceases. A variety of mechanisms may lead to saturation, but two are seen most commonly as: either the excess kinetic energy of the electrons is exhausted and the electron oscillation falls out of resonance, or the electron bunches become trapped in the strong potential wells of the electromagnetic waves and begin to reabsorb energy from the wave as they move around in the well.

All these types of device described above have one (or more) thing in common. They all possess an interaction region, i.e. a place where the energy can be generated, in some form or another. One of the main goals of this thesis is to demonstrate the possibility of obtaining MW level radiation at high frequencies (~90 GHz) from either one of the device types described above. Currently the output power limitation is the restriction in transverse size of the interaction space which is required so as to avoid the excitation of spurious modes. This limitation of the interaction space may result in either: breakdown due to the high power density, or electron beam instabilities due to the high space charge density. An increase in the transverse size is therefore necessary in order to maintain a

low beam current density as well as to keep down the field strength if any increase in power is desired, but this generally leads to a loss of mode selectivity (if single mode operation is desired). The use of distributed feedback was suggested to overcome these problems associated with mode control inside the oversized region and help to achieve single mode operation.

1.4 Periodic Structures

Periodic structures have been used to provide distributed feedback in optics [36] and in vacuum electronics over a broad spectral range, from the millimetre through to optical wavelengths [37-40]. The advantage of using these structures is that they can provide selective feedback where the performance is limited only by the technology available to obtain the periodic perturbation of either the waveguide walls or refractive index of the dielectric material.

The method of distributed feedback via Bragg scattering has been successfully employed in a variety of devices, where it is used to provide coherent radiation by synchronization of transverse components of an oversized active medium, in return allowing for specific mode selection and control. There are two distinct types of periodic corrugation relative to this work; they are one dimensional structures, having variation in only the longitudinal coordinate, and two-dimensional, or 'doubly periodic' structures, consisting of perturbations not only along the length but across the transverse range also.

1.4.1 1D and 2D Periodic Structures

The one-dimensional perturbation can be realised by machining a shallow corrugation on the surface of an annular waveguide and may be presented analytically as:

$$a = a_0 + a_1 \cos\left(Kz + M\varphi\right) \tag{1.9}$$

where a_0 is the radius of the unperturbed waveguide, a_1 is the amplitude of the corrugation, $K = \frac{2\pi}{d}$, d is the period of the corrugation along the *z* direction and M is the corrugation azimuthal index. The wave propagating through the waveguide will reflect from each small perturbation of the waveguide wall, where, due to the periodicity of the wall perturbations, only waves which satisfy the Bragg resonance conditions [38] will be effectively coupled on such a corrugation

$$\vec{K}_z \approx \vec{k}_+ - \vec{k}_- \qquad M = \pm\left(m_1 - m_2\right) \tag{1.10}$$

where $k_\pm$ are the longitudinal wave numbers and $m_{1,2}$ are the azimuthal numbers of the incident (forward) and scattered (backward) waves respectively. Assuming azimuthal symmetry, denoted by $M = 0$, coupling between the forward and backward waves is possible. The coupling coefficient is proportional to the corrugation amplitude a_1 and if the amplitude of the perturbation tends to zero no coupling will exist. An increase in the amplitude will result in increased wave coupling and the appearance of reflection zones, otherwise known as band gaps. This effect is known as Bragg scattering and can be illustrated using a Brillouin diagram, Figure 1.9, where both cases are shown, i.e. a) corrugation equal to zero and b) finite corrugation. The harmonics of the waveguide eigenmodes are shifted along the *k*-axis according to $K_n = \frac{2\pi n}{d_z}$, where *n* is an integer. This direct coupling of forward and backward waves on the 1D corrugation provides synchronization of radiation in the transverse direction from different parts of an oversized electron beam although cannot provide feedback over the transverse index of the wave [41].

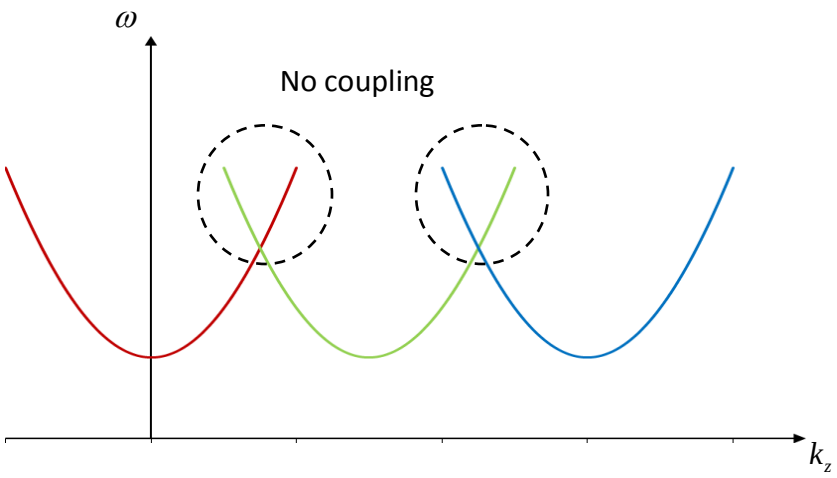

Figure 1.9a: Brillouin diagram illustrating when the corrugation amplitude tends to zero there is no coupling between modes.

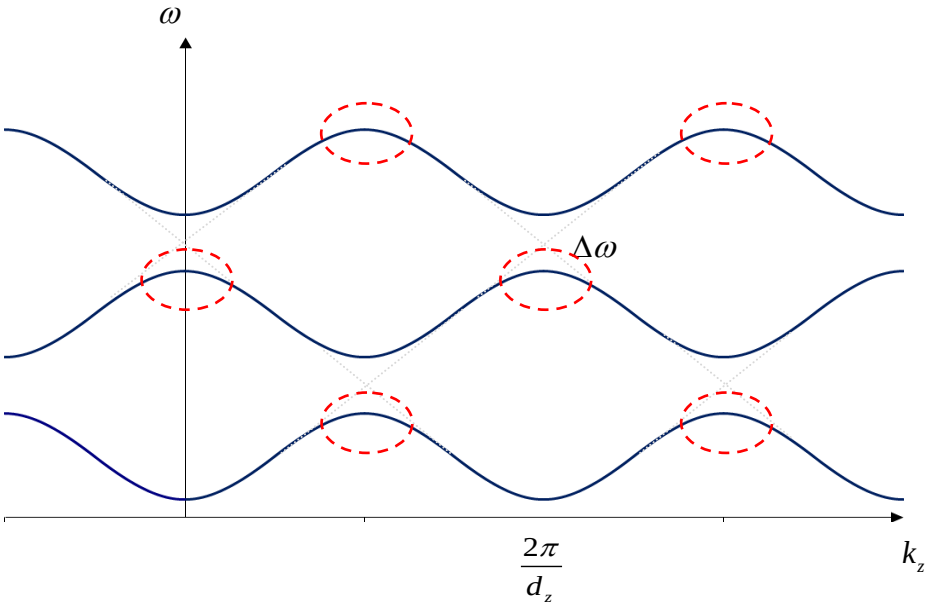

Figure 1.9b: Brillouin diagram illustrating a finite corrugation which leads to mode coupling, where the coupled mode regions are outlined via red dashed circles.

In order to obtain spatially coherent radiation from the oversized electron beam and improve mode control, the use of two-dimensional feedback has been successfully

implemented [42-51]. This type of feedback can be realised by introducing a shallow, periodic double corrugation to the waveguide wall, and can be written as:

$$r = a_1\left[\cos\left(\vec{k}_z z + \vec{k}_\zeta \zeta\right) + \cos\left(\vec{k}_z z - \vec{k}_\zeta \zeta\right)\right] = \frac{a_1}{2}\cos\vec{k}_z z \cos\vec{k}_\zeta \zeta \tag{1.11}$$

where a_1 represents the waveguide cross section radius.

This type of lattice offers indirect coupling of nearby waves via near cut off waves of the waveguide structure, where the coupling occurs due to Bragg scattering of waves propagating through the structure. Only waves satisfying the Bragg resonance condition will couple to the corrugation

$$\vec{\vec{K}}_\pm \approx \vec{k}_i - \vec{k}_s \qquad\qquad M = \pm\left(m_1 - m_2\right) \tag{1.12}$$

where $\vec{\vec{K}}_\pm$ are the longitudinal wave vectors of the structure, corresponding to the incident and scattered waves $\vec{k}_i$ and $\vec{k}_s$, and m_1 and m_2 represent the azimuthal numbers of the incident and scattered waves.

1.5 Previous Studies & Statement of Problem

Previous studies have shown both 1D and 2D reflectors are a highly efficient method of providing feedback in an oversized system [48-51].

An important point to note is that all of these previous studies listed have only considered the use of 1D and/or 2D periodic structures in either planar or coaxial configuration, on either one or both conductors. This coaxial geometry has its limitations, in that we are restricted to the fact that coupling can only occur for waves having zero radial variations as the presence inner conductor limits the generation of these modes, even in the presence of the 2D structure, we can still only achieve mode selectivity over the azimuthal index. No attempt, prior to this thesis, has been made to investigate the effects a doubly periodic corrugation has upon removal of the central line, although it is believed that removal of this additional surface will allow for the enhanced modal coupling, due to the additional modes being present, whilst still maintaining the coherence and selectivity representative of the coaxial setup.

1.6 Thesis Layout

The thesis begins with an introduction to the history of microwave engineering and the different classes of generating source available and prevalent to date further to discussing the method of distributed feedback and its history, including citations to previous successful applications which incorporate this feature. The chapter discusses the current limitations and restrictions of these regimes before proposing a possible solution. The layout of work is then given before proceeding to Chapter 2, which is primarily devoted to theoretical analysis of a 2D square corrugation in cylindrical geometry. Chapter 2 begins with the well known fundamentals of Bragg reflection and applies specific boundary conditions relative to our system before suggesting two methods with which mode structure and modal dispersion can be calculated. This leads us to Chapter 3, where numerical analysis of a cylindrical waveguide encompassing a shallow square corrugation is carried out using two very different types of Numerical Algorithm solvers, which should help us to identify mode structure and any subsequent interactions taking place. This is applied, not only to one, but three variants of cavity, each designed to operate across a different frequency range (Ka-W-THz). Chapter 4 gives consideration to the experimental analysis of a cylindrical periodic cavity, and includes a range of measurements including transmission and reflection profiles, demonstration of transverse mode scattering in addition to power density and Q-factor measurements. With theoretical, numerical and experimental analysis complete, Chapter 5 is devoted to providing applications of this cavity to specific types of microwave device. Several examples are given and discussed in detail, i.e. beam voltage, current, field strength in order to illustrate the wide range of applications possible for this novel design. Chapter 6 is the concluding chapter, bringing together all conclusions and points of interest discovered throughout this work which also dedicates a significant section to possible future work.

2 Theoretical Model

2.1 Introduction

In order for us to understand the interaction(s) taking place inside the system, we must consider the modes present and how they evolve through the interaction region. This chapter will firstly consider EM wave evolution and propagation in a perfectly conducting cylindrical waveguide and then advance on these fundamentals to accommodate for the perturbation in our cavity, thus providing us with a more accurate analytical description of wave propagation and behaviour in our system.

Attempts will be made to provide a possible numerical and/or graphical solution to this problem and relevant conclusions are discussed.

This chapter commences with a brief description of the 2D feedback mechanism and how it affects the EM fields propagating in its vicinity (known as surface modes)

followed then by a description of the field structure in a smooth cylindrical waveguide (volume modes). An analytical proposal is then given which describes how these fields interact with each other leading us to decipher a dispersion diagram for the overall system.

2.2 Model Description

The interaction region used in this work consists of a shallow, chess-board type corrugation on the outer wall of a smooth cylindrical waveguide. The introduction of this corrugation allows for scattering of electromagnetic waves as they propagate in the vicinity of the corrugation. We will consider this design for cavities operating at a number of different frequencies (Ka – THz), which are all fundamentally similar in operation principle, where the corrugation amplitude is far less than the transverse dimension therefore the proposed theory applies to all cases where $a << D$, where a is the corrugation amplitude and D is the radius of the waveguide.

As our system is grossly oversized we must consider the modes propagating through the centre, also known as volume modes. These 'volume' modes are akin to those present in a smooth cylindrical waveguide. This issue was not present in the previous studies due to the presence of the inner conductor

2.2.1 Field Components

This section is given to finding the general solutions to Maxwell's equations for the specific case of wave propagation in a cylindrical transmission line or waveguide, having perfectly conducting (i.e. no attenuation) boundaries parallel to the *z*-axis. Application of the appropriate boundary conditions allows us to find a possible solution for wave dispersion in this cavity.

Assuming time harmonic fields with an $e^{i\omega t}$ dependence propagating along the z-axis, the electric and magnetic fields may be written as

$$\vec{\mathbf{E}} = \mathrm{Re}\left\{ A(z,t)\vec{\mathbf{E}}_s(r_\perp)e^{i(\omega t - k_z z)} \right\} \tag{2.1}$$

$$\vec{\mathbf{H}} = \mathrm{Re}\left\{ A(z,t)\vec{\mathbf{H}}_s(r_\perp)e^{i(\omega t - k_z z)} \right\} \tag{2.2}$$

Where $\vec{\mathbf{E}}_s$ and $\vec{\mathbf{H}}_s$ describe the transverse field structure inside the guide, $A(z,t)$ is the field amplitude, $r_\perp$ represents the transverse coordinates (r,θ) and k_z is the axial wave number. All fields obey the source free time harmonic Maxwell equations, which, for a simple, homogeneous, isotropic, linear medium where $\vec{\mathbf{D}} = \varepsilon\vec{\mathbf{E}}$ and $\vec{\mathbf{B}} = \mu\vec{\mathbf{H}}$ are given as

$$\nabla.\vec{\mathbf{E}} = \frac{\rho}{\varepsilon_0} \tag{2.3}$$

$$\nabla.\vec{\mathbf{B}} = 0 \tag{2.4}$$

$$\nabla\times\vec{\mathbf{E}} = -\frac{\partial\vec{\mathbf{B}}}{\partial t} \tag{2.5}$$

$$\nabla\times\vec{\mathbf{B}} = \mu_0\vec{\mathbf{J}} + \mu_0\varepsilon_0\frac{\partial\vec{\mathbf{E}}}{\partial t} \tag{2.6}$$

Manipulation of these allows us to obtain the field components of an electromagnetic wave. The corresponding field components are written as:

$$E_r = \frac{1}{p^2}\left(-j\beta\frac{\partial E_z}{\partial r} - \frac{j\omega\mu}{r}\frac{\partial H_z}{\partial\theta} \right) \tag{2.7}$$

$$E_\theta = \frac{1}{p^2}\left(-\frac{j\beta}{r}\frac{\partial E_z}{\partial \theta} + j\omega\mu\frac{\partial H_z}{\partial r} \right) \tag{2.8}$$

$$H_r = \frac{1}{p^2}\left(\frac{j\omega\varepsilon}{r}\frac{\partial E_z}{\partial \theta} - j\beta\frac{\partial H_z}{\partial r} \right) \tag{2.9}$$

$$H_\theta = \frac{1}{p^2}\left(-j\omega\varepsilon\frac{\partial E_z}{\partial r} - \frac{j\beta}{r}\frac{\partial H_z}{\partial \theta} \right) \tag{2.10}$$

$$\left[\frac{1}{r}\left(\frac{\partial}{\partial r} r \frac{\partial}{\partial r} + \frac{\partial}{\partial \theta}\frac{1}{r}\frac{\partial}{\partial \theta} \right) + p^2 \right] \begin{bmatrix} E_z \\ H_z \end{bmatrix} = 0 \tag{2.11}$$

$$p^2 = \omega^2 \mu_0 \varepsilon - \beta^2 \tag{2.12}$$

The term p represents the transverse wave number, ω the angular frequency, β the propagation constant of the fields and (ε, μ_0) the constitutive parameters of the medium in which the fields reside.

In general, the dielectric waveguide of circular geometry can support a family of circularly symmetric TE_{0m} and TM_{0m} modes (whose fields are independent of azimuthal coordinate) in addition to a range of hybrid HE_{nm} and EH_{nm} modes. Also, studies [1-3] have shown that improved guidance of surface waves is achieved when a perfectly conducting metal wire is coated with a thin sheet of low-loss dielectric material, this technique is also more commonly known as The Sommerfeld-Goubau (SG) Wire. The reader will be aware that this SG approximation is indeed different from that depicted in textbooks in that for the purpose of this work we have reversed the system such that we no longer have a solid core dielectric radiating into free space, instead we have a vacuum core encompassed by a thin dielectric layer. This is the approximation we will use for the purpose of our analytical studies as it allows us to fully describe the mode properties, both in the volume of our cavity, simultaneously and on the complex surface.

2.3 Formulation of Problem

The reader must understand that all prior analytical studies involving the 2D chessboard type corrugation were done so using a planar approximation of the system due to the presence of the inner conductor and/or consideration of a perturbation in one direction only, i.e. a 1D corrugation. This same approximation cannot be adopted here due to the absence of a central conductor and the presence of a 2D corrugation. The resulting field components can only be depicted as a sum of spatial harmonics of the system and not as a superposition of individual propagating waves, as per [4-7]. The shallow corrugation on the outer wall acts as to provide a perturbation in the effective permittivity of the electric fields in the vicinity of the structure, i.e. at the walls and can therefore be described as an effective dielectric, in that its presence has the same effect on overall field structure as an equivalent layer of low loss dielectric.

The full model can be considered similar to that of a radially inhomogeneous cylinder (a full generic description is given in Appendix B), consisting of three regions, with each concentric layer having its own permittivity, as illustrated in Figure 2.1.

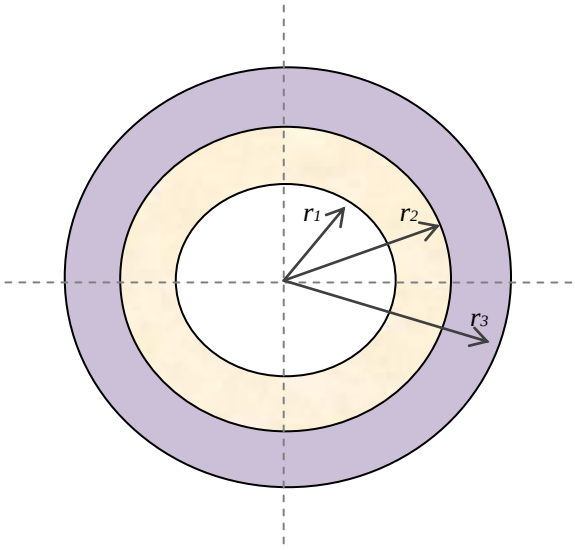

Figure 2.1: Cross sectional view of schematic model of shallow corrugation on the outer wall of metallic waveguide, represented as a thin layer dielectric.

The concentric layers of Figure 2.1 may be described as follows:

- Region 1, for $r < r_1$, is representative of the vacuum region, having permittivity ε_1 where $\varepsilon_1 \simeq \varepsilon_0$ as in this case this region is denoted by vacuum.

- Region 2, $r_1 < r < r_2$, is representative of the shallow corrugation and has permittivity ε_2.

- Region 3, for which $r_2 < r < r_3$ corresponds to the outer copper wall of our structure and is assumed to be a perfect conductor, having permittivity denoted by ε_3 . Beyond the perfect conductor, i.e. for $r > r_3$, in our case corresponds to free space. Only by consideration of the individual field components in each of these regions and simultaneous satisfaction of all corresponding boundary conditions, can an accurate analytical analysis of the field behaviour inside this complex system be given.

In general, the dielectric waveguide of circular geometry can support a family of circularly symmetric TE_{0m} and TM_{0m} modes (whose fields are independent of azimuthal coordinate) in addition to a range of hybrid HE_{nm} and EH_{nm} modes.

2.3.1 The Regional Field Components

The field components for each region are depicted via the use of equations (2.7) – (2.12) with the appropriate substitutions in place for permittivity. In Region 1, all field components must be finite, thus are represented as:

$$E_z^{(1)}(r,\theta) = \sum_{n=-\infty}^{\infty} A_1 J_n(p_1 r) e^{jn\theta} \tag{2.13}$$

$$H_z^{(1)}(r,\theta) = \sum_{n=-\infty}^{\infty} B_1 J_n(p_1 r) e^{jn\theta} \tag{2.14}$$

where the coefficients A_1 and B_1 are arbitrary constants which are also functions of *n*, such that $A_1 = A_1(n)$, where $n = (1,2,3,.....\infty)$. The transverse field components are found using equations (2.7) – (2.10) and using the appropriate substitutions for wave number $(p \equiv p_1)$ and permittivity $(\varepsilon \equiv \varepsilon_1)$

$$E_\theta^{(1)}(r,\theta) = \frac{1}{p_1^2} \sum_{n=-\infty}^{\infty} \left[\frac{\beta n}{r} A_1 J_n(p_1 r) + j\omega\mu_0 p_1 B_1 J_n'(p_1 r) \right] e^{jn\theta} \tag{2.15}$$

$$E_r^{(1)}(r,\theta) = \frac{1}{p_1^2} \sum_{n=-\infty}^{\infty} \left[-j\beta p_1 A_1 J_n'(p_1 r) + \frac{\omega\mu_0 n}{r} B_1 J_n(p_1 r) \right] e^{jn\theta} \tag{2.16}$$

$$H_r^{(1)}(r,\theta) = \frac{1}{p_1^2} \sum_{n=-\infty}^{\infty} \left[-\frac{\omega\varepsilon_1 n}{r} A_1 J_n(p_1 r) - j\beta p_1 B_1 J_n'(p_1 r) \right] e^{jn\theta} \tag{2.17}$$

$$H_\theta^{(1)}(r,\theta) = \frac{1}{p_1^2} \sum_{n=-\infty}^{\infty} \left[-j\omega\varepsilon_1 p_1 A_1 J_n'(p_1 r) + \frac{\beta n}{r} B_1 J_n(p_1 r) \right] e^{jn\theta} \tag{2.18}$$

Where the prime signifies the derivative of the Bessel function with respect to its argument, $J_n(p_1 r)$ is the Bessel function of the first kind of order n having argument $p_1 r$, and

$$p_1^{\,2} = k_1^{\,2} - \beta^2 \tag{2.19}$$

$$k_1^{\,2} = \omega^2 \mu_0 \varepsilon_1 \tag{2.20}$$

where p_1 represents the transverse wave number, k_1 the total wave number, β is the propagation constant, and ε_1 the effective permittivity of Region 1.

Similarly for Region 2, the low loss dielectric layer having permittivity ε_2, the axial field components are given as follows:

$$E_z^{(2)}(r,\theta) = \sum_{n=-\infty}^{\infty} \left[C_2 J_n(p_2 r) + C_2' Y_n(p_2 r) \right] e^{jn\theta} \tag{2.21}$$

$$H_z^{(2)}(r,\theta) = \sum_{n=-\infty}^{\infty} \left[D_2 J_n(p_2 r) + D_2' Y_n(p_2 r) \right] e^{jn\theta} \tag{2.22}$$

where C_2, C_2', D_2, D_2' are arbitrary constants.

Before calculating the transverse field components it is important to note that, due to the presence of the perfect conducting outer boundary in our system at $r \geq r_2$ there can be no outward flow of field beyond the r_2 boundary, i.e. the tangential fields must be zero:

$$E_z^{(2)}(r_2,\theta) = 0 \tag{2.23}$$

$$H_z^{(2)}(r_2,\theta) = 0 \tag{2.24}$$

Thus allowing us to express C_2' and D_2' in terms of C_2 and D_2 and simplify (2.21) and (2.22) as:

$$C_2' = -C_2 \frac{J_n(p_2 r_2)}{Y_n(p_2 r_2)} \tag{2.25}$$

$$D_2' = -D_2 \frac{J_n(p_2 r_2)}{Y_n(p_2 r_2)} \tag{2.26}$$

Allowing (2.23) and (2.24) to be written as

$$E_z^{(2)}(r,\theta)=\sum_{n=-\infty}^{\infty}\left[C_2 J_n(p_2 r)-C_2\frac{J_n(p_2 r_2)Y_n(p_2 r)}{Y_n(p_2 r_2)}\right]e^{jn\theta}, \tag{2.27}$$

and

$$H_z^{(2)}(r,\theta)=\sum_{n=-\infty}^{\infty}\left[D_2 J_n(p_2 r)-D_2\frac{J_n(p_2 r_2)Y_n(p_2 r)}{Y_n(p_2 r_2)}\right]e^{jn\theta} \tag{2.28}$$

Using these substitutions, the transverse fields can be found in the similar manner to Region 1, with the appropriate substitution of p by p_2 and ε by ε_2 and are given over the page in equations (2.29 – 2.32).

The transverse field components are:

$$E_r^{(2)}(r,\theta)=\frac{1}{p_2^2}\sum_{n=-\infty}^{\infty}\left[\begin{array}{l}-j\beta p_2 C_2\left(J_n'(p_2 r)+\dfrac{J_n(p_2 r_2)Y_n'(p_2 r)}{Y_n(p_2 r_2)}\right)+\\ \dfrac{\omega\mu_0 n}{r}D_2\left(J_n(p_2 r)-\dfrac{J_n(p_2 r_2)Y_n(p_2 r)}{Y_n(p_2 r_2)}\right)\end{array}\right]e^{jn\theta} \tag{2.29}$$

$$E_\theta^{(2)}(r,\theta)=\frac{1}{p_2^2}\sum_{n=-\infty}^{\infty}\left[\begin{array}{l}\dfrac{\beta n}{r}C_2\left(J_n(p_2 r)-\dfrac{J_n(p_2 r_2)Y_n(p_2 r)}{Y_n(p_2 r_2)}\right)\\ +j\omega\mu_0 p_2 D_2\left(J_n'(p_2 r)-\dfrac{J_n(p_2 r_2)Y_n'(p_2 r)}{Y_n(p_2 r_2)}\right)\end{array}\right]e^{jn\theta} \tag{2.30}$$

$$H_r^{(2)}(r,\theta)=\frac{1}{p_2^2}\sum_{n=-\infty}^{\infty}\left[\begin{array}{l}-\dfrac{\omega\varepsilon_2 n}{r}C_2\left(J_n(p_2 r)-\dfrac{J_n(p_2 r_2)Y_n(p_2 r)}{Y_n(p_2 r_2)}\right)-\\ j\beta p_2 D_2\left(J_n'(p_2 r)-\dfrac{J_n(p_2 r_2)Y_n'(p_2 r)}{Y_n(p_2 r_2)}\right)\end{array}\right]e^{jn\theta} \tag{2.31}$$

$$H_\theta^{(2)}(r,\theta)=\frac{1}{p_2^2}\sum_{n=-\infty}^{\infty}\begin{bmatrix}-j\omega\varepsilon_2 p_2 C_2\left(J_n'(p_2r)+\dfrac{J_n(p_2r_2)Y_n'(p_2r)}{Y_n(p_2r_2)}\right)+\\ \dfrac{\beta n}{r}D_2\left(J_n(p_2r)-\dfrac{J_n(p_2r_2)Y_n(p_2r)}{Y_n(p_2r_2)}\right)\end{bmatrix}e^{jn\theta} \quad (2.32)$$

Where the prime signifies the derivative of the function with respect to its argument, $Y_n(p_2r)$ is the second order Bessel function of order n and argument p_2r, and

$$p_2^{\,2}=\omega^2\mu_0\varepsilon_2-\beta^2 \quad (2.33)$$

$$k_2^{\,2}=\omega^2\mu_0\varepsilon_2 \quad (2.34)$$

In the case of Region 3, the assumed perfect conductor, it is not necessary to consider the decay or propagation of field components, as by definition the fields do not penetrate the surface of a perfect conductor. This somewhat simplifies our situation as we now have only two sets of field components and two boundary conditions to satisfy, although it is possible to include the resistive effect of the non-perfect metal which would in turn lead to a more complex situation as the modal dispersion would then have to be examined for at least three regions inclusive of the three simultaneous boundary conditions, added to the fact that one of these regions being metal, we then would then enter the territory of surface plasmons and related phenomenon. Although a very interesting and progressive area of scientific research, the time limitations on this work do not allow for such considerations to be adopted as yet.

2.3.2 A Method for Calculating the Dispersion Profile

The propagation constant β of the guided waves on this dielectric lined waveguide will be obtained via the dispersion relation, which is derived by enforcing the satisfaction of

all boundary conditions simultaneously. At the boundary surface $r = r_1$ the tangential fields must be continuous, that is,

$$E_z^{(1)}(r_1,\theta) = E_z^{(2)}(r_1,\theta) \tag{2.35}$$

$$H_z^{(1)}(r_1,\theta) = H_z^{(2)}(r_1,\theta) \tag{2.36}$$

$$E_\theta^{(1)}(r_1,\theta) = E_\theta^{(2)}(r_1,\theta) \tag{2.37}$$

$$H_\theta^{(1)}(r_1,\theta) = H_\theta^{(2)}(r_1,\theta) \tag{2.38}$$

Thus, expanding these out yields the following:

$$A_1 J_n(p_1 r_1) = C_2 J_n(p_2 r_1) - C_2 \frac{J_n(p_2 r_2) Y_n(p_2 r_1)}{Y_n(p_2 r_2)} \tag{2.39}$$

$$B_1 J_n(p_1 r_1) = D_2 J_n(p_2 r_1) - D_2 \frac{J_n(p_2 r_2) Y_n(p_2 r_1)}{Y_n(p_2 r_2)} \tag{2.40}$$

$$\begin{aligned} &\frac{\beta n}{r} A_1 J_n(p_1 r_1) + j\omega\mu_0 p_1 B_1 J_n'(p_1 r_1) = \\ &\frac{\beta n}{r} C_2 \left(J_n(p_2 r_1) - \frac{J_n(p_2 r_2) Y_n(p_2 r_1)}{Y_n(p_2 r_2)} \right) + j\omega\mu_0 p_2 D_2 \left(J_n'(p_2 r_1) - \frac{J_n(p_2 r_2) Y_n'(p_2 r_1)}{Y_n(p_2 r_2)} \right) \end{aligned} \tag{2.41}$$

$$-j\omega\varepsilon_1 p_1 A_1 J_n'(p_1 r_1) + \frac{\beta n}{r} B_1 J_n(p_1 r_1) =$$
$$-j\omega\varepsilon_2 p_2 C_2 \left(J_n'(p_2 r_1) + \frac{J_n(p_2 r_2) Y_n'(p_2 r_1)}{Y_n(p_2 r_2)} \right) + \frac{\beta n}{r} D_2 \left(J_n(p_2 r_1) - \frac{J_n(p_2 r_2) Y_n(p_2 r_1)}{Y_n(p_2 r_2)} \right)$$

(2.42).

The θ dependence and the summation have been eliminated for simplicity. Similarly, by satisfaction at the $r = r_2$ boundary such that the tangential fields must equal zero, i.e.:

$$E_z^{(2)}(r_2, \theta) = 0 \tag{2.43}$$

$$H_z^{(2)}(r_2, \theta) = 0 \tag{2.44}$$

$$E_\theta^{(2)}(r_2, \theta) = 0 \tag{2.45}$$

$$H_r^{(2)}(r_2, \theta) = 0 \tag{2.46}$$

Corresponding to (again omitting the summation and exponent terms);

$$C_2 J_n(p_2 r_2) - C_2 \frac{J_n(p_2 r_2) Y_n(p_2 r_2)}{Y_n(p_2 r_2)} = 0 \tag{2.47}$$

$$D_2 J_n(p_2 r_2) - D_2 \frac{J_n(p_2 r_2) Y_n(p_2 r_2)}{Y_n(p_2 r_2)} = 0 \tag{2.48}$$

$$\frac{\beta n}{p_2^2 r_2} C_2 \left(J_n(p_2 r_2) - \frac{J_n(p_2 r_2) Y_n(p_2 r_2)}{Y_n(p_2 r_2)} \right) + \frac{j\omega\mu_0 D_2}{p_2} \left(J_n'(p_2 r_2) - \frac{J_n(p_2 r_2) Y_n'(p_2 r_2)}{Y_n(p_2 r_2)} \right) = 0$$

(2.49)

$$-\frac{\omega\varepsilon_2 n}{p_2^2 r_2}C_2\left(J_n(p_2r_2)-\frac{J_n(p_2r_2)Y_n(p_2r_2)}{Y_n(p_2r_2)}\right)-\frac{j\beta D_2}{p_2}\left(J_n'(p_2r_2)-\frac{J_n(p_2r_2)Y_n'(p_2r_2)}{Y_n(p_2r_2)}\right)=0 \tag{2.50}$$

There now exists two sets of simultaneous equations for the unknown coefficients:

$$A_1, B_1, C_2(r_1), C_2(r_2), D_2(r_1), D_2(r_2)$$

where: $C_2(r_1) \neq C_2(r_2)$ *and* $D_2(r_1) \neq D_2(r_2)$.

The fields at the r_1 boundary satisfy:

$$\begin{bmatrix} A_1 \\ B_1 \\ C_2(r_1) \\ D_2(r_1) \end{bmatrix} \begin{bmatrix} m_{11} & 0 & m_{13} & 0 \\ 0 & m_{22} & 0 & m_{24} \\ m_{31} & m_{32} & m_{33} & m_{34} \\ m_{41} & m_{42} & m_{43} & m_{44} \end{bmatrix} = 0 \tag{2.51}$$

where:

$$m_{11} = -J_n(p_1r_1) \tag{2.52}$$

$$m_{13} = J_n(p_2r_1) - \frac{J_n(p_2r_2)Y_n(p_2r_1)}{Y_n(p_2r_2)} \tag{2.53}$$

$$m_{22} = -J_n(p_1r_1) \tag{2.54}$$

$$m_{24} = J_n\left(p_2 r_1\right) - \frac{J_n\left(p_2 r_2\right) Y_n\left(p_2 r_1\right)}{Y_n\left(p_2 r_2\right)} \tag{2.56}$$

$$m_{31} = -\frac{\beta n}{r_1} J_n(p_1 r_1) \tag{2.56}$$

$$m_{32} = -j\omega\mu_0 p_1 J_n'(p_1 r_1) \tag{2.57}$$

$$m_{33} = \frac{\beta n}{r_1}\left(J_n\left(p_2 r_1\right) - \frac{J_n\left(p_2 r_2\right) Y_n\left(p_2 r_1\right)}{Y_n\left(p_2 r_2\right)} \right) \tag{2.58}$$

$$m_{34} = j\omega\mu_0 p_2\left(J_n'\left(p_2 r_1\right) - \frac{J_n\left(p_2 r_2\right) Y_n'\left(p_2 r_1\right)}{Y_n\left(p_2 r_2\right)} \right) \tag{2.59}$$

$$m_{41} = j\omega\varepsilon_1 p_1 J_n'(p_1 r_1) \tag{2.60}$$

$$m_{42} = -\frac{\beta n}{r_1} J_n(p_1 r_1) \tag{2.61}$$

$$m_{43} = -j\omega\epsilon_2 p_2\left(J_n'\left(p_2 r_1\right) + \frac{J_n\left(p_2 r_2\right) Y_n'\left(p_2 r_1\right)}{Y_n\left(p_2 r_2\right)} \right) \tag{2.62}$$

$$m_{44} = \frac{\beta n}{r_1}\left(J_n\left(p_2 r_1\right) - \frac{J_n\left(p_2 r_2\right) Y_n\left(p_2 r_1\right)}{Y_n\left(p_2 r_2\right)} \right) \tag{2.63}$$

The fields at the r_2 boundary satisfy: (overpage)

$$\begin{bmatrix} A_1 \\ B_1 \\ C_2(r_2) \\ D_2(r_2) \end{bmatrix} \begin{bmatrix} 0 & 0 & n_{13} & 0 \\ 0 & 0 & 0 & n_{24} \\ 0 & 0 & n_{33} & n_{34} \\ 0 & 0 & n_{43} & n_{44} \end{bmatrix} = 0 \tag{2.64}$$

where:

$$n_{13} = J_n(p_2 r_2) - \frac{J_n(p_2 r_2) Y_n(p_2 r_2)}{Y_n(p_2 r_2)} \tag{2.64}$$

$$n_{24} = J_n(p_2 r_2) - \frac{J_n(p_2 r_2) Y_n(p_2 r_2)}{Y_n(p_2 r_2)} \tag{2.66}$$

$$n_{33} = \frac{\beta n}{p_2^2 r_2}\left(J_n(p_2 r_2) - \frac{J_n(p_2 r_2) Y_n(p_2 r_2)}{Y_n(p_2 r_2)} \right) \tag{2.67}$$

$$n_{34} = \frac{j\omega\mu_0}{p_2}\left(J_n'(p_2 r_2) - \frac{J_n(p_2 r_2) Y_n'(p_2 r_2)}{Y_n(p_2 r_2)} \right) \tag{2.68}$$

$$n_{43} = -\frac{j\omega\varepsilon_2}{p_2}\left(J_n'(p_2 r_2) - \frac{J_n(p_2 r_2) Y_n'(p_2 r_2)}{Y_n(p_2 r_2)} \right) \tag{2.69}$$

$$n_{44} = \frac{\beta n}{p_2^2 r_2}\left(J_n(p_2 r_2) - \frac{J_n(p_2 r_2) Y_n(p_2 r_2)}{Y_n(p_2 r_2)} \right) \tag{2.70}$$

It is clear that if the determinant of the above set of simultaneous equations is set to zero, the dispersion relation for the inhomogeneous dielectric cylinder may be achieved. However, as the size of the resultant is directly proportional to the number of layers, it becomes efficient to try to reduce the problem. One such proposed method is described in [52] which involves the reduction of a large matrix to a set of, more manageable, 4 x 4 matrices, thus eliminating the need for computation of large matrices. This aside, the task of identifying the $\omega vs.\beta$ behaviour for various modes is complex and difficult, although not impossible, to solve analytically for each specific mode as both β and permittivity ε are frequency dependant.

Due to various time constraints I did not manage to complete this task of reducing (and solving) for the dispersion profile of the multi-layer system, although without a doubt it can be added to a list of 'future developments' necessary in order for the mode behaviours in this system to be fully understood. I did however commence numerical calculations so as to try to understand how the dispersion plots could be formed. I consulted reference [53] and tried to replicate the plots given on page 250 which is a single boundary system and is formed by a solid core dielectric, i.e. the boundary is the dielectric-air interface. The graphs represent only the TE and TM modes having zero azimuthal dependence, which allow each of them to be graphed separately and overlaid to find the intersection points. This process is only possible for azimuthally symmetric waves, where the total field can be split into its TE and TM counterparts; generally due to the more involved boundary conditions it is not possible to separate the fields.

My reasoning behind this task was with the idea that I could separate both the surface fields propagating along the dielectric and volume modes propagating through the body of the structure of the system; plot them separately then overlay them to find the intersection points allowing me to construct a dispersion diagram. I did manage to successfully replicate the individual plots (of page 250, reference [2]) using Mathematica®, although upon trying to superimpose them yielded an error in Mathematica®. This clearly needs further investigation as does this 'graph overlay'

method in general as to whether or not it would provide viable results (if any) as to describe the modal dispersion for a multi-layer model.

2.4 Discussion

This chapter has given careful consideration to the analytical description of the mode structure inside this complex cavity structure and also how a potential solution can be reached. The modes propagating in the volume of our system are akin to those of a smooth cylindrical waveguide, whilst modes present on the surface are consequently presented as hybrids, due to the dielectric representation of the 2D lattice. Together the entire system may be approximated to that of a smooth perfect conducting system, having hybrid mode 'regions' that correspond to the interactions between these surface and volume waves. This of course needs further investigation in itself as the prospect of wave propagation in a single boundary dielectric is complex in its own rights without the further introduction of additional boundary conditions.

3 Numerical Modelling

3.1 Introduction

This chapter gives consideration to the electromagnetic wave evolution and interactions taking place inside an interaction region defined by a low contrast periodic lattice. Numerical investigations were carried out in order to determine the mode structure inside various geometry cavities where the sizes were chosen such that the interaction regions would operate at specific frequencies, predominantly in the Ka – W – THz frequency ranges, independently. In order to provide coupling between the input fields and the waves of the cavity it is necessary to incorporate a TEM stub to the input port, this is not required in the presence of an active media such as an electron beam as there will be fields present.

3.2 Numerical Modelling Methods

There are many different numerical techniques used for solving the Maxwell equations although common to all numerical approaches is the act of separating the desired space into sub-domains, where solutions can be found more easily. To solve the full problem, all single-entity solutions are summed up in a usually large system of equations, which need to be solved in one way or another. When discussing the properties of the different methods, it is necessary to classify them where the major point of difference is the domain in which they are operating. This is either the time domain or the frequency domain. On the time domain side we have the Finite Integration Technique (FIT) [54,55], the Finite Difference Time Domain (FDTD) in its explicit [56], [57] or implicit [58,59] variants and also the Transmission Line Matrix (TLM) method [60], [61]. The frequency domain is represented by the Finite Element (FE) method [62,63], the FIT and the Method of Moments solvers. All of these methods are volume discretization methods, except for the MoM, which is a surface discretization method.

For the purposes of this research, both FDTD and FI solver based codes were used. The FDTD code used was Magic©, which solves the partial differential form of the Maxwell equations which are discretized using the central-difference approximation to the space and time partial derivatives. The Finite Integration based modeller used was CST Microwave Studio, where the FI technique solves the integral form of Maxwell's equations. The use of these two different types of solver allows for consistency checks to be carried out.

3.3 Numerical Study of Ka-Band Cavity

Performed using both Magic and CST Microwave Studio, the mode structure inside the Ka-band cavity was derived in combination with analytical predictions. The dimensions of the structure are as follows: radius = 40mm, number of azimuthal variations = 28, periodicity of corrugation is 8mm longitudinal with corrugation amplitude equal to 1mm, can be seen in Figure 3.1.

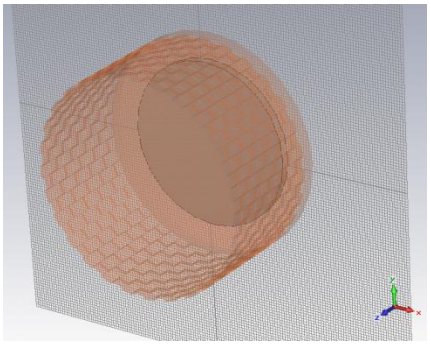

Figure 3.1: Cavity design for operation in the Ka frequency region.

3.3.1 Magic Results

Using Magic we were able to find the resonant frequency of this cavity and at this frequency view the corresponding field components. The relevant Magic output files are show in Figure 2. The system is excited by a broadband TEM pulse (30 – 40GHz) resulting in the main resonant frequency occurring at ~37GHz with smaller, although notable peaks occurring at ~29GHz and ~33GHz, as per Figure 3.2(a). Although these are small compared to the main resonance but they are worth noting and will be discussed later in this section. Considering only the main resonance observed at ~37GHz and looking at its field components, we can clearly see the induction of surface current. This is identified by looking at the E_ϕ, B_ρ and B_z field structure shown in Figure 3.2, parts (b) – (d), where the number of azimuthal variations is exactly equal to that of the structure which in this case is equal to 28, and the number of radial variations is equal to one.

If we now consider the remaining field components B_ϕ, E_ρ and E_z, shown in Figure 3.2, parts (e) – (i), we can see that there exists variation across the radius but there is no variation in azimuthal field. This suggests the strong presence of a type $TM_{0,n}$ mode, where *n* relates to the number of radial field variations present, and in this case equal to ten.

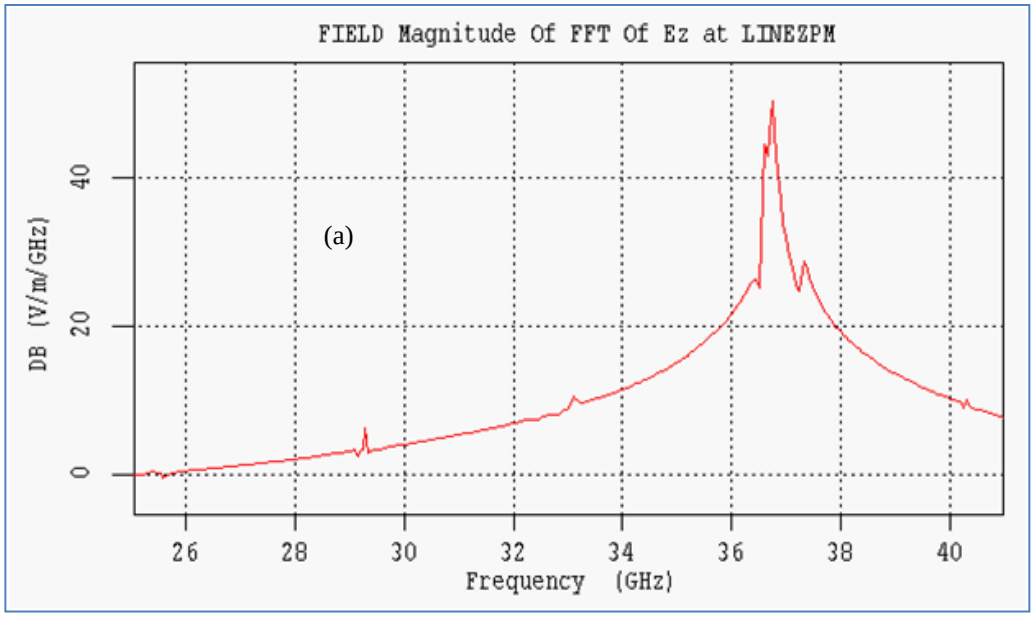

Figure 3.2(a): Magic output results for Ka-band simulation, demonstrating the resonant frequency of the cavity to be ~37GHz.

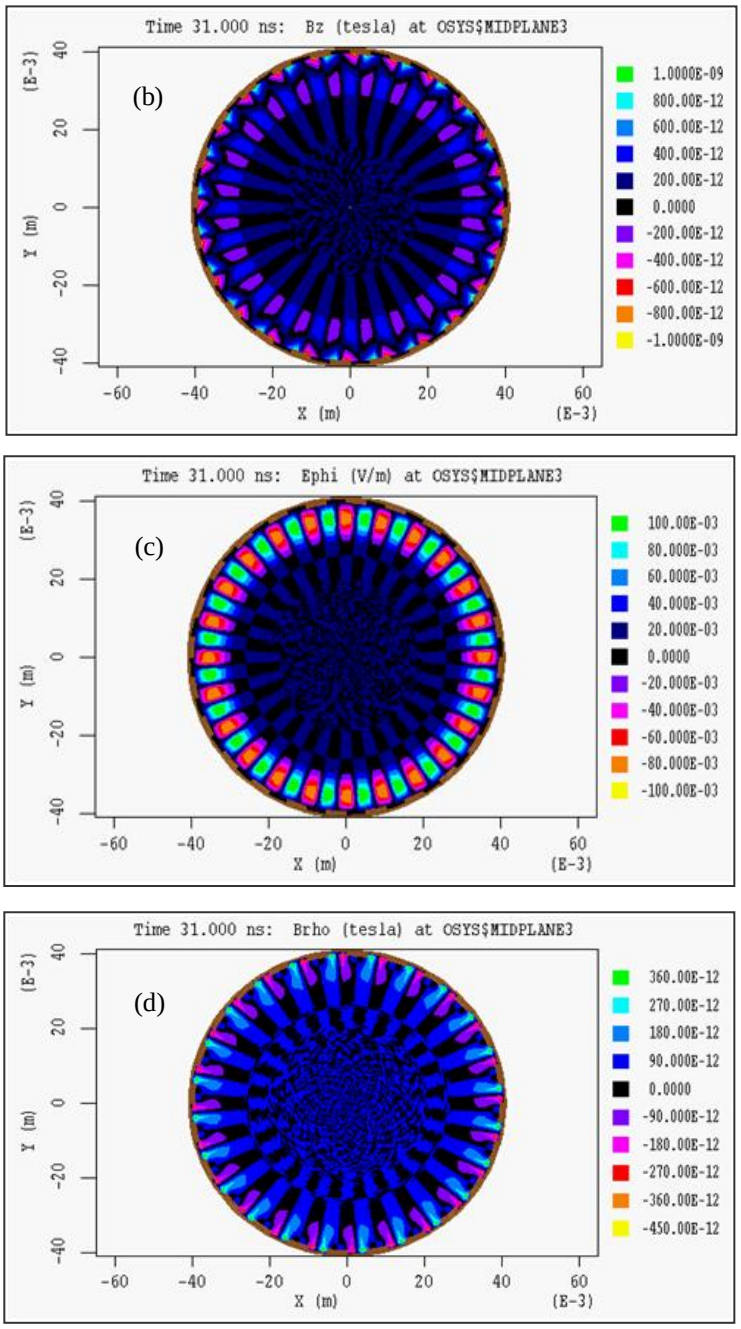

Figure 3.2 (b) – (d): Magic output graphics for the Ka-band simulation showing the field components corresponding to the excitation of surface currents on the structure, where b) is a cross-section view of the longitudinal magnetic component, c) is a cross-sectional view of the azimuthal electric field and d) is the radial magnetic field, again as a cross-section.

(e)

(f)

(g)

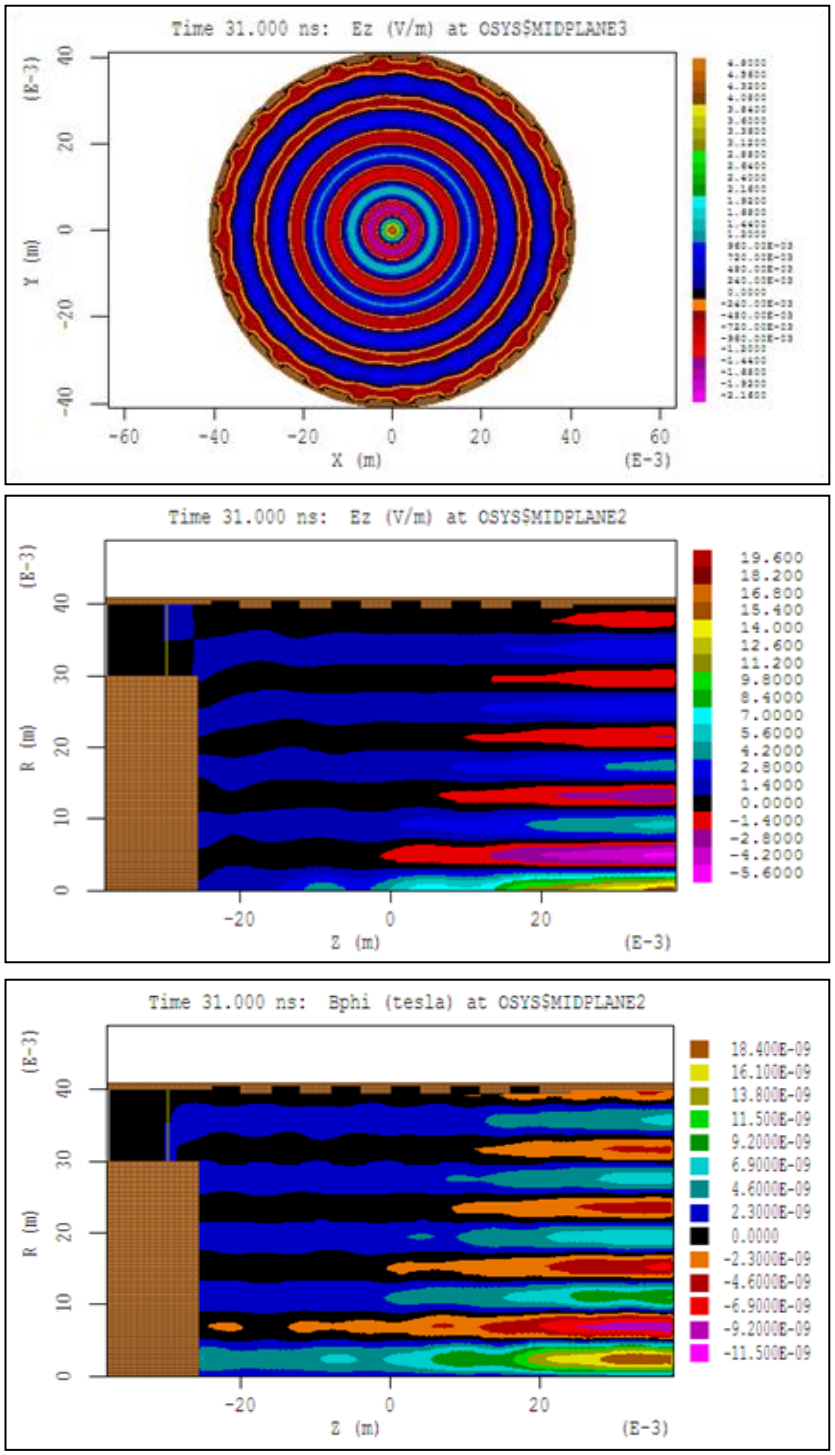

Figure 3.2 (e) – (g): Magic output graphics for the Ka-band simulation showing the field components corresponding to the excitation of volume modes at the main resonance of approx. 37GHz and displaying no azimuthal variation and 10 radial variations, with e) showing a cross-section view of the longitudinal electric component, f) is the equivalent longitudinal view and g) is the magnetic field around the azimuth.

(h)

(i)

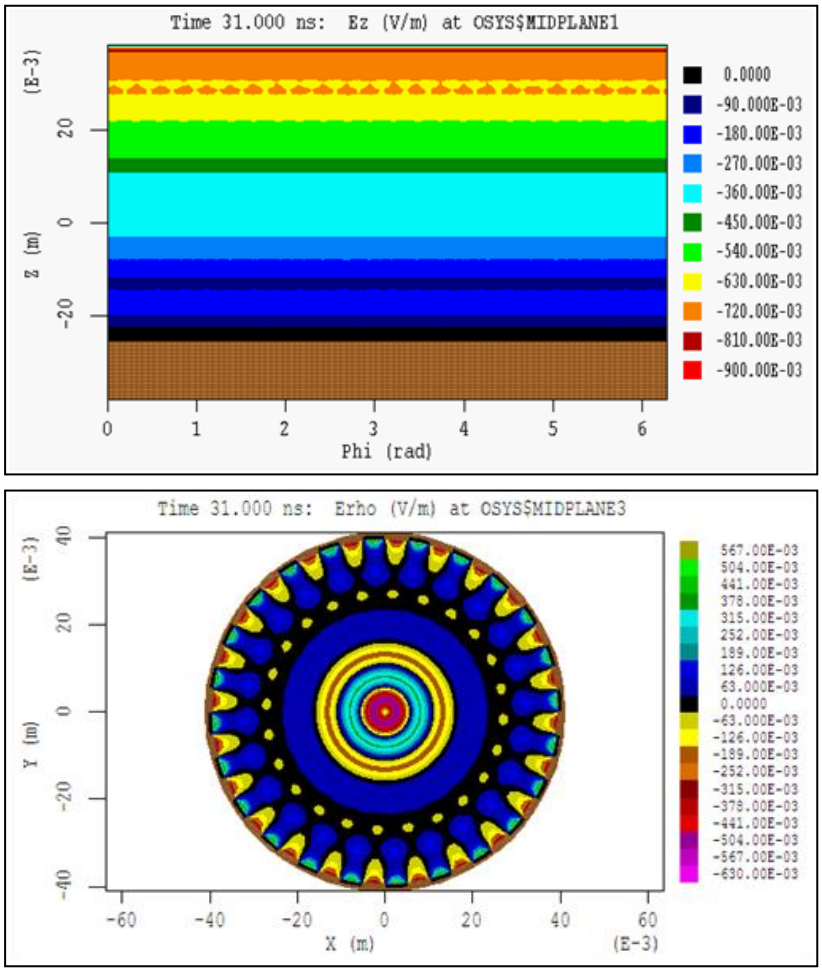

Figure 3.2 (h) – (i): Magic output graphics for the Ka-band simulation showing the field components corresponding to the excitation of volume modes at the main resonance of approx. 37GHz and displaying no azimuthal variation and 10 radial variations, h) is the axial electric field only as viewed from top down, i.e. bird's eye view, and i) is the radial electric field component, when viewed as a cross-section.

Looking at all components of Figure 3.2 it can be deducted that the resonant frequency of this cavity occurs at ~37GHz which may correspond to the interaction between two types of mode:

- A mode whose components are predominantly transverse, having 28 azimuthal variations and one radial, we call this the surface mode $EH_{28,1}$

- A mode having no azimuthal variation and 10 radial variations, i.e. the volume mode $TM_{0,10}$.

This concludes the field analysis for resonance corresponding to ~37GHz and now (briefly) the smaller resonance, occurring at ~33GHz is discussed in the next sub-section.

Resonance at 33GHz

In order to examine only this resonance, the program was edited to narrow the bandwidth of the incident TEM pulse, i.e. in the range 32 – 34GHz. Looking at the field components corresponding to the resonance occurring at ~33GHz, given in Figure 3.3, we can see a very similar mode structure to that depicted previously for the 37GHz resonance, namely the presence of both surface and volume modes. The field structure of the surface mode is demonstrated in Figure 3.3(a) – (c) and is in fact identical to that of the 37GHz resonance with the only exception that the amplitude of the relative field strength is much lower than those corresponding to the 37GHz peak. Likewise, the components relating to the volume mode: B_ϕ, E_z and E_ρ (shown in Figure 3.3(d) – (f)) are comparable in that they display a definite number of radial variations and none around the azimuth. For this 33GHz resonance the number of radial variations is equal to 9 and not 10 as in the 37GHz resonant case, this is evident upon comparison of the B_ϕ components of each interaction, displayed in Figure 3.4.

(a)

(b)

(c)

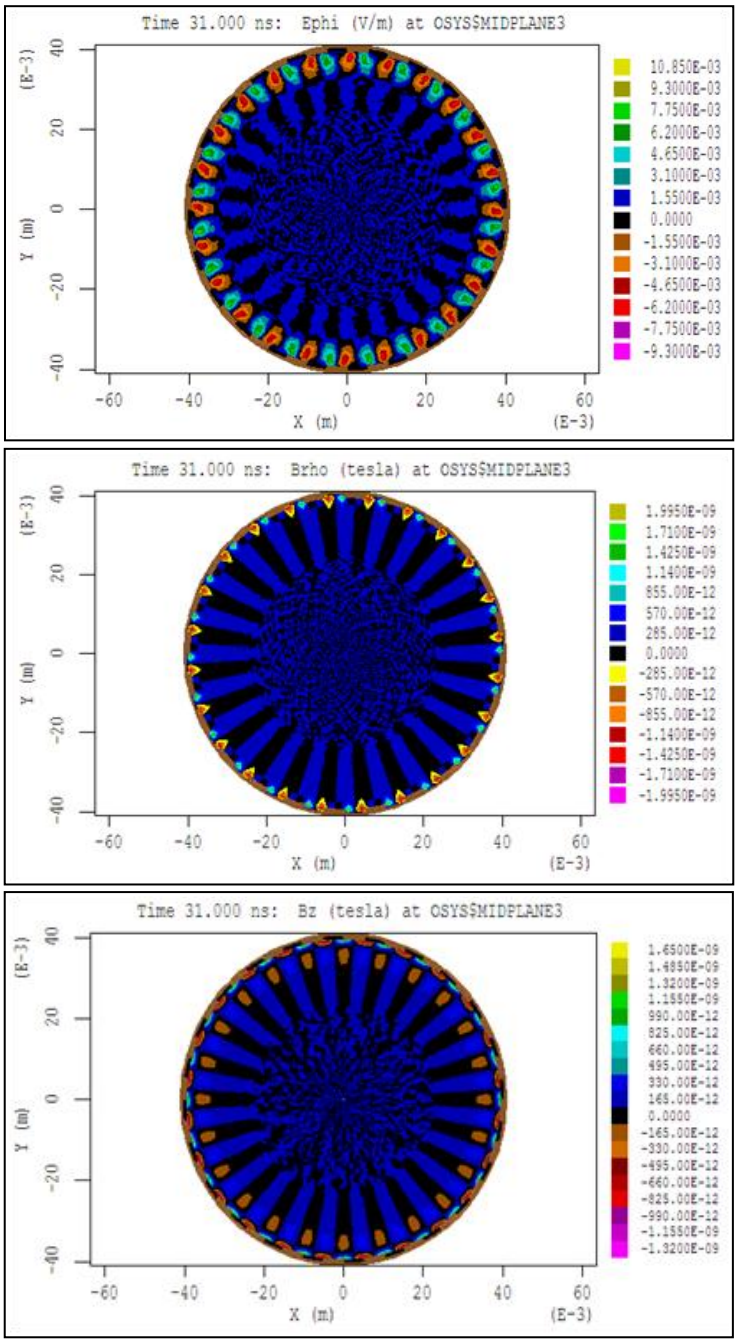

Figure 3.3(a) – (c): Field components corresponding to the surface mode of the 33GHz observed resonance, where a) is a cross-section view of the radial electric field, b) and c) are the same views of the magnetic radial and axial components.

(d)

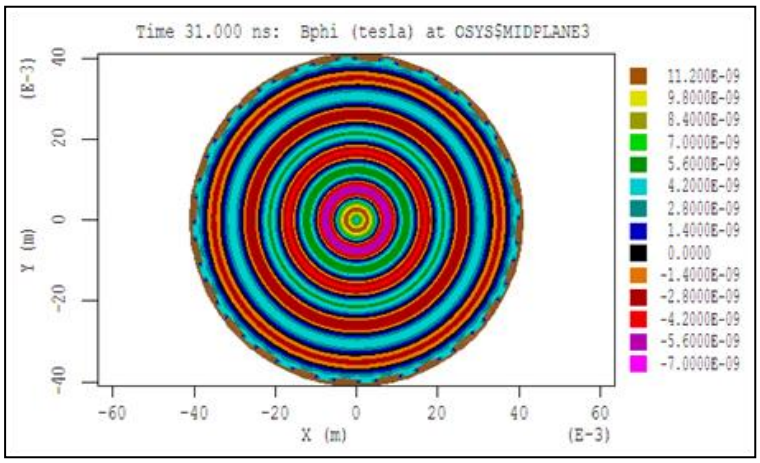

(e)

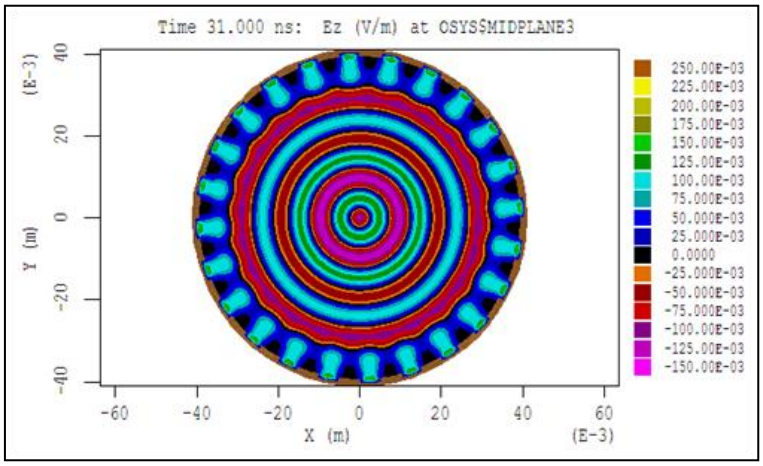

(f)

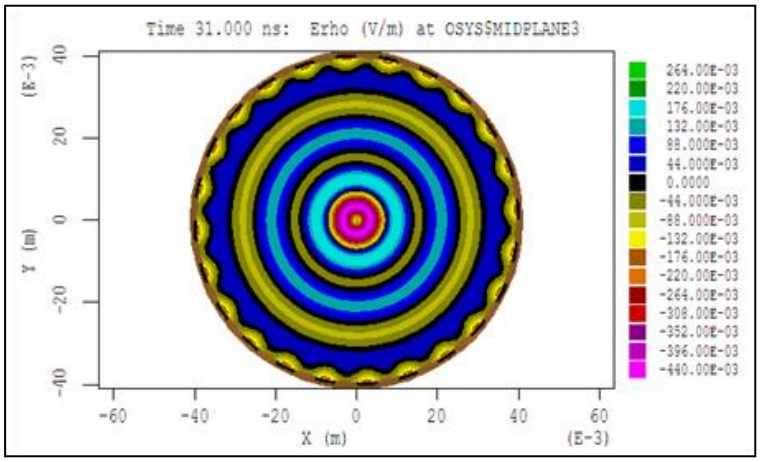

Figure 3.3 (d) – (f): Magic output graphics for the Ka-band simulation showing the field components corresponding to the volume mode of the 33GHz resonance, where d) is the radial magnetic flux component, e) is the axial electric and f) the radial electric fields, all viewed along a cross-section.

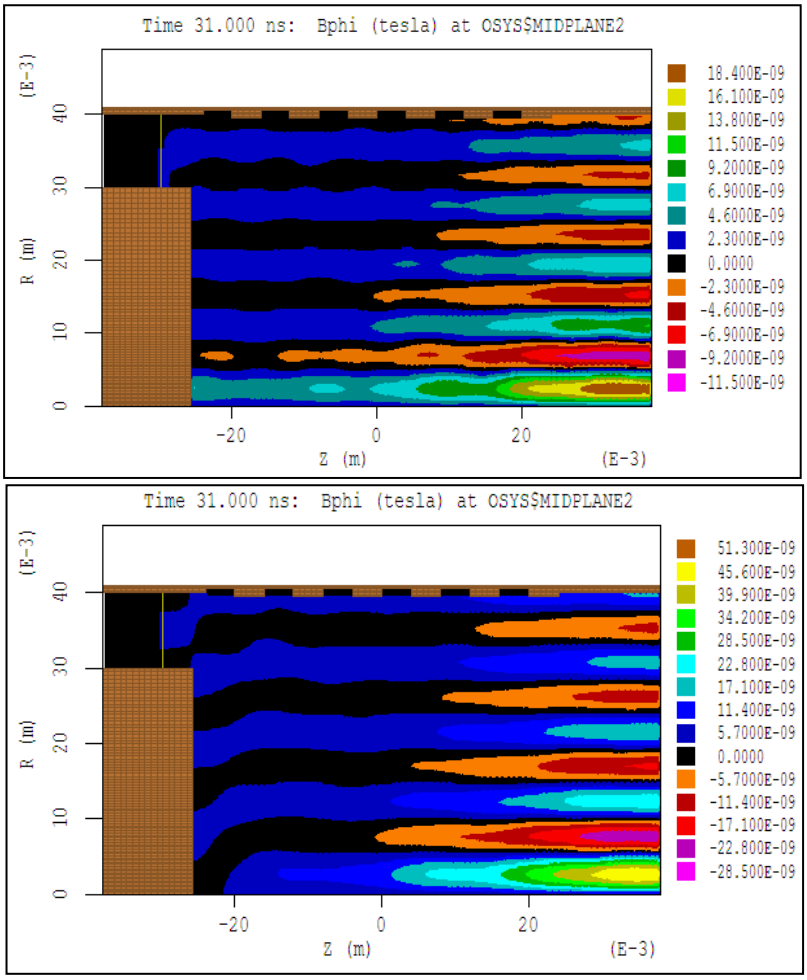

Figure 3.4: Comparison of field components illustrating different radial variations and their respective field strengths where a) is the 33GHz resonance and b) that of 37GHz.

In summary to this section it has been found that coupling between a surface wave having 28 azimuthal and one radial variation, i.e. $EH_{28,1}$ and a volume wave having zero azimuthal and nine radial, i.e. $TM_{0,9}$ occurs, resulting in a resonance peak at ~33GHz.

This resonance however is minor in comparison to the dominant resonance of ~37GHz, which occurs for the $EH_{24,1}$ - $TM_{0,10}$ interaction.

An important point to note is that we cannot say for sure whether the surface mode is in fact EH or HE type or the relative compositions of each, as we can only (using Magic) visualise the resultant field components. Extensive analysis of mode patterns, and indeed their excitation order within the system, is achievable via the use of Microwave Studio and is detailed in the next section.

3.3.2 CST Microwave Studio Results

Using CST Microwave Studio (MWS) it is possible to identify the mode excitation order inside the specified interaction region. The exact same cavity dimensions were entered into MWS and run through the 'transient' solver and it was found that the modes excited (and their order) follow closely to those of the equivalent smooth waveguide system (assuming a perfect electrical and thermal conductor). The modes excited are in fact identical with the exception that, at specific frequency 'bands' there exists coupling between adjacent modes, resulting in the designation 'hybrid' in MWS. Table 3.1 (given below) is an extract taken from the full mode order list, which is provided in Appendix C, and includes results predicted by theory and those given by MWS. To give the reader better understanding the first 40 modes for the Ka-band design (radius of 40mm) are given below and the term 'Designation' refers to the mode number as assigned by MWS and the asterisk to some of the designations is indicative of a hybrid mode labelling. It's important to point out that MWS list both polarisations for each mode as separate independent modes as observed in the Table 3.1. Looking at these mode numbers, we can easily see the presence of the 2D corrugation having an effect on specific modes – denoted by the term 'hybrid', all other modes are almost a perfect match to those of an equivalent smooth waveguide. These modes can also be visualised by means of contour plots as shown below, where the first hybrid mode is shown. We know from the table above that this hybrid lies in place of the $TE_{1,2}$ (modes 15* & 16*) and also in place of

the left hand polarisation of the $TE_{4,1}$ mode (mode 14*) and we therefore assume that these hybrids are as a result of these combinations. This fits well with the corresponding contour plot, Figure 3.5, and is a perfect demonstration of surface mode coupling via the chessboard structure.

Mode Order Listing

		Analytical		MWS	
Mode	Root	Kc (m-1)	fc (GHz)	fc (GHz)	Designation
TE1,1	1.84118	46.6121519	2.2255663	2.22	1 & 2
TM0,1	2.40483	60.88177215	2.9068905	2.92	3
TE 2,1	3.05424	77.32253165	3.6918789	3.67	4 & 5
TM11/TE01	3.83171	97.00531646	4.6316627	4.63	6 & 7, 8
TE3,1	4.20119	106.3592405	5.0782797	5.04	9 & 10
TM2,1	5.13562	130.0156962	6.2077922	6.24	11 & 12
TE4,1	5.31755	134.621519	6.4277041	6.34	13 & 14*
TE1,2	5.33144	134.9731646	6.4444939	HYBRID	15* & 16*
TM0,2	5.52008	139.7488608	6.6725166	6.7	17
TM3,1	6.38016	161.523038	7.712157	7.75	20 & 21
TE5,1	6.41562	162.4207595	7.75502	7.68	18 & 19
TE2,2	6.70613	169.775443	8.1061803	8.09	22 & 23
TE0,2	7.01559	177.6098734	8.4802468	8.477	24
TM1,2	7.01559	177.6098734	8.4802468	8.525	25 & 26
TE6,1	7.50127	189.9055696	9.067323	8.966	27 & 28
TM4,1	7.58834	192.1098734	9.1725708	8.22	29 & 30
TE3,2	8.01524	202.9174684	9.6885954	9.67	31 & 32
TM2,2	8.41724	213.0946835	10.174522	HYBRID	33* & 34*
TE1,3	8.53632	216.1093671	10.318462	HYBRID	35* & 36*
TE7,1	8.57784	217.1605063	10.36865	10.31	37 & 38*
TM0,3	8.65373	219.0817722	10.460384	10.51	39
TM5,1	8.77148	222.0627848	10.602717	10.65	40 & 41

* = Denotes Hybrid mode

Table 3.1. Mode Order Comparison with analytical predictions listed against MWS output.

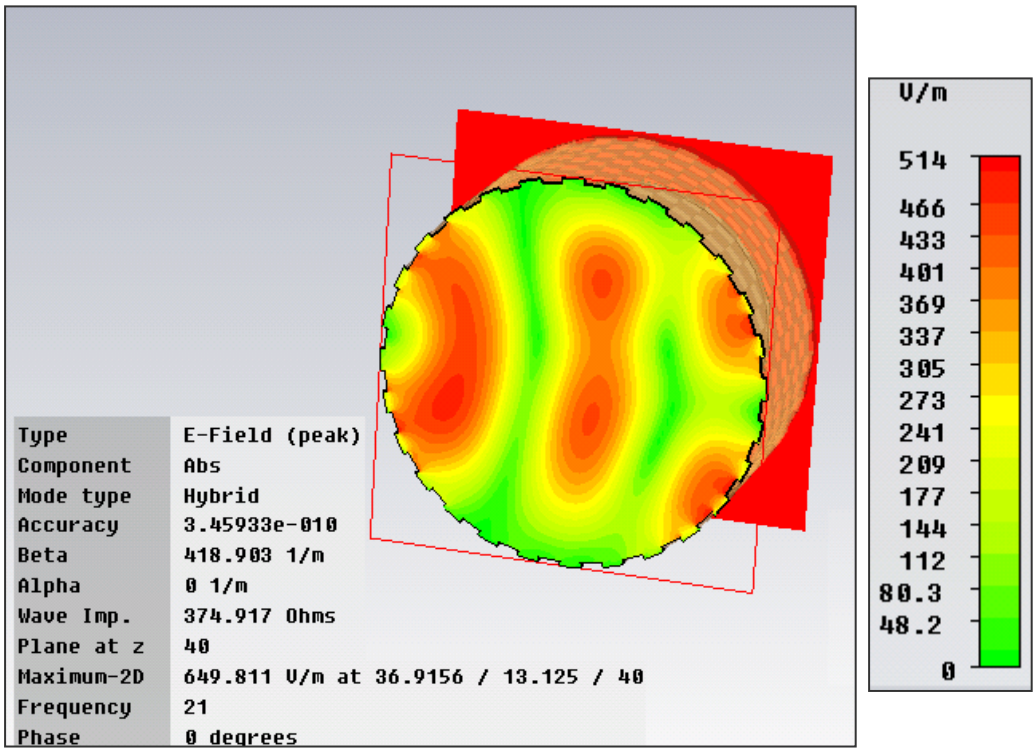

Figure 3.5: Microwave Studio Results demonstrating the coupling of waves on the surface of the 2D corrugation and resulting in hybrid mode formation.

This example of transverse wave coupling was given to show that it is indeed possible to identify, to a degree, which modes are being effectively coupled via the corrugation. This example was straightforward as we were considering only the first say 20 - 15 modes. The problem however becomes far more complex as we climb through the mode probabilities as one must consider not only the modes in the vicinity of the 'hybrid' mode (or modes) but we must also consider each and every other mode present in the system at that instance, i.e. give consideration to all the other modes as propagating modes up until that point. This makes the task of identifying the individual modes coupled on the corrugation impossible. With this in mind we then look at the other region of hybrid modes present in this system which occurs at frequencies ~33GHz and then again ~37GHz. These results are given in Table 3.2 where (a) corresponds to ~

33GHz and (b) to ~37GHz. Only the sections involving the hybrid modes have been shown here all the modes before/after these follow the order of the smooth waveguide.

(a) (b)

Resonance @ 33GHz			Resonance @ 37GHz		
Designation	Type	fc(GHz)	Designation	Type	fc(GHz)
367	TE5,7	32.665	447 & 448	TE27,1	36.05
368	Hybrid	-	449	TE18,3	36.32
369	Hybrid	-	450	TM24,1	36.61
370	Hybrid	-	451	Hybrid	-
371	Hybrid	-	452	Hybrid	-
372	Hybrid	-	453	Hybrid	-
373	Hybrid	-	454	Hybrid	-
374	TM4,7	32.905	455	Hybrid	-
375 & 376	TE16,3	33.02	456	Hybrid	-
377	Hybrid	-	457	Hybrid	-
378 & 379	TM9,5	33.155	458 & 459	TM6,7	-
380	Hybrid	-	460	Hybrid	-
381	Hybrid	-	461	Hybrid	-
382	Hybrid	-	462	Hybrid	-
383	Hybrid	-	463	Hybrid	-
384	Hybrid	-	464	Hybrid	-
385	Hybrid	-	465	Hybrid	-
386	Hybrid	-	466	Hybrid	-
387	Hybrid	-	467	Hybrid	-
388	Hybrid	-	468	Hybrid	-
389	Hybrid	-	469	Hybrid	-
390	Hybrid	-	470	Hybrid	-
391	Hybrid	-	471	Hybrid	-
392	TM12,4	33.79	472	Hybrid	-
393	TE8,6	33.79	473	Hybrid	-
394	Hybrid		474	TM14,4	37.34
395	TM15,3	33.9	475	Hybrid	-
			476	Hybrid	-
			477	TE10,6	37.38
			478	Hybrid	-
			479	Hybrid	-
			480	Hybrid	-

Table 3.2. Extracts from MWS mode order table for both (a) ~33GHz and (b) ~37GHz resonance.

The corresponding contour plots are also shown for each of the resonances, Figure 3.6, and although it's difficult to determine anything useful from the 'absolute' contour plot we can break down the resultant plot into its respective electric and magnetic components, thus simplifying the model greatly. In doing this it was discovered that the majority of hybrid modes in and around the 33GHz region posses fields having 28 azimuthal variations in combination with a varying number of radial indices. Shown in Figure 3.6 are (a) the electric and (b) the magnetic longitudinal components of mode number 372, corresponding to the ~33GHz resonance, and (c) the electric and (d) the magnetic profiles for mode number 486 which lies in the ~37GHz range of hybrids.

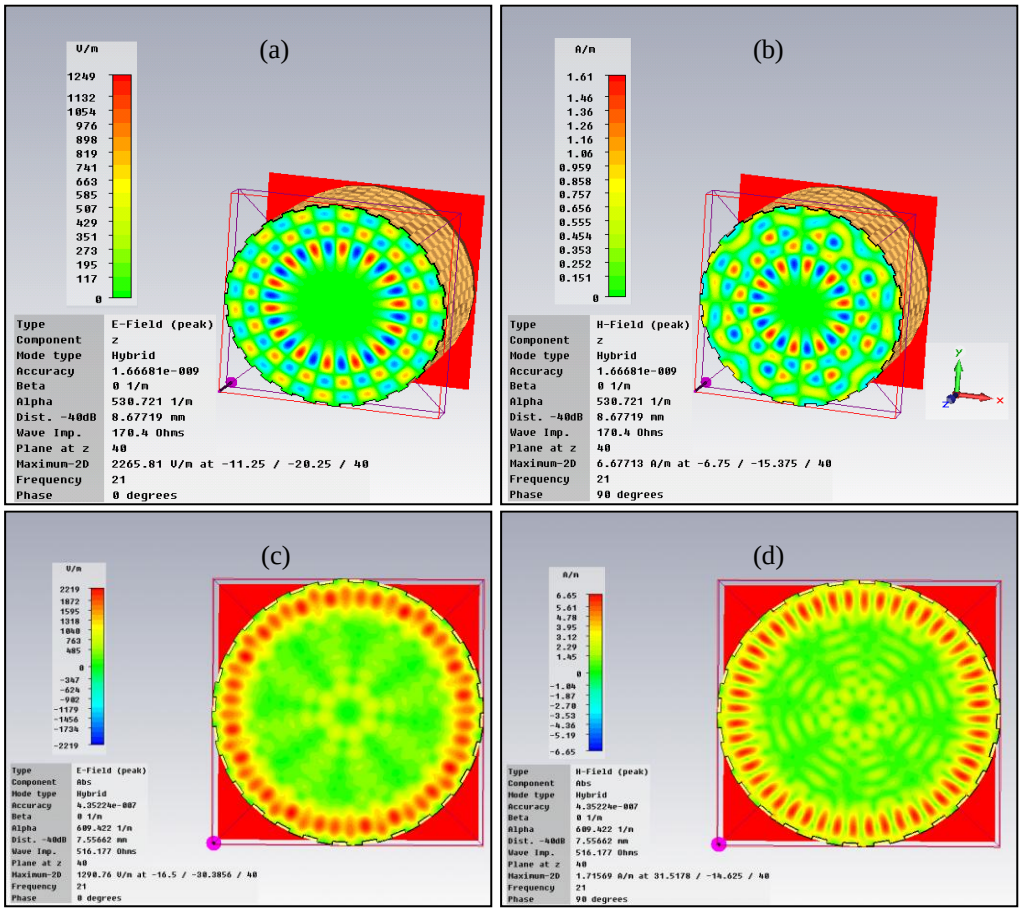

Figure 3.6: Results from Microwave Studio illustrating the field components for both the 33GHz and 37GHz resonances, where a) is the electric field of the 33GHz resonance with b) the magnetic longitudinal component and both c) and d) correspond the electric and magnetic components for the 37GHz resonance.

In summary to the section devoted to the Ka-band cavity analysis, it has been shown that the mode structure can be identified, and this is concurrent across two very different numerical codes. It has to be said that in this case, for Ka dimension, that the performance of the FDTD code Magic was far superior to that of the finite integration code MWS. Full analysis of this design is not possible in MWS due 'insufficient memory requirements', most probably due to the oversized nature of the cavity in comparison to the corrugation depth (40mm vs. 1mm). Despite this, it was still possible to deduce the resonant frequency of this structure to be ~37GHz, corresponding to interaction between $EH_{21,1}$ surface mode and a $TM_{0,10}$ volume mode. It was also noted that other resonances are indeed possible, due do interaction of this surface mode with different radial modes, although the coupling is not as strong – it is still present. This allows for a certain degree of freedom as we can choose which frequency to resonate by simple adjustment of the input pulse.

It is a well known fact that the resonant frequency of any cylindrical waveguide structure is of course dependant on its transverse dimension, with frequency increasing as the radial dimension is decreased. If we apply this, in combination with exactly the same reasoning and numerical investigation methods carried out at Ka-band dimensions, we should be able to create a cavity whose resonant frequency lies above the 37GHz we currently have. This is discussed in the proceeding section.

3.4 Numerical Study of W-Band Cavity

The dimensions for the system designed to operate at or around 90GHz are as follows: Radius of cavity – 10mm, 16 azimuthal variations, amplitude of corrugation is 1mm having a periodicity in the longitudinal direction of 3.2mm and overall length of 44.8cm. This is visualised in Figure 3.7 which is the output from both Magic (a) and MWS (b).

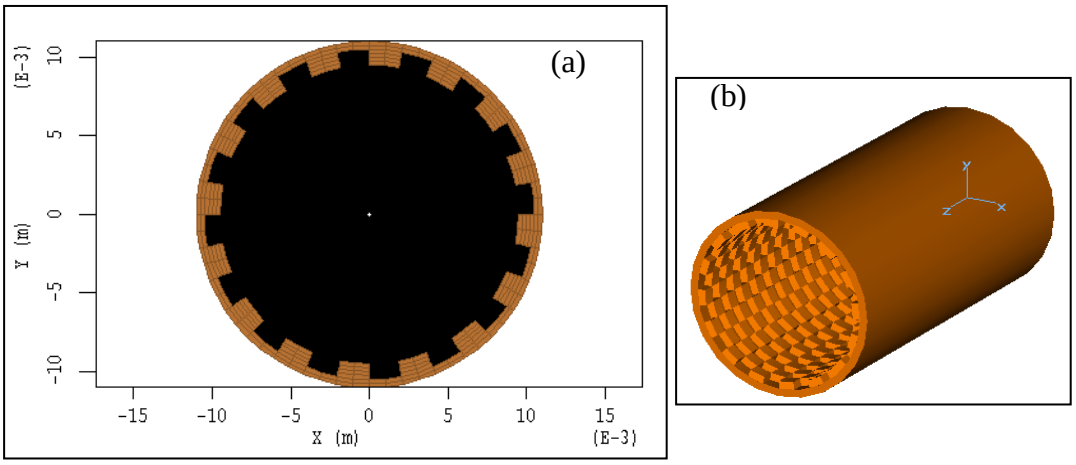

Figure 3.7: Numerical setup of the 90GHz cavity as given by a) Magic® and b) MWS.

3.4.1 Magic Results

The cavity was first excited by a TEM pulse 85 – 95 GHz, shown in Figure 3.8(a); this resulted in the appearance of two distinct resonances, one at ~88GHz and the other at ~96GHz, shown in Figure 3.8(b). The range of the input pulse was then reduced, 86 – 88GHz shown in Figure 3.8(c), so as to identify only one resonance which resultantly occurred at ~88GHz, Figure 3.8(d). This peak, at ~88GHz, was found to correspond to the interaction occurring between a $TM_{0,5}$ volume mode and an $EH_{16,1}$ surface mode, with the relevant field components given in Figure 3.9.

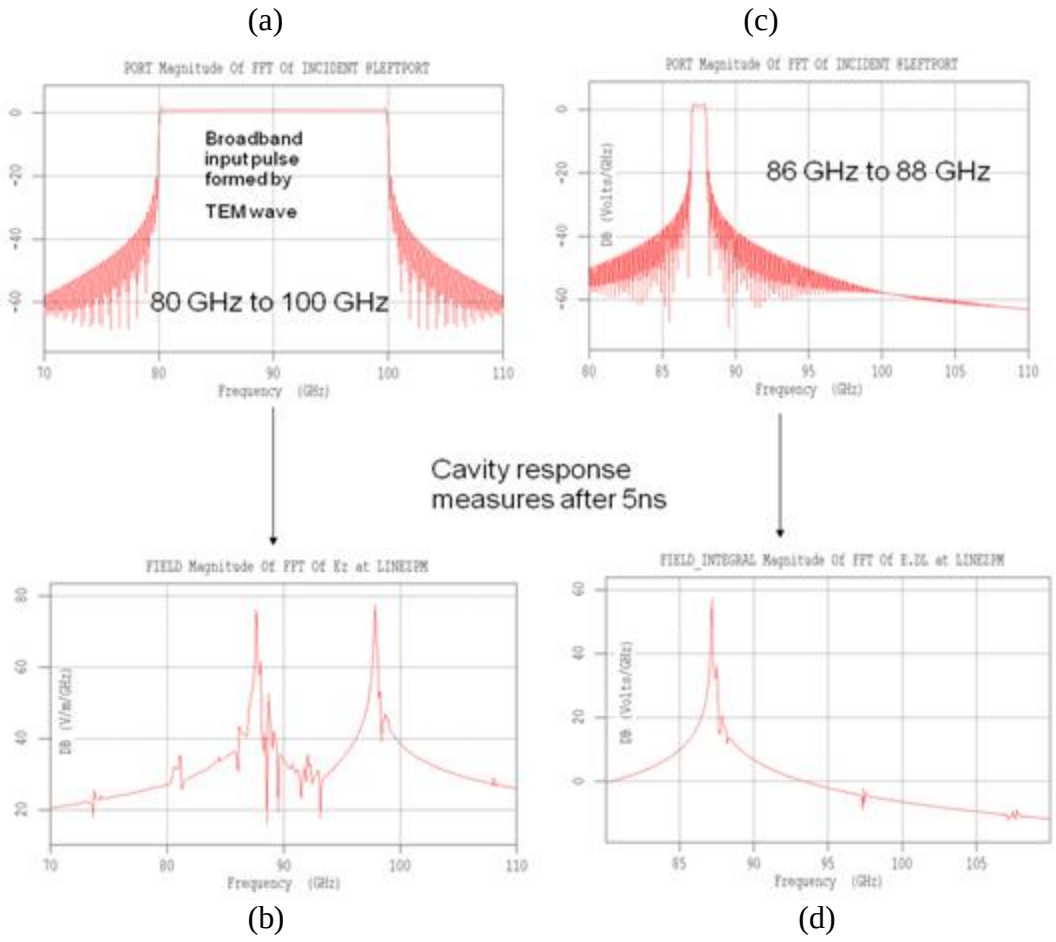

Figure 3.8: Various resonances corresponding to differing input pulse characteristics, where a) is the broadband TEM pulse, b) is the two resonances produced, c) is the narrower band excitation signal with d) the resulting resonance.

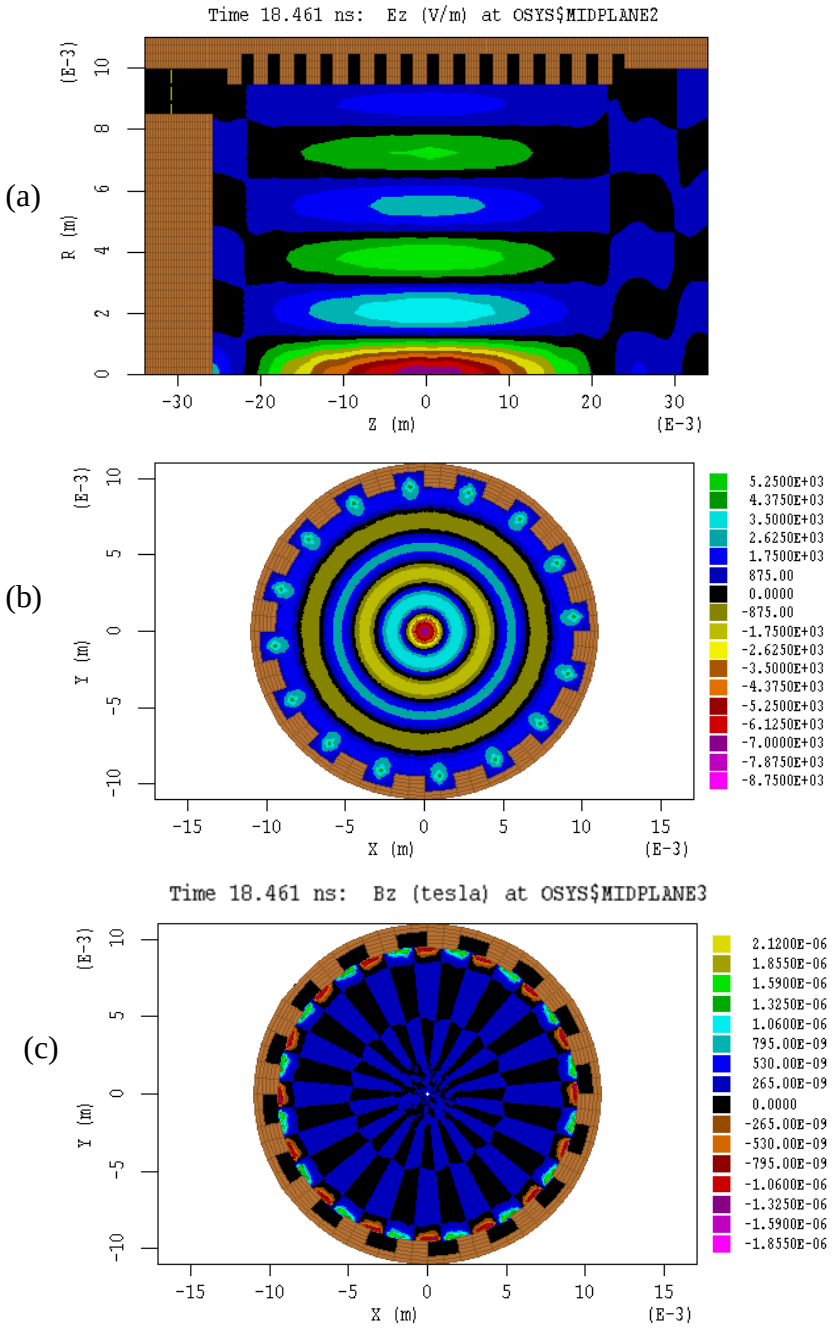

Figure 3.9: Field components corresponding to the resonant frequency of ~88GHz, which denotes surface wave interaction with the $TM_{0,5}$ mode, where a) and b) are different views of the same axial electric field at the same time instance and c) is the axial magnetic flux at the same point in time.

3.4.2 CST Microwave Studio Results

Similarly Microwave Studio predicted a resonant frequency of ~96GHz for this design; it did not however pick up on the resonance occurring at ~88GHz. This is due to the excitation pulse being of Gaussian nature, Figure 3.10 (a). We can see dominant E_z field located towards the centre consistent with TM mode presence, and similarly the magnetic component is located to the surface, representing excitation of surface current, Fig. 3.10(b)-(d).

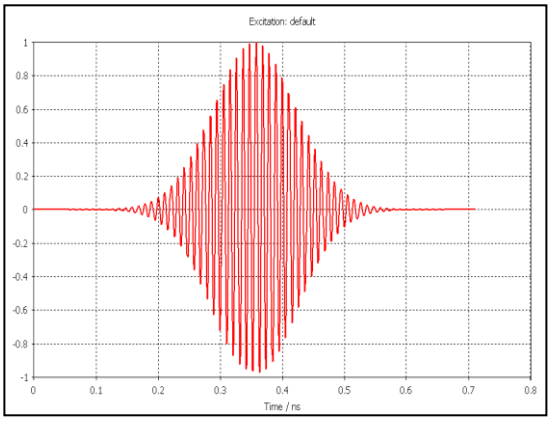

(a)

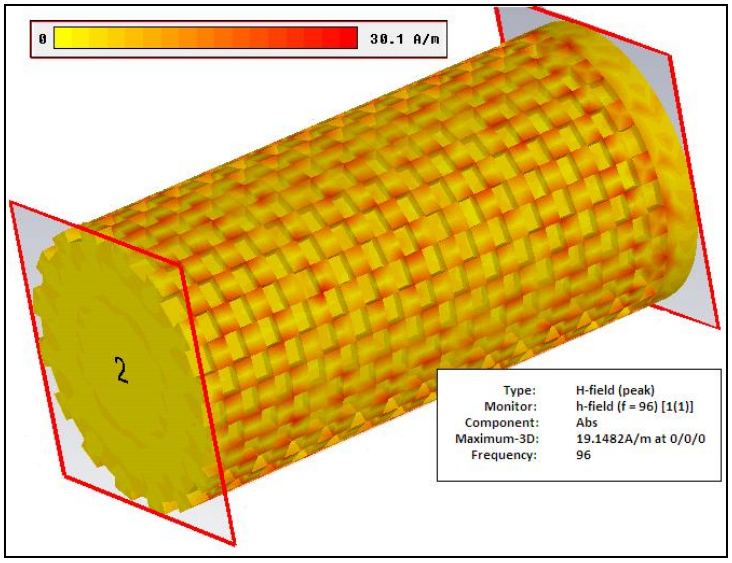

(b)

Figure 3.10: Microwave Studio output graphics showing a) The Gaussian Excitation Signal and b) The stimulation of surface currents.

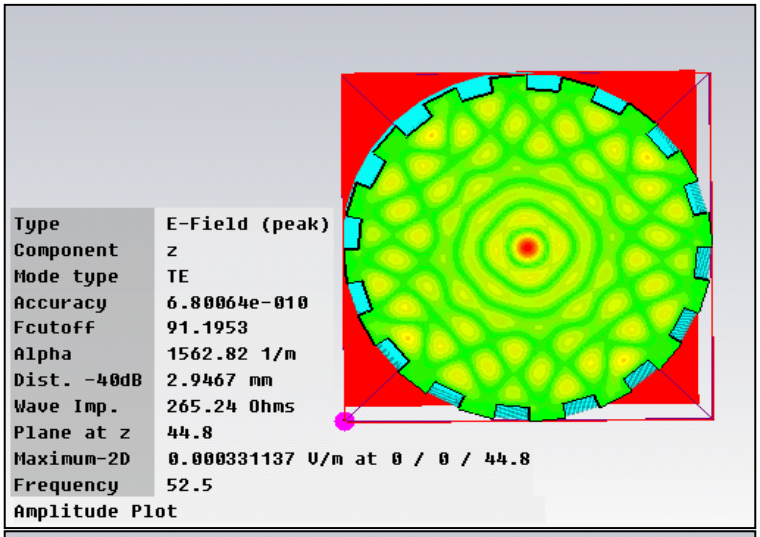

(c)

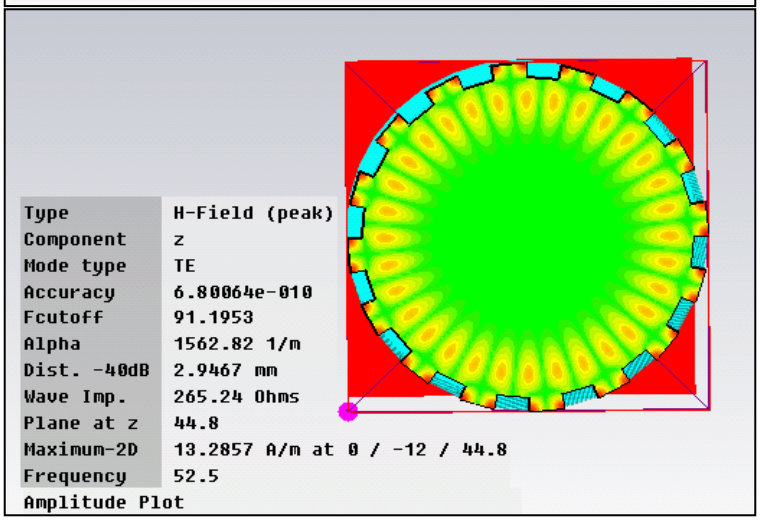

(d)

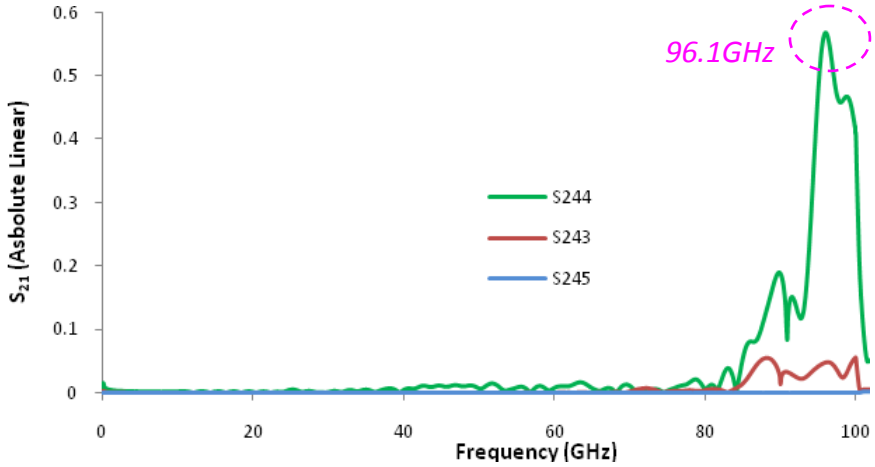

(e)

Figure 3.10(c – e): MWS results showing resonance at ~ 97GHz, where c) and d) are the electric and magnetic components of the resonance and e) is a graph of the corresponding transmission profile.

3.5 Numerical Study of THz Cavity

The studies were performed using both Magic and CST Studio and the results were once again compared. The design parameters of the THz cavity are as follows; the pump TEM wave is launched in to a cavity of radius 5mm having 20 azimuthal variations and a longitudinal period equal to 1.25mm. The amplitude of the corrugation is 0.8mm and overall length is 18cm, shown in Figure 3.11.

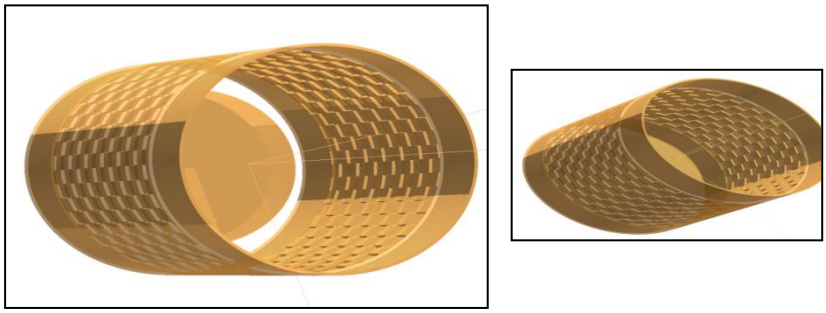

Figure 3.11: Cavity design for THz resonance as viewed using Magic.

3.5.1 Magic Results

In the first instance, the system was excited via a 170-180GHz TEM pulse, allowing it resonate at ~ 172GHz, shown Figure 3.12(a)-(b). This corresponds to surface wave interaction with the type $TM_{0,6}$ wave. This may be visualised in Figure 3.12(c)-(d), where one can easily depict the number of radial variations as being six.

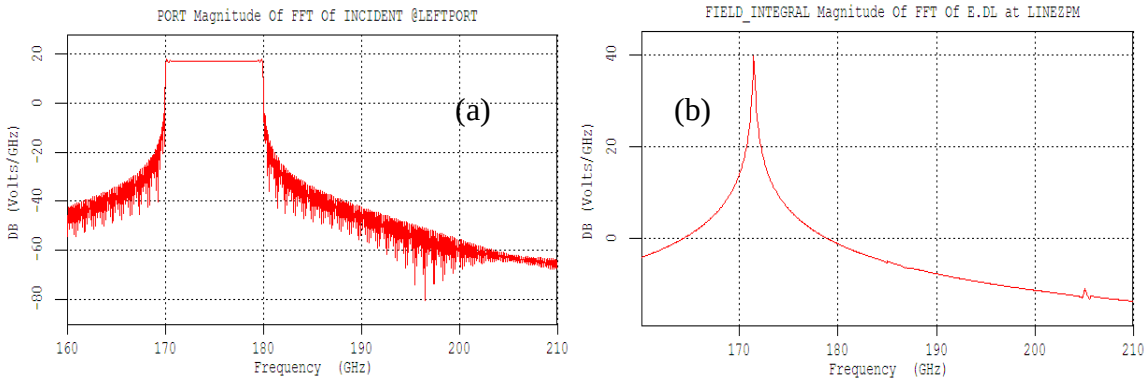

Figure 3.12(a-b): Magic output for the THz design showing a) the launch TEM pulse profile and b) the resonant frequency.

(c)

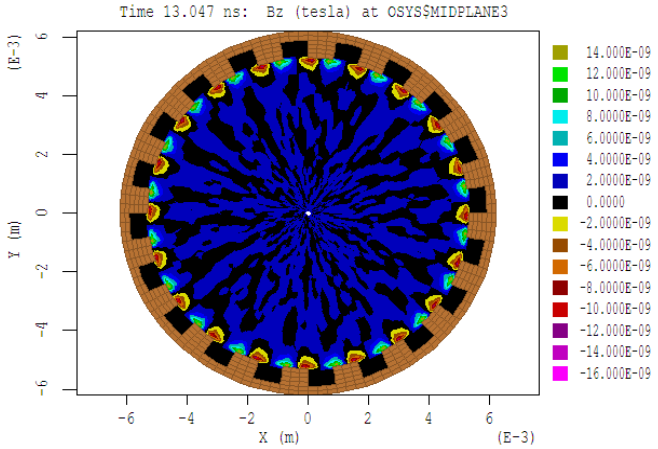

(d)

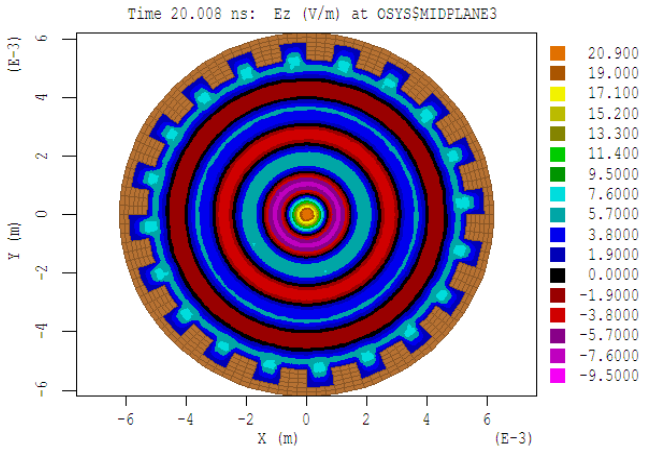

(e)

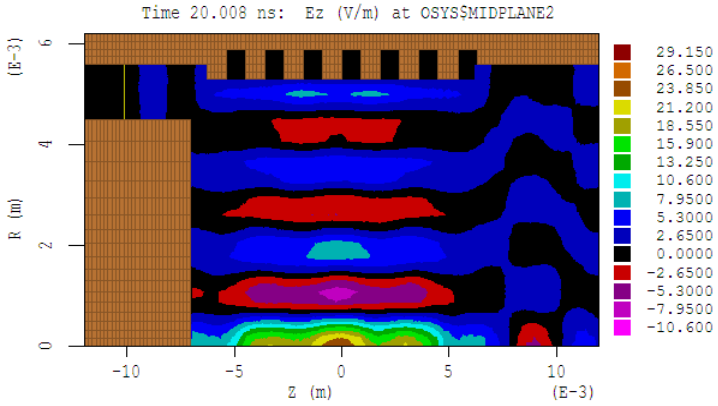

Figure 3.12(c-e): Magic output for the THz design where c) is the longitudinal magnetic component, located at the surface, d) the cross-sectional view of the longitudinal electric field, which is located to the volume, and e) is the axial view of same electric field component.

Further to this the same cavity was then excited again with the same 10GHz TEM pulse profile, only this time shifted in frequency where the occupied range is now 175-185GHz. The corresponding output is shown in Figure 3.13, and resultantly causing the cavity to resonate at ~182GHz, with a radial variation number equal to seven and surface mode number still equal to sixteen. The shallow corrugation has no effect on the radial field structure, only the azimuthal structure. Note also, for comparison, the relative electric field strength values in both cases, the higher field amplitudes are associated with the $TM_{0,7}$ interaction, when compared to the $TM_{0,6}$.

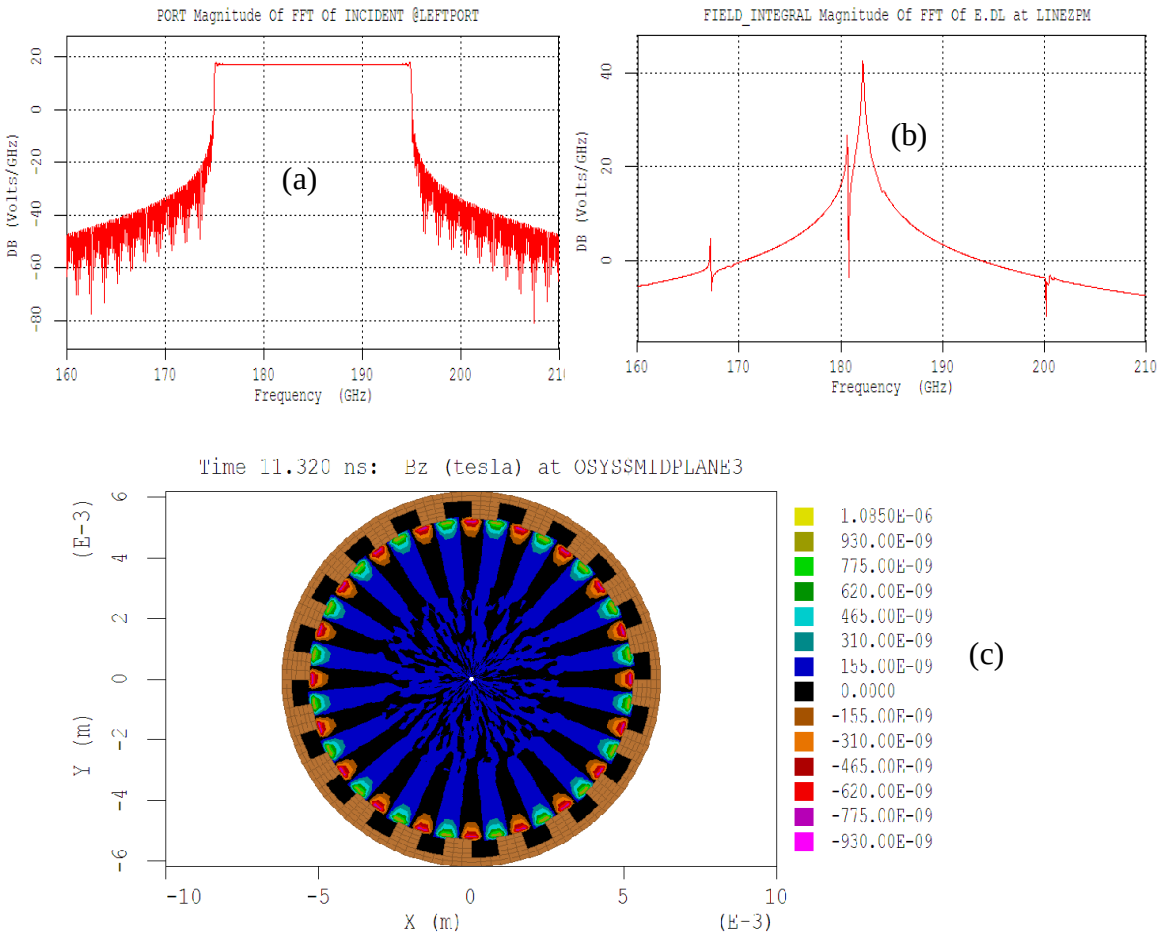

Figure 3.13(a-c): Magic Output for the THz design where a) is the 10GHz excitation signal, b) is the resonant frequency in the 180 GHz range and c) is the corresponding surface excitation fields.

(d)

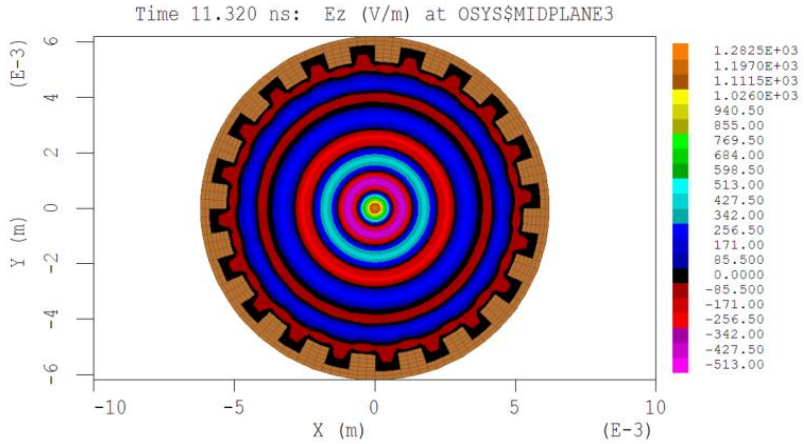

(e)

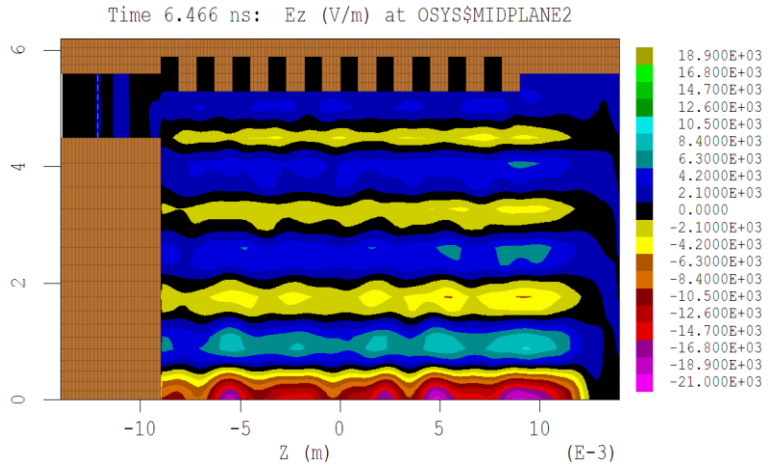

Figure 3.13(d-e): Magic Output for THz cavity design outlining the presence of the volume mode where d) and e) are the axial electric field, viewed as a cross-section and axially, where seven radial variations are observed.

We also gave consideration as to how the system would behave if the input bandwidth were increased from 10GHz to 30GHz, i.e. 155 - 185GHz. The resonant frequency in this case was prominent around ~165GHz, but note relatively wide band and low amplitude of this pulse in comparison to those of previous, Figures 3.14(a)-(b). With respect to identifying mode structure, the results proved inconclusive as although we can identify six radial variations along *Ez*, there also exists now a longitudinal variation which was NOT present in any previous case, Figure 3.14(c).

From these we can see the currents induced on the surface of the corrugation only, i.e. the shallow periodic structure has no effect on the radial fields of the waveguide, shown in the figures previous.

(a)

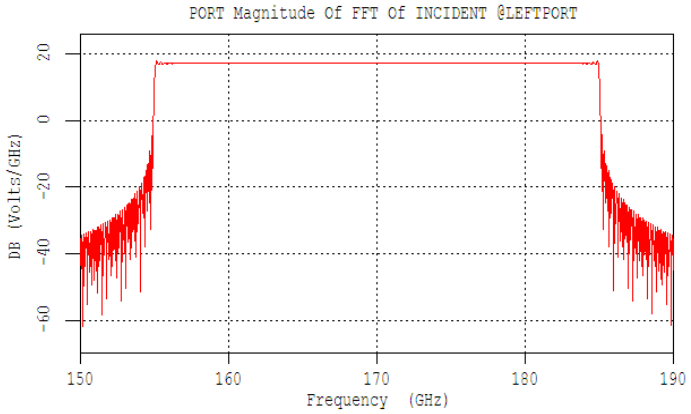

(b)

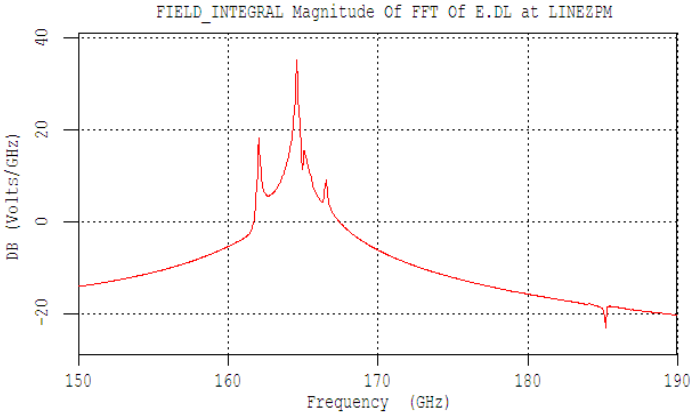

(c)

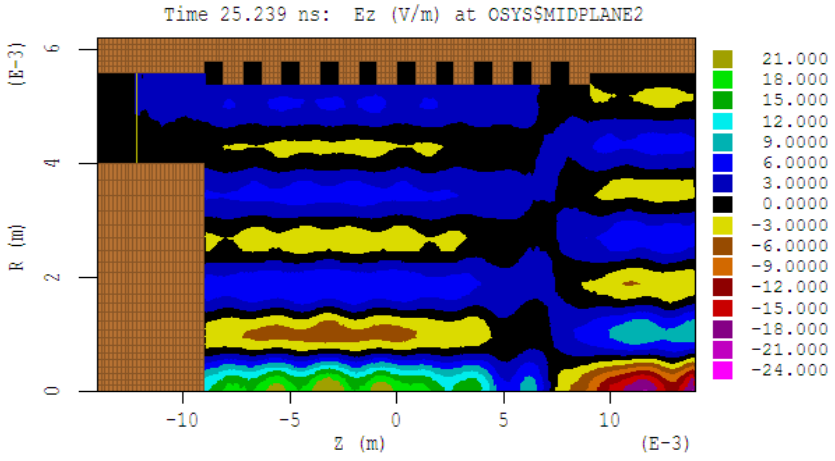

Figure 3.14: Resultant output files corresponding to the TEM 155 - 185GHz input signal, where a) is the launched TEM pulse, b) is the resonance(s), and c) is the electric field profile.

3.6 Chapter Conclusions

In conclusion to this chapter we now have a more complete picture of the field behaviour inside a (cylindrical) periodic cavity, and have also demonstrated that the method of surface mode to volume mode coupling is indifferent to the dimensions of the system. Of course, the interacting modes will be different for each system, but the principle remains the same throughout and concurrent across a range of frequencies, as demonstrated.

Both codes agree with the mode prediction, but MWS has the advantage that it can tell you the exact mode order, cut off frequency and wave impedance and display these in an 'on call' tab, whereas Magic only allows us to visually 'see' the resultant field components, as 'snapshots' through the system, the rest must be pieced together by the user.

Generally, all the results show a 'range' of coupling zones which is present regardless of the cavity dimensions. This is believed to correspond to the 'surface' mode of the structure interacting with different radial type modes. Analysis of both field strength and surface current density, given from both codes, allows us to determine which radial number will provide the most effective interaction for each of our systems. Also, via the CST Studio code, we can visualise the entire hybrid mode pattern in addition to the individual field components as given by magic, this enables us to determine the exact point at which to locate our electron beam, should this cavity design be incorporated into such an experiment.

4 Experimental Analysis

4.1 Introduction

Experimental investigation of a cavity based on a 2D square lattice type corrugation was carried out in order to physically demonstrate the excitation of cavity eigenmodes and also provide an estimate for loss and gain factors of the cavity. The cavity considered for these sets of experiments is of cylindrical geometry, 80mm diameter and has a 1mm corrugation on the outer surface, shown in Figure 4.1, where a photograph of the experimental set up with an insert showing the structure studied is presented. The periodic structure (insert to Fig.1a) made of copper has the following parameters: radius = 40 mm, total lattice length 48 mm, number of azimuthal variations = 28 with a longitudinal periodicity equal to 8 mm and a corrugation amplitude equal to 1mm.

To study the 2D surface wave cavity experimentally a set up similar to one used for studying coaxial structures [64] has been adopted, with the appropriate adjustments in place. In this Chapter results of experimental studies of the Ka-band 2D periodic structure are presented. The microwave measurements of the transmission and reflection

profiles were conducted, in addition to near and far field measurements of the signal amplitude. The apparatus and techniques used in each of the experiments are detailed in this next section.

Figure 4.1(a): Photograph of the cylindrical 2D periodic structure which forms the cavity, having diameter 80mm, corrugation depth 1mm, 28 azimuthal variations and longitudinal period equal to 8mm.

4.2 Apparatus and Diagnostics

The apparatus and diagnostics used in each of the cavity analysis experiments are detailed in this section. Each of the experiments utilised a network analyser in conjunction with a number of compatible mode convertors and an oversized transmission line containing the band gap cavity as the device under test.

4.2.1 Network Analysers

Network Analysers may be used to measure a wide variation of device and network properties, including impedance, Voltage Standing Wave Ratio (VSWR), energy loss/gain, isolation and group delay [64,65]. The purpose of network analysers in this instance was to measure the transmission and reflection of microwave radiation in the upper Ka-band (30 – 40) GHz frequency range. There are two different types of

Network Analyser used in these distributed feedback measurements, the Hewlett Packard 8757D Scalar Network Analyser, and the Anritsu 37397A Vector Network Analyser. The scalar network analyser will measure power against frequency (frequency domain measurements) whereas a vector network analyser will measure power with phase against frequency (time domain measurements). This extra phase information given by the VNA allows for greater calibration accuracy of microwave components.

Using the Scalar Network Analyser in conjunction with a frequency sweeper, it was possible to measure the scattered wave reflections produced in a Bragg cavity as a function of frequency. This is helpful when identifying mode structure and interactions taking place inside the cavity. Using the Vector Network Analyser allowed us to analyse the reflection and transmission properties of the electromagnetic wave cavity. The HP8757D scalar Network Analyser is used in conjunction with the HP83752B synthesized microwave sweeper. The SNA has an operating bandwidth of (0.01 – 20) GHz and a maximum power output of 10dBm @ 20GHz [66]. This bandwidth can be extended via the use of a frequency doubling head, allowing for operation in the (26.5 – 40) GHz range, however, the maximum power achievable @ 40 GHz is reduced to 7dBm. In order to successfully transfer electromagnetic energy from the network analyser to our system, we must make use of a series of compatible mode converters. These are detailed in the following section.

The components and mode transitions that occur from left to right are as follows;

a) Rectangular $TE_{1,0} \leftrightarrow TE_{1,1}$ Circular

b) Waveguide connector

c) Circular $TE_{1,1} \leftrightarrow TM_{0,1}$ Circular

d) Waveguide connector

e) Circular $TM_{0,1} \leftrightarrow TEM$ Coaxial

4.2.2 Mode Converters

A series of mode converters are used in these experiments and in order to successfully connect either the VNA or SNA to our transmission line system and device under test. Illustrated below in Figure 4.2 is a schematic showing the mode convertors used in these experiments. The setup consists of three mode convertors which perform the required transformation in the desired frequency band, which for Ka is defined as between 35 and 38GHz [67].

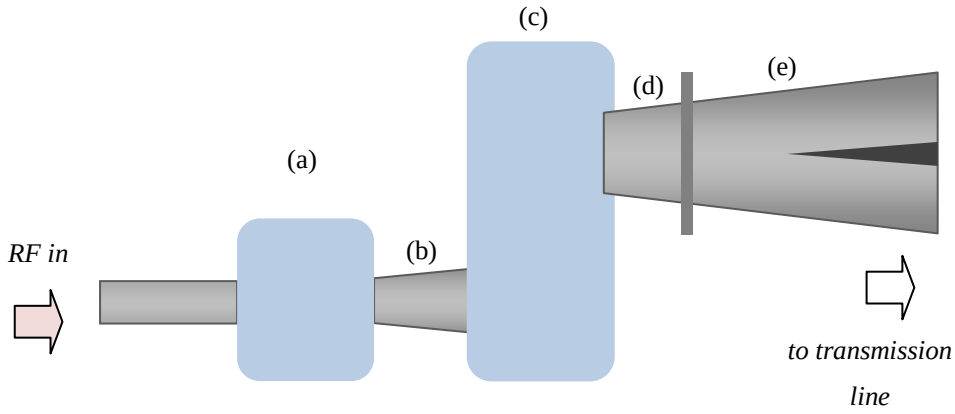

Figure 4.2: Schematic showing the mode conversion section of the experimental set up, a) rectangular to circular converter, b) the gradually opening waveguide connector, c) the Serpentine mode convertor, d) waveguide connector, e) circular to coaxial adaptor.

- Section (a) consists of a typical Flann Microwave Ka-band rectangular to circular converter, where, the waveguide operates at the fundamental mode in both geometries in the region 26.5GHz and 40.0GHz. The cut-off frequency of the fundamental mode in the circular waveguide section of 22GHz is the limiting factor in this section; however, single mode operation is possible in the region up to and including 40GHz. This mode convertor is achieved by gradually changing the geometry of the waveguide cross section, shown in Figure 4.3.

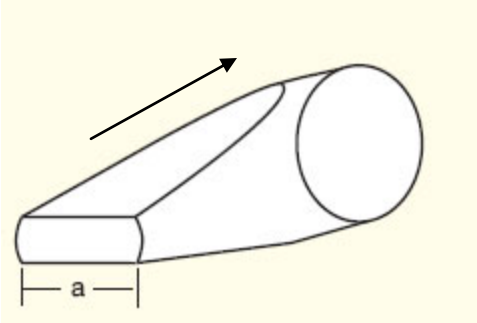

Figure 4.3: Schematic diagram of the rectangular $TE_{1,0} \leftrightarrow TE_{1,1}$ circular mode converter, where '*a*' denotes the standard waveguide dimension. The arrows indicate the electric field structure at the input and output of the converter.

- Section (b) is a gradually opening section of circular waveguide, from 7.2mm to 9mm. This allows connection to the next section (c) to be made.

- Section (c) is a serpentine mode converter, consisting of two curved sections of waveguide connected to form an 'S' shape. It is this shape modification that allows for the mode transformation via an intermediate mode, this is by varying the phase of the coupling coefficient along the axial direction. The serpentine mode converter is required, in this instance, to convert a $TE_{1,1}$ wave to a $TM_{0,1}$ wave whilst maintaining high conversion efficiency across the upper region of the Ka-band frequency range of 30-40GHz [68]. The serpentine mode converter is capable of converting both the forward and backward waves, enabling them to be used at both ends of the transmission line. Care must be taken to ensure the polarity of both serpentines is matched in order to avoid any parasitic mode reflections due to a mismatch in phase.

- Section (d) is another waveguide connector of increasing aperture, from 9mm to 12mm. The increase in waveguide diameter is important in order to increase the conversion factor of the $TM_{0,1}$ wave into the TEM wave of the coaxial guide.

- Section (e) is a circular to coaxial adapter. This consists of a cylindrical waveguide in which the azimuthally symmetric $TM_{0,1}$ wave traverses and where a central cylindrical conductor having 8mm diameter is introduced. This then follows on through a gradually opening coaxial horn of length ~60cm and gradually increases the radius until the separation between the inner and outer conductors reaches a value of 10mm. It is at this point the mode is transformed fully into the TEM geometry, thus enabling it to pass in to the transmission line. The TEM mode passes through without producing any spurious mode transformations and therefore is suitable for launching into the large diameter coaxial waveguide section in which the 2D structure is located.

4.2.2.1 Verifying the Operating Range of the Mode Converters

In order to verify this array of mode converters operates effectively in the desired frequency region (26.5 – 40GHz), the transmission properties were measured using the Anritsu Vector Network Analyser. A schematic of the experimental setup is presented in Figure 4.4 where the serpentines are held together via cylindrical waveguide. The signal is fed from the VNA into the mode conversion section via waveguide connections, and allowed to return to the VNA via identical mode converters on the return side, allowing the transmission properties to be measured.

The setup was calibrated at the reference planes numbered 1 & 2 prior to any recording of measurements. A through-reflect-line (TRL) calibration was performed using two lengths of Ka-band waveguide, at 95.30mm and 88.40mm in length combined with the appropriate short circuits for the reflection measurements.

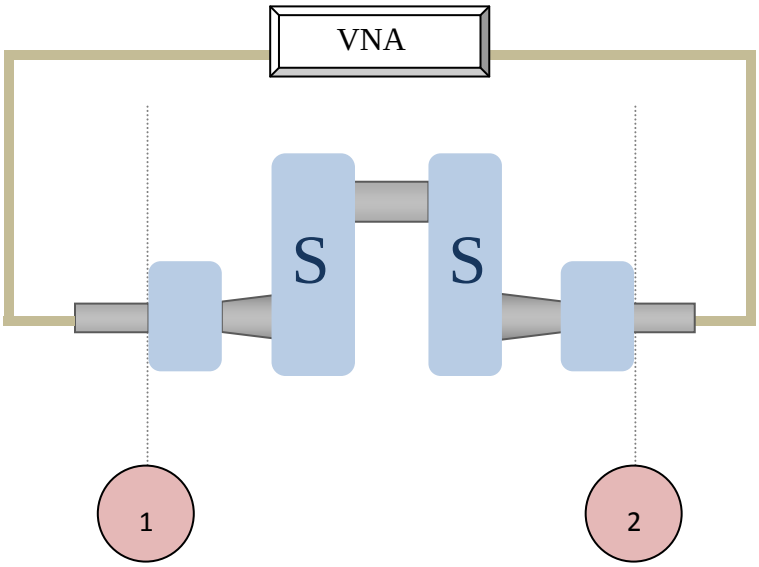

Figure 4.4: Schematic diagram of the experimental set up used to define the operating bandwidth of the S-type mode converter.

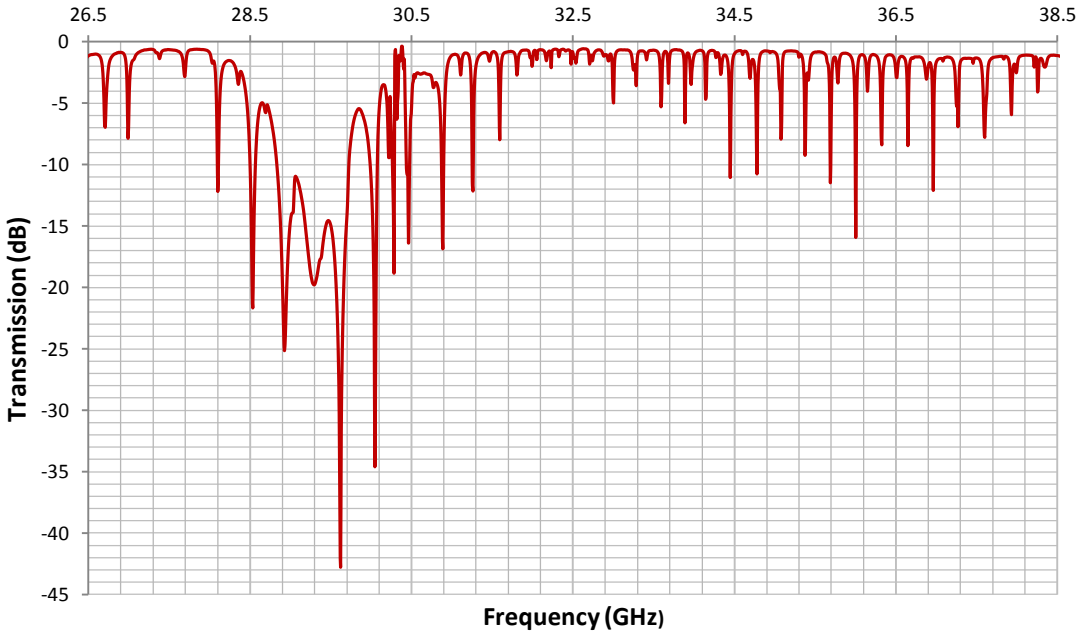

Figure 4.5: The transmission coefficient of the S-type mode converters in the frequency interval 26.5 – 40 GHz.

From the results shown it can be seen that the effective operating frequency range lies inside the frequency interval 30 to 40 GHz.

4.2.3 The Transmission Line System

The Transmission Line System is common to all of the following experimental configurations, and is illustrated in Figure 4.6. Coaxial transmission lines, each consisting of an input and an output section were used in the investigation of the distributed feedback cavity. The central section of the coaxial transmission line consisted of inner and outer diameters of 60mm and 80mm, respectively. The operating frequency of the DUT is centred around 37.4GHz and a smaller dimension of transmission line was applied at both the input and output of the cold test system. Diameters of the inner and outer conductors at the transmission line input/output were 10mm and 28mm respectively. These were then tapered up and connected to the oversized cavity.

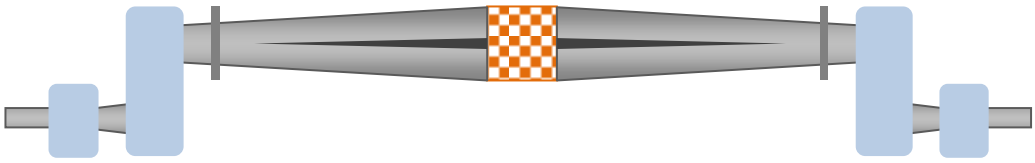

Figure 4.6: Sketch of the transmission line system inclusive of mode converters.

The entire transmission line is axially symmetrical with corresponding down tapers and mode converters, in reverse order, at the output of the DUT (where necessary). This enables propagation of radiation through the device with a stated efficiency in the range 0.9 – 0.99 in the frequency band 30 – 40 GHz, with the highest efficiency achievable in the range 35 – 40 GHz [68].

4.3 Experimental Observations

In order to fully understand the interactions taking place inside the interaction region it is necessary to consider the waves inside in absence of any active media, this is otherwise referred to as a cold test.

All of the following experiments were carried out on the Ka-band cavity utilised successfully in the previous experiments [69 - 72]. The difference here is that the setup is of cylindrical geometry as opposed to the coaxial system used in the above stated references. It is important to note that as the following tests omit the use of an active media, i.e. an electron beam, it is necessary to introduce a coaxial "stub" at the beginning of the launch to allow for efficient mode coupling inside the interaction region.

4.3.1 Experiment One – Measuring the Transmission Profile

An important characteristic of any resonant structure is the excitation of one or several eigenmodes which dominate/characterise/define the operating range of such a device.

An important characteristic of any cavity type structure is to understand how it behaves in the absence of any type of active media, for instance and electron beam, more specifically examine its ability to transfer or store energy in the form of resonant frequencies. Knowing the resonant frequencies of a system allows it to be calibrated to a specific user.

The resonance profile of the system was analysed using a vector network analyser setup, as depicted in the section below.

4.3.1.1 Experimental Setup and Procedure

The transmission and reflection properties of our Bragg structure were measured using a Vector Network Analyser connected, via a series of mode transformers, to an oversized coaxial transmission line. A schematic of the setup is shown below in Figure. 4.7(a)

which consists of the Anritsu 37397A Vector Network Analyser connected to the waveguide mode converters and transmission line system, with the 2D cavity as the device under test. The connections were made using Ka-band rectangular waveguide (7.2mm x 3.8mm). This setup allows us to determine the transmission through the system as a function of frequency, i.e. dB vs. freq. (GHz). Also shown in Figure 4.7(b) is a photograph of the completed setup prior to measurement.

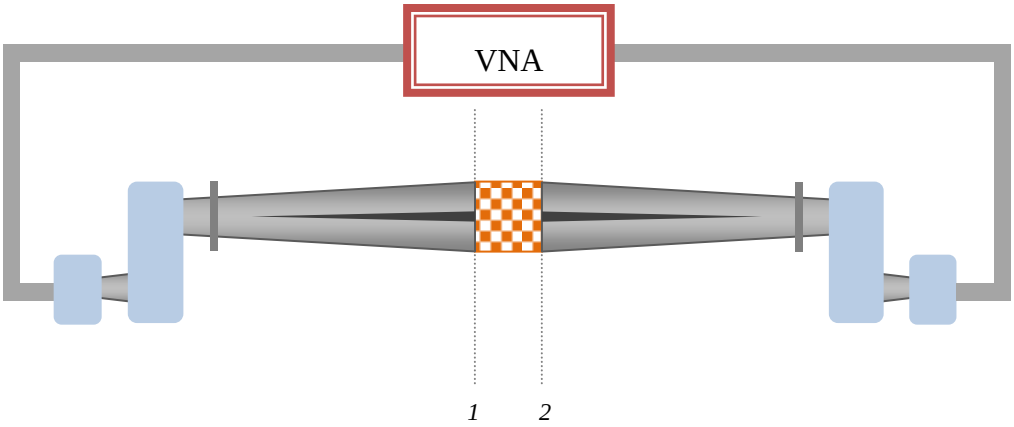

(a)

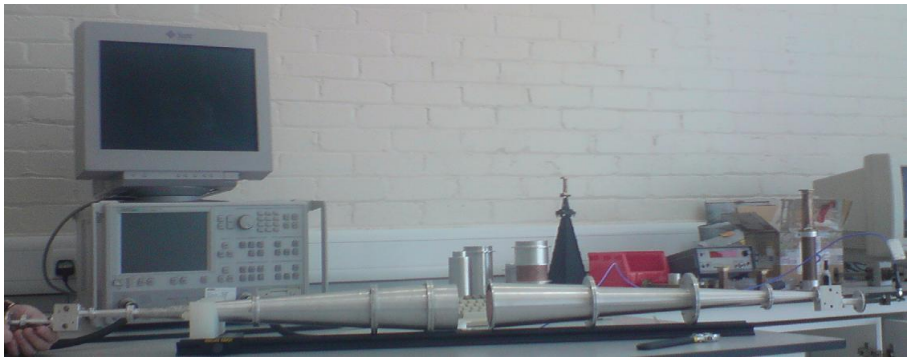

(b)

Figure 4.7: Experimental measurements where a) is an Illustration of the setup used to measure the transmission properties of the Ka-band interaction region and b) is a photograph of the completed *e*xperimental setup, the insert between the two figures is the numerical output from magic of the same scenario.

In order to achieve the highest possible accuracy results it is necessary to calibrate the transmission line system prior to any measurements being recorded. This was achieved by performing a thru cal at reference planes 1 & 2 using two lengths of cylindrical waveguide, less than one half wavelength differences (72mm and 126mm). As a reference the same measurement was carried out for a smooth wall cavity having exactly the same dimensions as the corrugated cavity.

4.3.1.2 Results & Discussion

The transmission profile for this design was obtained and is shown below in Figure 4.8(b), represented by the blue line, alongside the same measurement performed for a smooth cavity of equal dimensions in length and diameter, shown in red. Photographs of the setup are given in Figure 4.8(a). The transmission plot (blue) clearly shows a reflection band in the region 37.5 – 37.8 GHz, with the deepest minima occurring at 37.65GHz. This gap in the spectra is associated with the resonant scattering of the incident wave into a surface waves and a near cut-off mode i.e. excitation of the cavity eigenmode. This is the value that will be assumed for all proceeding experiments as it corresponds to maximum energy transfer/mode excitation for this design of cavity.

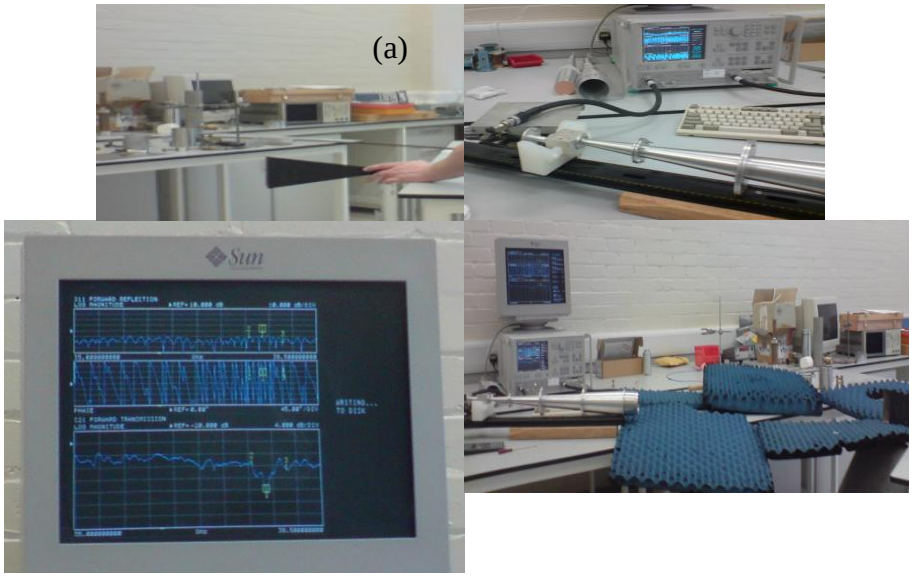

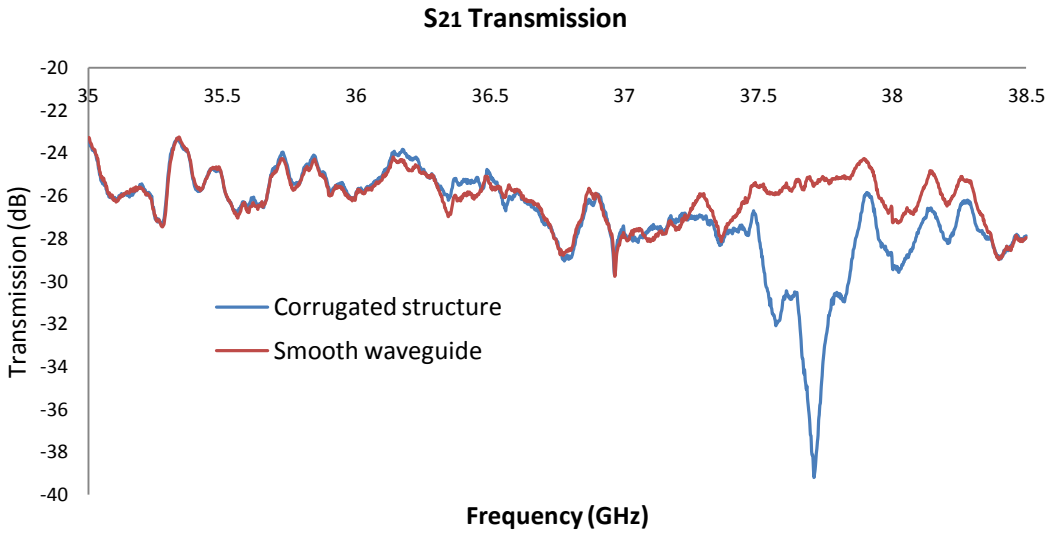

Figure 4.8: Measurement of transmission line system using open cal method, where a) is pictures of the setup and b) the graph showing the frequency dependence of the transmission coefficient through both smooth and periodic waveguide as measured using open cal method.

4.3.2 Experiment Two – Analysis of the Radiated Mode Pattern

Another important characteristic of microwave radiation from a launching antenna is the spatial distribution of power, or mode pattern. Measurement of the spatial structure can provide information as to the resonant cavity mode(s) and hence allow us to understand further the interaction(s) taking place inside the cavity.

4.3.2.1 Background

Both the power and field distribution are similar in appearance and are proportional to the distance separating the launching antenna and the receiver/detector. The distance between the launching antenna and the detector can be divided into three identifiable regions without sharp boundaries and are: The reactive near field region (Rayleigh field), the radiating near field region (Fresnel region) and the far field (Fraunhofer) region. These are all linked to the quantity: $R_s = \frac{D^2}{\lambda}$, where D is the largest dimension of the antenna, in this case the circular diameter of the conical horn and λ is the wavelength of the radiating source. If the distance between the detector and the launch horn is denoted by r, then the equation below clearly shows the boundaries for these three regions.

$$r < \frac{R_s}{2} = \frac{D^2}{2\lambda} \qquad \textit{Reactive near field region}$$

$$\frac{R_s}{2} < r < 2R_s \qquad \textit{Radiating near field region}$$

$$r > 2R_s = \frac{2D^2}{\lambda} \qquad \textit{Far field region}$$

Measurements of power distribution are usually conducted in the far field region as in the immediate vicinity of the launch antenna there exists a considerable amount of incoherent scattering fields in addition to the radiated fields. For our setup the diameter of the output horn is 80mm whilst the dominant frequency of the source is

approximately 40GHz, thus leading to (as per equation above) the criteria that the far field boundary should lie beyond 170cm.

4.3.2.2 Experimental Setup

The radiation mode pattern measurements were conducted by a Signal generator (HP Sweeper) with direct power meter gives Power, in units of nano-Watt, against Angle, in degrees, for a fixed frequency as set by the user. In this case equal to 37.64GHz, as depicted via experiment one. The radiation was picked up using a scanning detector (Ka-band detector) in the radial direction, centred on the aperture of the output horn and was fixed according to the point of symmetry, which in this case was at a height of 85cm from ground. The detector was positioned at a 2.95m distance from the emitting horn, as depicted via the far field relation and shown in Figure 4.9.

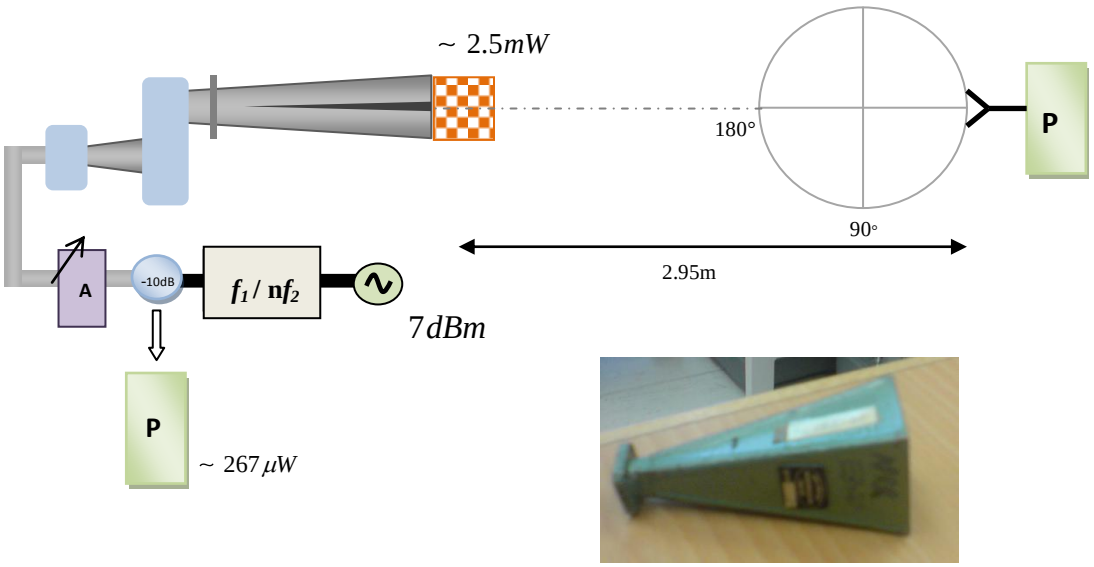

Figure 4.9: Schematic of the experimental setup for the far field radial mode pattern scan and the detector (enlarged photograph).

In this configuration the reference detector system was held at a fixed position throughout the mode scan before being rotated 90° and repeating the measurements so as to obtain a complete measurement of both horizontal and vertical field polarisations. The reference system consisted of an identical setup and procedure only with the cavity replaced with a smooth cavity of equal dimensions. The system was also checked for alignment prior to results being recorded, results of which are presented below and demonstrate symmetrical radiation pattern, as expected from a half wave dipole. The terms 'horizontal' and 'vertical' here refer to the change in cross section distance from point of minimum signal, in this case located at a height of 85cm from ground. The power measurement values are given as a sum of both detector polarisations with error bars added in the enlarged section for completeness.

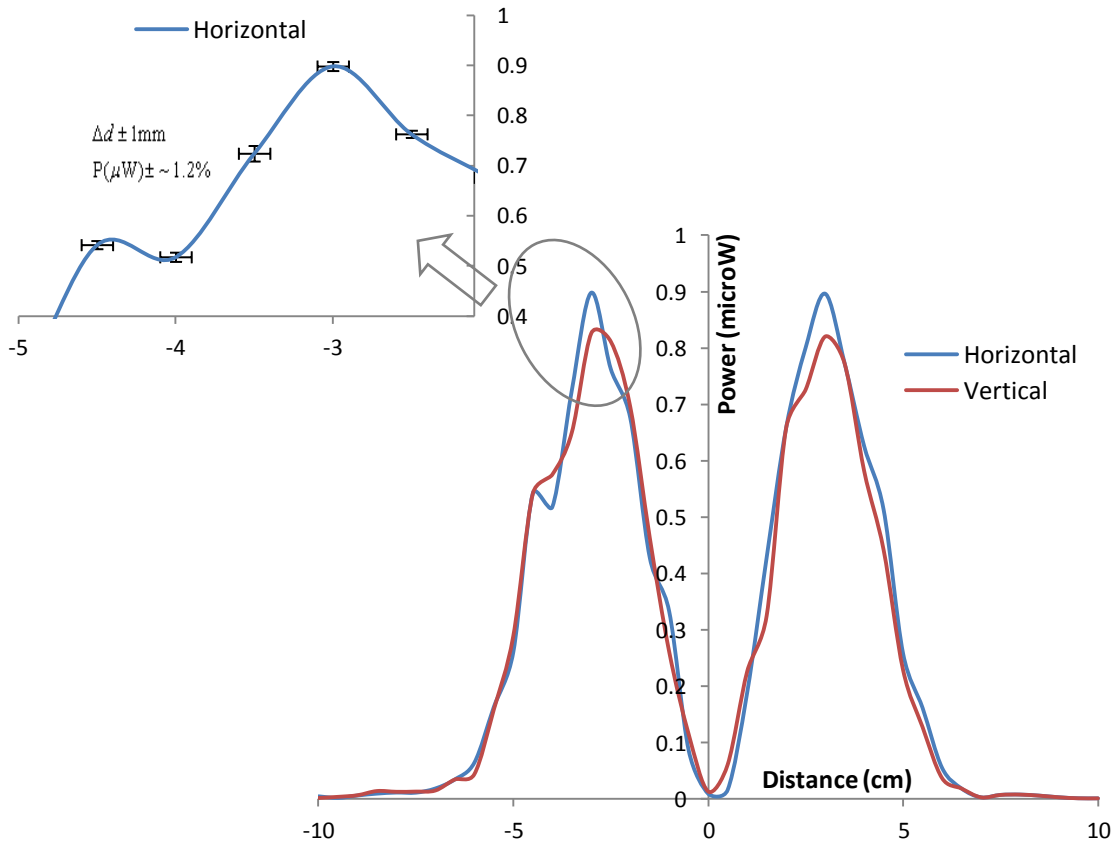

Figure 4.10: Alignment check where blue is the radial and red the azimuthal measurements. The insert is representative of error-bars which are too small to visualise on the main graph.

4.3.2.3 Results & Discussion

Results indicate coherent scattering of radiation at the Bragg frequency due to the 2D corrugation, as compared to the smooth waveguide of similar dimensions. The results of the experimental measurements of the periodic cavity are shown in Figure 4.11 (green line) as compared with the scan when the lattice is substituted with the smooth cylindrical waveguide (red line). We can see that the radiation from the smooth waveguide consists mainly of lower order propagating modes (i.e. majority of the energy concentrated at a small angle) with a small presence of higher order modes. The cavity radiation mode patterns indicate strong presence of the near cut-off high-order mode manifesting itself as periodic variations (periodicity ~5°) of the field intensity for the observation angle above 45° , Figure 4.11(b) and much smaller radiation intensity for angles less than 45°, Figure 4.11(a). These are also plotted in polar form and displayed in Figure 4.12.

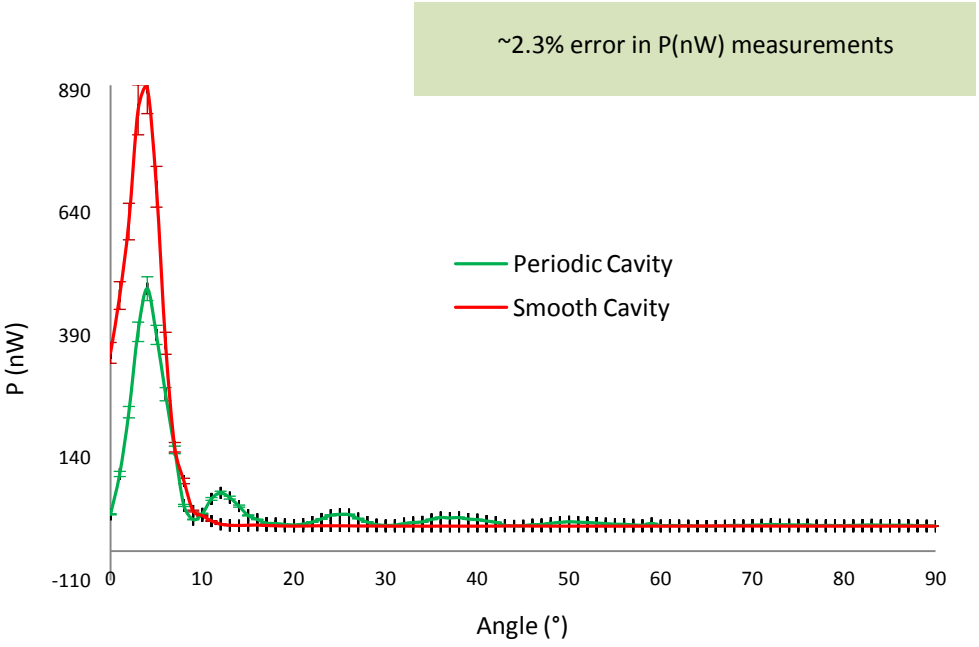

Figure 4.11(a): Experimental results from both periodic and smooth walled waveguide showing the majority of the radiation passing through at small angles for the smooth case (red) and for the periodic case (green) there is a reduction in the amplitudes at lower angles.

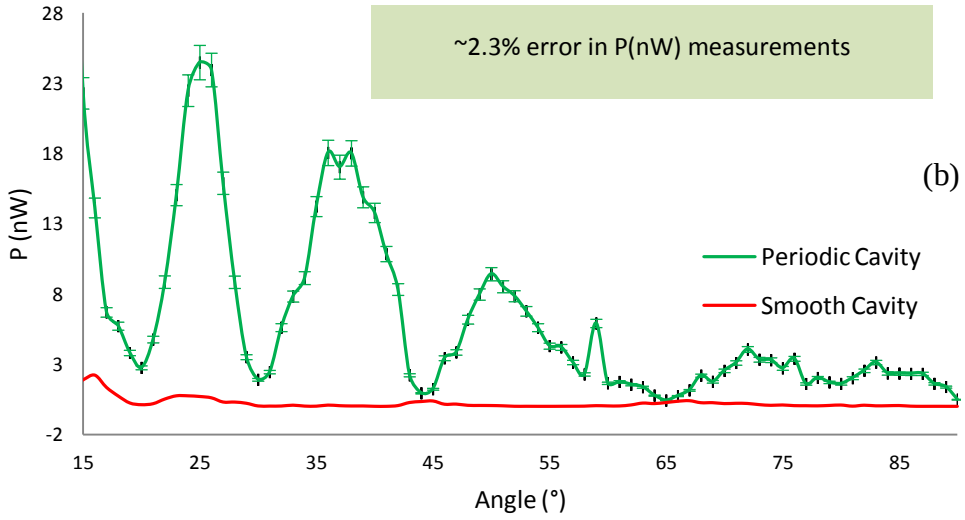

Figure 4.11(b): Experimental results from both periodic and smooth walled waveguide showing the periodic variations at higher angles (green) for the corrugated waveguide.

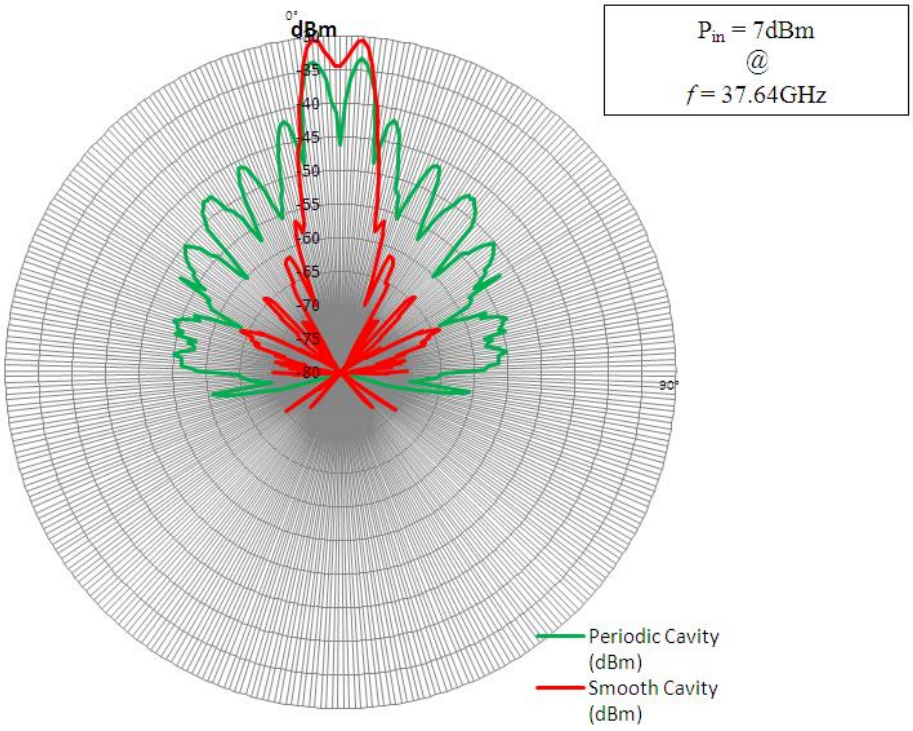

Figure 4.12: A polar plot of the same data, i.e. cold test of the smooth waveguide as compared to the equivalent corrugated region.

4.3.3 Experiment Three – Frequency Dependence

In order to obtain a complete picture of the cavity behaviour, it is necessary to study the frequency dependence of the radiated power, as this provides crucial insight into optimisation of signal and how any associated device may operate.

4.3.3.1 Experimental Setup

The setup depicted here, is similar to that of the previous experiment only with the addition of a Scalar Network Analyser (HP 8757D). This allows us to measure the transmission and reflection properties of the specific two-port network as a function of both angle and frequency over a given range, i.e. $P(\theta, f)$ where the units of measurement are dBm for power, degrees for angle and GHz for frequency.

The signal is once again generated via the synthesized sweeper (including doubler), only now it is fed directly into port 1 of the SNA. This acts as our test signal. This signal is then launched into the transmission line system as before and allowed to radiate into free space, where the signal is detected by the same Ka-band receiving horn as before (mounted on the scan plate), only this time the horn is connected back to the SNA (port 2). This allows us, by definition of scalar network analyser, determine the power density variation, if any, with frequency variation, where the frequency range is user defined and controlled via LabView. Prior to any measurement being recorded, a system alignment check was performed in both the radial and azimuthal planes to ensure symmetry. Results are given below.

4.3.3.2 Results

Frequency variation – frequencies away from resonance pass through unaffected by the corrugations, these are represented via the high values at shallow angles, shown in Figure 4.13(a). However at transverse angle values there is no field present. This is in

direct contrast to the case where resonant frequency is launched – at small angles there is a reduced value due to scattering into transverse wave components which is evident in the angle range 45° – 90°. Transverse coupling is evident in the region 60° - 80° and only occurs at and around the frequency of resonance, Figure 4.13(b). This demonstrates that it is imperative the resonance conditions are satisfied in order to achieve successful coupling between propagating volume modes and evanescent surface modes.

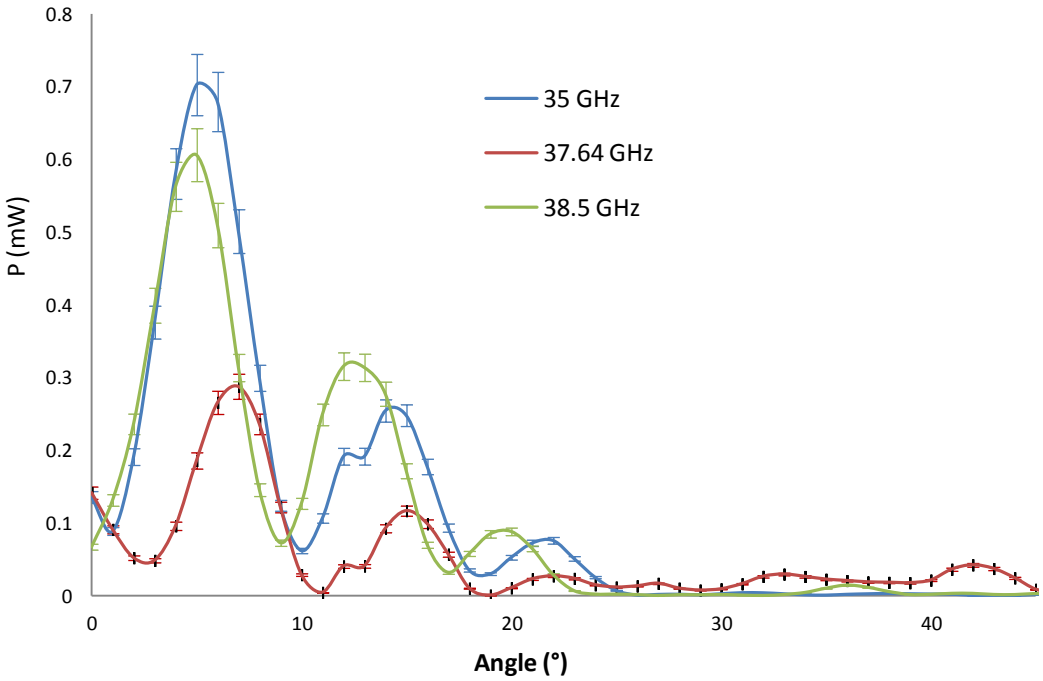

Figure 4.13(a): Frequency dependence of the signal transmission through the surface field cavity as measured by the receiving horn antenna at 2.95m distance from the output, where frequencies away from resonance pass through unaffected.

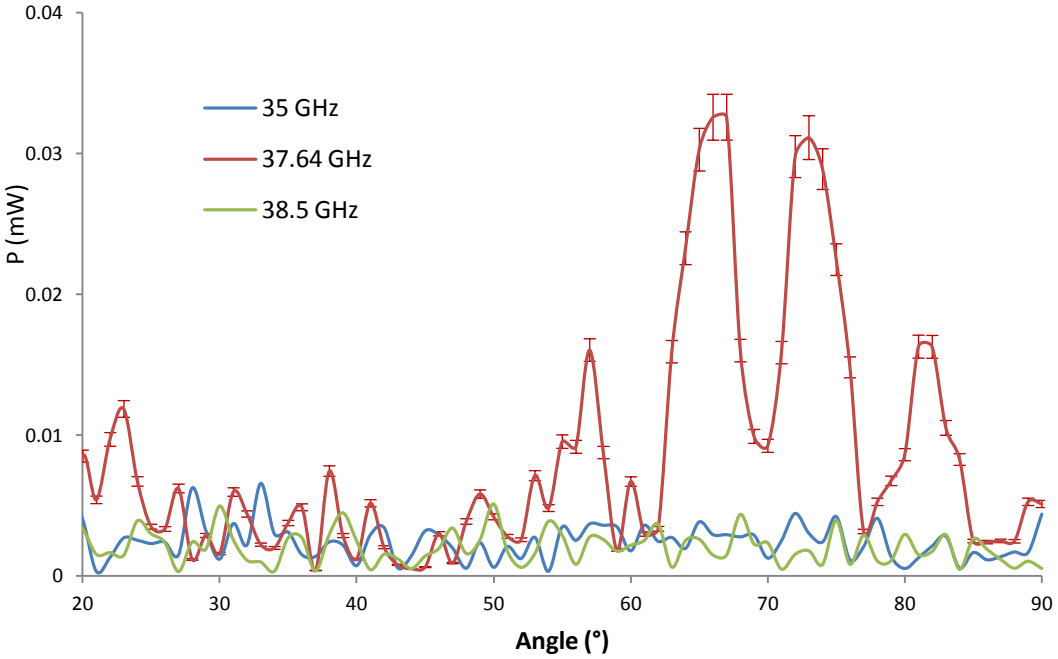

Figure 4.13(b): Frequency dependence of the signal transmission through the surface field cavity as measured by the receiving horn antenna at 2.95m distance from the output, viewing the region [20°-90°] where transverse coupling is evident for the resonance frequency at high angles.

4.3.4 Experiment Four - Energy Storage

When measurements are to be made on either non-linear active microwave systems, the waveform may not be sinusoidal. This may be due to either amplitude or frequency modulations or due to the presence of harmonics or spurious frequencies caused by parasitic oscillations. In all these cases it is useful to analyse the actual waveform in the time domain and analyse it into its frequency components. This is achieved via the use of a fast (12GHz) single shot digitising oscilloscope to measure the output from a 50GHz rectifying crystal microwave detector in combination with a Vector Signal Generator (VSG) where 20ns pulses of a set carrier frequency are launched into the cavity and response observed. The experimental setup is pictured below in Figure 4.14. The transmission line and all components are the same as before, the only difference is the inclusion of the VSG.

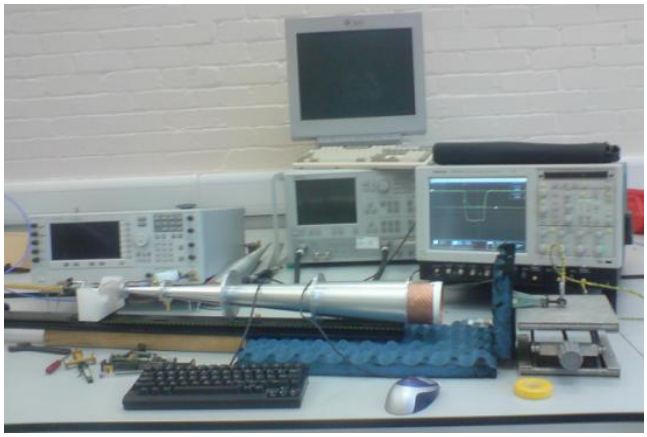

Figure 4.14: Experimental setup to determine the energy storage of the makeshift cavity.

Results demonstrate that the pulses propagate through the structure without experiencing any interference effects if the carrier frequency is located far from the resonance frequency, i.e. at 36.9 GHz and 38 GHz. If however the central frequency is located in the vicinity of the resonance, Figure 4.15, a decrease in pulse amplitude is observed at the cavity exit, this is also visualised in the graph of Figure 4.16 (purple line). This fill

and decay time is evidence that the interaction region is storing energy and will only do so when the resonance conditions are satisfied.

It is useful at this point to insert a small discussion regarding the quality factor, *Q*. The quality factor describes how under-damped an oscillator or resonator is, or equivalently, characterizes a resonator's bandwidth relative to its centre frequency. A higher *Q* value indicates a lower rate of energy loss relative to the stored energy of the oscillator hence the oscillations die out more slowly. The textbook definition for quality factor is defined very generally, regardless of the cavity shape, as 2π times the ratio of the time-averaged field energy stored in the cavity to the energy lost per cycle:

$$Q = 2\pi \frac{average\,stored\,energy}{energy\,lost\ per\,cycle} = \omega \frac{average\,stored\,energy}{power\,loss\,rate}$$

where ω is the centre frequency. This definition holds regardless of the cavity shape and additionally, *Q* is related to the resonance line width $\Delta\omega$ by: $Q = \frac{\omega}{2\Delta\omega}$

The power loss from a cavity arises from two factors, that is the radiated output power and parasitic losses, and, as power losses are additive we can write: $\frac{1}{Q} = \frac{1}{Q_r} + \frac{1}{Q_p}$

where both *r* and *p* represent the parasitic loss terms and of course depend on the configuration and the mode used.

At first glance it may appear that maximizing *Q* is desirable, however for these applications the challenge is handling high power in the cavity, it is actually desirable to have lower *Q* at higher values of power. The reason is that the output power is proportional to the stored energy divided by *Q*, therefore a high *Q* implies high values of stored energy and larger electric fields in the cavity. This will raise the wall heating and potentially lead to breakdown. Looking at the issue of fill time for cavities, which is the

time required for the fields in a cavity to build up to a steady-state level. Looking at the definition for *Q* factor it is apparent that the fill time is proportional to *Q*, and, for certain HPM applications involving cavities, fill time can be an important factor to consider. In the accelerating cavity of an RF linac, for example, the goal is to transfer energy to electrons rather than extract it. Therefore, a trade-off must be made between raising *Q* to maximize the accelerating field and lowering *Q* to limit the fill time and resultant requirement it places on RF pulse lengths. More information regarding the quality factor can be found in almost any accelerator reference text.

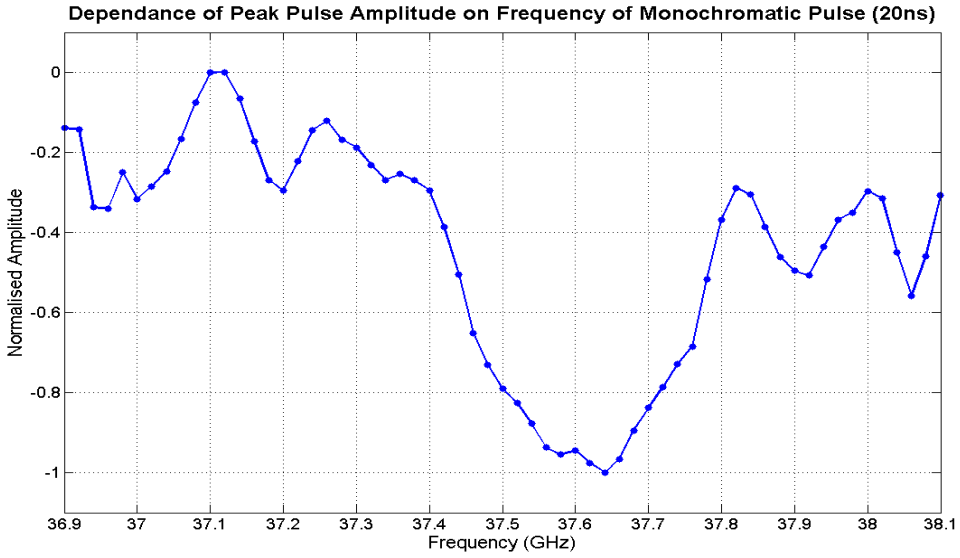

Figure 4.15: Experimental results showing the variation in pulse amplitude with time and that maximum absorption occurs at the resonance frequency, i.e. 37.64GHz.

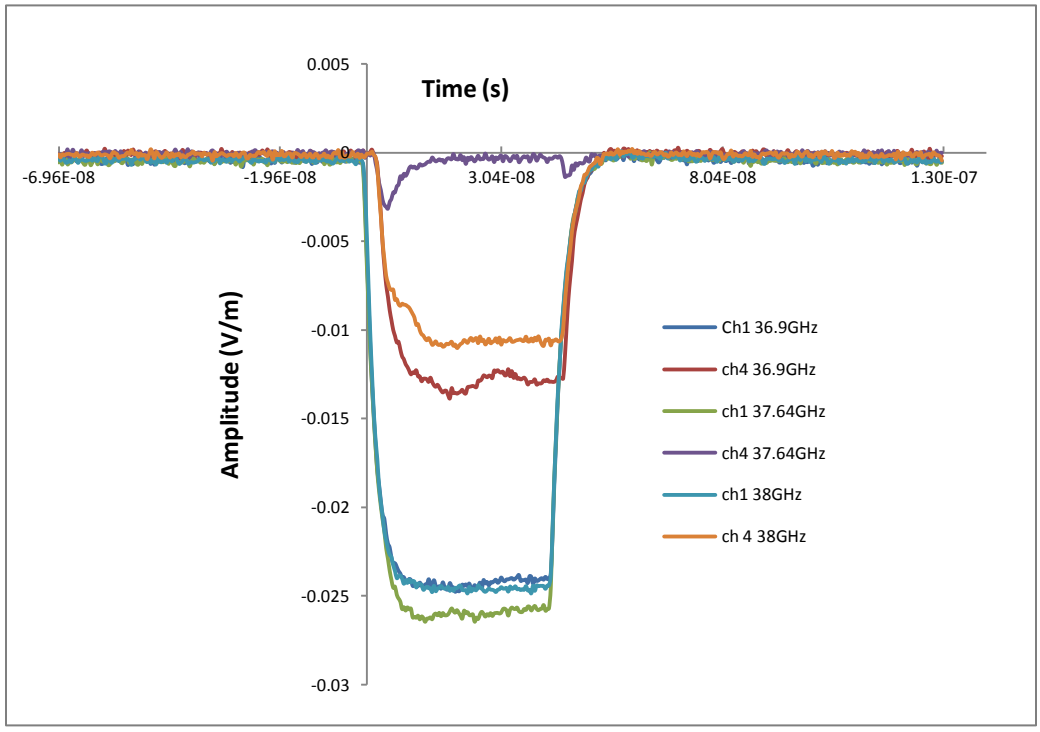

Figure 4.16: Experimental results show that maximum absorption is clearly observed at the resonance of ~ 37.64GHz (which is coloured purple in the graph above) as compared to the frequencies away from resonance.

4.4 Chapter Results & Discussion

This chapter served as to verify the results obtained in chapter 3 relating to the resonance frequency and mode behaviour inside the interaction space. The initial experiment verified the transmission profile of the Ka-band cavity and from this it was very clear that these geometries resulted in specific coupling behaviour for the frequency value equal to 37.64GHz. This is the resonance frequency of the device. The following experiment, number 2, then looked at the corresponding radiated mode pattern for this

fixed frequency. This was viewed in the far-field by making a direct measure of power, and, once again results demonstrated that for f = 37.64GHz, the 2D corrugation couples near-cut off waves thus resulting in the observed scattering of field amplitude at large transverse angles. This was not present for the equivalent section of smooth walled waveguide.

The third experiment looked again at the radiated mode pattern, as in experiment two, only this time considered how the pattern is affected by the presence of frequencies away from resonance, again strengthening the fact that this coupling is only achievable if the resonance conditions are satisfied. It is important to mention that both experiments two and three demonstrated a loss factor of around 10% which agrees with the equation relating to the definition of a far-field signal.

As a final experiment the energy storage ability of the cavity was tested and it was discovered that it does indeed display the so-called ‘rabbit ears’ phenomenon relating to the rise and decay times of the interaction space. However, this needs further investigation as it was included towards the end of the research and time constraints didn’t allow for further analysis or investigation.

5 Applications

5.1 Introduction

This chapter is devoted to providing the reader with examples of how this unique interaction region may be applied to a variety of microwave generation mechanisms for the successful generation of high levels of power at high frequencies, and providing enhanced mode selectivity. The examples are performed using Magic, where the interaction region consists only of cylindrical waveguide, having a 2D square corrugation on the outer wall. Magic was chosen as it can evaluate both the electromagnetic properties and relative particle position properties throughout time simultaneously where many other codes fail. Our interaction region is then excited by an oversized, annular electron beam and the results observed. For completeness, the theoretical basis of both cavity and waveguide excitation is given in Appendix D, as is consideration to the dynamics of charged particles.

The dimensions chosen for the following designs correspond to the initial statement made in Chapter 1, where we seek to obtain high levels of power at equally high frequencies, say >40GHz, and also based upon the results of Chapters 3 and 4 where cavity resonances were evaluated. With this in mind, this chapter considers one cavity which is designed to operate on the ~90GHz range and another, whose design is prevalent to the THz range. Both designs are fundamentally similar, the only difference being the dimensions, i.e. cross section, period, etc.., where both cases will be discussed and be subject to optimisation before any conclusions are drawn.

5.2 High Power 90GHz Maser

The preliminary design consisted of our cylindrical waveguide having a 2D periodic corrugation on the outer conductor as the interaction region, having 16 variations along both the azimuthal and longitudinal coordinate with the period of the corrugation d_z equal to 3.2 mm. The mean radius of the waveguide was 1 cm with a corrugation amplitude equal to 1mm. In order to excite our interaction region, an annular electron beam of 0.85cm radius is applied. Note the relative position of the beam, it's located close to the surface of the corrugation so as to achieve maximum coupling to the surface modes (as discussed Chapter 3). The beam current was set to 1.6kA for the entire system and the accelerating potential was set to equal 300kV, estimated from the equation

$$U_e(kV) \approx 510(kV) \times \left(\sqrt{\lambda^2 / (\lambda^2 - d_z^2)} - 1 \right) \tag{5.1}$$

where $\lambda = d_z / \beta_z$ is the desired frequency of operation for a given lattice parameter, and $\beta_z = c / v_z$.

The beam is confined in a guide magnetic field of strength 3T (only to suppress any transverse oscillation) and is transported through an interaction space of 6 cm in length.

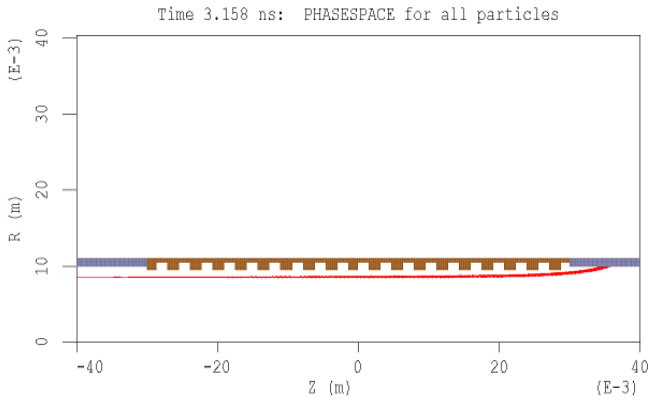

Figure 5.1: Simulation the beam propagating through the structure as given by Magic.

The results from this study are presented in Figure 5.2, from which we can see bunching of the electron beam occurring close to the structure, Figure 5.2 (a-b), with the operating frequency to be in the region of 91GHz and having an average output power of approximately 10MW(x16). Note that this study is only performed for one sector of the entire structure due to the extensive run time (>50hrs), the corresponding power value should therefore be multiplied by 16, giving a value ~150MW. If we now consider these results with respect to the initial input power, the efficiency (assume lossless) of this design equates to ~30%, which greatly exceeds the current status of other sources to date, where values as low as 5% are deemed viable for operation.

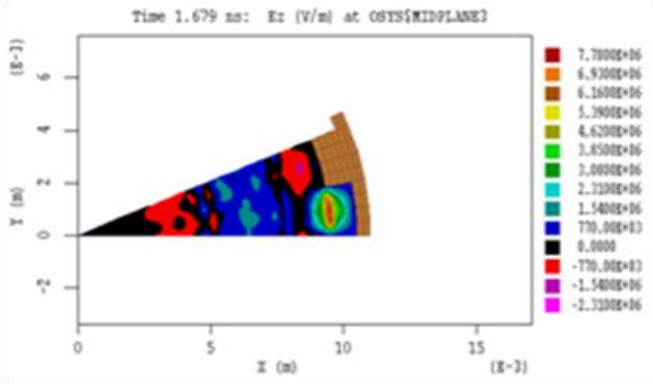

Figure 5.2(a): Simulation results of the maser cross section showing one period, where surface currents are easily identified

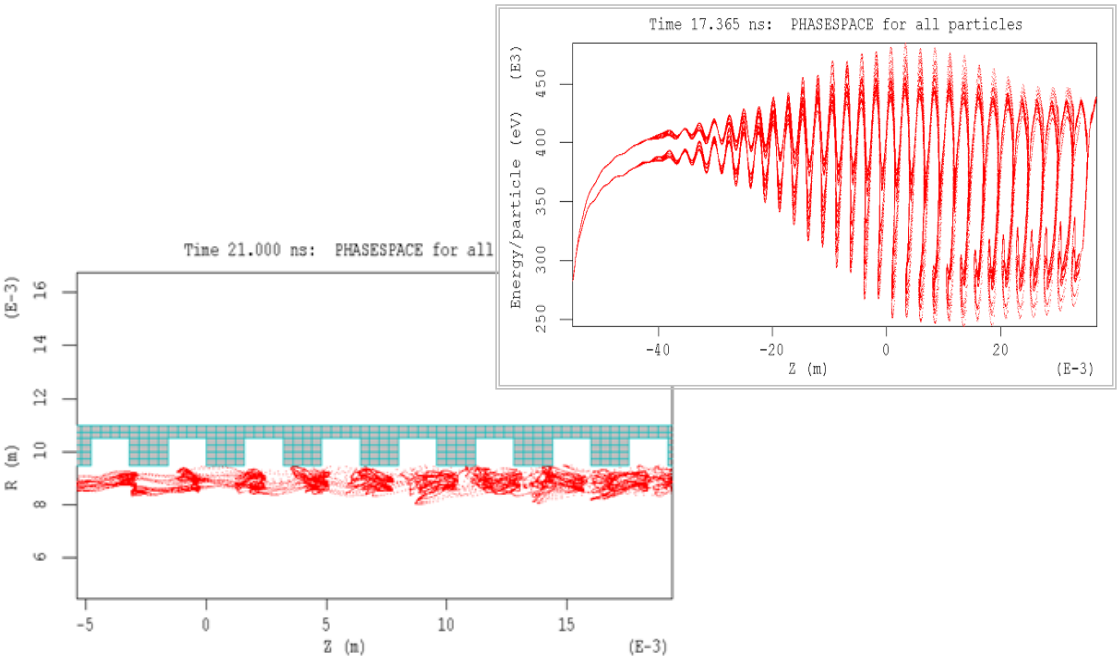

Figure 5.2(b): Simulation results of the maser illustrating the axial bunching of the electron beam inside the interaction space.

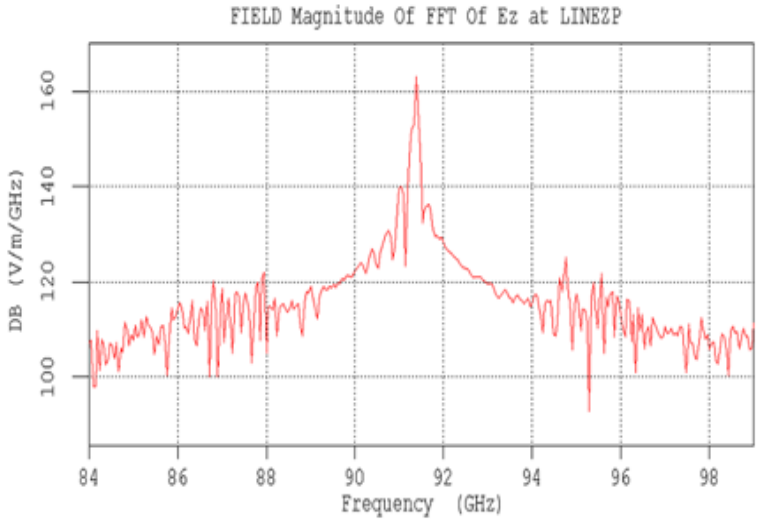

Figure 5.2(c): Simulation results of the W-Band maser showing an operating frequency of ~91 GHz.

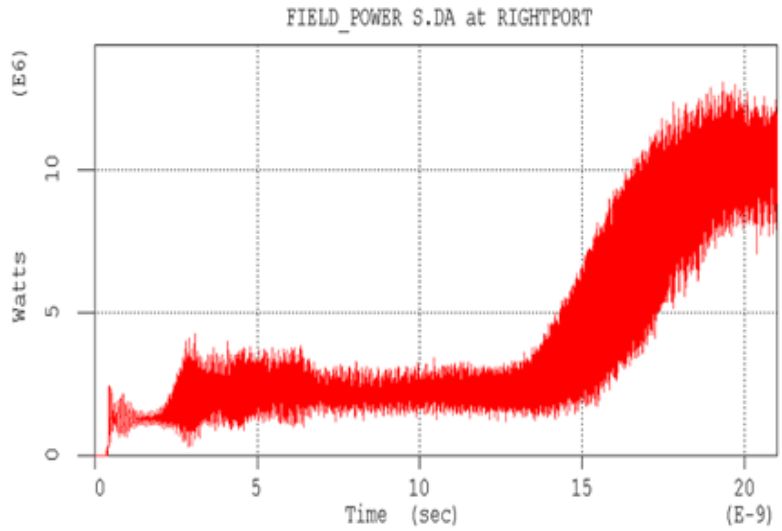

Figure 5.2(d): Simulation results of the maser showing an average power output of~10MW. Note that this is only for the sector simulated, not the entire structure.

Further to this, we gave consideration to maser optimisation, not only the gun but also of the cavity itself. We considered variants such as; accelerating, potential, current, magnetic field strength for the gun, in addition to corrugation amplitude, structure period, and length of the interaction region. This led to an interesting discovery when applying variation to the magnetic field strength, we seen that despite any increase in applied magnetic field, the operating frequency remained constant at ~91GHz.

This illustrates that the interaction mechanism is of the Cherenkov type, as it bears no response to the applied magnetic field, unlike gyro-devices whose frequency would increase in value at a rate proportional to any increase in field.

Following the optimization period (for achievable maximum power at single mode operation), the maser was found to be most responsive to the following parameters; accelerating potential equal to 300kV, beam current of 3.2kA, a longitudinal corrugation period equal to 3.2mm and amplitude 1mm, and a confining magnetic field strength of 6 Tesla, shown Figure 5.3 where the dotted lines represent multiple measurements. Any

deviation from these selections resulted in either a loss in reproducible power or a loss in mode selectivity therefore not viable solutions should we require any form of mode control.

This design was then scaled in order to allow for an increase in the operating frequency, detailed in the proceeding section, where THz operation is considered.

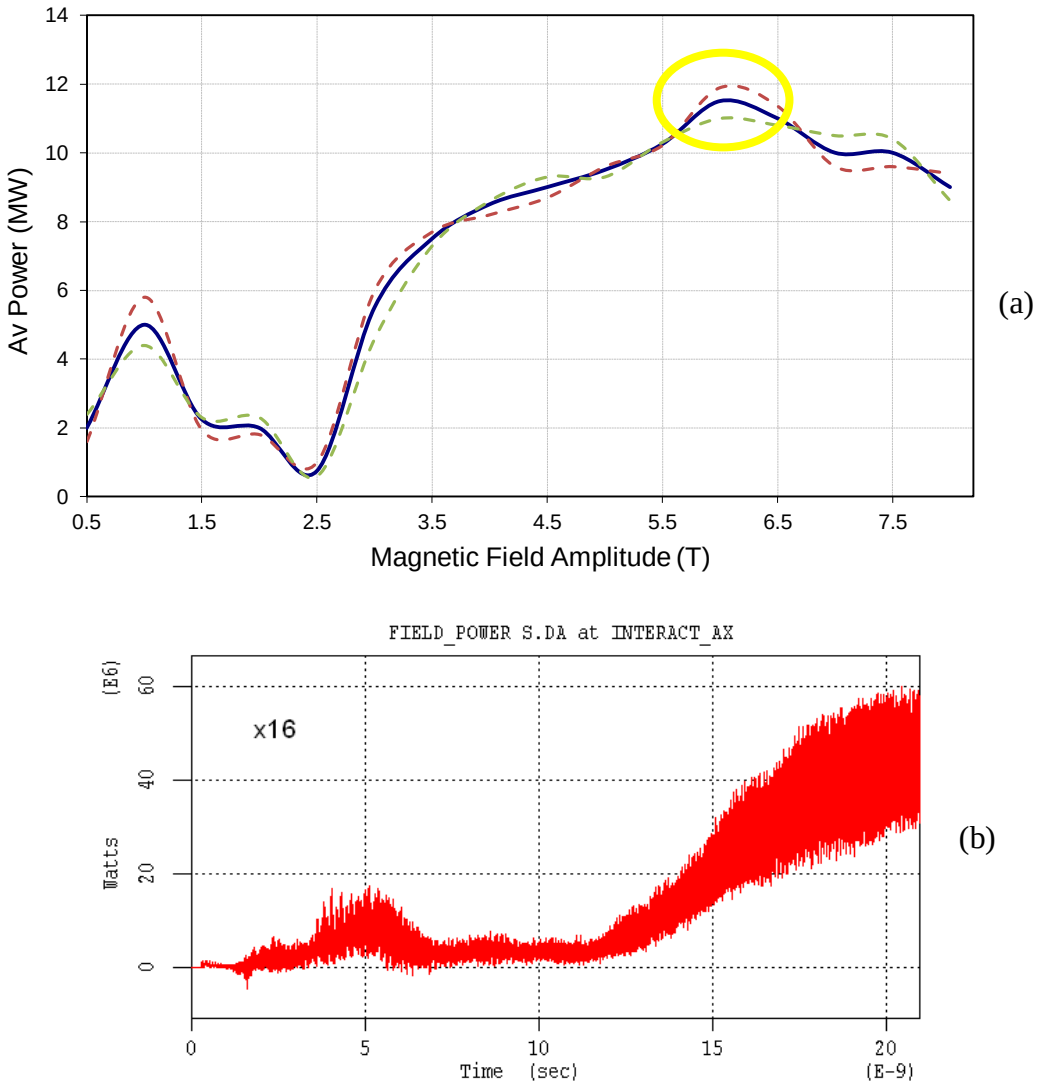

Figure 5.3: Design and optimisation, where a) demonstrates the point in field where maximum output power may be achieved, and b) illustrates this maximum power as given by Magic.

Following the optimization period (for achievable maximum power at single mode operation), the maser was found to be most responsive to the following parameters; accelerating potential equal to 300kV, beam current of 3.2kA, a longitudinal corrugation period equal to 3.2mm and amplitude 1mm, and a confining magnetic field strength of 6 Tesla, shown Figure 5.3. Any deviation from these selections resulted in either a loss in reproducible power or a loss in mode selectivity therefore not viable solutions should we require any form of mode control.

This design was then scaled in order to allow for an increase in the operating frequency, detailed in the proceeding section, where THz operation is considered.

5.3 High Power THz Maser

Numerical simulations were performed using Magic to illustrate a THz Cherenkov maser where the 0.8cm radius cavity, having 20 azimuthal variations and d_z = 1.28cm, is driven by a 20A annular electron beam having a 0.5cm radius and accelerating potential of 100kV, with a pulse length of 10ns. The beam is confined, in this first instance, by a 1 Tesla magnetic field coil. This initial study demonstrated resonance at ~196GHz and average power somewhere in the region of 100kW, Figure 5.4.

(a)

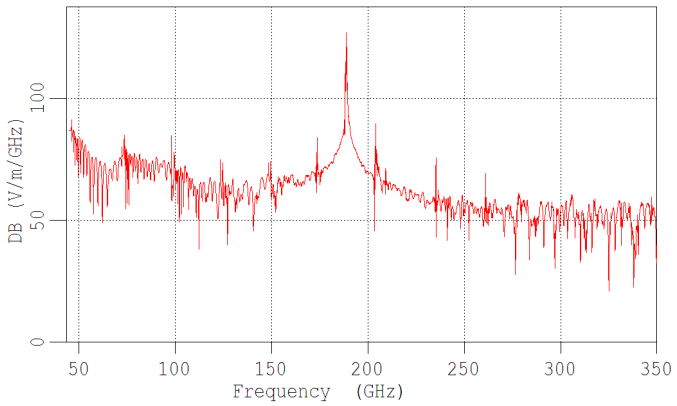

(b)

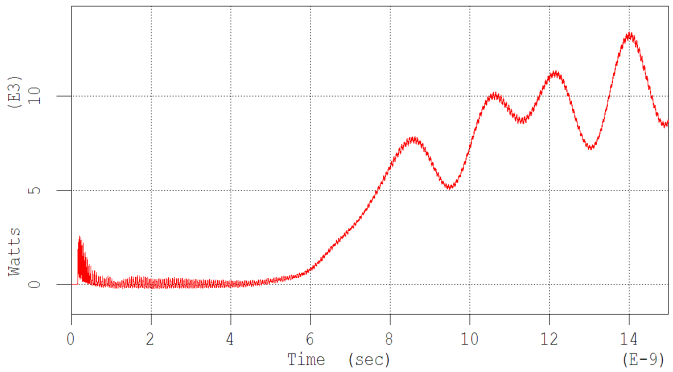

Figure 5.4: Magic simulation of THz cavity, demonstrating frequency equal to 196GHz, with an average power b) equal to ~100kW.

Once again, optimization of this design, with respect to accelerating potential, beam current, magnetic flux density, we found that a maximum power of ~200kW can be achieved when the magnetic field is 2T, and beam current 20Amps at a 300kV potential. Notice also that the frequency spectrum is more defined than in the previous case for a 100kV potential. Overall the resonant frequency did indeed remain constant with the variation in magnetic field, as predicted by the Cherenkov condition. Once again we observed a reduction in mode selectivity when we moved away from these optimised parameters, illustrated in Figure 5.5(c) where the accelerating potential has been reduced to 50kV, for the exact system above.

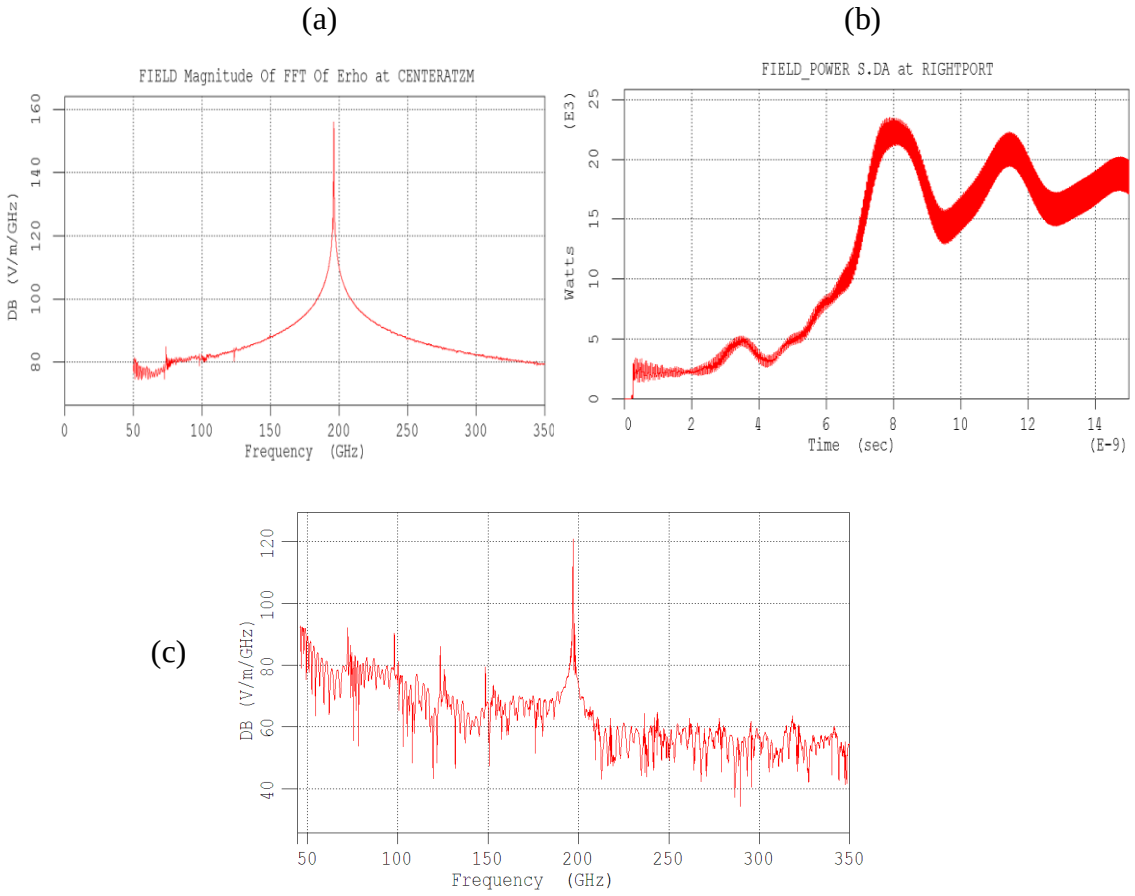

Figure 5.5: Optimized THz design where a) the frequency spectrum is refined and remains unchanged at ~200GHz, b) maximum radiation power of 200kW, and c) mode selectivity loss for a decreased beam voltage.

In order to make this study somewhat more complete, it is necessary to mention, if only briefly, some points to consider with regard to the experimental design of a high power Cherenkov maser. Incidentally, these points relate to the construction of any HOM device and are not restricted to the Cherenkov maser. There are a number of factors to consider when designing high power microwave experiments least of all safety.

In its most basic configuration an electron beam guided by a strong axial magnetic field is injected into a slow-wave structure, where the microwaves are generated. After passing through the slow-wave structure, the beam flares to the wall in the beam dump. The key elements may be extracted as:

- The electron beam (see below)
- The axial magnet producing the field that guides the beam through the device; this field can affect the output resonance and is a major contributor to system power demands and size and mass.
- The slow-wave structure design; this determines the device essentially as well as the frequency, output mode structure, and ultimate power- and energy-handling capabilities.
- The beam dump, which is a driver for system cooling and x-ray shielding requirements.

The production of an intense beam of electrons begins at the electron source. The most commonly used electron sources in modern day pulsed HPM devices are based on the process of explosive emission [108] although other types do exist, namely; field emission thermionic emission and photoemission types. Each of these types has their own set of working conditions and requirements therefore choice must be made carefully. Also, at the end of the interaction region there will be an output port which will couple the RF power through an isolator to the output filter.

The collector is critical to efficient operation. It is the objective of operation that energy be transferred from beam to signal, which implies that the velocity of the beam gradually decreases as it moves towards the output end. By the time the electrons reach the collector they still posses considerable energy and travelling at a lower velocity that when they left the gun. Efficient operation is achieved if the electrons are collected in

such a way that their velocity is reduced to near zero before they actually hit the collector, and this can be achieved by placing a negative voltage on certain collector stages to repel the electrons and slow them down. This is referred to as a depressed collector.

Finally, attention must also be given to the diagnostics used as high power devices tend to differ from their conventional relatives in several ways, namely:

- High power means that high electric fields exist and all diagnostics must avoid breakdown.
- The pulse durations are short, less than a microsecond and typically less than 100 nanoseconds, hence fast response times will be critical.
- HPM sources have yet to be operated at high repetition rates or continuously, therefore diagnostics are typically required only to analyze a single or a few shots.

Although the list is not all bad there are some advantages in that high power often means that it is possible to directly measure the energy of a pulse in a single shot, and also a low shot number means that complex data handling methods are not necessary.

5.4 Discussion

In conclusion to this chapter it has been shown that the novel cylindrical cavity based on a 2D square corrugation to the outer wall, can be applied, in conjunction with an annular electron beam, and used to generate high power, frequency specific, microwave devices. Not only do we have a coherent radiation source capable of generating high levels of power, but we also demonstrate frequency stability and mode control under these conditions through the interactions between 'surface' waves and 'volume' modes. Furthermore we have also identified the interaction mechanism responsible for the energy transfer between the electron beam and the electromagnetic wave as being that of Cherenkov type and this can be verified by examination of the relevant coupled beam-wave simulations where the transfer of energy from beam to wave is clear. Also demonstrated was the fact that this cavity, and indeed its entire operating principles, are scalable across an entire range of frequencies – the method of operation remains constant throughout, more specifically we gave an example of high power THz wave generation. This novel design as compared to the current high frequency power sources available today, which involve semiconductors or complex etching techniques, requires only the machining of a copper cavity.

6 Conclusions & Future Work

This chapter brings together all conclusions reached throughout this work before giving consideration to potential future work on this project and related areas of interest.

6.1 Conclusions

We have shown numerically using the 3D code MAGIC that the resonant coupling between surface waves and near cut-off waves takes place on the periodic structure surface. The full 3D model was used allowing excitation and evolution of the azimuthally symmetric and non-symmetric fields to be simulated. The cavity excitation and the mode structure were analyzed. Experimental studies of the structure have also been conducted and the results observed from numerical simulations agree well with the experimental measurements. The radiation mode pattern has been studied and incident wave resonant scattering on the periodic lattice demonstrated. A cavity of this nature could be used to ensure the stable operation of high-power masers capable of producing kW levels of output power at THz frequencies. The topology of the cavity make it also

compatible with a broad variety of active media, including relativistic electron beams, plasmas and solid matter which can be used as the external drive. The results obtained provide a strong basis for the concept and design of a high power maser operating in the THz and infrared frequency ranges using a 2D periodic lattice.

The application of the 2D cylindrical lattice allows mode selection along the radial and azimuthal coordinates as well as energy storage in the combined fields of the volume and surface waves. This allows one to form the interaction region having the transverse dimension (aperture) much larger than the operating wavelength.

6.2 Future Research

Further work on this project may involve construction of both W and THz type cavities and subjecting them to the very same cold test as for the ka-band case; this would allow us to experimentally verify the results we observed numerically, via CST Studio and Magic, with respect to the transmission properties and dominant resonances of the cavity.

Further on from this it would be advantageous to also set up 'hot' experiments, i.e. inclusive of the electron beam, initially using the Ka-design, simply as all the mechanisms are present to run the experiment, although prior consideration must be given to the choice of beam generation mechanism, subsequent filters, and also as to how the energy may be successfully extracted from the interaction region and measured. This active experiment may then be repeated for the pre-constructed W/THz designs, again these would require manufacture of subsequent peripherals, i.e. transmission line and mode conversion system before any measurement can be made.

Another possible avenue of exploration would be to further exploit the current ever-increasing demand for THz technologies, whereby the current market is currently dominated by quantum cascade lasers and similar solid state electronic devices, although

despite their ability to generate coherent CW in to the infrared spectral regions, their power outputs correspondingly lower, generally below milliWatt level at the 1THz region [73, 74] (for example, for example, 50 μW at 1.8 THz for a Schottky multiplier chain [75, 76]. This combined with the fact that their manufacture process is often complex due to a) their compact size and b) their solid-state nature.

This work, based on numerical predictions, is able to reproduce coherent and significant levels of power (~kW) at frequencies ~ 3THz, by using a straightforward (in comparison to complex etching techniques) workshop manufacturable copper cavity, encompassing a square two-dimensional corrugation. Obviously there will be a limitation point whereby machining process become impossible, but then again, variants of the 2D corrugation could also be considered to see if coherence and/or mode coupling may be further enhanced, for example a change in the square pattern for, say rectangular, or even circular geometries. Again these are just some thoughts as to how our design may be further enhanced so as to maximize the number of potential applications, at minimal cost to the user.

As a final word, the area surrounding surface plasmon research is also of potential interest with regard to this work as the results presented here bare striking similarities to those obtained in various surface plasmon research experiments, [77-80], where current is effectively 'induced' upon some surface, (typically silica of some other substrate) at a specific angle via a 'beam' of active media. Again this has only just recently been touched upon and further investigations are needed into this phenomenon, those of which are currently being carried forward at Strathclyde.

References

1 B. I. Cohen, R. H. Cohen, W. M. Nevins, T. D. Rognlien, Theory of free-electron laser heating and current drive in magnetized plasmas, Rev. Mod. Phys. 63. 1991.

2 V. L. Granetstein, W. Lawson, Gyro-Amplifiers as Candidate RF Drivers for TeV Linear colliders, IEEE Trans. Plasma Sci., 24, 1996.

3 W. P. Leemans, C. G. R. Geddes, J. Faure, Cs. Tóth, J. van Tilborg, C. B. Schroeder, E. Esarey, G. Fubiani, D. Auerbach, B. Marcelis, M. A. Carnahan, R. A. Kaindl, J. Byrd, and M. C. Martin, Phys. Rev. Lett. 91, 074802, 2003.

4 P. Weightman, in Proccedings of the 32nd International Conference on Infrared and Millimetre Waves and 15th International Conference on Terahertz Electronics", pp.1-3, v.1. September 2-7, 2007.

5 I. Evgenya, I. Smirnova, Amit S. Kesar, Ivan Mastovsky, Michael A. Shapiro, and Richard J. Temkin, Phys. Rev. Lett. 95, 074801 (2005).

6 J. R. Sirigiri, M. A. Shapiro, and R. J. Temkin, Phys. Rev. Lett. 90, 258302 (2003).

7 N. S. Ginzburg, A. A. Kaminsky, A. K. Kaminsky, N. Yu. Peskov, S. N. Sedykh, A. P. Sergeev, and A. S. Sergeev, Phys. Rev. Lett. 84 3574 (2000).

8 N. S. Ginzburg, N. Yu. Peskov, A. S. Sergeev, Opt. Commun., 96, p.254, 1993.

9 I. V. Konoplev, A. W. Cross, P. MacInnes, W. He, C. G. Whyte, A. D. R. Phelps, C. W. Robertson, K. Ronald, A. R. Young, Appl. Phys. Lett., 89, 171503, 2006

10 C. C. Cutler, J. Appl. Phys., 27(9), p.1028, 1956; H. F. Webster, J. Appl. Phys., 28(12), p.1388, 1957; H. F. Webster, Phys. of Plasmas, 7(1), p.94, 2000.

11 N. S. Ginzburg, N. Yu. Peskov, and A. S. Sergeev, Opt. Commun. 112, 151 (1994).

12 N. S. Ginzburg, A. S. Sergeev, N. Yu. Peskov, G. R. M. Robb, A. D. R. Phelps, IEEE Trans. Plasma Sci. 24, p.770, 1996.

13 N. S. Ginzburg, N. Yu. Peskov, A. S. Sergeev, I. V. Konoplev, A. W. Cross, A. D. R. Phelps, G. R. M. Robb, K. Ronald, W. He, C. G. Whyte, J. Appl. Phys. 92, p.1619, 2002.

14 A. W. Cross, I. V. Konoplev , A. D. R. Phelps, K. Ronald, J. Appl. Phys., 93, p.2208, 2003.

15 I. V. Konoplev, A. W. Cross, A. D. R. Phelps, K. Ronald, Phys. Rev. E, 68, 066613, 2003.

16 W. Cross, I. V. Konoplev, K. Ronald, A. D. R. Phelps, W. He, C. G. Whyte, N. S. Ginzburg, N. Yu. Peskov, and A. S. Sergeev, Appl. Phys. Lett., 80, 1517, 2002.

17 J. Benford and J. Swegle, "High Power Microwaves", Artech House, 1992.

18 V. L. Granatstein and I. Alexeff, "High Power Microwave Sources", Artech House, Boston and London, 1987.

19 S. H. Gold and G. S. Nusinovich, American Institute of Physics, Rev. Sci. Instrum., 68 (11) Nov. 1997.

20 G. S. Nusinovich, Physics of Plasmas, Vol.13, 053107 (2006).

21 A. T. Lin, W. W. Chang and K. R. Chu, Int. Journal Infrared and Millimetre Waves, Vol. 5, No. 4, 1984.

22 K. R. Chu, Review of Modern Physics, Vol. 76, April 2004.

23 V. A. Flyagin, A. V. Gaponov, M. I. Petelin, and V. K. Yulpatov, IEEE Trans. on Microwave Theory and Tech., Vol. MTT-25, No. 6, June 1977.

24 S. C. Zhang and M. Thumm, Appl. Phys. Lett. 88, 033514 (2006).

25 A. Grudiev and K. Schunemann, IEEE Trans. Plasma Sci. Vol. 30, No. 3, June 2002.

26 K. K. Chow, and R. H. Pantell, Proceedings of the IRE, Vol. 48, Issue 11, p 1865-1870, Nov. 1960.

27 P. Sprangle and A. T. Drobot, IEEE Trans. Microwave Theory Tech. 25, 528 (1977).

28 V. Ayvazyan et. al., 'First operation of a free-electron laser generating GW power radiation at 32nm wavelength', Eur. Phys. J. D. 37, pp. 297 – 303 (2006).

29 E. D. Courant, C. Pellegrini and W. Zakowicz, 'High energy inverse free-electron-laser accelerator', Phys. Rev. A, Vol. 32, No. 5, (1985).

30 R. B. Yoder, T. B. Zhang, T. C. Marshall and J. L. Hirshfield, 'Simulation results and experimental design for the microwave inverse FEL accelerator', AIP conference proceedings, Vol. 398, pp. 629 – 637, 1996.

31 N. S. Ginzburg, N. Yu. Peskov, and A. S. Sergeev, I. V. Konoplev, A W. Cross, A. D. R. Phelps, G. R. M. Robb, K. Ronald, W. He, and C. G. Whyte, J. Appl. Phys., Vol. 92, No. 3, 1 August 2002.

32 I. V. Konoplev, P. McGrane, W. He, A. W. Cross, A. D. R. Phelps, C. G. Whyte, K. Ronald, and C. W. Robertson, Phys. Rev. Lett. 96, 035002 (2006).

33 I. V. Konoplev, P. McGrane, K. Ronald, A. W. Cross, W. He, C. G. Whyte, A. D. R. Phelps, C. W. Robertson, D. C. Speirs, N. S. Ginzburg, N. Yu. Peskov, A. S. Sergeev and M. Thumm, Free Electron Lasers and Synchrotron Radiation, Joint 30th Int. Conf. on Infrared and Millimeter Waver & 13th Intl. Conf. on Teraherthz Electronics, 2005.

34 I. V. Konoplev, A. W. Cross, W. He, A. D. R. Phelps, K. Ronald, G. R. M. Robb, C. G. Whyte, N. S. Ginzburg, N. Yu. Peskov, and A. S. Sergeev, Nuclear Instruments and Methods in Physics Research, A, 445 (2000) p236-240.

35 I. V. Konoplev, A. D. R. Phelps, A. W. Cross, K. Ronald, P. McGrane, W. He, C. G. Whyte, N. S. Ginzburg, N. Yu. Peskov, A. S. Sergeev and M. Thumm, Nuclear Instruments and Methods in Physics Research, A, 528 (2004) p101-105

36 J. M. Watson, "Status of the Los Alamos FEL", Nuclear Instrumentation Methods, A250, p1, 1986.

37 M. A. Agafonov et al. "Generation of hundered joule pulses at 4mm wavelength by FEM with a sheet electron beam", IEEE Trans. Plasma Science, 26(3), p531, 1998.

38 S. Nakamura and G. Fasol, The Blue Laser Diode (Springer, Berlin 1997).

39 G. G. Denisov and M. G. Resnikov, Izvest. Vyssh. Ucheb. Zaved. Radiofizkika, 25, 5, 1982.

40 H. Kogelink and C. V. Shank, "Coupled Wave Theory of Distributed Feedback Dye-lasers", J. App. Phys., 43 1972, 2382.

41 N. S. Ginzburg, A. S. Sergeev, N. Yu. Peskov, G. R. M. Robb, A. D. R. Phelps, "Mode Competition and control in free electron lasers with one and two-dimensional Bragg resonators", IEEE Transactions on Plasma science, 24(3), 1996.

42 I. V. Konoplev, A. W. Cross, A. D. R. Phelps, W. He, K. Ronald, C. G. Whyte, C. W. Robertson, P. MacInnes, N. S. Ginzburg, N. Yu. Peskov, A. S. Sergeev, V. Yu. Zaslavsky, and M. Thumm, "Experimental and theoretical studies of a coaxial free-electron maser based on two-dimensional distributed feedback", Phys. Rev. E 76, 056406 (2007).

43 I. V. Konoplev, A. W. Cross, W. He, A. D. R. Phelps, K. Ronald, G. R. M. Robb, C. G. Whyte, N. S. Ginzburg, N. Yu. Peskov and A. S. Sergeev, "Progress of the Strathclyde Free Electron Maser experiment using a 2D Bragg structure", Nuclear Instruments and Methods in Physics Research Section A: Accelerators, Spectrometers, Detectors and Associated Equipment, Volume 445, Issues 1-3, 1 May 2000, Pages 236-240

44 I. V. Konoplev, A. W. Cross, A. D. R.Phelps, K. Ronald, M. Thumm, "Coaxial 2D Bragg structures for microwave electronics", 36th European Microwave Conference, 2006, p1366 – 1369.

45 P. MacInnes, I. V. Konoplev, A. W. Cross, W. He, A. D. R. Phelps, C. G. Whyte, K. Ronald, C. Robertson, M. Thumm, "Coaxial 2D-1D two-mirror cavity free-electron maser experiment", IEEE 35th International Conference on Plasma Science, 2008.

46 I. V. Konoplev, P. MacInnes, A. W. Cross, W. He, A. D. R. Phelps, K. Ronald, C. G. Whyte, C. W. Robertson, "2D AND 1D SURFACE PHOTONIC BAND GAP STRUCTURES FOR ACCELERATOR APPLICATIONS", Proceedings of EPAC 2006, Edinburgh, Scotland.

47 N. S. Ginzburg, N. Y. Peskov, A. S Sergeev, A. D. R. Phelps, I. V. Konoplev, G. R. Robb, A. W. Cross, A. V. Arzhannikov, S. L. Sinitsky, "Theory and design of a free-electron maser with two-dimensional feedback driven by a sheet electron beam", Phys Rev E Stat Phys Plasmas Fluids Relat. Interdiscip. Topics, 1999, 60(1):935-45.

48 N. S. Ginzburg, V. Yu. Zaslavskii, A. M. Malkin, N. Yu. Peskov and A. S. Sergeev, "Frequency stabilization in free-electron masers with 2D and 1D distributed feedback", Volume 54, Number 9, 1384-1388, Short Communications, Technical Physics.

49 N. S. Ginzburg, V. Yu. Zaslavskii, A. M. Malkin, N. Yu. Peskov, A. S. Sergeev and M. Tumm, "Azimuthal selection of modes in free-electron masers with coaxial Bragg resonators", Journal of Communications Technology and Electronics Volume 54, Number 9, 1015-1026, Microwave Electronics.

50 A. W. Cross, W. He, I. V. Konoplev, A. D. R. Phelps, K. Ronald, G. R. M. Robb, C. G. Whyte, N. S. Ginzburg, N. Y. Peskov, A. S. Sergeev, "Experimental and theoretical study of 2D Bragg structures for a coaxial free electron maser "Nuclear Instrum. Methods Phys. Res., A 475, 1-3 (2001) 164-172.

51 A. W. Cross, N. S. Ginzburg, W. He, I. V. Konoplev, N. Y. Peskov, A. D. R. Phelps, G. R. Robb, K. Ronald, A. S. Sergeev and C. G. Whyte, 2000, 'Experimental and theoretical study of a high-power co-axial FEM with 2-D distributed feedback', International FEL Conference, Duke Free electron Laser laboratory (USA).

52 C. Yeh and G. Lindgren, "Computing the propagation characteristics of radially stratified fibers – An efficient method," Appl. Opt. **16**, 483 (1977).

53 J. Vanderlinde, 'Classical Electromagnetic Theory', John Wiley & Sons, 1993.

54 T.Weiland, "A discretization method for the solution of Maxwell's equations for six-component fields," Electron. Communication (AEÜ), vol. 31, no. 3, p. 116, 1977.

55 T.Weiland, "Time domain electromagnetic field computation with finite difference methods," Int. J. Numer. Model., vol. 9, no. 4, pp. 295–319, 1996.

56 K.S.Yee, "Numerical solution of initial boundary value problems involving Maxwell's equations in Isotropic media," IEEE Antennas Propagation, vol. 14, no. 5, pp. 302–307, 1966.

57 A. Taflove and S.C. Hagness, Computational Electrodynamics: The Finite-Difference Time-Domain Method, 3rd ed. Norwood, MA:Artech House, 2005.

58 F. Zheng, Z. Chen, and J. Zhang, "A finite-difference time-domain method without the Courant stability conditions," IEEE Microwave Guided Wave Lett., vol. 9, no. 11, pp. 441–443, 1999.

59 E.P. Li, I. Ahmed, and R. Vahldieck, "Numerical dispersion analysis with improved LOD-FDTD method," IEEE Microwave Wireless Components Lett., vol. 17, no. 5, pp. 319–321, May 2007.

60 P.B. Johns and R.L. Beurle, "Numerical solutions of 2-dimensional scattering problems using a transmission-line matrix," Proc. Inst. Elect. Eng.,vol. 118, no. 9, pp. 1203–1208, 1971.

61 C. Christopoulos, The Transmission-Line Modeling Method: TLM. Piscataway,NJ: IEEE Press, 1995.

62 A. Bossavit, Computational Electromagnetism Variational Formulations, Complementarity, Edge Elements. New York: Academic Press, 1998.

63 J. Jin, The Finite Element Method in Electromagnetics, 2nd ed. Piscataway,NJ: IEEE Press, 2002.

64 A. W. Cross, et al., Journal of Appl. Phys., 93, p.2208, 2003; A. W. Cross, et al., Nucl. Instr. and Meth. In Phys. Res. A, 475, p.164, 2001.

65 D. Pozar, Microwave Engineering, John Wiley and Sons, 1997. .

66 Agilent Technologies, HP 8757D SNA Technical Manual.

67 Flann Microwaves, Waveguide Component Sheet, www.flann.com.

68 I. V. Konoplev,"Free-Electron Maser with Two Dimensional Distributed Feedback', PhD Thesis, University of Strathclyde, June 2001.

69 I. V. Konoplev, A. W. Cross, P. MacInnes, W. He, A. D. R. Phelps, C. G. Whyte, K. Ronald, and C. W. Robertson, 'Free-electron maser based on a cavity with two- and one-dimensional distributed feedback', Appl. Phys. Lett. 92, 211501 (2008).

70 I.V Konoplev, A. D. R. Phelps, A. W. Cross, K. Ronald, P McGrane W He, C. G. Whyte, N. S. Ginzburg, N. Yu. Peskov, A. S. Sergeev, M. Thumm, 'Experimental and computational studies of novel coaxial 2D Bragg structures for a high-power FEM', Nuclear Instruments and Methods in Physics Research, Section A, Volume 528, Issues 1–2, August 2004, Pages 101–105.

71 I.V. Konoplev, A.W. Cross, W. He, A.D.R. Phelps, K. Ronald, G.R.M. Robb, C.G. Whyte, N.S. Ginzburg, N.Yu. Peskov, A.S. Sergeev, "Progress of the Strathclyde Free Electron Maser experiment using a 2D Bragg structure", Nuclear Instruments and Methods in Physics Research A 445 (2000).

72 I.V. Konoplev, P. McGrane, K. Ronald, A.W. Cross, W. He, C.G. Whyte, A.D.R. Phelps, C.W. Robertson, "Free electron maser experiments based on a coaxial 2d bragg cavity", Conference digest of the joint 29th international conference on infrared and millimeter waves and 12th international conference on terahertz electronics, 2004.

73 P. H. Siegel, Terahertz technology. IEEE Trans. Microwave Theory Tech. 50, 910–928 (2002).

74 D. L. Woolard, E. R. Brown, M. Pepper, & M. Kemp, Terahertz frequency sensing and imaging: A time of reckoning future applications? Proc. IEEE 93, 1722–1743 (2005).

75 I. Mehdi et al. Terahertz multiplier circuits in 2006 IEEE MTT-S International Microwave Symposium Digest 341–344 (IEEE, San Fransisco, California, 2006).

76 A. Maestrini et al. A 1.7–1.9 THz local oscillator source. IEEE Microwave Wireless Components, Lett. 14, 253–255 (2004).

77 William L. Barnes, Alain Dereux & Thomas W. Ebbesen, "Surface plasmon subwavelength optics", *Nature* **424**, 824-830 (14th August 2003).

78 Y. Zhao, and D. Grischkowsky, "Terahertz demonstrations of effectively two-dimensional photonic bandgap structures," Opt. Lett. 31(10), 1534–1536 (2006).

79 L. S. Mukina, M. M. Nazarov, and A. P. Shkurinov, "Propagation of THz plasmon pulse on corrugated and flat metal surfaces," Surf. Sci. 600(20), 4771–4776 (2006).

80 T.I. Jeon, J. Zhang, and D. Grischkowsky, "THz Sommerfeld wave propagation on a single metal wire," Appl. Phys. Lett. 86(16), 161904 (2005).

81 K. E. Kreischer and R. J. Temkin, "Infrared and Millimeter Waves," K. Button, Ed. NY: Academic, vol. 7, pp. 377-485, 1983.

82 V. A. Flyagin and G. S. Nusinovich, Proc. IEEE, vol. 76, pp. 644-656, 1988.

83 G. S. Nusinovich, Int. J. Electronics, vol. 51, no. 4, pp. 457-474, 1981.

84 B. Levush and T. Antonsen, Jr., IEEE-PS, PS-18, vol. 3, pp. 260-272, 1990.

85 S. H. Gold and A. W. Fliflet, Int. J. Electronics, vol. 72, nos. 5-6, pp.779-794, 1992.

86 G. S. Nusinovich, M. E. Read, O. Dumbrajs, and K. E. Kreischer, IEEE-ED, vol. 41, no. 3, March 1994.

87 N. P. Venediktov, V. E. Zapevalov, and A. N. Kuftin, *Gyrotrons*, V. A. Flyagin, Ed. Gorky, USSR, IAP, pp. 12-19, 1989.

88 K. E. Kreischer, T. L. Grimm, W. C. Guss, A. W. Mobius, and R. J. Temkin, Phy. Fluids, B, 2, no. 3, pp. 640-646, 1990.

89 M. I. Petelin and V. K. Yulpatov, Linear theory of a CRM-monotron, Radiophys. Quantum Electron., vol. 18, pp. 212-219, 1975.

90 M. V. Kartikeyan, E. Borie, and M. K. A. Thumm, Gyrotrons, High Power Millimeter Wave Technology, Springer-Verlag Berlin Heidelberg, 2004.

91 J. J. Barroso, P. J. Castro, and R. A. Correa, IEEE Trans. Plas. Sci., vol. 43, No. 6, June 1995.

92 K. A. Avramides, C. T. Iatrou and J. L. Vomvoridis, Design Considerations for Powerful Continous-Wave Second-Cyclotron-Harmonic Coaxial-Cavity Gyrotrons, IEEE Trans., Plasma Sci., Vol. 32, No. 3, June 2004.

93 K. Singh, P. K. Jain, and B. N. Basu, Progress In Electromagnetic Research, PIER 47, 297-312, 2004.

94 G. S. Nusinovich, M. E. Read, O. Dumbrajs, and K. E. Kreischer, Theory of gyrotrons with coaxial resonators, IEEE Trans. Electron Devices, vol. 41, pp. 433-438, Apr. 1994.

95 V. A. Flyagin, V. I. Khiznyak, V. N. Manuilov, A. B. Pavelyev, V. G. Pavelyev, B. Piosczyk, G. Dammertz, O. Hochtl, C. T. Iatrou, S. Kern, H.-U. Nickel, M. Thumm, A. Wien, and O. Dumbrajs, Development of a 1.5 MW coaxial cavity gyrotron at 140 GHz, in Dig. 19th Int. Conf. Infrared Millimeter Waves Sendai, Japan, JSAP AP 941228, 1994, pp. 75-76.

96 C. T. Iatrou, S. Kern, and A. B. Pavelyev, Coaxial cavities with corrugated inner conductor for gyrotrons, IEEE Trans. Microwave Theory Tech., vol. 44, pp. 56-64, 1996.

97 C. T. Iatrou, Mode selective properties of coaxial gyrotron resonators, IEEE Trans. Plasma Sci., vol. 24, pp. 596-605, 1996.

98 P. J. B. Clarricoats and P. K. Saha, Attenuation in corrugated circular waveguide, Electron. Lett., vol. 6, pp. 370–372, 1970.

99 O. Dumbrajs, A novel method of improving performance of coaxial gyrotron resonators, IEEE Trans.. Plasma Sci., vol. 30, pp. 836-839, 2002.

100 B. Piosczyk et al., "2.2 MW, 165 GHz coaxial cavity gyrotron," in Proceedings of the 25th International Conference on Infrared and Millimeter Waves, Beijing, China, 2000, pp.19-20.

101 Z. C. Ioannidis, O. Dumbrajs, and I. G. Tigelis, Eigenvalues and Ohmic Losses in Coaxial Gyrotron Cavity, IEEE Transactions on Plasma Science, Vol. 34, No.4, Aug. 2006.

102 S. N. Vlasov, L. I. Zagryadskaya, I. M. Orlova, Radio Eng. and Electron Phys., vol. 21, no. 7, pp. 96-102, 1976.

103 J.-Y. Raguin and K. Schuenemann, Analysis of gyrotron coaxial cavities with corrugated inner conductor based on the method of moments, in Proceedings of the International Conference on Electronics and Radiophysics of Ultra-High Frequencies, St. Petersburg, Russia, 1999, pp. 403-409.

104 O. Dumbrajs and G .S. Nusinovich, Coaxial gyrotrons: past, present, and future, IEEE Transactions on Plasma Science, vol.32, no. 3, pp. 934-946, 2004.

105 O. Dumbrajs and G .I. Zaginaylov, Ohmic losses in coaxial gyrotron cavities with corrugated insert, IEEE Transactions on Plasma Science, vol.32, no. 3, pp. 861- 866, 2004.

106 G. I. Zaginaylov, N. N. Tkachuk, V. I. Scherbinin and K. Schunemann, Rigorous Calculation of Energy Losses in Cavity of ITER Relevant Coaxial Gyrotron, August 2000.

107 G. S. Nusinovich, Introduction to the Physics of Gyrotrons, The John Hopkins University Press, Baltimore, 2004.

108 Bugaev, P.S. et al., Explosive electron emission, *Sov. Phys. Usp.*, 18, 51, 1975.

Appendix A

A1. Gyrotron Review

A1.1 Introduction

In its conventional arrangement (shown in Figure A1 below), the gyrotron consists of a Magnetron Injection Gun (MIG) that produces an annular beam, an interaction region, an output window and a beam collector. The interaction space of the gyrotron is immersed in a strong magnet known as a solenoid.

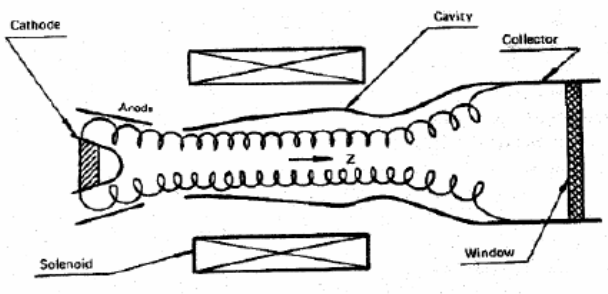

Figure A1: Conventional gyrotron arrangement.

When a voltage is applied to the gun, an electric field is created at the cathode and leads to electron beam production and acceleration towards the anode. In the region between the cathode and the anode the electric field is mostly perpendicular to the magnetic field generated by the solenoid. In this region the electrons are in crossed fields and start to drift along the azimuthal direction while still moving in $\vec{E}$ and $\vec{B}$ fields, thus obtaining rotational velocity which increases significantly as the electron beam passes through the increasing amplitude of guide field. As the electrons reach the end of the cathode-anode region, the electric field lines change from mostly perpendicular to parallel to the magnetic field lines and the electrons acquire both transverse and axial velocity

components before entry into the drift tube. They gyrate helically about a guiding centre defined by the magnetic field line, shown in Figure A2, where the radius of the path is known as the Larmour radius ($r_L = \frac{\upsilon_\perp}{\omega_c}$). This is usually small compared to the radius of the beam, so that the beam remains annular as it propagates. A schematic of the MIG is shown in Figure A3 below.

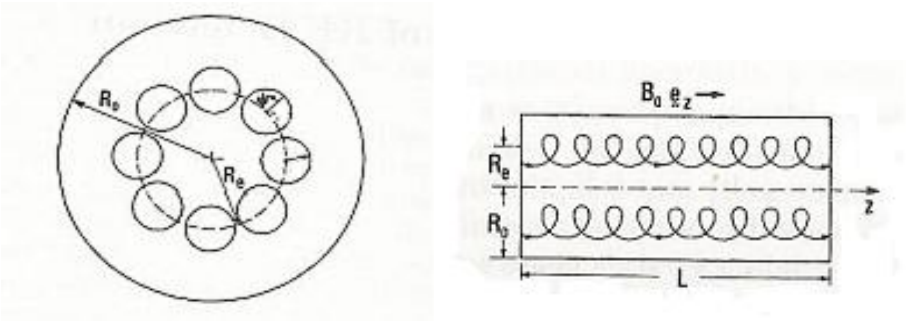

Figure A2: Beam geometry in a gyrotron resonator.

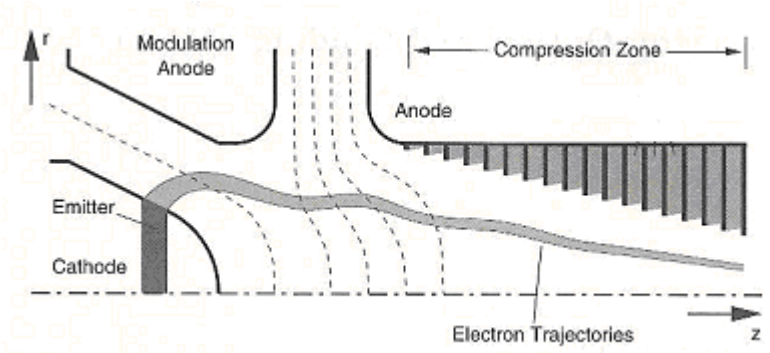

Figure A3: Schematic of a Magnetron Injection Gun.

The electrons move toward the interaction region through a growing magnetic field and the orbital momentum of the electron increases due to magnetic compression, $\frac{p_\perp^2}{B} = const.$ In the interaction region the magnetic field is uniform and it is here that the

electrons interact with the transverse electric (TE) eigenmode of the cavity and transform a part of their kinetic energy associated with the transverse momentum into microwave energy. The generated microwave power is extracted through an output window. For efficient coupling to the wave, the electrons must have a significant transverse velocity component as energy transfer occurs as a result of the interaction between the transverse velocity component of the gyrating electrons and the transverse electric field of the TE modes (RF fields) of the cavity structure. This is known as the Cyclotron Resonance Maser (CRM) instability and illustrated in Figure A4.

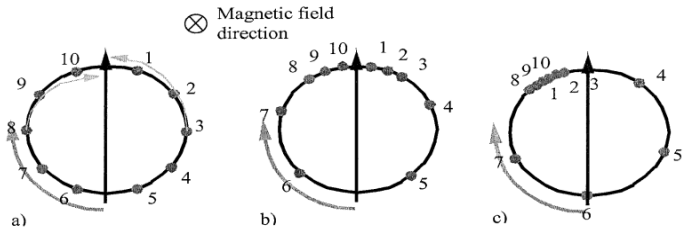

Figure A4: Phase bunching in a CRM device, a) Shows the initial position of the electrons, b) Shows the interaction between the beam and the wave and c) shows the phase slippage between the beam and the electric field.

From the very beginning of the gyrotron development, it was proposed to use resonators that were open in the axial direction in contrast with klystrons and magnetrons. This axially open design enables selection of modes with different axial indexes; this is because the diffractive losses of modes with only one axial variation in such resonators is much smaller than losses for modes which have a larger axial index. Such resonators, however, do not provide the selection of modes with different transverse indexes. Therefore, in the late 1960s, Goldenberg proposed using coaxial resonators for this purpose, because these types of resonators can offer an improved selectivity of modes with different radial indexes.

A1.2 High Power Gyrotrons

One of the main issues associated with the development of long pulse/CW operation of gyrotrons is heating of the resonator/cavity. This heating is caused by ohmic losses of

the microwave power in the cavity walls [81,82]. In order to solve this problem it's necessary to increase the volume of the resonator. However an increase in the resonator volume results in the generation of very high order modes. This leads to mode competition [83-85] and development of the stochastic regime of oscillations. One method of mode selection is by appropriate choice of radius of the electron beam, which corresponds to the maximum value of coupling impedance between such beam and the rotating TE_{mp} mode [86]. This method is especially advantageous for selection of whispering gallery modes TE_{mp}, where the azimuthal index, m, is much larger than the radial index, p. For the case where the radial index is small (p = 1, 2, 3), the modes will be discriminated because the radii of the electron guiding centres are smaller than that of their caustics. This is shown in Figure A5. This means that if the electron beam is located in the decay region of the mode along the radial coordinate the coupling impedance between the beam and the mode is very small. Contrary to the modes with larger radial indices which occupy a large part of resonator volume, in spite of the fact that it may be stronger coupled to the electron beam, will have larger starting currents [86]. The starting current is proportional to the energy density stored in the cavity; therefore the effective volume which needs to be filled with RF energy to start oscillations is larger for higher order modes.

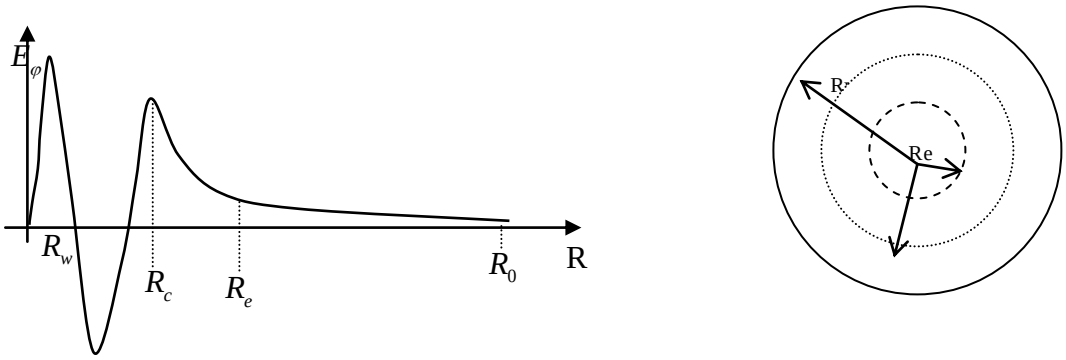

Figure A5: Schematic of caustic radius and electric field profile for small radial index. In the case of large radial index the electron beam radius exceeds the caustic radius, $R_e > R_c$.

This method has proved useful for stable operation at higher modes [87] and [88], however due to the fields of these modes being concentrated near the walls of the cavity; the ohmic heating is relatively high at megawatts of microwave output power inside the interaction space. Therefore if the desired microwave and/or operating frequency is to increase then so does the radial index of the operating mode and hence selectivity of modes using the above method becomes insufficient.

A1.3 Basic features of mode selectivity in Gyrotron Resonators

Selection of modes with large radial indexes can be provided by the use of coaxial resonators. Typically, in gyrotrons, a thin annular electron beam is used. Their coupling to the transverse-electric (TE) modes of cylindrical resonators are described [89] by Bessel functions $J^2_{m\pm s}(k_\perp R_0)$, where m is the azimuthal mode index, s is the cyclotron resonance harmonic number, and the "minus" and "plus" signs correspond to the co- and counter-rotating modes with respect to the gyration of the electrons in the external magnetic field, $k_\perp = \upsilon_{m,p}/R_w$ is the transverse wave number which is determined by the mode eigennumber $\upsilon_{m,p}$ and R_w is the resonator wall radius with R_0 the radius of the electron guiding centres. (For TE_{mp} modes this eigennumber is the p^{th} root of the equation $J'_m(\upsilon_{mp}) = 0$). The Bessel functions have the largest maximum closest to the axis, i.e. when the radial coordinate is close to the caustic radius, which is defined as $R_c = (m/\upsilon_{m,p})R_w$. Therefore by locating the beam at this position one can provide the maximum coupling to the field of the desired mode. For the modes having smaller radial indexes the beam is located within the exponentially decaying field (along the radial coordinate), and therefore beam coupling to these modes is small. For modes with a large radial index it is difficult to provide good selection as the beam has to be located at a precise radius. These modes do occupy a larger cross section and therefore their starting currents can be higher for specific cavity configurations, than that for the desired

mode. The effectiveness of this method of mode selection depends on the density of the mode spectrum in the vicinity of the desired mode.

A1.4 Coaxial geometry and mode separation

In a coaxial geometry, the presence of an inner conductor, first of all, changes the spectrum of mode eigenfrequencies. In the coaxial resonator the cut off frequencies, $\omega_{cut} = k_{\perp} c$, depend on the ratio of outer to inner conductor, $C = R_{out}/R_{in}$ where R_{out} and R_{in} are the outer and inner wall radii respectively. More exactly these frequencies are determined by the characteristic (or eigenvalue) equation for $k_c \left(\equiv k_{\perp}\right)$ [90]

$$J'_m(\chi) N'_m\left(\frac{\chi}{C}\right) = N'_m(\chi) J'_m\left(\frac{\chi}{C}\right) \tag{A1a}$$

where J'_m and N'_m are the derivatives of the Bessel and Neumann functions of order *m*, and $\chi = \chi_{m,p} = k_{\perp m,p} R_{out}$ is the transverse eigenvalue. A derivation of this characteristic equation starting from Maxwell's equations is given in Section A2 of this Appendix. Equation (A1a) is a transcendental equation (has a algebraic solution) and must be solved numerically for $k_{\perp}$. Once $k_{\perp}$ is known the cut-off frequency can be determined. Solutions for the TM modes can be found in the same manner; the required determinental equation is the same as (A1a) except for the derivatives, i.e.

$$J_m(\chi) N_m\left(\frac{\chi}{C}\right) = N_m(\chi) J_m\left(\frac{\chi}{C}\right). \tag{A1b}$$

A typical example of eigenvalue dependence on the ratio of outer to inner conductor is shown in Figure A6. This is similar to that presented in [91].

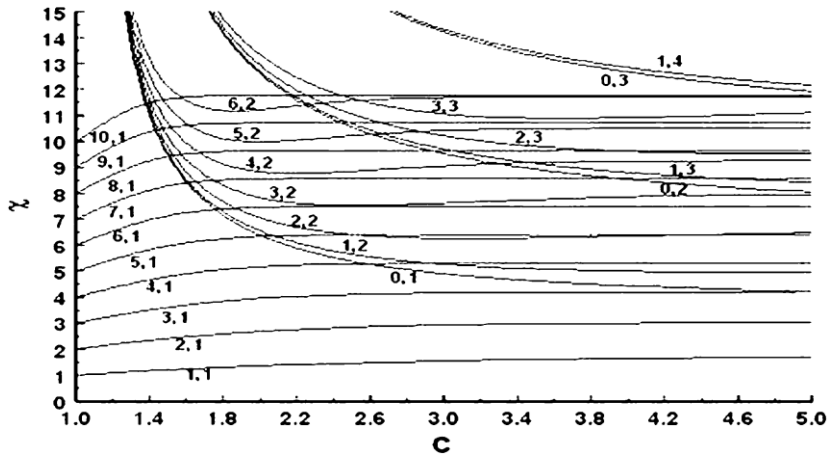

Figure A6: Dependence of transverse eigenvalue $\chi_{m,p}$ on coaxial parameter C.

As can be seen from Figure A6, there is a region in which the increase in *C*, caused by the decrease in diameter of the coaxial insert, results in the increase of the cut-off frequency where $\omega_{cut} = k_{\perp} c$. Even for the case where a coaxial insert of constant radius is used, the spectrum in the vicinity of the desired mode can be verified and improved mode selectivity can be observed. It should be noted that in the case of operating at very high order modes it is necessary to position the inner coax close to the caustic region of the operating mode, this suppressed modes with a higher radial variation than the desired mode. However the ohmic losses of the later mode become too high for continuous wave (CW) operation.

The coaxial waveguide can support TE and TM waveguide modes in addition to the TEM mode. In practice these modes are usually cut off (evanescent), and so have only a reactive effect near discontinuities or sources, where they are excited. It is important to be aware of the cut off frequencies of the lowest order waveguide modes if the propagation of these modes is to be avoided. Avoiding the propagation of higher order modes sets an upper limit on the size of the waveguide cross-section, thus limiting the power handling capability. A derivation of the solution for TE modes of the coaxial waveguide is given in section 2 of this Appendix which gives derivations for various

electromagnetic dispersion relations, (specific location is Appendix A2.3). The TE_{11} mode is the dominant waveguide mode of the coaxial line therefore is of primary importance.

A1.5 Tapering of the Inner Conductor

The coaxial insert can also be tapered axially; this yields another opportunity for mode selection. If we let any mode be represented by a set of rays propagating in the cavity and reflecting from its walls, the rays, which upon being reflected from a down tapered insert propagate towards an open output end of the cavity. This reflection from the down tapered insert increases the axial wave number, and hence also the group velocity of the wave. It also increases the diffractive losses of modes with large radial indexes. This may be explained by consideration of the inhomogeneous "string" equation, which, when treated with the appropriate boundary conditions, determines the axial structure of the mode f_s (s denotes the mode index) in a cold cavity approximation (i.e. neglecting the effects of the electron beam). The string equation takes the form $\frac{d^2 f_s}{dz^2} + k_{s,z}^2 f_s = 0$ where $k_{s,z}$ is the mode axial wave number determined by the equation $k_{s,z}^2 = (\omega/c)^2 - k_{\perp,m,p}^2(z)$. In cylindrical resonators the transverse wave number depends upon the resonator wall radius, and this dependence is generally the same for all modes. In coaxial resonators this number depends on both the radii of the outer and inner conductors. When these radii are slightly tapered such that $R_{out}(z) = R_{out,0} + \Delta R_{out}(z)$ and $R_{in}(z) = R_{in,0} + \Delta R_{in}(z)$ (where $R_{out,0}$ and $R_{in,0}$ indicate some initial values of there radii), the transverse wave number can be expanded in a Taylor series in the vicinity of their values for $R_{out,0}$ and $R_{in,0}$, and correspondingly the axial wave number can be determined by the expression:

$$k_{s,z}^2 = (\omega/c)^2 - k_{s,\perp,0}^2 + 2k_{s,\perp,0}^2 \left[\frac{\Delta R_{out}}{R_{out,0}} \times \left(1 - \frac{C}{\chi_{s,0}} \frac{d\chi_s}{dC}_{R_{out,0}} \right) + \frac{\Delta R_{in}}{R_{in}} \frac{C}{\chi_{s,0}} \frac{d\chi_s}{dC}_{R_{in,0}} \right] \quad \text{(A2).}$$

From these equations it is evident that for coaxial resonators with tapered conductors, in contrast to conventional cylindrical resonators, modes that are closely related in frequency but have different derivatives, $d\chi_s/dC$, will have different axial structures and therefore different diffractive losses.

Considering the case where the outer wall of the coaxial resonator has a constant radius and the coaxial insert is down-tapered, i.e. $R_{out}(z) = \Delta R_{out} = 0, \Delta R_{in} < 0$. In this case modes which have $\frac{d\chi_s}{dC}_{R_{in,0}} > 0$ will have an axial structure which corresponds to that of modes in an empty cylindrical resonator with a down-tapered outer wall, i.e. $R_{w,eq} < 0$. This down tapering reduces diffractive losses of the outgoing radiation, or, in other words, increases the diffractive Q factor of the resonator. On the contrary, the modes with $\frac{d\chi_s}{dC}_{R_{in,0}} < 0$ in the same resonator will have an axial structure similar to that in a cylindrical resonator with an up-tapered wall, i.e. $R_{w,eq} > 0$, resulting in large diffractive losses, therefore low diffractive Q_s (stored energy in resonator). The propagation of modes in such a resonator is shown in Figure A7.

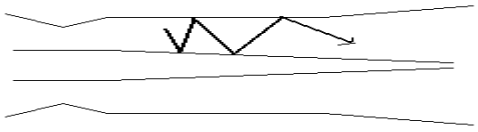

Figure A7: Propagation of modes in a coaxial resonator

It should be noted that, in parallel with the analysis of coaxial resonators with tapered walls, resonators with a periodically slotted outer wall and an absorbing inner coax were also studied [92]. This concept was driven by the idea that in the process of their

azimuthal rotation, all modes whose azimuthal indexes are not equal to the number of azimuthal variations in the corrugation, will be transformed by the corrugated outer wall into the modes with large radial indexes whose fields penetrate into the inner absorber. It was found, however, that this method of mode selection is sufficiently efficient only for operating modes with very small radial indexes. Theoretical studies have also been carried out [93] into coaxial gyrotrons in which the outer wall is provided with radial metal wedges, also referred to as a magnetron-like structure.

A1.6 Restrictions on the Choice of Operating Modes

As mentioned earlier, in the CW and high power regimes of operation, one of the most critical issues in gyrotron design is accounting for ohmic heating in the resonator walls. Since the ohmic Q factor can be estimated by the ratio of the radial distance occupied by the RF field, (which in cylindrical resonators is the distance $R_{out} - R_{in}$), to the skin depth, it is evident that to increase the ohmic Q, one should operate at modes with larger radial indexes. However, when the radial index becomes very large and the beam remains positioned near the caustic of the chosen mode, voltage depression becomes a significant issue as the beam is far from the wall of the waveguide. This results not only in the decrease of the electron kinetic energy, but also in the increase in the electron velocity spread. In such situations, the introduction of an inner coaxial insert is extremely beneficial, because locating this insert near the beam solves the problem of voltage depression. As was noted above, however, there is a tradeoff between efficient mode selection and maintaining sufficiently low ohmic losses in the coax. For efficient mode selection, the radius of the coaxial insert should be close to the caustic radius of the operating TE_{mp} mode; in this case the modes with larger radial indexes will experience a strong influence from this insert, which will result in increasing their diffractive losses. Such a positioning, however, can lead to unacceptably high ohmic losses of the operating mode power in the coax, because close to the caustic, the field of this mode can be sufficiently strong.

A1.7 A Gyrotron with a Corrugated Inner Conductor

Previous analysis of coaxial gyrotrons with a smooth-walled tapered inner conductor [86] have shown that in order to provide efficient mode selection, i.e. to enable the discrimination of modes with radial indexes larger than that of the operating high-order mode, it is necessary to locate the inner coax rather close to the caustic region of the desired mode. Such a location results in excessive ohmic losses of microwave power, which leads to overheating of the coax in CW and long-pulse operation [94]. Also, diffractive Q factors of the modes with the positive slope of the derivative $\frac{d\chi_s}{dC} > 0$ increase, therefore complicating the problem of mode selection. To address these issues, it was proposed to use an inner conductor with axial slots, instead of a smooth-walled coax [95]. The transverse cross section of such a resonator is shown in Figure A8.

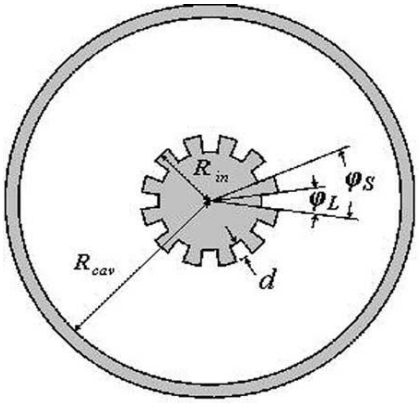

Figure A8: Cross section of coaxial cavity gyrotron with a corrugated inner conductor.

When the number of slots N on the surface of the coax is large enough, i.e. $N > 2m$, this surface can be characterized by an average surface impedance. This greatly simplifies the treatment of such cavities. The first papers on the theory of such resonators based on this approach are presented in [96, 97]. When the condition given above holds, ($N > 2m$), the corrugation parameter W, which represents a normalized surface impedance, can be expressed as

$$W = \frac{L}{S}\tan\left(\frac{2\pi}{\lambda}d\right) \qquad \text{(A3)}$$

where

$$S = \frac{2\pi R_{in}}{N} \tag{A4}$$

is the period, L is the width, and d is the depth of the corrugation, φ_L and φ_S are the azimuthal angles corresponding to the width and periodicity of the corrugation. Following from Equation A3, when the corrugation depth is equal to $\frac{\lambda}{4}$ the surface impedance becomes infinitely large and, correspondingly, the RF magnetic field at the surface becomes very small. This is the only field that penetrates into the wall of the metal (which has finite conductivity) and means that ohmic losses in such a corrugated insert can be rather small, much smaller than in the case of the smooth walled insert. This is analyzed in [98]. This fact alone is extremely important for multimegawatt class gyrotrons intended for operation in the CW and long-pulse regimes. In such a case, the Helmholtz equation, which determines the membrane function describing the transverse magnetic structure of the TE modes, should be supplemented by the appropriate boundary conditions, i.e. the Neumann boundary condition in the case of TM modes and the Dirichlet condition $\left(E_\varphi = 0\right)$ typical for TE modes. The use of this impedance in the corresponding boundary conditions results in the following characteristic equation (full derivation given in Section A13, which replaces that for the cylindrical case in Equation (A1.1):

$$J'_m\left(\chi_{mp}\right)\left[N'_m\left(\frac{\chi_{mp}}{C}\right) + WN_m\left(\frac{\chi_{mp}}{C}\right)\right] - N'_m\left(\chi_{mp}\right)\left[J'_m\left(\frac{\chi_{mp}}{C}\right) + WJ_m\left(\frac{\chi_{mp}}{C}\right)\right] = 0 \tag{A5}$$

It can be seen from this that when the depth of the corrugations is made vanishing small, $d \to 0$ this equation simply reduces to that of the cylindrical waveguide. However at finite values of W the above equation yields solutions which are quite different to those shown in Figure A6. In general, the axial corrugations offer a way to avoid the positive slope of the eigenvalue curve. The part of the eigenvalue curve with positive slope does

not disappear, but as the corrugation depth increases, it moves toward higher values of C beyond the typical operating range. Considering the fact that the minimum of the eigenvalue curve $\chi(C)$ in a non-corrugated system corresponds to the caustic radius of the mode, modes with larger radial indexes than that of the operating one will exhibit a positive slope $\frac{d\chi}{dC} > 0$ at even higher values of C. In the operating range of C, an even greater number of modes with large radial indexes will have negative slopes $\frac{d\chi}{dC} < 0$ which mean that their diffractive Q factors will become smaller. On the other hand, there are always modes with eigenvalues that are close to the eigenvalue of the operating mode with large positive slopes, $\frac{d\chi}{dC} > 0$, in the operating C range. These modes however, are strongly perturbed by the inner conductor and their field energy is almost completely localized inside the grooves. Due to their large positive slope, these modes could become serious competitors for the operating mode. However, if the coaxial insert were to contain some absorbers, the ohmic Q factor of these modes would be very low, and therefore would not cause problems with mode competition.

It is worth noting here an important result presented in [96]. It states that in order to improve stability of the operating mode against competing modes at the fundamental and second cyclotron harmonics, it is advisable to choose the depth of the corrugations close to 20% of the cut-off wavelength.

A1.8 Variable corrugation depth

A further improvement of coaxial resonators was proposed in [99]. It was based on the use of a corrugated insert with longitudinal corrugations of a variable depth. Here, both the corrugation depth and the impedance parameter W depend upon the longitudinal coordinate z, therefore the solution $\chi_{mp}(C)$ to the above equation may become a complicated implicit function of z. Results indicate that it is possible to improve the

mode selectivity and redistribute and/or diminish the density of ohmic losses in the insert by varying the depth of the corrugations along the axial direction. It was also found that when the corrugation depth is constant, at high voltages, the gyrotron oscillates in the multimode regime whereas when the corrugation depth is variable all parasitic modes are suppressed.

A1.9 Energy losses in coaxial gyrotron with corrugated insert

As is already known the corrugated insert plays an important role in a highly overmoded coaxial gyrotron cavity making problems of mode selection and beam voltage depression less serious. Therefore, these devices are expected to be capable to reach an output power of more than 2 MW in CW regime, that is far beyond of capabilities of present-day conventional cavity gyrotrons. The achievement of the record for this type of gyrotron in output power (2.2 MW at 165 GHz,) by the Forschungszentrum Karlsruhe (FZK) gyrotron group was reported [100]. It should be noted that the increase in power level of coaxial gyrotrons is rigidly connected with increasing the azimuthal and radial numbers of the operating mode. In particular, a calculation of energy losses in the inner conductor of a coaxial cavity is of interest as it may allow future designs to overcome one of the main technological restrictions in the coaxial cavity gyrotron progress – ohmic overloading of inner conductor walls.

Mathematical Models used for estimation of ohmic losses

- Spatial harmonics method (SHM) – This is based on the assumption that the corrugation width is less than half the oscillation wavelength, therefore the fields are homogeneous inside the grooves, although vary between grooves according to the azimuthal wave number. An example of this ohmic loss calculation is applicable to the coaxial cavity gyrotron with corrugated inner conductor, with slots of different sizes, presented in [101, 102].

- Surface impedance model (SIM) – This method relies on the assumption that the ratio between tangential $\underline{E}$ and $\underline{H}$ fields can be expressed as an impedance type boundary condition. It is based on the assumption that the width of the corrugation is less than half the wavelength of the oscillations $\left(L < \lambda/2\right)$, which means that the field variation along a slot interval is negligible and the corrugations may be represented as a homogeneous reactive surface. The groove may be approximated as part of a rectangular waveguide. This approximation improves as the number of slots per wavelength increases and the thickness of the ridge decreases. It is only good for a large number of slots where generally $N > 2m$. Correct calculations of energy losses at the inner conductor by this method are not very good as the field near the corrugated surface of the inner conductor is enriched by higher spatial harmonics – which are ignored in this model.

- Method of moments – This is a general procedure for solving linear equations. It therefore can only account for a limited number of spatial harmonics. It is only valid for modes with not too large an azimuthal index, for an example of this see [103].

- Singular integral equation (SIE) – This is the most accurate method used for such calculations.

A1.10 Calculation of Gyrotron Energy Losses

So far, the theory of coaxial cavity gyrotrons was based on the simplified Surface Impedance Model (SIM) of the corrugated inner conductor however, the range of the applicability of this model is not completely clear. Usually, the SIM is believed to be feasible for gyrotron considerations if $N > 2m$, where N is the number of slots on the surface of the inner conductor, and m is the azimuthal number of the mode (see, for example [104]). Hence, as one goes to higher output powers, it becomes increasingly

difficult to validate this condition, since N must be very large and is difficult to fabricate. For early versions of coaxial gyrotron cavities, it holds with some conditions, i.e. for the relevant ITER $TE_{34,19}$ coaxial gyrotron cavity, it holds very marginally ($N = 72$), and it will certainly be violated for the forthcoming designs. Moreover, correct calculation of energy losses in the inner conductor using the SIM is hardly possible at all [105], since the field near the corrugated surface of the inner conductor is significantly enriched by higher spatial or Fourier harmonics, which are ignored in the SIM approach.

Mathematical details

The fields inside the coaxial gyrotron cavity with corrugated inner conductor (see Fig. A4) contain an infinite number of spatial or Fourier harmonics. The field distribution near the corrugated surface is mainly formed by the higher spatial or Fourier harmonics, which are either neglected (as in SIM), or for which just a limited number are taken into account, (Method of Moments). Since the corrugated surface of the inner conductor contains sharp edges, the convergence of the infinite sums in terms of which the total fields are expressed, is very bad. They converge non-uniformly and their sharp edges result in a strong instability of the numerical results. Moreover, due to the large azimuthal and radial numbers of the operating mode, the higher terms of the sums contain cylindrical functions of very high order and argument. They cannot be computed using standard built-in programs which are restricted in both index and argument. A direct computer calculation of them is also impossible since they become either very small or even very large which is beyond the tractability of computer calculations. To overcome these problems, an approach has been developed which reduces the initial multidimensional boundary-value problem for Maxwell's equations in order to search for a function of one variable, in an interval of length which is shorter than the wavelength of the cavity field. This allows singularities of the field near the sharp edges of the slots (on the surface of the inner conductor) to be treated in a mathematically correct manner, allowing for accurate calculations of the field distribution on the corrugated surface of the inner conductor. This is known as the Singular Integral

Equation method (SIE) and has no simplifying assumptions. Details of the energy loss calculation can be found in references [106, 107].

A2. Derivation of Electromagnetic Dispersion relations

The construction of a dispersion diagram allows us to visualize how electromagnetic waves will behave and interact. This interaction can be explained following a derivation of the transverse field components of the cylindrical waveguide.

A2.1 Field components for the TE modes of a Cylindrical Waveguide

Let the electric and magnetic fields, in a waveguide of length *L*, be represented as

$$\vec{E} = \mathrm{Re}\left\{ A(z,t)\vec{E}_s(r_\perp)e^{i(\omega t - k_z z)} \right\} \tag{A6}$$

and

$$\vec{H} = \mathrm{Re}\left\{ A(z,t)\vec{H}_s(r_\perp)e^{i(\omega t - k_z z)} \right\} \tag{A7}$$

where $\vec{E}_s$ and $\vec{H}_s$ describe the transverse structure of the fields inside the guide, $A(z,t)$ is the amplitude of the EM field, $r_\perp$ represents the transverse coordinate (r,φ), and k_z is the axial wave number. The fields $\vec{E}_s$ and $\vec{H}_s$ obey the following Maxwell equations for waves with frequency ω and wave number $k = \omega/c$ in a source-free waveguide:

$$\nabla \times \vec{E}_s = -\frac{i\omega}{c}\vec{H}_s \tag{A8}$$

and

$$\nabla \times \vec{H}_s = \frac{i\omega}{c}\vec{E}_s \tag{A9}$$

These equations assume that both the permittivity and permeability are equal to unity. From these equations the wave equation can be obtained as

$$\nabla^2 \vec{H}_s + \frac{\omega^2}{c^2} \vec{H}_s = 0 \tag{A10}$$

This is the vector Helmholtz partial differential equation (PDE).

In the case of TE modes, the longitudinal magnetic field is given as $\vec{H}_z = \vec{H}_s(r,\varphi)e^{-ik_z z}$. This is a solution of the wave equation and $\vec{E}_z = 0$. The other EM field components can be written in terms of $\vec{H}_z$ via the Maxwell equations as follows:

$$\vec{H}_r = -\frac{ik_z}{k_\perp^2}\frac{dH_z}{dr}\hat{r} \qquad \vec{E}_\varphi = \frac{ik_z}{k_\perp^2}\frac{\partial H_z}{\partial r}\hat{\varphi}$$

$$\vec{H}_\varphi = -\frac{ik_z}{k_\perp^2 r}\frac{\partial H_z}{\partial \varphi}\hat{\varphi} \qquad \vec{E}_r = -\frac{ik_z}{k_\perp^2 r}\frac{\partial H_z}{\partial \varphi}\hat{r} \tag{A11}$$

where $k_\perp^2 = \omega^2/c^2 - k_z^2$. Expressing the wave equation as a function of H_z in cylindrical coordinates

$$\left(\frac{\partial^2}{\partial r^2} + \frac{1}{r}\frac{\partial}{\partial r} + \frac{1}{r^2}\frac{\partial^2}{\partial \varphi^2} + k_\perp^2\right)\vec{H}_z = 0 \tag{A12}$$

A solution of this equation is found using the separation of variables method. Let it be assumed that $H_s(r_\perp) = R(r)P(\varphi)$ and substitute into the above, to give

$$\frac{r^2}{R}\frac{d^2R}{dr^2} + \frac{r}{R}\frac{dR}{dr} + r^2 k_\perp = -\frac{1}{P}\frac{d^2P}{d\varphi^2} \tag{A13}$$

Each side of this equation depends only on one single variable. Both sides can therefore be equated to a constant, $-k_\varphi^2$, and represented as

$$-\frac{1}{P}\frac{d^2P}{d\varphi^2} = k_\varphi^2 \quad \text{or} \qquad \frac{d^2P}{d\varphi^2} + k_\varphi^2 P = 0 \tag{A14}$$

also,

$$r^2\frac{d^2R}{dr^2} + r\frac{dR}{dr} + \left(r^2k_\perp^2 - k_\varphi^2\right)R = 0 \tag{A15}$$

The general solution to (A14) takes the form of a standing wave

$$P(\varphi) = A\sin m\varphi \pm B\cos m\varphi = Ce^{\pm im\varphi} \tag{A16}$$

where *A*, *B* and *C* are constant and *m* replaces k_φ and must be an integer to ensure that H_z is periodic in the azimuthal angle φ. This then leaves us with the radial differential equation, as Equation (A15) becomes $r^2\frac{d^2R}{dr^2} + r\frac{dR}{dr} + \left(r^2k_\perp^2 - m^2\right)R = 0$. This is Bessel's differential equation whose general solution is of the form

$$R(r) = DJ_m\left(k_\perp r\right) + EY_m\left(k_\perp r\right) \tag{A17}$$

where J_m and Y_m are the Bessel and Neumann functions respectively. This general solution must be well behaved at *r* = 0, therefore the expansion coefficient *E* must be set to zero. As the second order function $Y_m\left(k_\perp r\right)$ tends to infinity as $r \to 0$ the expression for the transverse field component is only a function of the first order Bessel function, i.e. $H_s\left(r_\perp\right) = J_m\left(k_\perp r\right)e^{\pm im\varphi}$, where the product of the two constants *D* and E has been set

to unity. Taking into account the boundary condition that the tangential electric field at the waveguide wall must be zero, at radius $\left(r = R_w\right)$ allows us to express the azimuthal electric field variation as

$$E_\varphi\left(r_\perp, z\right) = \frac{ik}{k_\perp} J'_m\left(k_\perp r\right) e^{-i\left(k_z z \pm m\varphi\right)} \tag{A18}$$

In order for E_φ to vanish at the conducting surface $\left(r = R_w\right)$ it must hold that $J'_m\left(k_\perp R_w\right) = 0$. This is the Dirichlet boundary condition. Allowing υ_{mp} to represent the roots of $J'_m\left(x\right)$, i.e. $J'_m\left(\upsilon_{mp}\right) = 0$, where υ_{mp} is the p^{th} root of J'_m, then $k_\perp$ takes the value $k_\perp = \frac{\upsilon_{mp}}{R_w}$.

Values of υ_{mp} are given in mathematical tables.

It is also known that the given TE_{mp} modes which can propagate in a cylindrical waveguide are determined by the perpendicular wave number given above, where *m* refers to the number of azimuthal $\left(\varphi\right)$ variations, and *p* refers to the number of radial $\left(r\right)$variations. It is therefore evident that the transverse wave number $k_\perp$ is a function of the waveguide cut off frequency. The propagation constant of the TE_{mp} mode is given by

$$\beta_{mp} = k_z = \sqrt{k^2 - k_c^2} = \sqrt{k^2 - \left(\frac{\upsilon_{mp}}{R_w}\right)} \tag{A19}$$

with a cutoff frequency of

$$f_{c_{mp}} = \frac{k_\perp}{2\pi\sqrt{\mu\varepsilon}} = \frac{\upsilon_{mp}}{2\pi a\sqrt{\mu\varepsilon}} \tag{A20}$$

The first TE mode to propagate is the mode with the smallest υ_{mp}, which is the TE_{11} mode. The other transverse field components are obtained in the same manner and given as

$$\vec{H}_r = -\frac{ik_z}{k_\perp} J'_m\left(k_\perp r\right) e^{-i(k_z z \pm m\varphi)} \hat{r} \tag{A21}$$

$$\vec{H}_\varphi = \pm\frac{ik_z}{k_\perp^2}\frac{m}{r} J_m\left(k_\perp r\right) e^{-i(k_z z \pm m\varphi)} \hat{\varphi} \tag{A22}$$

$$\vec{E}_r = \pm\frac{ik}{k_\perp^2}\frac{m}{r} J_m\left(k_\perp r\right) e^{-i(k_z z \pm m\varphi)} \hat{r} \tag{A23}$$

From the wave equation it is known that $\omega^2 = c^2\left(k_\perp^2 + k_z^2\right)$. In order to simplify the problem, let us neglect any changes in axial momentum of the beam i.e. $k_z \ll \omega/c$, and also ignore and interaction with backward waves, represented by the condition $k_z \gg \pi/L$.

By plotting the dependence of wave frequency upon axial wave number using both the synchronous condition $\omega - k\upsilon_z = s\Omega_c$ and the expression for a cavity mode a dispersion diagram for the waveguide can be obtained. The point of efficient interaction between the beam and the wave is located where the beam line grazes the waveguide mode curve(s).

A2.2 The Characteristic Equation for Coaxial Waveguide Modes

We are interested in the electromagnetic wave confined between two concentric, conducting cylindrical surfaces. The TE_{11} mode is the dominant mode of the coaxial waveguide therefore is of primary importance. For TE modes, $E_z = 0$, and H_z satisfies the wave equation

$$\nabla^2 H_z + k^2 H_z = 0 \tag{A24}$$

where $H_z(r,\varphi,z) = h_z(r,\varphi)e^{-i\beta z}$, and $k_c^2 = k^2 - \beta^2$.

The general solution to this equation, as derived previously, is given by the product of equations (A16) and (A17):

$$H_s(r_\perp) = Ce^{\pm im\varphi}\left(DJ_m(k_\perp r) + EY_m(k_\perp r)\right) \tag{A25}$$

In this case, the boundary condition at $r = 0$ does not hold, i.e. $R_{inner} \le r \le R_{outer}$, $(R_{outer} \equiv R_{wall})$ therefore Y_m cannot be disregarded. In this case the boundary conditions are

$$E_\varphi(r,\varphi,z) = 0 \quad \text{for} \quad r = R_{inner,}R_{outer} \tag{A26}$$

As following the previous derivation, the azimuthal component of electric field is found to equal

$$E_\varphi(r_\perp, z) = \frac{ik}{k_\perp}\left(DJ'_m(k_\perp r) + EY'_m(k_\perp r)\right)Ce^{-i(k_z z \pm m\varphi)} \tag{A27}$$

Applying the boundary condition (A26) to equation (A27) gives the following set of equations

$$DJ'_m(k_\perp R_{in}) + EY'_m(k_\perp R_{in}) = 0 \tag{A27}$$

$$DJ'_m(k_\perp R_{out}) + EY'_m(k_\perp R_{out}) = 0 \tag{A28}$$

This is a homogeneous set of equations, the only nontrivial $(C \neq 0, D \neq 0)$ part occurs when the determinant is zero, therefore

$$J'_m\left(k_\perp R_{in}\right)Y'_m\left(k_\perp R_{out}\right)=J'_m\left(k_\perp R_{out}\right)Y'_m\left(k_\perp R_{in}\right) \tag{A29}$$

This is the characteristic equation for $k_\perp$. The values of $k_\perp$ that satisfy (A29) define the TE_{mp} modes of the coaxial waveguide. Once $k_\perp$ is known, the propagation constant, or cut off frequency can be determined. Solutions for the TM modes of the coaxial waveguide are found in a similar manner with the exception that the detrimental equation (A29) does not contain derivatives.

A2.3 The Transverse Electric (TE) Mode Solution for a Coaxial Waveguide Having a 1D Corrugated Insert

The TE_{11} mode is the dominant mode of the coaxial waveguide therefore is of primary importance. For TE modes, $E_z=0$, and H_z satisfies the wave equation

$$\nabla^2 H_z+k^2H_z=0 \tag{A30}$$

where $H_z\left(r,\varphi,z\right)=h_z\left(r,\varphi\right)e^{-j\beta z}$, and $k_c^2=k^2-\beta^2$. The general solution to this equation is given by:

$$H_s\left(r_\perp\right)=Ce^{\pm im\varphi}\left(DJ_m\left(k_\perp r\right)+E\left(Y_m\left(k_\perp r\right)+Y_m\left(k_\perp\varphi\right)\right)\right) \tag{A31}$$

This is the same as before only now there is an additional boundary to consider.

As before, the boundary condition at $r=0$ does not hold, i.e. $R_{inner}\le r\le R_{outer}$, $\left(R_{outer}\equiv R_{wall}\right)$ therefore Y_m cannot be disregarded. In this case the boundary conditions are

$$E_{\varphi}(r,\varphi,z)=0 \quad \text{for} \quad r=R_{inner},WR_{inner},R_{outer} \tag{A32}$$

where W is the corrugation parameter.

As following the previous derivation, the azimuthal component of electric field is found to equal

$$E_{\varphi}(r_{\perp},z)=\frac{ik}{k_{\perp}}\left(DJ'_{m}(k_{\perp}r)+E\left(Y'_{m}(k_{\perp}r)+Y_{m}(k_{\perp}\varphi)\right)\right)Ce^{-i(k_{z}z\pm m\varphi)}S \tag{A33}$$

Applying the boundary condition (A32) to equation (A33) gives the following set of equations

$$\left[J'_{m}(k_{\perp}R_{in})+WJ_{m}(k_{\perp}R_{in})\right]+\left[Y'_{m}(k_{\perp}R_{in})+WY_{m}(k_{\perp}R_{in})\right]=0 \tag{A34}$$

$$J'_{m}(k_{\perp}R_{out})+Y'_{m}(k_{\perp}R_{out})=0 \tag{A35}$$

This is a homogeneous set of equations, the only nontrivial root occurs when the determinant is zero, therefore

$$\left[J'_{m}(k_{\perp}R_{in})+WJ_{m}(k_{\perp}R_{in})\right]Y'_{m}(k_{\perp}R_{out})=\left[Y'_{m}(k_{\perp}R_{in})+WY_{m}(k_{\perp}R_{in})\right]J'_{m}(k_{\perp}R_{out})$$

(A36)

This is the characteristic equation for $k_{\perp}$. The values of $k_{\perp}$ that satisfy (A36) define the TE_{mp} modes of the coaxial waveguide with a 1D azimuthal corrugation. A similar solution can be found for the TM modes of a coaxial waveguide.

A3. Derivation of the Gyro-Averaged Equations

The gyro-averaged equations are a set of equations which are used to describe the electron motion. This section considers the interaction taking place between electrons and a transverse electric (TE) wave inside a cylindrical interaction region.

A3.1 Evolution of Electron Phase and Momentum

The motion of an electron in a guiding magnetic field interacting with a TE wave can be represented by the Lorentz force equation:

$$\frac{d\vec{P}}{dt} = -e\left\{\vec{E} + \frac{1}{c}\left[\vec{\upsilon} \times \left(\vec{H}_0 + \vec{H}\right)\right]\right\} \tag{A37}$$

where $\vec{P}$ is the electron momentum, $\vec{\upsilon}$ is the electron velocity, $\vec{H}_0$ is the external magnetic field, $\vec{E}$ and $\vec{H}$ are the electric and magnetic fields of the wave respectively. Introduction of the following normalization parameters

$$z' = \omega z / c \tag{A38}$$

$$\vec{p}' = \vec{p} / m_0 c, \tag{A39}$$

$$A' = eA / m_0 c\omega, \tag{A40}$$

$$\mu = eH_0 / m_0 c\omega = \Omega_0 \omega, \tag{A41}$$

$$\beta_z = \upsilon_z / c \tag{A42}$$

$$\beta_\perp = \upsilon_\perp / c \tag{A43}$$

allows the above equation (A37) to normalize to:

$$\frac{d\vec{p}'}{dz'}+\mu\left(\frac{\vec{p}'}{p_z'}\times\vec{z}'\right)=-\frac{1}{\beta_z}\mathrm{Re}\left\{A'e^{i(\omega t-k_z z)}\left[\vec{E}_s+\left(\vec{\beta}\times\vec{H}_s\right)\right]\right\}=-\frac{1}{\beta_z}\mathrm{Re}\left\{A'e^{i(\omega t-k_z z)}\vec{G}\right\} \tag{A44}$$

Where

$$\vec{G}=\vec{E}_s+\left(\beta_s\times\vec{H}_s\right) \tag{A45}$$

is the Lorentz force. If we assume that the EM field is much weaker than the external magnetic field, the transverse momentum and position of the gyrating electron can be written as:

$$p_x'=-p_\perp'\sin\theta \qquad p_y'=p_\perp'\cos\theta \tag{A46a&b}$$

$$x'=X'+r_L'\cos\theta \qquad y'=Y'+r_L'\sin\theta \tag{A47a&b}$$

where

$$\theta=\Omega_0\tau+\phi \qquad t=t_0+\tau \qquad X'=\omega X/c \qquad Y'=\omega Y/c \qquad r_L'=\omega r_L/c$$

This is illustrated in the Figure A9 where the parameters r_L', X' and Y' represent the normalized Larmour radius and guiding centre coordinates of the gyrating electrons. These parameters, along with $p_\perp'$ and ϕ , remain constant when the EM field is absent.

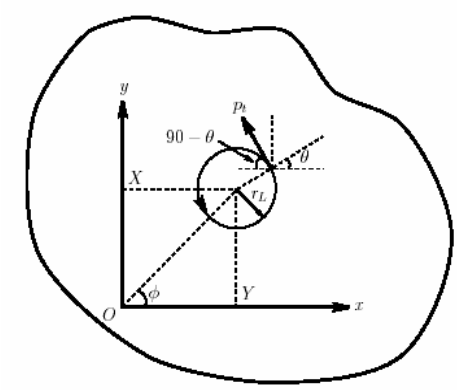

Figure A9: Projection of an electron orbit on cross sectional plane.

Using the previous relations, the components of the Lorentz force equation can be written as:

$$\frac{dp'_x}{dz} = \frac{dp'_\perp}{dz}\sin\theta + p'_\perp \cos\theta \frac{d\theta}{dz} = \frac{1}{\beta_z}\mathrm{Re}\left\{A' e^{i(\omega t - k_z z)} G_x\right\} \tag{A48}$$

$$\frac{dp'_y}{dz} = \frac{dp'_\perp}{dz}\cos\theta - p'_\perp \sin\theta \frac{d\theta}{dz} = -\frac{1}{\beta_z}\mathrm{Re}\left\{A' e^{i(\omega t - k_z z)} G_y\right\} \tag{A49}$$

$$\frac{dx'}{dz'} = \frac{dX'}{dz'} + \frac{dr'_L}{dz'}\cos\theta - r'_L \sin\theta \frac{d\theta}{dz} = \dot{X}' + \dot{r}'_L \cos\theta - r'_L \sin\theta\dot{\theta} = 0 \tag{A50}$$

$$\frac{dy'}{dz'} = \frac{dY'}{dz'} + \frac{dr'_L}{dz'}\sin\theta - r'_L \cos\theta \frac{d\theta}{dz} = \dot{Y}' + \dot{r}'_L \sin\theta - r'_L \cos\theta\dot{\theta} = 0 \tag{A51}$$

These are the equations describing the motion of the electron. The transverse components of the EM Lorentz force are denoted by G_x and G_y , these may be replaced by their polar equivalents

$$G_r = G_x \cos\theta + G_y \sin\theta$$

$$G_\theta = -G_x \sin\theta + G_y \cos\theta \tag{A52}$$

Performing the polar transformations of the equations of motion yields the following expressions for electron motion

$$\dot{p}'_\perp = -\frac{1}{\beta_z}\mathrm{Re}\left\{A' e^{i(\omega t - k_z z)} G_\theta\right\} \tag{A53}$$

$$p'_\perp \dot{\theta} = \frac{1}{\beta_z}\mathrm{Re}\left\{A' e^{i(\omega t - k_z z)} G_r\right\} \tag{A54}$$

$$\dot{p}'_z = -\frac{1}{\beta_z}\mathrm{Re}\left\{A' e^{i(\omega t - k_z z)} G_z\right\} \tag{A55}$$

$$\dot{X}' = \frac{1}{\beta_z}\mathrm{Re}\left\{A' e^{i(\omega t - k_z z)} G_y\right\} \tag{A56}$$

$$\dot{Y}' = -\frac{1}{\beta_z}\mathrm{Re}\left\{A' e^{i(\omega t - k_z z)} G_x\right\} \tag{A56}$$

It is clear that the Lorentz force $\vec{G}$ is a periodic function of the angular coordinate θ, it can therefore be represented as a Fourier series via

$$\vec{G} = \sum_{l=-\infty}^{\infty} \vec{G}_l e^{-il\theta} \qquad \text{where} \qquad \vec{G}_l = \frac{1}{2\pi}\int_0^{2\pi} \vec{G} e^{il\theta} d\theta \tag{A57}$$

Substituting these into the above equations defining the following phase variable $\vartheta_l = \omega t - k_z \upsilon_z - l\theta$, the equations governing electron motion may be written as

$$\dot{p}'_{\perp} = -\frac{1}{\beta_z}\,\mathrm{Re}\left\{A' G_{l\theta} e^{i\vartheta_l}\right\} \tag{A58}$$

$$p'_{\perp}\left[\frac{\gamma}{p_z} - h - \dot{\vartheta}_l - l\frac{\mu}{p'_z}\right] = \frac{1}{\beta_z}\,\mathrm{Re}\left\{A' G_{lr} e^{i\vartheta_l}\right\} \tag{A59}$$

$$\dot{p}'_z = -\frac{1}{\beta_z}\,\mathrm{Re}\left\{A' G_{lz} e^{i\vartheta_l}\right\} \tag{A60}$$

$$\dot{X}' = \frac{1}{\beta_z}\,\mathrm{Re}\left\{A' G_{ly} e^{i\vartheta_l}\right\} \tag{A61}$$

$$\dot{Y}' = -\frac{1}{\beta_z}\,\mathrm{Re}\left\{A' G_{lx} e^{i\vartheta_l}\right\} \tag{A62}$$

where it is assumed that $p'_{\perp}$, p'_z, θ, $\dot{X}'$, $\dot{Y}'$ and r'_L vary slowly during the interaction between the electrons and the electromagnetic field such that the equations may be averaged over fast gyrations. These equations are reduced (or gyro-averaged) and are similar to (A58 - A62).

The components of the Lorentz force can be expressed through the membrane function

$$\Psi(x,y) = \int_0^{2\pi} \Psi(\varphi) e^{ik_{\perp}(x\cos\varphi + y\sin\varphi)} d\varphi \tag{A63}$$

Since Ψ is periodic in the θ direction it can be represented as an infinite sum of harmonics as

$$\Psi(x,y) = \sum_{l=-\infty}^{\infty} \Psi_l e^{-il\theta}, \qquad \text{where} \qquad \Psi_l = \frac{1}{2\pi}\int_0^{2\pi} \Psi e^{il\theta} d\theta \tag{A64a\&b}$$

Substitution of the membrane function (A63) into the expression for the l^{th} harmonic, and allowing for the position of the gyrating electron to be expressed as

$$x = X + r_L \cos\theta \qquad\qquad y = Y + r_L \sin\theta \tag{A65}$$

the function becomes

$$\Psi_l = \frac{1}{2\pi}\left[\int_0^{2\pi} \Psi(\varphi) e^{ik_\perp\left((X + r_L\cos\theta)\cos\varphi + (Y + r_L\sin\theta)\sin\varphi\right)} d\varphi\right].e^{il\theta} d\theta \tag{A66}$$

If we let $\bar{\theta} = \theta - \varphi$, the last integral takes the form of a Bessel function

$$\Psi_l = \left[\int_0^{2\pi} \Psi(\varphi) e^{ik_\perp(X\cos\varphi + Y\sin\varphi) + il\varphi} d\varphi\right].\frac{1}{2\pi} e^{i\left(k_\perp r_L\cos\bar{\theta} + l\bar{\theta}\right)} d\bar{\theta}$$

$$\begin{aligned} &= \frac{1}{k_\perp}\left(\frac{\partial}{\partial X} + i\frac{\partial}{\partial Y}\right)^l \Psi(X,Y).J_l\left(k_\perp r_L\right) \\ &= J_l\left(k_\perp r_L\right) L_l(X,Y) \end{aligned} \tag{A67}$$

Substituting this into $\Psi_l = \frac{1}{2\pi}\int_0^{2\pi} \Psi e^{il\theta} d\theta$ yields the simplified form of the membrane function

$$\Psi(x,y) = \sum_{l=-\infty}^{\infty} J_l\left(k_\perp r_L\right) L_l(X,Y) e^{-il\theta} \tag{A68}$$

where

$$L_l = \frac{1}{k_\perp}\left(\frac{\partial}{\partial X} + i\frac{\partial}{\partial Y}\right)^l \Psi(X,Y) \tag{A69}.$$

In this case the waveguide is of cylindrical geometry therefore the expressions regarding the electron guiding centre must be transferred to polar coordinates using the relations

$$X = r\cos\phi \qquad \text{and} \qquad Y = r\sin\phi. \tag{A70}$$

The differential operator in L_l can also be transformed into polar coordinates as

$$\frac{\partial}{\partial X} = \cos\phi\frac{\partial}{\partial r} - \frac{\sin\phi}{r}\frac{\partial}{\partial\phi} \qquad \text{and} \qquad \frac{\partial}{\partial Y} = \sin\phi\frac{\partial}{\partial r} + \frac{\cos\phi}{r}\frac{\partial}{\partial\phi} \tag{A71}$$

thus obtaining

$$L_l = \left\{ e^{i\phi}\frac{1}{k_\perp}\left(\frac{\partial}{\partial r} + i\frac{\partial}{\partial\phi}\right)\right\}^l \Psi(r,\phi) \tag{A72}.$$

As is known, the membrane function for a TE_{mp} mode of a cylindrical resonator is equal to $J_m(k_\perp r)e^{\mp im\phi}$. Here m is the azimuthal index of the mode and p its radial index. The transverse wave number $k_\perp = \upsilon_{mp}/R_w$ where R_w is the radius of the waveguide and υ_{mp} the p^{th} root of the equation $dJ_m(\upsilon)/d\upsilon = 0$.

Using the following recurrent relation for Bessel functions

$$\frac{dJ_m(x)}{dx} = \frac{m}{x}J_m(x) - J_{m+1}(x) \tag{A73}$$

it can be shown that the differential operator given in L_l is equal to

$$L_l = J_{m\mp l}(k_\perp r)e^{i(l\mp m)\phi} \tag{A74}$$

where $m-1$ and $m+1$ correspond to the co- and counter rotating waves with respect to the electron gyration. In the case of TE waves, the axial component of the magnetic field

H_z can be represented as $H_z = i\Psi$. Substituting this into equations A71 to A74, the transverse field components can be expressed in terms of the membrane function, i.e.

$$H_r = \frac{k_z}{k_\perp^2}\frac{\partial \Psi}{\partial r} \tag{A75}$$

$$E_\theta = -\frac{k}{k_\perp^2}\frac{\partial \Psi}{\partial r} \tag{A76}$$

$$H_\theta = \frac{k_z}{k_\perp^2 r}\frac{\partial \Psi}{\partial \theta} \tag{A77}$$

$$E_\theta = \frac{k}{k_\perp^2 r}\frac{\partial \Psi}{\partial \theta} \tag{A78}$$

Substituting these into (A74) and remembering the constraint given earlier $\left(k_z \ll k \text{ or } k_\perp \simeq k\right)$ allows us to express the components of the Lorentz force relation as

$$G_r \simeq \frac{1}{k_\perp r_L}\frac{\partial \Psi}{\partial \theta} + i\beta_\perp \Psi \qquad G_\theta \simeq -\frac{1}{k_\perp}\frac{\partial \Psi}{\partial r} \qquad G_z \simeq 0 \tag{A79}.$$

If the membrane function Ψ is now replaced with its full expression given in (A67), the equations of electron motion (A53 – A55) become:

$$\dot{p}'_\perp = \frac{1}{\beta_z}\mathrm{Re}\left\{A' e^{i(\omega t - k_z z)} \sum_{l=1}^{3} J'_l\left(k_\perp r_L\right) L_l e^{-il\theta}\right\} \tag{A80}$$

$$p'_\perp\left(\dot{\theta} - \frac{\mu}{p'_z}\right) = \frac{1}{\beta_z}\mathrm{Re}\left\{A' e^{i(\omega t - k_z z)} \sum_{l=1}^{3}\left(\beta_\perp - \frac{1}{k_\perp r_L}\right) J_l\left(k_\perp r_L\right) L_l e^{-il\theta}\right\} \tag{A81}$$

$$\dot{p}'_z = 0 \tag{A82}$$

The last equation shows that the axial momentum of the electron remains essentially unchanged throughout the interaction with the EM field. These equations describe the electron phase and orbital momentum as the electron traverses the resonator.

A3.2 Evolution of Electron Energy

The rate of change in electron energy along the axial length is denoted by the equation of motion for a charged particle which is give as

$$\frac{d\varepsilon}{dt} = -e\left(\vec{\upsilon}.\vec{E}\right) \tag{A83}$$

which, using normalized variables, may be expressed as

$$\frac{d\gamma}{dz'} = \left(\frac{\vec{\upsilon}_{\perp}}{\upsilon_z}.\frac{eE_{\theta}}{m_0 c\omega}\right) \tag{A84}$$

Recalling the expression for the azimuthal/orbital component of electric field as $E_{\theta} = \frac{-k}{k_{\perp}^2}\frac{\partial\Psi}{\partial r}$

The equation A84 may be written as

$$\frac{d\gamma}{dz'} = -\left(\frac{\vec{\upsilon}_{\perp}}{\upsilon_z}.\frac{e}{m_0 c\omega}.\frac{-k}{k_{\perp}^2}\frac{\partial\Psi}{\partial r}\right) \tag{A85}$$

(remembering that $\vec{\Psi}(x,y) = \sum_{l=-\infty}^{\infty}\vec{\Psi}_l e^{-il\theta}$) and substituting the membrane function into this yields

$$\frac{d\gamma}{dz'} = \frac{p'_{\perp}}{p'_{z0}} \mathrm{Re}\left\{ A' e^{i(\omega t - k_z z)} \sum_{l=-\infty}^{\infty} J'_l\left(k_{\perp} r_l\right) L_l e^{-il\theta} \right\} \tag{A86}$$

Recalling (A81) from the previous section (evolution of orbital momentum) and rearranging for θ

$$\dot{\theta} = \frac{1}{p'_{\perp}\beta_z}\left\{ iA' e^{i(\omega t - k_z z)} \sum_{l=-\infty}^{\infty} \left(\beta_{\perp} - \frac{1}{k_{\perp} r_L} \right) J'_l\left(k_{\perp} r_L\right) L_l e^{-il\theta} \right\} + \frac{\mu}{p'_{z_0}} \tag{A87}$$

where it is assumed that $\dot{\theta} = \dfrac{d\theta}{dz}$.

Normalizing all parameters with respect to the ignition electron energy γ_o as follows

$$\hat{\gamma} = \frac{\gamma}{\gamma_o}, \qquad \hat{p}_{\perp} = \frac{p'_{\perp}}{\gamma_o}, \qquad \hat{\mu} = \frac{\mu}{\gamma_o} = \frac{\Omega_o}{\omega}, \qquad \hat{A} = \frac{A'}{\gamma_o} \tag{A88}$$

and introducing the normalized axial length $\xi = \dfrac{z'}{\beta_{z_o}} = \dfrac{\omega z}{\beta_{z_o}}$, allows the rate of change of electron energy along the axis to be expressed as

$$\frac{d\hat{\gamma}}{d\xi}.\frac{1}{\beta_{z_0}} = \frac{\hat{p}_{\perp}}{p_{z_0}} \mathrm{Re}\left\{ \frac{A'}{\gamma_0} e^{i(\omega t - k_z z)} \sum_{l=-\infty}^{\infty} J'_l\left(k_{\perp} r_L\right) L_l e^{-il\theta} \right\} \tag{A89}$$

Appendix B

B1. The Radially Inhomogeneous Cylindrical Fibre

Here, an efficient analytical method is given which allows us to calculate the propagation characteristics of various modes in fibres whose core radius are not constant, i.e. a multi-layer concentric system. Following the same procedure as in chapter 2 and dividing the cylinder into *s+1* regions, expressions for the tangential field components* can be written as follows:

*Assume that expressions for field components of all modes are multiplied by $e^{j(n\theta-\beta z+\omega t)}$ which is suppressed throughout.

Region 1:

$$\begin{bmatrix} E_z^{(1)} \\ H_z^{(1)} \\ E_\theta^{(1)} \\ H_\theta^{(1)} \end{bmatrix} = \begin{bmatrix} c_1(r) & 0 & 0 & 0 \\ 0 & d_1(r) & 0 & 0 \\ e_1(r) & f_1(r) & 0 & 0 \\ g_1(r) & h_1(r) & 0 & 0 \end{bmatrix} \begin{bmatrix} C_1 \\ D_1 \\ 0 \\ 0 \end{bmatrix} \tag{B1}$$

Region S, (S > 1):

$$\begin{bmatrix} E_z^{(s)} \\ H_z^{(s)} \\ E_\theta^{(s)} \\ H_\theta^{(s)} \end{bmatrix} = \begin{bmatrix} c_s(r) & 0 & c_s'(r) & 0 \\ 0 & d_s(r) & 0 & d_s'(r) \\ e_s(r) & f_s(r) & e_s'(r) & f_s'(r) \\ g_s(r) & h_s(r) & g_s'(r) & h_s'(r) \end{bmatrix} \begin{bmatrix} C_s \\ D_s \\ C_s' \\ D_s' \end{bmatrix} \tag{B2}$$

Region S + 1:

$$\begin{bmatrix} E_z^{(s+1)} \\ H_z^{(s+1)} \\ E_\theta^{(s+1)} \\ H_\theta^{(s+1)} \end{bmatrix} = \begin{bmatrix} 0 & 0 & s(r) & 0 \\ 0 & 0 & 0 & \tau(r) \\ 0 & 0 & \upsilon(r) & \nu(r) \\ 0 & 0 & \kappa(r) & \chi(r) \end{bmatrix} \begin{bmatrix} 0 \\ 0 \\ G \\ F \end{bmatrix} \tag{B3}$$

$$c_s(r) = J_n(p_s r) \tag{B4}$$

$$c_s'(r) = Y_n(p_s r) \tag{B5}$$

$$d_s(r) = J_n(p_s r) \tag{B6}$$

$$d_s'(r) = Y_n(p_s r) \tag{B7}$$

$$e_s(r) = \frac{\beta n}{p_s^2 r} J_n(p_s r) \tag{B8}$$

$$e_s'(r) = \frac{\beta n}{p_s^2 r} Y_n(p_s r) \tag{B9}$$

$$f_s(r) = \frac{j\omega\mu_0}{p_s} J_n'(p_s r) \tag{B10}$$

$$f_s'(r) = \frac{j\omega\mu_0}{p_s} Y_n'(p_s r) \tag{B11}$$

$$g_s(r) = -\frac{j\omega\varepsilon_s}{p_s} J_n'(p_s r) \tag{B12}$$

$$g_s'(r) = -\frac{j\omega\varepsilon_s}{p_s} Y_n'(p_s r) \tag{B13}$$

$$h_s(r) = \frac{\beta n}{p_s^2 r} J_n(p_s r) \tag{B14}$$

$$h_s'(r) = \frac{\beta n}{p_s^2 r} Y_n(p_s r) \tag{B15}$$

$$s(r) = K_n(qr) \tag{B16}$$

$$\tau(r) = K_n(qr) \tag{B17}$$

$$\upsilon(r) = -\frac{\beta n}{q^2 r} K_n(qr) \tag{B18}$$

$$\nu(r) = -\frac{j\omega\mu_0}{q} K_n'(qr) \tag{B19}$$

$$\kappa(r) = \frac{j\omega\varepsilon_{s+1}}{q} K_n'(qr) \tag{B20}$$

$$\chi(r) = -\frac{\beta n}{q^2 r} K_n(qr) \tag{B21}$$

$$q^2 = \beta^2 - \omega^2 \mu_0 \varepsilon_{s+1} \tag{B22}$$

$$p_s^2 = \omega^2 \mu_0 \varepsilon_{s+1} - \beta^2 \tag{B23}$$

Appendix C

C1. Tables of Bessel Roots

These values, for both TE and TM modes were obtained using Mathematica®, where *v* relates to the number of azimuthal variations and *n* the number across the radius.

TE*v,n* ROOTS

Bessel order v	*n* 1	2	3	4	5	6	7	8	9	10	11	12
J'0	3.83171	7.01559	10.1735	13.3237	16.4706	19.6159	22.7601	25.9037	29.0468	32.1897	35.3323	38.4748
J'1	1.84118	5.33144	8.53632	11.706	14.8636	18.0155	21.1644	24.3113	27.4571	30.6019	33.7462	36.89
J'2	3.05424	6.70613	9.96947	13.1704	16.3475	19.5129	22.6716	25.826	28.9777	32.1273	35.2755	38.4227
J'3	4.20119	8.01524	11.3459	14.5858	17.7887	20.9725	24.1449	27.3101	30.4703	33.6269	36.781	39.9331
J'4	5.31755	9.2824	12.6819	15.9641	19.196	22.401	25.5898	28.7678	31.9385	35.1039	38.2653	41.4237
J'5	6.41562	10.5199	13.9872	17.3128	20.5755	23.8036	27.0103	30.2028	33.3854	36.5608	39.7306	42.8963
J'6	7.50127	11.7349	15.2682	18.6374	21.9317	25.1839	28.4098	31.6179	34.8134	37.9996	41.1788	44.3526
J'7	8.57784	12.9324	16.5294	19.9419	23.2681	26.545	29.7907	33.0152	36.2244	39.4223	42.6115	45.794
J'8	9.64742	14.1155	17.774	21.2291	24.5872	27.8893	31.1553	34.3966	37.6201	40.8302	44.03	47.2218
J'9	10.7114	15.2867	19.0046	22.5014	25.8913	29.2186	32.5052	35.7638	39.0019	42.2246	45.4355	48.6369
J'10	11.7709	16.4479	20.223	23.7607	27.182	30.5345	33.842	37.118	40.3711	43.6068	46.829	50.0404
J'11	12.8265	17.6003	21.4309	25.0085	28.4609	31.8384	35.1667	38.4604	41.7286	44.9775	48.2113	51.4331
J'12	13.8788	18.7451	22.6293	26.246	29.729	33.1314	36.4805	39.7919	43.0755	46.3378	49.5834	52.8157
J'13	14.9284	19.8832	23.8194	27.4743	30.9874	34.4145	37.7844	41.1135	44.4125	47.6883	50.9458	54.1888
J'14	15.9754	21.0154	25.002	28.6943	32.237	35.6885	39.079	42.4259	45.7402	49.0296	52.2993	55.5531
J'15	17.0203	22.1422	26.1778	29.9066	33.4784	36.9542	40.3651	43.7296	47.0595	50.3625	53.6444	56.9091
J'16	18.0633	23.2643	27.3474	31.1119	34.7125	38.2121	41.6433	45.0254	48.3707	51.6874	54.9815	58.2573
J'17	19.1045	24.3819	28.5114	32.3109	35.9396	39.4628	42.9142	46.3138	49.6744	53.0048	56.3112	59.598
J'18	20.1441	25.4956	29.6701	33.5039	37.1604	40.7068	44.1781	47.5951	50.9711	54.3152	57.6338	60.9318
J'19	21.1823	26.6055	30.8241	34.6915	38.3752	41.9446	45.4357	48.8699	52.2612	55.6189	58.9498	62.2589
J'20	22.2191	27.7121	31.9737	35.8739	39.5845	43.1765	46.6872	50.1386	53.545	56.9163	60.2595	63.5797
J'21	23.2548	28.8156	33.1192	37.0516	40.7886	44.403	47.933	51.4014	54.8229	58.2078	61.5632	64.8945
J'22	24.2894	29.9161	34.2608	38.2249	41.9879	45.6243	49.1734	52.6587	56.0952	59.4936	62.8612	66.2037
J'23	25.3229	31.014	35.3988	39.394	43.1825	46.8408	50.4088	53.9107	57.3622	60.774	64.1538	67.5073
J'24	26.3555	32.1093	36.5334	40.5591	44.3729	48.0526	51.6394	55.1579	58.6241	62.0493	65.4412	68.8058
J'25	27.3872	33.2023	37.6649	41.7206	45.5592	49.2601	52.8654	56.4003	59.8813	63.3197	66.7237	70.0993
J'26	28.4181	34.293	38.7934	42.8786	46.7416	50.4634	54.0871	57.6382	61.1338	64.5854	68.0014	71.3881
J'27	29.4482	35.3816	39.9191	44.0332	47.9203	51.6629	55.3046	58.8719	62.3819	65.8466	69.2746	72.6723
J'28	30.4775	36.4683	41.0421	45.1847	49.0956	52.8586	56.5182	60.1015	63.6259	67.1036	70.5435	73.9521
J'29	31.5062	37.5531	42.1626	46.3333	50.2676	54.0507	57.7281	61.3272	64.8658	68.3565	71.8082	75.2276
J'30	32.5342	38.6361	43.2807	47.479	51.4364	55.2395	58.9344	62.5491	66.1019	69.6054	73.0689	76.4992

TMv,n ROOTS

Bessel order v	n											
	1	*2*	*3*	*4*	*5*	*6*	*7*	*8*	*9*	*10*	*11*	*12*
J0	2.40483	5.52008	8.65373	11.7915	14.9309	18.0711	21.2116	24.3525	27.4935	30.6346	33.7758	36.9171
J1	3.83171	7.01559	10.1735	13.3237	16.4706	19.6159	22.7601	25.9037	29.0468	32.1897	35.3323	38.4748
J2	5.13562	8.41724	11.6198	14.796	17.9598	21.117	24.2701	27.4206	30.5692	33.7165	36.8629	40.0084
J3	6.38016	9.76102	13.0152	16.2235	19.4094	22.5827	25.7482	28.9084	32.0649	35.2187	38.3705	41.5207
J4	7.58834	11.0647	14.3725	17.616	20.8269	24.019	27.1991	30.371	33.5371	36.699	39.8576	43.0137
J5	8.77148	12.3386	15.7002	18.9801	22.2178	25.4303	28.6266	31.8117	34.9888	38.1599	41.3264	44.4893
J6	9.93611	13.5893	17.0038	20.3208	23.5861	26.8202	30.0337	33.233	36.422	39.6032	42.7785	45.949
J7	11.0864	14.8213	18.2876	21.6415	24.9349	28.1912	31.4228	34.6371	37.8387	41.0308	44.2154	47.3942
J8	12.2251	16.0378	19.5545	22.9452	26.2668	29.5457	32.7958	36.0256	39.2404	42.4439	45.6384	48.8259
J9	13.3543	17.2412	20.807	24.2339	27.5837	30.8854	34.1544	37.4001	40.6286	43.8438	47.0487	50.2453
J10	14.4755	18.4335	22.047	25.5095	28.8874	32.2119	35.4999	38.7618	42.0042	45.2316	48.4472	51.6533
J11	15.5898	19.616	23.2759	26.7733	30.1791	33.5264	36.8336	40.1118	43.3684	46.6081	49.8347	53.0505
J12	16.6982	20.7899	24.4949	28.0267	31.46	34.83	38.1564	41.4511	44.7219	47.9743	51.212	54.4378
J13	17.8014	21.9562	25.7051	29.2706	32.7311	36.1237	39.4692	42.7804	46.0657	49.3308	52.5798	55.8157
J14	18.9	23.1158	26.9074	30.506	33.9932	37.4082	40.7728	44.1006	47.4003	50.6782	53.9387	57.1849
J15	19.9944	24.2692	28.1024	31.7334	35.2471	38.6843	42.0679	45.4122	48.7265	52.0172	55.2892	58.5458
J16	21.0851	25.417	29.2909	32.9537	36.4934	39.9526	43.3551	46.7158	50.0446	53.3483	56.6319	59.899
J17	22.1725	26.5598	30.4733	34.1673	37.7327	41.2136	44.6348	48.012	51.3553	54.6719	57.9671	61.2448
J18	23.2568	27.6979	31.6501	35.3747	38.9654	42.4678	45.9077	49.3011	52.6589	55.9885	59.2954	62.5836
J19	24.3382	28.8317	32.8218	36.5765	40.1921	43.7157	47.174	50.5837	53.9559	57.2984	60.617	63.9158
J20	25.4171	29.9616	33.9887	37.7729	41.4131	44.9577	48.4342	51.86	55.2466	58.602	61.9323	65.2418
J21	26.4936	31.0878	35.1511	38.9643	42.6287	46.1941	49.6887	53.1305	56.5313	59.8997	63.2416	66.5617
J22	27.5679	32.2106	36.3094	40.151	43.8393	47.4252	50.9378	54.3954	57.8105	61.1916	64.5452	67.876
J23	28.6402	33.3302	37.4638	41.3334	45.0452	48.6513	52.1817	55.6551	59.0843	62.4782	65.8434	69.1848
J24	29.7105	34.4468	38.6145	42.5117	46.2466	49.8728	53.4207	56.9097	60.353	63.7596	67.1364	70.4884
J25	30.779	35.5606	39.7618	43.686	47.4438	51.0897	54.6551	58.1596	61.6168	65.0361	68.4244	71.7871
J26	31.8459	36.6717	40.9058	44.8567	48.6371	52.3025	55.8851	59.405	62.8761	66.3079	69.7077	73.0809
J27	32.9112	37.7804	42.0467	46.0239	49.8265	53.5112	57.1108	60.646	64.1309	67.5752	70.9865	74.3702
J28	33.9749	38.8867	43.1848	47.1877	51.0123	54.7161	58.3326	61.8829	65.3814	68.8382	72.2609	75.6551
J29	35.0373	39.9908	44.32	48.3485	52.1946	55.9174	59.5506	63.1159	66.6279	70.0971	73.5311	76.9358
J30	36.0983	41.0928	45.4527	49.5062	53.3737	57.1151	60.7649	64.345	67.8705	71.352	74.7973	78.2124

C2. Mode Excitation Order

Mode excitation order for smooth cylindrical waveguide of radius 0.0395m (39.5mm), as output from CST Microwave Studio.

Mode	Root	K_c (m^{-1})	f_c (GHz)
TE1,1	1.84118	47.20974359	2.2540992
TM0,1	2.40483	61.66230769	2.9441583
TM11/TE01	3.83171	98.24897436	4.691043
TE 2,1	3.05424	78.31384615	3.7392107
TE3,1	4.20119	107.7228205	5.1433858
TM2,1	5.13562	131.6825641	6.2873793
TE4,1	5.31755	136.3474359	6.5101105
TE1,2	5.33144	136.7035897	6.5271156
TM0,2	5.52008	141.5405128	6.7580617
TM3,1	6.38016	163.5938462	7.8110308
TE5,1	6.41562	164.5030769	7.8544434
TE2,2	6.70613	171.9520513	8.2101057
TE0,2/TM1,2	7.01559	179.8869231	8.5889679
TE6,1	7.50127	192.3402564	9.1835708
TM4,1	7.58834	194.5728205	9.2901679
TE3,2	8.01524	205.5189744	9.8128082
TM2,2	8.41724	215.8266667	10.304964
TE1,3	8.53632	218.88	10.45075
TE7,1	8.57784	219.9446154	10.501582
TM0,3	8.65373	221.8905128	10.594492
TM5,1	8.77148	224.9097436	10.738649
TE4,2	9.2824	238.0102564	11.364153
TE8,1	9.64742	247.3697436	11.811035
TM3,2	9.76102	250.2825641	11.950112
TM6,1	9.93611	254.7720513	12.164469
TE2,3	9.96947	255.6274359	12.205311
TE0,3	10.1735	260.8589744	12.455099
TM1,3	10.1735	260.8589744	12.455099
TE5,2	10.5199	269.7410256	12.879185
TE9,1	10.7114	274.6512821	13.113633
TM4,2	11.0647	283.7102564	13.546167
TM7,1	11.0864	284.2666667	13.572734
TE3,3	11.3459	290.9205128	13.890431
TM2,3	11.6198	297.9435897	14.225759
TE1,4	11.706	300.1538462	14.33129
TE6,2	11.7349	300.8948718	14.366672
TE10,1	11.7709	301.8179487	14.410746
TM0,4	11.7915	302.3461538	14.435965
TM8,1	12.2251	313.4641026	14.966808
TM5,2	12.3386	316.374359	15.105763
TE4,3	12.6819	325.1769231	15.526054
TE11,1	12.8265	328.8846154	15.703084
TE7,2	12.9324	331.6	15.832734

TM3,3	13.0152	333.7230769	15.934103
TE2,4	13.1704	337.7025641	16.12411
TM1,4	13.3237	341.6333333	16.31179
TE0,4	13.3237	341.6333333	16.31179
TM9,1	13.3543	342.4179487	16.349253
TM6,2	13.5893	348.4435897	16.636956
TE12,1	13.8788	355.8666667	16.991382
TE5,3	13.9872	358.6461538	17.124092
TE8,2	14.1155	361.9358974	17.281166
TM4,3	14.3725	368.525641	17.595803
TM10,1	14.4755	371.1666667	17.721903
TE3,4	14.5858	373.9948718	17.85694
TM2,4	14.796	379.3846154	18.114281
TM7,2	14.8213	380.0333333	18.145255
TE1,5	14.8636	381.1179487	18.197042
TE13,1	14.9284	382.7794872	18.276374
TM0,5	14.9309	382.8435897	18.279435
TE6,3	15.2682	391.4923077	18.692381
TE9,2	15.2867	391.9666667	18.71503
TM11,1	15.5898	399.7384615	19.086106
TM5,3	15.7002	402.5692308	19.221265
TE4,4	15.9641	409.3358974	19.544349
TE14,1	15.9754	409.625641	19.558184
TM8,2	16.0378	411.225641	19.634578
TM3,4	16.2235	415.9871795	19.861925
TE2,5	16.3475	419.1666667	20.013734
TE10,2	16.4479	421.7410256	20.136651
TE0,5	16.4706	422.3230769	20.164442
TM1,5	16.4706	422.3230769	20.164442
TE7,3	16.5294	423.8307692	20.236429
TM12,1	16.6982	428.1589744	20.443085
TM6,3	17.0038	435.9948718	20.817222
TE15,1	17.0203	436.4179487	20.837422
TM9,2	17.2412	442.0820513	21.107863
TE5,4	17.3128	443.9179487	21.195521
TE11,2	17.6003	451.2897436	21.547498
TM4,4	17.616	451.6923077	21.566719
TE8,3	17.774	455.7435897	21.760154
TE3,5	17.7887	456.1205128	21.77815
TM13,1	17.8014	456.4461538	21.793698
TM2,5	17.9598	460.5076923	21.987623
TE1,6	18.0155	461.9358974	22.055814
TE16,1	18.0633	463.1615385	22.114334
TM0,6	18.0711	463.3615385	22.123884
TM7,3	18.2876	468.9128205	22.388938
TM10,2	18.4335	472.6538462	22.567559
TE6,4	18.6374	477.8820513	22.817187
TE12,2	18.7451	480.6435897	22.949041
TM14,1	18.9	484.6153846	23.13868
TM5,4	18.9801	486.6692308	23.236744
TE9,3	19.0046	487.2974359	23.266739
TE17,1	19.1045	489.8589744	23.389043
TE4,5	19.196	492.2051282	23.501064
TM3,5	19.4094	497.6769231	23.762323
TE2,6	19.5129	500.3307692	23.889035

TM8,3	19.5545	501.3974359	23.939964
TM1,6	19.6159	502.9717949	24.015134
TE0,6	19.6159	502.9717949	24.015134
TM11,2	19.616	502.974359	24.015257
TE13,2	19.8832	509.825641	24.342381
TE7,4	19.9419	511.3307692	24.414246
TM15,1	19.9944	512.6769231	24.47852
TE18,1	20.1441	516.5153846	24.661793
TE10,3	20.223	518.5384615	24.758388
TM6,4	20.3208	521.0461538	24.878121
TE4,5	20.5755	527.5769231	25.189943
TM12,2	20.7899	533.074359	25.452426
TM9,3	20.807	533.5128205	25.473361
TM4,5	20.8269	534.0230769	25.497724
TE3,6	20.9725	537.7564103	25.675977
TE14,2	21.0154	538.8564103	25.728498
TM16,1	21.0851	540.6435897	25.81383
TM2,6	21.117	541.4615385	25.852884
TE1,7	21.1644	542.6769231	25.910914
TE19,1	21.1823	543.1358974	25.932829
TM0,7	21.2116	543.8871795	25.9687
TE8,4	21.2291	544.3358974	25.990125
TE11,3	21.4309	549.5102564	26.237182
TM7,4	21.6415	554.9102564	26.495013
TE6,5	21.9317	562.3512821	26.850296
TM13,2	21.9562	562.9794872	26.88029
TM10,3	22.047	565.3076923	26.991454
TE15,2	22.1422	567.7487179	27.108004
TM17,1	22.1725	568.525641	27.1451
TM5,5	22.2178	569.6871795	27.200559
TE20,1	22.2191	569.7205128	27.202151
TE4,6	22.401	574.3846154	27.424845
TE9,4	22.5014	576.9589744	27.547762
TM3,6	22.5827	579.0435897	27.647295
TE12,3	22.6293	580.2384615	27.704346
TE2,7	22.6716	581.3230769	27.756132
TM1,7	22.7601	583.5923077	27.86448
TE0,7	22.7601	583.5923077	27.86448
TM8,4	22.9452	588.3384615	28.091092
TM14,2	23.1158	592.7128205	28.299953
TE21,1	23.2548	596.2769231	28.470126
TM18,1	23.2568	596.3282051	28.472574
TE16,2	23.2643	596.5205128	28.481756
TE7,5	23.2681	596.6179487	28.486409
TM11,3	23.2759	596.8179487	28.495958
TM6,5	23.5861	604.7717949	28.875726
TE10,4	23.7607	609.2487179	29.089484
TE5,6	23.8036	610.3487179	29.142005
TE13,3	23.8194	610.7538462	29.161348
TM4,6	24.019	615.8717949	29.405712
TE3,7	24.1449	619.1	29.559848
TM9,4	24.2339	621.3820513	29.668808
TM15,2	24.2692	622.2871795	29.712024
TM2,7	24.2701	622.3102564	29.713126
TE22,1	24.2894	622.8051282	29.736754

TE1,8	24.3113	623.3666667	29.763566
TM19,1	24.3382	624.0564103	29.796499
TM0,8	24.3525	624.4230769	29.814006
TE17,2	24.3819	625.1769231	29.849999
TM12,3	24.4949	628.074359	29.988342
TE8,5	24.5872	630.4410256	30.101342
TM7,5	24.9349	639.3564103	30.52702
TE14,3	25.002	641.0769231	30.609168
TE11,4	25.0085	641.2435897	30.617126
TE6,6	25.1839	645.7410256	30.831863
TE23,1	25.3229	649.3051282	31.002036
TM16,2	25.417	651.7179487	31.11724
TM20,1	25.4171	651.7205128	31.117362
TM5,6	25.4303	652.0589744	31.133523
TE18,2	25.4956	653.7333333	31.213467
TM10,4	25.5095	654.0897436	31.230485
TE4,7	25.5898	656.1487179	31.328794
TM13,3	25.7051	659.1051282	31.469952
TM3,7	25.7482	660.2102564	31.522718
TE2,8	25.826	662.2051282	31.617966
TE9,5	25.8913	663.8794872	31.697911
TM1,8	25.9037	664.1974359	31.713092
TE0,8	25.9037	664.1974359	31.713092
TE15,3	26.1778	671.225641	32.048664
TE12,4	26.246	672.974359	32.132159
TM8,5	26.2668	673.5076923	32.157624
TE24,1	26.3555	675.7820513	32.266216
TM21,1	26.4936	679.3230769	32.435288
TE7,6	26.545	680.6410256	32.498215
TM17,2	26.5598	681.0205128	32.516334
TE19,2	26.6055	682.1923077	32.572283
TM11,4	26.7733	686.4948718	32.777716
TM6,6	26.8202	687.6974359	32.835134
TM14,3	26.9074	689.9333333	32.94189
TE5,7	27.0103	692.5717949	33.067867
TE10,5	27.182	696.974359	33.278074
TM4,7	27.1991	697.4128205	33.299009
TE3,8	27.3101	700.2589744	33.434903
TE16,3	27.3474	701.2153846	33.480568
TE25,1	27.3872	702.2358974	33.529294
TM2,8	27.4206	703.0923077	33.570185
TE1,9	27.4571	704.0282051	33.614871
TE13,4	27.4743	704.4692308	33.635928
TM0,9	27.4935	704.9615385	33.659434
TM22,1	27.5679	706.8692308	33.75052
TM9,5	27.5837	707.274359	33.769863
TM18,2	27.6979	710.2025641	33.909675
TE20,2	27.7121	710.5666667	33.927059
TE8,6	27.8893	715.1102564	34.144
TM12,4	28.0267	718.6333333	34.312214
TM15,3	28.1024	720.574359	34.404891
TE7,6	28.1912	722.8512821	34.513606
TE6,7	28.4098	728.4564103	34.781232
TE26,1	28.4181	728.6692308	34.791393
TE11,5	28.4609	729.7666667	34.843792

TE17,3	28.5114	731.0615385	34.905617
TM5,7	28.6266	734.0153846	35.046653
TM23,1	28.6402	734.3641026	35.063303
TE14,4	28.6943	735.7512821	35.129536
TE3,8	28.7678	737.6358974	35.21952
TE21,2	28.8156	738.8615385	35.27804
TM19,2	28.8317	739.274359	35.297751
TM10,5	28.8874	740.7025641	35.365942
TM3,8	28.9084	741.2410256	35.391652
TE2,9	28.9777	743.0179487	35.476494
TM1,9	29.0468	744.7897436	35.561091
TE0,9	29.0468	744.7897436	35.561091
TE9,6	29.2186	749.1948718	35.77142
TM13,4	29.2706	750.5282051	35.835082
TM16,3	29.2909	751.0487179	35.859935
TE27,1	29.4482	755.0820513	36.052512
TM8,6	29.5457	757.5820513	36.171878
TE18,3	29.6701	760.7717949	36.324178
TM24,1	29.7105	761.8076923	36.373638
TE12,5	29.729	762.2820513	36.396287
TE7,7	29.7907	763.8641026	36.471824
TE15,4	29.9066	766.8358974	36.613717
TE22,2	29.9161	767.0794872	36.625348
TM20,2	29.9616	768.2461538	36.681052
TM6,7	30.0337	770.0948718	36.769322
TM11,5	30.1791	773.8230769	36.94733
TE5,8	30.2028	774.4307692	36.976346
TM4,8	30.371	778.7435897	37.182268
TE3,9	30.4703	781.2897436	37.303837
TM17,3	30.4733	781.3666667	37.30751
TE28,1	30.4775	781.474359	37.312652
TM14,4	30.506	782.2051282	37.347544
TE10,6	30.5345	782.9358974	37.382435
TM2,9	30.5692	783.825641	37.424918
TE1,10	30.6019	784.6641026	37.464951
TM0,10	30.6346	785.5025641	37.504985
TM25,1	30.779	789.2051282	37.681769
TE19,3	30.8241	790.3615385	37.736984
TM9,6	30.8854	791.9333333	37.812031
TE13,5	30.9874	794.5487179	37.936907
TE23,2	31.014	795.2307692	37.969472
TM21,2	31.0878	797.1230769	38.059823
TE16,4	31.1119	797.7410256	38.089328
TE8,7	31.1553	798.8538462	38.142462
TM7,7	31.4228	805.7128205	38.469953
TM12,5	31.46	806.6666667	38.515496
TE29,1	31.5062	807.8512821	38.572057
TE6,8	31.6179	810.7153846	38.708808
TM18,3	31.6501	811.5410256	38.74823
TM15,4	31.7334	813.6769231	38.850211
TM5,8	31.8117	815.6846154	38.946072
TE11,6	31.8384	816.3692308	38.97876
TM26,1	31.8459	816.5615385	38.987942
TE4,9	31.9385	818.9358974	39.101309
TE20,3	31.9737	819.8384615	39.144403

TM3,9	32.0649	822.1769231	39.256056
TE24,2	32.1093	823.3153846	39.310414
TE2,10	32.1273	823.7769231	39.332451
TM1,10	32.1897	825.3769231	39.408845
TE0,10	32.1897	825.3769231	39.408845
TM22,2	32.2106	825.9128205	39.434432
TM10,6	32.2119	825.9461538	39.436024
TE14,5	32.237	826.5897436	39.466753
TE17,4	32.3109	828.4846154	39.557227
TE9,7	32.5052	833.4666667	39.795102
TE30,1	32.5342	834.2102564	39.830606
TM13,5	32.7311	839.2589744	40.071664
TM8,7	32.7958	840.9179487	40.150874
TM19,3	32.8218	841.5846154	40.182705
TM27,1	32.9112	843.8769231	40.292155
TM16,4	32.9537	844.9666667	40.344187
TE7,8	33.0152	846.5435897	40.419479
TE21,3	33.1192	849.2102564	40.546803
TE12,6	33.1314	849.5230769	40.561739
TE25,2	33.2023	851.3410256	40.64854
TM6,8	33.233	852.1282051	40.686125
TM23,2	33.3302	854.6205128	40.805124
TE5,9	33.3854	856.0358974	40.872703
TE15,5	33.4784	858.4205128	40.98656
TE18,4	33.5039	859.074359	41.017779
TM11,6	33.5264	859.6512821	41.045325
TM4,9	33.5371	859.925641	41.058425
TE3,10	33.6269	862.2282051	41.168364
TM2,10	33.7165	864.525641	41.278059
TE1,11	33.7462	865.2871795	41.31442
TM0,11	33.7758	866.0461538	41.350658

Appendix D

D1. Cavity and Waveguide Excitation by External Sources

The interaction region is an important part of any EM wave device and understanding how energy is created and transferred is essential towards future development. This section explains how eigenmodes are excited for the case of both cavities and waveguides.

D1.1 Cavity Excitation

It is assumed here that the cavity eigenmodes are excited by the external current on the cavity. The current density of the cavity is given by $\underline{J} = \sigma \underline{E}$ and the electric field $\underline{E}$, in a cavity can be represented by

$$\underline{E} = \sum_s A_s \underline{E}_s \tag{D1}$$

where $\underline{E}_s$ is the eigenmode of the cavity and A_s is the amplitude of the eigenmode and can be written as:

$$A_s = \frac{i\omega \int \underline{J}.\underline{E}_s dV}{(\omega^2 - \omega_s^2)N_s} = \frac{i\omega\sigma A_s \int |E_s|^2 dV}{(\omega^2 - \omega_s^2)N_s} \tag{D2}$$

where $N_s = \frac{1}{4\pi}\int_V |E_s^2| dV$.

Assuming that the frequency is approximately equal to the frequency of the eigenmode

$(\omega \sim \omega_s)$ then this reduced to

$$A_s = \frac{2\pi i \sigma A_s}{\omega - \omega_0} \tag{D3}$$

Therefore and equation relating the electronic adjustment of the eigen-frequency, ω_s, is found to be

$$\omega = \omega_s + i2\pi\sigma \tag{D4}$$

where the conductivity has both real and imaginary parts, i.e. $\sigma = \sigma' + i\sigma''$. This can also be represented in an expression for the electric field strength as

$$E \sim E_0 e^{i(\omega_s + 2i\pi\sigma)t} = E_0 e^{i\omega_s t}.e^{-2\pi\sigma t} \tag{D5}$$

Now let us introduce the Gain factor, Γ of the cavity as

$$\Gamma = 2\pi\sigma' \tag{D6}$$

where σ' is the real part of the complex conductivity.

If the gain of the cavity is less than zero, $\Gamma < 0$ then electromagnetic field emission takes place. The frequency of the eigenmode can be represented by

$$\omega_s = \omega'_s + i\omega''_s \tag{D7a}$$

where $i\omega''_s$ represents the power losses. As stated previously if $\Gamma < 0$ then EM field emission will take place, therefore if $\left(\Gamma + \omega''_s\right) < 0$ then EM field generation **and** amplification of signal will occur. The expression:

$$\omega - \omega_s^{'} = -2\pi\sigma^{"} \tag{D7b}$$

is known as the detuning of the eigen-frequency of a cold cavity by an electron beam

and the equation: $$\omega^{"}{}_s = -2\pi\sigma^{'} \tag{D7c}$$

illustrates the situation when power losses are equal to power gain. Using this condition the start current can be calculated.

The modes excited may be calculated via consideration of the propagation of Maxwell's Equations through a lossy medium which is also conductive. The Faraday and Ampere Laws may be written as:

$$\underline{\nabla} \times \underline{E} = ik\mu \underline{H} - \frac{4\pi}{c} \underline{J}_m \tag{D8}$$

$$\underline{\nabla} \times \underline{H} = -ik\varepsilon \underline{E} + \frac{4\pi}{c} \underline{J}_e \tag{D9}$$

Let us assume for clarity that $\underline{J}_e$ and $\underline{J}_m$ are monochromatic and that the excited eigenmode is also monochromatic. Let permittivity and permeability be complex functions such that

$$\varepsilon = \varepsilon_1 + i\varepsilon_2 \qquad \text{and} \qquad \mu = \mu_1 + i\mu_2 \tag{D10}$$

and also let there be no fields on the surface S_0, i.e.

$$\underline{E}\big|_{S_0} = 0 \qquad \text{and} \qquad \underline{H}\big|_{S_0} = 0\,. \tag{D11}$$

This is a perfectly conducting metal box, with no flux through the walls. Assuming that the eigenmodes of the cavity are well known, and ω_s is well defined, we can write

$$\underline{\nabla} \times \underline{E}_s = ik_s \mu \underline{H}_s \quad \text{and} \quad \underline{\nabla} \times \underline{H}_s = -ik_s \varepsilon \underline{E}_s \tag{D12a,b}$$

where

$$\underline{E}_s(t) = \mathrm{Re}\left(\underline{E}_s e^{-i\omega_s t}\right) \qquad \underline{H}_s(t) = \mathrm{Re}\left(\underline{H}_s e^{-i\omega_s t}\right) \tag{D13}$$

$$\text{and} \qquad \omega_s = \omega'_s + i\omega''_s \tag{D14}$$

Orthogonality of the Cavity Eigenmodes

The orthogonality of the eigenmodes $\underline{E}_s \; \underline{E}_{s'}$ is the important property which indicates that the eigenmodes are mutually independent. If we take equation (D12a) and multiplying by a different mode of magnetic field strength, denoted by $\underline{H}_{s'}$ as follows

$$\underline{\nabla} \times \underline{E}_s = ik_s \mu \underline{H}_s \tag{D15a}$$

$$\underline{H}_{s'} . \left(\underline{\nabla} \times \underline{E}_s\right) = ik_s \mu \underline{H}_s . \underline{H}_{s'} \tag{D15b}$$

and adapting equation (D12b) for a different mode of electric field strength, $\underline{H}_{s'}$ and multiplying by a different mode denoted by $\underline{E}_s$ gives us

$$\underline{\nabla} \times \underline{H}_{s'} = -ik_{s'} \varepsilon \underline{E}_{s'} \tag{D16a}$$

$$\underline{E}_s . \left(\underline{\nabla} \times \underline{H}_{s'}\right) = -ik_{s'} \varepsilon \underline{E}_{s'} . \underline{E}_s \tag{D16b}$$

Combining both (D15b) and (D16b) gives

$$\underline{H}'_s . \left(\underline{\nabla} \times \underline{E}_s\right) - \underline{E}_s . \left(\underline{\nabla} \times \underline{H}_{s'}\right) = ik_{s'} \varepsilon \underline{E}_{s'} . \underline{E}_s + ik_s \mu \underline{H}_s . \underline{H}'_s \tag{D17}$$

Using the vector relation $\underline{\nabla}.(\underline{A}\times\underline{B}) = \underline{B}.(\underline{\nabla}\times\underline{A}) - \underline{A}.(\underline{\nabla}\times\underline{B})$, the expression (D17) can be simplified to

$$\underline{\nabla}.(\underline{E}_s \times \underline{H}_{s'}) = ik_{s'}\varepsilon\underline{E}_{s'}\underline{E}_s + ik_s\mu\underline{H}_s\underline{H}_s^{'} \tag{D18}$$

therefore it must also be true that

$$\underline{\nabla}.(\underline{E}_{s'} \times \underline{H}_s) = ik_s\varepsilon\underline{E}_s\underline{E}_{s'} + ik_{s'}\mu\underline{H}_{s'}\underline{H}_s \tag{D19}$$

If we integrate expressions (D18) and (D19), taking into account that there is no net flow over the surface, $H_s\big|_{S_0} = E_s\big|_{S_0} = 0$, and using Stokes theorem to convert from a volume to a surface integral, the two above equations (D18) and (D19) become:

$$\int_{S_0}\left(\underline{E}_s \times \underline{H}_{s'}\right).\underline{dS} = i\left[\int_V k_s\mu\underline{H}_s\underline{H}_s^{'}dV + \int_V k_{s'}\varepsilon\underline{E}_{s'}\underline{E}_s dV\right] = 0 \tag{D20}$$

$$\int_{S_0}(\underline{E}_{s'} \times \underline{H}_s).\underline{dS} = i\left[\int_V k_{s'}\mu\underline{H}_{s'}\underline{H}_s dV + \int_V k_s\varepsilon\underline{E}_s\underline{E}_{s'}dV\right] = 0 \tag{D21}$$

These can be easily simplified to

$$\begin{aligned} k_{s'}X + k_sY &= 0 \\ k_sX + k_{s'}Y &= 0 \end{aligned} \tag{D22}$$

where X and Y are independent variables such that

$$\det\begin{pmatrix} k_{s'} & k_s \\ k_s & k_{s'} \end{pmatrix} = k_{s'}^2 - k_s^2 \neq 0 \tag{D23}$$

It is clear that (D23) is only equal to zero if both modes are the same i.e. $\omega_{s'} = \omega_s$ and $k_{s'} = k_s$. This demonstrates the orthogonality of the eigenmodes.

The Eigenmode Amplitudes

In order to determine the amplitudes of the eigenmodes, it is necessary to assume that the electric and magnetic fields may be split into their transverse and longitudinal components such that

$$\underline{E} = \underline{E}_t + \underline{E}_l \qquad \text{and} \qquad \underline{H} = \underline{H}_t + \underline{H}_l \qquad \text{(D24a,b)}$$

where

$$\underline{E}_t = \sum A_S \underline{E}_s \qquad \text{and} \qquad \underline{H}_t = \sum B_S \underline{H}_s \qquad \text{(D25a,b)}$$

$$\underline{E}_l = -\underline{\nabla}\varphi_e \qquad \text{and} \qquad \underline{H}_l = -\underline{\nabla}\varphi_m \qquad \text{(D26a,b)}$$

where φ_e and φ_m represent the electric and magnetic scalar potentials. If it is assumed that there is no net flux flow in the transverse direction, i.e.:

$$\underline{\nabla}.\left(\varepsilon \underline{E}_t\right) = 0 \qquad \text{and} \qquad \underline{\nabla}.\left(\mu \underline{H}_t\right) = 0 \qquad \text{(D27)}$$

In order to find the amplitudes of the eigenmodes, the curl of the electric and magnetic field must be found. Therefore

$$\underline{\nabla} \times \underline{E} = \left(\underline{\nabla} \times \underline{E}_t\right) + \left(\underline{\nabla} \times \underline{E}_l\right) \qquad \text{(D28a)}$$

$$\underline{\nabla} \times \underline{H} = \left(\underline{\nabla} \times \underline{H}_t\right) + \left(\underline{\nabla} \times \underline{H}_l\right) \qquad \text{(D28b)}$$

Using the vector identity $\underline{\nabla} \times \left(\underline{\nabla}\varphi\right) = 0$ with equations (D26a) and (D26b) these become

$$\underline{\nabla} \times \underline{E} = \left(\underline{\nabla} \times \underline{E}_t\right) = i\mu \sum k_s A_s \underline{H}_s \qquad \text{(D29a)}$$

$$\underline{\nabla} \times \underline{H} = \left(\underline{\nabla} \times \underline{H}_t\right) = -i\varepsilon \sum k_s B_s \underline{E}_s \tag{D29b}$$

Substituting these into Maxwell's equations (D8) and (D9) yields

$$i\mu \sum \left(k_s A_s - kB_s\right)\underline{H}_s = -\frac{4\pi}{c} J_m + ik\mu \underline{H}_l \tag{D30}$$

and

$$i\varepsilon \sum \left(kA_s - k_s B_s\right)\underline{E}_s = \frac{4\pi}{c} J_e - ik\varepsilon \underline{E}_l \tag{D31}$$

therefore rearranging gives

$$-\frac{4\pi}{c} J_m + ik\mu \underline{H}_l = \frac{\mu}{c} \sum_s b_s \underline{H}_s \tag{D32}$$

and

$$\frac{4\pi}{c} J_e - ik\varepsilon \underline{E}_l = \frac{\varepsilon}{c} \sum_s a_s \underline{E}_s \tag{D33}$$

where

$$a_s = ic\left(kA_s - k_s B_s\right) \quad \text{and} \quad b_s = ic\left(k_s A_s - kB_s\right) \tag{D34}$$

The parameters a_s and b_s are functions of the eigenmode amplitudes A_s and B_s.

In order to find a_s and b_s as functions of the eigenmodes $\underline{E}_s$ and $\underline{H}_s$, it is necessary to multiply (D32) by $\underline{H}_s$ and (D33) by $\underline{E}_s$ and then integrate over the entire volume, taking into account that:

$$\int_V \varepsilon \underline{E}_s \underline{E}_l dV = 0 \qquad \text{and} \qquad \int_V \mu \underline{H}_s \underline{H}_l dV = 0 \tag{D35a,b}$$

equation (D32) becomes:

$$-4\pi\int_V \underline{J}_m.\underline{H}_s dV = b_s\int_V \mu H_s^2 dV \tag{D36}$$

therefore rearranging for b_s gives

$$b_s = \frac{1}{N_s}\int_V \underline{J}_m.\underline{H}_s dV \tag{D37}$$

and (D33) becomes

$$4\pi\int_V \underline{J}_e.\underline{E}_s dV = a_s\int_V \varepsilon E_s^2 dV \tag{D38}$$

So rearranging for a_s gives

$$a_s = \frac{1}{N_s}\int_V \underline{J}_e.\underline{E}_s dV \tag{D39}$$

where

$$N_s = \frac{1}{4\pi}\int_V \varepsilon E_s^2 dV = -\frac{1}{4\pi}\int_V \mu H_s^2 dV \tag{D40}$$

This is the Norm of the *s* eigenmode, it is a normalisation parameter.

Looking back to (D34), it is clear that the eigenmode amplitudes A_s and B_s can be expressed in terms of a_s and b_s by simple rearrangement, such that

$$A_s = -i\frac{\omega a_s - \omega_s b_s}{\omega^2 - \omega_s^2} \quad \text{and} \quad B_s = -i\frac{\omega_s a_s - \omega b_s}{\omega^2 - \omega_s^2} \tag{D41a, b}$$

D1.2 Waveguide Excitation

In the case of amplifiers or oscillators based on absolute instabilities, the cavity is not required. Therefore the investigation of waveguide excitation becomes essential. As with the cavity it is necessary to be able to find the modes excited in a waveguide.

The modes excited in a waveguide can be viewed as similar to the fields induced by a dipole, which obey the Lorentz Lemma. This can be found by returning to Maxwell's equations and assuming that the RF field, denoted by $\underline{E}_1$, $\underline{H}_1$ is excited by $\underline{J}_1^e$, $\underline{J}_1^m$ and $\underline{E}_2$, $\underline{H}_2$ is excited by $\underline{J}_2^e$ and $\underline{J}_2^m$. Maxwell's equations become:

$$\underline{\nabla} \times \underline{E}_{1,2} = ik\mu \underline{H}_{1,2} - \frac{4\pi}{c} \underline{J}_{1,2}^m \tag{D42}$$

$$\underline{\nabla} \times \underline{H}_{1,2} = -ik\varepsilon \underline{E}_{1,2} + \frac{4\pi}{c} \underline{J}_{1,2}^e \tag{D43}$$

If we assume that both RF fields have the same frequency. It is then possible to show that the current and induced fields are reciprocal, i.e. Dot (D42) with $\underline{H}_2$ to give:

$$\underline{H}_2 . \left(\underline{\nabla} \times \underline{E}_1 \right) = ik\mu \underline{H}_1 . \underline{H}_2 - \frac{4\pi}{c} \underline{J}_1^m . \underline{H}_2 \tag{D44}$$

Dot (D43) with - $\underline{E}_1$ to give

$$\underline{E}_1 . \left(\underline{\nabla} \times \underline{H}_2 \right) = -ik\mu \underline{E}_2 . \underline{E}_1 + \frac{4\pi}{c} \underline{J}_2^e . \underline{E}_1 \tag{D45}$$

Subtracting (D45) from (D44) and using the vector identity as before to give

$$\underline{\nabla} . \left(\underline{E}_1 \times \underline{H}_2 \right) = ik \left(\varepsilon \underline{E}_2 . \underline{E}_1 + \mu \underline{H}_1 . \underline{H}_2 \right) - \frac{4\pi}{c} \left(\underline{J}_2^e . \underline{E}_1 + \underline{J}_1^m . \underline{H}_2 \right) \tag{D46}$$

Similarly multiply (D43) by - $\underline{E}_2$ to give

$$-\underline{E}_2.\left(\underline{\nabla}\times\underline{H}_1\right)=ik\varepsilon\underline{E}_1.\underline{E}_2-\frac{4\pi}{c}\underline{J}_1^e.\underline{E}_2 \tag{D47}$$

Multiply (D42) by $\underline{H}_1$ to give

$$\underline{H}_1.\left(\underline{\nabla}\times\underline{E}_2\right)=ik\mu\underline{H}_2.\underline{H}_1-\frac{4\pi}{c}\underline{J}_2^m.\underline{H}_1 \tag{D48}$$

Subtract (D48) from (D47) to give

$$\underline{\nabla}.\left(\underline{E}_2\times\underline{H}_1\right)=ik\left(\varepsilon\underline{E}_1.\underline{E}_2+\mu\underline{H}_1.\underline{H}_2\right)-\frac{4\pi}{c}\left(\underline{J}_1^e.\underline{E}_2+\underline{J}_2^m.\underline{H}_1\right) \tag{D49}$$

Now subtract (D49) from (D46) to give

$$\underline{\nabla}.\left(\underline{E}_1\times\underline{H}_2\right)-\underline{\nabla}.\left(\underline{E}_2\times\underline{H}_1\right)=\frac{4\pi}{c}\left(\underline{J}_1^e.\underline{E}_2+\underline{J}_2^m.\underline{H}_1-\underline{J}_2^e.\underline{E}_1-\underline{J}_1^m.\underline{H}_2\right) \tag{D50}$$

Taking the volume integral of (D50) and using Stokes theorem to convert from volume to surface integral

$$\oint_S\left[\left(\underline{E}_1\times\underline{H}_2\right)-\left(\underline{E}_2\times\underline{H}_1\right)\right]\hat{n}\underline{dS}=\frac{4\pi}{c}\int_V(\underline{J}_1^e.\underline{E}_2-\underline{J}_2^e.\underline{E}_1-\underline{J}_1^m.\underline{H}_2+\underline{J}_2^m.\underline{H}_1)dV \tag{D51}$$

where S is the boundary surface of volume V.

Assuming that both surface and volume are infinite such that $S\to\infty$ and $V\to\infty$ gives

$$\int_V(\underline{J}_1^e.\underline{E}_2-\underline{J}_2^e.\underline{E}_1-\underline{J}_1^m.\underline{H}_2+\underline{J}_2^m.\underline{H}_1)dV=0 \tag{D52}$$

This is the Lorentz Lemma, or reciprocity principle. It states that the relationship between an oscillating current and the resulting electric field is unchanged if one interchanges the points at which the current is placed and where the field is measured. It can be represented more simply as a pair of dipoles

$$P_1 E_2(1) = P_2 E_1(2) \tag{D53}$$

where $E_2(1)$ is the electric field induced by dipole P_2 at point 1, and $E_1(2)$ is the electric field induced by dipole P_1 at point 2. The current induced by each electric dipole may be written as

$$\underline{J}_1^e = -i\omega \underline{P}_1 \delta(\underline{r} - \underline{r}_1) \quad \text{And} \quad \underline{J}_2^e = -i\omega \underline{P}_2 \delta(\underline{r} - \underline{r}_2) \tag{D54a,b}$$

where $\underline{r}_1$ and $\underline{r}_2$ are coordinates of the dipole locations.

D1.2.1 Magnetic Dipole as a Current source

If the corrugation depth is very small, the field scattering on such a small corrugation can be described as coupling between incident and scattered waves via magnetic current induction by the incident wave on the surface of the unperturbed waveguide with a pattern similar to that of the corrugation. The induced current may be anomalous to that induced by a magnetic dipole around a closed loop.

Consider the integral of magnetic flux density through an element of volume V as

$$\int_V \underline{J}^m dV = -i\omega \underline{m} \tag{D55}$$

where $\underline{m}$ is a magnetic dipole. If we now multiply these by the magnetic field induced so as to obtain:

$$\underline{H}_2(1)\int_V \underline{J}_1^m dV = -i\omega \underline{m}_1 \underline{H}_2(1) \tag{D56}$$

$$\underline{H}_1(2)\int_V \underline{J}_2^m dV = -i\omega \underline{m}_2 \underline{H}_1(2) \tag{D57}$$

we can achieve the Reciprocity Law: $\underline{m}_1 \underline{H}_2(1) = \underline{m}_2 \underline{H}_1(2)$.

It is also possible to show the magnetic dipole is related to the electric current density around a closed loop:

$$\underline{m} = \left(\frac{\mu}{c}\right) \underline{J}^e \underline{S} \tag{D58}$$

where $\underline{S} = \oint \underline{n} dS$ is the area vector of the closed loop C, μ is the magnetic moment, denoted by $\mu = IA$, where *A* is the area of the loop and *I* is the current.

A small contour C with electric current around it induces fields $\underline{E}_1$ $\underline{H}_1$. The fields $\underline{E}_2$ $\underline{H}_2$ are induced by dipole $\underline{P}_2$, therefore

$$\int_V \underline{J}_1^e \underline{E}_2 dV = J^e \oint \underline{E}_2 \underline{dS} = J^e \int_s \left(\underline{\nabla} \times \underline{E}_2\right).\underline{n} dS \tag{D59}$$

where $\underline{n}$ is a unit vector perpendicular to the surface S enclosed by the contour C, $\underline{J}_1^e dV = J^e \underline{dS}$, and $\underline{dS}$ is an elementary part of the contour C. Also from (D15a):

$$\underline{\nabla} \times \underline{E}_2 = ik\mu \underline{H}_2 \tag{D60}$$

with $\underline{J}_2^m = 0$.

Substituting this into (D59):

$$\int_V \underline{J}_1^e \underline{E}_2 dV = ikJ^e \int_S \mu \underline{H}_2 \underline{n} dS = ik\mu(1) J^e \underline{S}\underline{H}_2(1) \tag{D61a}$$

which is equal to the field induced by and electric dipole, i.e.

$$ik \frac{\mu(1)}{c} J^e \underline{S}\underline{H}_2(1) = -\underline{P}_2 \underline{E}_1(2) \tag{D61b}$$

This shows that the magnetic dipole m can be related to the electric field strength.

Now introduction of the following boundary conditions

$$\underline{n} \times \underline{H} = \frac{-4\pi}{c} \underline{J}^e \qquad \text{and} \qquad \underline{n} \times \underline{E} = \frac{4\pi}{c} \underline{J}^m \tag{D62a,b}$$

and taking into account the Maxwell equations presented in (D42) and (D43), the eigenmodes for the waveguide can be found.

The fields inside the waveguide can be expressed as

$$\underline{E} = \sum_s \left(C_s \underline{E}_s + C_{-s} \underline{E}_{-s} \right) \qquad \text{and} \qquad \underline{H} = \sum_s \left(C_s \underline{H}_s + C_{-s} \underline{H}_{-s} \right) \tag{D63}$$

where $\underline{E}_s$ and $\underline{E}_{-s}$ are the eigenmodes, C_{-s} and C_s are the eigenmodes amplitudes. If the modes $\underline{E}_s$ and $\underline{E}_{-s}$ are orthogonal, then the following holds

$$\oint_S \left[\left(\underline{E}_s \times \underline{H}_{s'} \right) - \left(\underline{E}_{s'} \times \underline{H}_s \right) \right] \underline{n} dS = 0 \tag{D64a}$$

This may be expanded as

$$\oint_S \left(\left(\underline{n} \times \underline{E}_s \right) \underline{H}_{s'} - \left(\underline{n} \times \underline{E}_s \right) \underline{H}_s \right) dS = 0 \qquad \text{(D64b)}$$

Where the boundary condition that there be no electric field tangential to the surface holds, i.e.

$$\left[\underline{n} \underline{E} \right]_{S_0} = 0 \qquad \text{(D64c).}$$

Therefore (D64b) becomes

$$\int_{S_1} \left(\left(\underline{n} \times \underline{E}_s \right) \underline{H}_{s'} - \left(\underline{n} \times \underline{E}_s \right) \underline{H}_s \right) dS + \int_{S_2} \left(\left(\underline{n} \times \underline{E}_s \right) \underline{H}_{s'} - \left(\underline{n} \times \underline{E}_s \right) \underline{H}_s \right) dS \qquad \text{(D65)}$$

where S_1 and S_2 are the surfaces transverse to the direction of propagation.

A schematic of cylindrical waveguide is shown in the Figure D1 below to illustrate the important parameters.

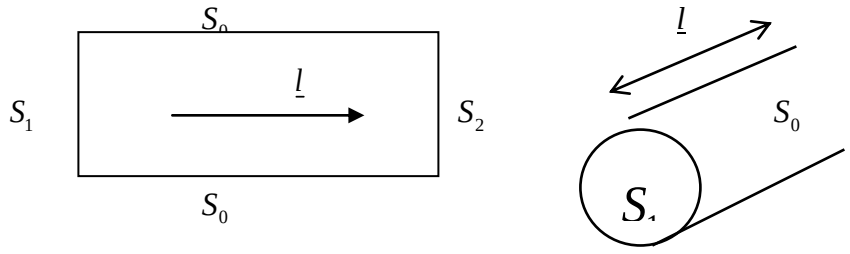

Figure D1: Cylindrical waveguide geometry, where the surface S_0 is parallel to the direction of propagation, denoted by $\underline{l}$.

Returning to Maxwell's equations and assuming that there are no currents, i.e. J^e and J^m both equal zero. Taking into account that for flow through surface S_2, $\underline{n} = \underline{l}$, and for

flow through S_1, $\underline{n} = -\underline{l}$, and also the boundary condition in (D64c), equation (D64a) can be written as

$$\oint_{S_1} \left[\left(\underline{E}_s \times \underline{H}_{s'} \right) - \left(\underline{E}_{s'} \times \underline{H}_s \right) \right] \underline{l} dS = J_{s,s'} e^{i(k_s + k_{s'})z} \tag{D66}$$

where $J_{s,s'}$ is the surface current density of the relevant mode and it is assumed that

$$E_s \sim e^{ik_s z} \qquad \text{and} \qquad E_{s'} \sim e^{ik_{s'} z} \tag{D67}$$

and the wave norm is written as:

$$N_s = \frac{c}{4\pi} J_{s,-s} = \frac{c}{4\pi} \oint_S \left[\left(\underline{E}_s \times \underline{H}_{-s} \right) - \left(\underline{E}_{-s} \times \underline{H}_s \right) \right] \underline{l} dS = \mp \frac{c}{2\pi} \int_S \left(\underline{E}_s \times \underline{H}_s \right) \underline{l} dS \tag{D68}$$

where the $\mp$ depend on the wave structure.

D1.2.2 Current sheets as sources of plane waves

The currents induced in a waveguide may be considered as a sheet of surface currents and therefore as a source for plane waves. If an electric surface current density exists on the *z = 0* plane in free space, the resulting fields can be found by assuming that plane waves exist on either side of the current sheet and taking into account boundary conditions.

The source does not vary with *x* or *y*, the fields will not vary with *x* or *y*, but will propagate away from the source in the $\pm z$ direction. The boundary conditions to be satisfied at the source are

$$\underline{n} \times \left(\underline{E}_{RHS} - \underline{E}_{LHS} \right) = \underline{z} \times \left(\underline{E}_{RHS} - \underline{E}_{LHS} \right) = 0 \tag{D69a}$$

$$\underline{n}\times\left(\underline{H}_{RHS}-\underline{H}_{LHS}\right)=\underline{z}\times\left(\underline{H}_{RHS}-\underline{H}_{LHS}\right)=J_0 \tag{D69b}$$

where, $\underline{E}_{LHS}$ $\underline{H}_{LHS}$ are the fields for $z<z_1$ and $\underline{E}_{RHS}$, $\underline{H}_{RHS}$ are associated with $z>z_2$.

Assume that all the current is located in one volume at the centre, and that there is only one current source. The electric and magnetic fields in the waveguide are denoted by

$$\underline{E}=\sum_s C_s\underline{E}_s \quad \text{and} \quad \underline{H}=\sum_s C_s\underline{H}_s \qquad \text{for } z>z_2 \tag{D70}$$

$$\underline{E}=\sum_s C_{-s}\underline{E}_{-s} \quad \text{and} \quad \underline{H}=\sum_s C_{-s}\underline{H}_{-s} \qquad \text{for } z<z_1 \tag{D71}$$

where *s* refers to modes propagating in the forward direction and -*s* refers to modes propagating in the backward direction. Using the equations above and the Lorentz lemma, expressions for forward and backward propagating waves can be found as follows:

For the case of backward Waves ($z<z_1$), the following is true:

$$\underline{E}_1=\sum_s C_{-s}\underline{E}_{-s} \qquad \underline{E}_2=\sum_s C_{-s'}\underline{E}_{-s'} \tag{D72}$$

$$\underline{H}_1=\sum_s C_{-s}\underline{H}_{-s} \qquad \underline{H}_2=\sum_s C_{-s'}\underline{H}_{-s'} \tag{D73}$$

where: -*s* indicated a backward mode, and *–s'* indicated a different backward mode.

Substitution into (D51) gives expression for backward modes

$$\oint_S\left(\underline{E}\times\underline{H}_{-s'}\right)-\left(\underline{E}_{-s'}\times\underline{H}\right)\underline{n}dS=\frac{4\pi}{c}\int_V(\underline{J}^e.\underline{E}_{-s'}-\underline{J}^m.\underline{H}_{-s'})dV \tag{D74}$$

and for the forward modes ($z>z_2$):

$$\underline{E}_1 = \sum_s C_s \underline{E}_s \qquad \underline{E}_2 = \sum_s C_{s'} \underline{E}_{s'} \tag{D75}$$

$$\underline{H}_1 = \sum_s C_s \underline{H}_s \qquad \underline{H}_2 = \sum_s C_{s'} \underline{H}_{s'} \tag{D76}$$

and the expression for the forward mode is therefore

$$\oint_S \left(\left(\underline{E} \times \underline{H}_{s'} \right) - \left(\underline{E}_{s'} \times \underline{H} \right) \right) \underline{n} dS = \frac{4\pi}{c} \int_V (\underline{J}^e . \underline{E}_{s'} - \underline{J}^m . \underline{H}_{s'}) dV \tag{D77}$$

These can be solved to give

$$\int_{S_0} \left(\underline{E} \times \underline{H}_{-s'} \right) - \left(\underline{E}_{-s'} \times \underline{H} \right) \underline{l} dS = \sum_s C_{-s'} J_{-s,-s'} = 0 \tag{D78}$$

$$\int_{S_2} \left(\underline{E} \times \underline{H}_{-s'} \right) - \left(\underline{E}_{-s'} \times \underline{H} \right) \underline{l} dS = \sum_s C_{s'} J_{s,-s'} = C_{s'} \frac{4\pi}{c} N_{s'} \tag{D79}$$

$$\int_{S_1} \left(\underline{E} \times \underline{H}_{s'} \right) - \left(\underline{E}_{s'} \times \underline{H} \right) \underline{l} dS = \sum_s C_{-s} J_{-s,s'} = -C_{-s'} \frac{4\pi}{c} N_{s'} \tag{D80}$$

$$\int_{S_0} \left(\underline{E} \times \underline{H}_{s'} \right) - \left(\underline{E}_{s'} \times \underline{H} \right) \underline{l} dS = \sum_s C_s J_{s,s'} = 0 \tag{D81}$$

where J is as defined in (D66).

Equations (D78) and (D81) are in agreement with the boundary condition (D64c). The amplitudes of the forward and backward waves are therefore found to be:

$$C_s = \frac{1}{N_s} \int_V \left(\underline{J}^e \underline{E}_{-s} - \underline{J}^m \underline{H}_{-s} \right) dV \tag{D82}$$

$$C_{-s} = \frac{1}{N_s}\int_V \left(\underline{J}^e \underline{E}_s - \underline{J}^m \underline{H}_s \right) dV \tag{D83}$$

Assuming now that there are electric and magnetic currents induced by the surface charges of the waveguide, i.e.

$$\frac{\partial \rho^e}{\partial t} = J_2^e \qquad \text{and} \qquad \frac{\partial \rho^m}{\partial t} = J_2^m \tag{D84}$$

where ρ represents the surface charge, and that they are periodic such that $\rho^{e,m} \approx e^{-i\omega t}$ and J_2^e and J_2^m become $-i\omega\rho^e$ and $-i\omega\rho^m$ respectively.

In this case the surface charges in the volume will tend to zero, i.e. $\left\{ z-\delta : z+\delta \right\}_{\delta \to 0}$

The surface charges will create additional fields denoted by

$$\underline{E}_{//} = -\frac{4\pi}{i\omega\varepsilon} \underline{J}_2^e . \underline{l} \qquad \text{and} \qquad \underline{H}_{//} = -\frac{4\pi}{i\omega\mu} \underline{J}_2^m . \underline{l} \tag{D85a,b}$$

Therefore the total fields will be a product of the above and (D63), hence equal to

$$\underline{E} = \sum_s \left(C_s \underline{E}_s + C_{-s} \underline{E}_{-s} \right) + \frac{4\pi}{i\omega\varepsilon} \underline{J}_2^e . \underline{l} \tag{D86}$$

$$\underline{H} = \sum_s \left(C_s \underline{H}_s + C_{-s} \underline{H}_{-s} \right) + \frac{4\pi}{i\omega\mu} \underline{J}_2^m . \underline{l} \tag{D87}$$

D2. Dynamics of Charged Particles

This section is devoted to the theory describing the motion of relativistic charged particles in external electromagnetic fields. We consider initially the motion of a single charged particle in both electric and magnetic fields before considering how this single particle interacts with the electromagnetic wave and then using this to see how an ensemble of electrons interact with EM fields, oscillating both in free space and a dielectric media.

D2.1 Charged Particle Motion in a Static Magnetic Field

The motion of a single electron in a uniform and static magnetic induction (no electric field) is described here. The force exerted of the electron is given by the Lorentz force equation

$$\frac{d\underline{P}}{dt} = \frac{e}{c}\left(\underline{v} \times \underline{B}\right) \tag{D88}$$

where $\underline{v}$ is the particle velocity, $\underline{B}$ the magnetic induction. It is important to note that the energy in a system is conserved, i.e.

$$\gamma = \frac{1}{\sqrt{1-\frac{v^2}{c^2}}} = const. \tag{D89}$$

and the gyration frequency can be written as

$$\omega_c = \frac{eH_o}{m_o \gamma c} \tag{D90}$$

where $\underline{v}$ is the particle's velocity and $\underline{H}_0$ the applied magnetic field strength, m_o is the rest mass, e is the electron charge, and γ is the relativistic (Lorentz) factor, and c is the speed of light. It is worth noting that an alternate equation for the relativistic factor may be given as

$$\gamma = 1 + \frac{eU}{m_0 c^2} \approx 1 + 2W(MeV) \tag{D91}$$

where e is the electron charge, U the accelerating beam potential, m_0 the electron rest mass, c the speed of light in vacuum.

D2.2 Charged Particle Motion in Static Electric and Magnetic Fields

If we now consider how a charged particle will move under the influence of static electric and magnetic fields. Generally the equations of motion for a relativistic charged particle in external static fields are as follows:

$$\frac{d\underline{P}}{dt} = \frac{e}{c}\left[\underline{E} + \left(\underline{v} \times \underline{B}\right)\right] \tag{D92}$$

$$\frac{d\psi}{dt} = e\underline{v}.\underline{E} \tag{D93}$$

where ψ is the energy, $\underline{E}$ is the electric field, $\underline{v}$ is the velocity, $\underline{P}$ is the momentum and $\underline{B}$ is the magnetic induction. It is important to note that in a vacuum $\underline{B} = \underline{H}_0 \mu$ (in SI units), and $\underline{B} = \underline{H}_0$ (CGS units). Assume that both fields are **perpendicular** to each other, i.e. $\underline{B} \perp \underline{E}$. Equation (D93) shows that the energy of the particle is not constant in time. Let us use a Lorentz transformation to simplify the equations of motion as follows:

Introducing the two different frames of reference:

Frame 1: Reference frame *K*, Velocity $\underline{u}$ (Original frame)

and

Frame 2: Reference frame K', Velocity $\underline{u}'$

where the Lorentz force equation for a particle in the K' frame is written as

$$\frac{d\underline{P}'}{dt'} = \frac{e}{c}\left[\underline{E}' + \left(\underline{v}' \times \underline{B}'\right)\right] \tag{D94}$$

where

$$\underline{E}' = \gamma\left(\underline{E} + \underline{\beta} \times \underline{B}\right) - \frac{\gamma^2}{\gamma+1}\underline{\beta}\left(\underline{\beta}.\underline{E}\right) \tag{D95}$$

and

$$\underline{B}' = \gamma\left(\underline{B} - \underline{\beta} \times \underline{E}\right) - \frac{\gamma^2}{\gamma+1}\underline{\beta}\left(\underline{\beta}.\underline{B}\right) \tag{D96}$$

with $\underline{\beta} = \frac{\underline{v}}{c}$. If we now assume that the electron's velocity is **perpendicular** to **both fields** and that $|\underline{E}| < |\underline{B}|$, then the velocity of the frame K' can be chosen to be

$$\underline{u}' = \frac{\underline{E} \times \underline{B}}{B^2} c \tag{D97}$$

Substituting (D97) into (D95) and (D96) we find the fields in the second frame of reference K' are

$$E_{//}^{'} = 0 \qquad E_{\perp}^{'} = \gamma\left(\underline{E} + \frac{\underline{u}}{c} \times \underline{B}\right) = 0 \tag{D98}$$

$$B_{//}^{'} = 0 \qquad B_{\perp}^{'} = \left(\frac{B^2 - E^2}{B^2} \right)^{\frac{1}{2}} \underline{B} = \frac{1}{\gamma} \underline{B} \tag{D99}$$

The parallel and perpendicular refer to the direction of $\underline{u}'$. In the frame K' the only field acting is a static magnetic field $\underline{B}'$ which acts in the direction of $\underline{B}$ but is weaker by a factor of $\frac{1}{\gamma}$. The motion in the *K'* frame is therefore as considered previously, for a static magnetic field only. The electron will spiral around the lines of force. When viewed from the original frame of reference, the gyration is accompanied by a 'drift' velocity $\underline{u}'$.

Let us note that due to particle motion with velocity $|u| = \left| \frac{cE}{B} \right|$, it is possible to separate charged particles according to their charge and energy (mass). For example if a beam of charged particles has a velocity spread, and is incident upon a region of crossed, uniform $\underline{E}$ & $\underline{B}$ fields, then only the particles with velocities equal to $\left| \frac{cE}{B} \right|$ will travel through without deflection. This allows only a narrow band of velocities around $\left| \frac{cE}{B} \right|$ to be transmitted. If this is then combined with a momentum selector, such as a deflecting magnet, then a very pure and mono-energetic beam of particles of definite mass and charge may be extracted from a beam of mixed energy and momenta. This is advantageous and used in mass/energy spectrometers as well as in accelerators.

In the case where the electric field amplitude exceeds that of the magnetic, i.e. $|\underline{E}| > |\underline{B}|$, the field components can be found via transforming from the original static frame K' to a dynamic one moving with a velocity which can be expressed as:

$$\underline{u}' = \frac{\underline{E} \times \underline{B}}{E^2} c \tag{D100}$$

The field components therefore become

$$E_{//}^{'} = 0 \qquad E_{\perp}^{'} = \left(\frac{E^2 - B^2}{E^2} \right)^{\frac{1}{2}} \underline{E} = \frac{1}{\gamma'} \underline{E} \tag{D101}$$

$$B_{//}^{'} = 0 \qquad B_{\perp}^{'} = \gamma' \left(\underline{B} - \frac{\underline{u}'}{c} \times \underline{E} \right) = 0 \tag{D102}$$

In the system K' the particle is acted on by a pure electrostatic field, this causes hyperbolic motion with ever increasing velocity and energy.

D2.3 Single Charged Particle Interacting with Electromagnetic Field

The interaction between a charged particle and an electromagnetic wave can be described by the pendulum equation which is used to represent simple harmonic periodic motion. The general expression for pendulum motion is denoted by the nonlinear second order Duffing Equation as:

$$\ddot{X} + \omega^2 \dot{X} = F(t) \tag{D103}$$

where *F(t)* is the time dependant external force, $\dot{X}$ is the pendulum velocity and X is the current coordinate. This describes the motion of a damped oscillator with a more complicated potential than simple harmonic motion, an example of which could be a spring whose stiffness does not exactly obey Hooke's Law.

Generally, the Duffing equation does not admit an exact symbolic solution. However, many approximate methods work well, such as:

- Expansion in a Fourier series will provide an equation of motion to arbitrary precision.

- The x^3 term also called the Duffing term can be approximated as small and the system treated as a perturbed simple harmonic oscillator.
- The Frobenius method yields a complicated but workable solution.
- Any of the various numeric methods such as Euler's method and Runge-Kutta can be used.

In the special case of the undamped ($\delta = 0$) and unforced ($\gamma = 0$) Duffing equation, an exact solution can be obtained using Jacobi's elliptic functions. One solution of the above equation is:

$$X = X_{free} + X_{force} \qquad \dot{X} = \dot{X}_{free} + \dot{X}_{force} \tag{D104}$$

where $X_{free} = X_0$ and $X_{force} = X(t) = X_1(t)$. (D105)

For an ensemble of pendulums we have to assume that at $t = 0$ the phases are uniformly distributed in the interval from $[0 : 2\pi)$, i.e. $\varphi_0 \in [0 : 2\pi)$.

In the "free" case, where $F(t) = 0$, the average position of the electrons is equal to zero, $\langle X \rangle_\varphi = 0$. However introducing $F(t) \neq 0$ results in $\langle X \rangle_\varphi \neq 0$ under certain conditions. Let us consider the non-relativistic case in which the energy conservation law can be presented as, (for $F(t) = 0$)

$$\psi = \frac{m\dot{X}^2}{2} + U = const. \tag{D106}$$

where U is the potential energy, $\frac{m\dot{X}^2}{2}$ is the kinetic energy and ψ the total energy of the system. The equation (D103) can be obtained via integration of (D106), i.e.

$$m\ddot{X}_0 + \frac{dU}{dX_0} = 0 \tag{D107}$$

where if $F(t) \neq 0$, then (D107) can be rewritten as

$$m\ddot{X}_0 + \frac{dU}{dX_0} = F(t) \tag{D108}$$

If, for single harmonic oscillations $X_0 = X_0(\psi, \varphi) = X_0(\psi, \varphi + 2\pi)$, (where ψ is energy and φ phase), is equal to $\sum_{n=-\infty}^{\infty} X_n^{(0)}(\psi) e^{in\varphi}$, where $\varphi = \omega t + \varphi_0$, with φ_0 the initial phase of a pendulum. This indicates linear oscillations, where ω is the oscillation frequency of the particles in the potential well defined by *U*.

If the well is not arbitrary and the frequency is a function of energy, i.e. $\omega = \omega(\psi)$, then assuming that the non-linear part is small i.e. $X = X_0 + X_1$ and $\frac{X_1}{X_0} << 1$, where X_0 indicates linear oscillations and X_1 the non-linear oscillations we can therefore substitute it into the equation of motion (D108) which gives:

$$m\ddot{X} = m\frac{\partial^2}{\partial t^2}(X_0 + X_1) = m\ddot{X}_0 + m\ddot{X}_1 \tag{D109}$$

and also performing a Taylor expansion for $U(X)$ around X_0, i.e.

$$\frac{dU}{dX_0} = \frac{d}{dX_0}\left(U(X_0 + X_1)\right) = \frac{d}{dX}\left(U(X_0) + \frac{dU}{dX_0}X_1 + ...\right) = \frac{d}{dX_0}U(X_0) + X_1\frac{d^2}{dX_0^2}U(X_0) + ...$$

we get

$$m\ddot{X}_0 + m\ddot{X}_1 + \frac{d}{dX_0}U(X_0) + X_1\frac{d^2}{dX_0^2}U(X_0) = F(t) \tag{D110}$$

Taking into account (D107) one gets

$$m\ddot{X}_1 + X_1\frac{d^2}{dX_0^2}U(X_0) = F(t) \equiv -eE(t) \tag{D111}$$

where

$$\frac{d^2}{dX_0^2}U(X_0) = f(X_0) \tag{D112}$$

This demonstrates that if the well is linear, i.e. $\frac{d^2U}{dX_0^2} = 0$ or parabolic, i.e. $\frac{d^2U}{dX_0^2} = const.$, there is no energy on average between the ensemble of oscillators with $\varphi_0 \in [0; 2\pi]$ and the wave. If $F(t) = 0$ the problem has solutions which can be presented as two independent variables known as the electron's energy and phase:

$$X_0 = X_0(\psi, \varphi) = C_1X_1^{(1)} + C_2X_2^{(1)} \tag{D113}.$$

It is possible to show that both $X_1^{(1)}$ and $X_2^{(1)}$ are linearly independent solutions i.e. they cannot be expressed in terms of each other. Taking into account that

$$\begin{aligned} X_1^{(1)} &= \frac{\partial X_0}{\partial \varphi_0} = \frac{\partial X_0}{\partial t}\frac{\partial t}{\partial \varphi} = \dot{X}^{(0)} \cdot \frac{1}{\omega_0} \\ X_2^{(1)} &= \frac{\partial X_0}{\partial \psi} \end{aligned} \tag{D114}$$

we find that

$$\det\begin{pmatrix} X_1^{(1)} & \dot{X}_1^{(1)} \\ X_2^{(1)} & \dot{X}_2^{(1)} \end{pmatrix} \neq 0 \tag{D115}$$

This implies that $X_1^{(1)}\dot{X}_2^{(1)} - X_2^{(1)}\dot{X}_1^{(1)} \neq 0$ and

$$\frac{\dot{X}_0}{\omega_0}\frac{\partial \dot{X}_0}{\partial \psi} - \frac{\partial X_0}{\partial \psi}\frac{\ddot{X}_0}{\omega_0} = -\frac{1}{m\omega_0}\left(\frac{\partial}{\partial \psi}\left(\frac{mX_0^2}{2}\right) + \frac{\partial X_0}{\partial \psi}\frac{\partial U}{\partial X_0}\right) = \frac{1}{m\omega_0}\frac{\partial \psi}{\partial \psi} = \frac{1}{m\omega_0} \tag{D116}$$

The general solution is therefore a linear superposition of the solutions $X_1^{(1)}$ and $X_2^{(1)}$

$$\begin{aligned} X_0 &= C_1 X_1^{(1)} + C_2 X_2^{(1)} \\ \dot{X}_0 &= C_1 \dot{X}_1^{(1)} + C_2 \dot{X}_2^{(1)} \end{aligned} \tag{D117}$$

Taking into account that $F(t) \neq 0$ the method of validation of the constants can be used to find the general solution X. We can now assume that both constants are functions of time i.e. $C_1 = C_1(t)$ and $C_2 = C_2(t)$. Taking these conditions into account, the solution of equation

$$m\ddot{X} + \frac{d^2U}{dX^2}X = F(t) \tag{D118}$$

can be represented as

$$X = C_1(t)X_1^{(1)} + C_2(t)X_2^{(1)} \tag{D119}$$

in this case: $$\dot{X} = \dot{C}_1 X_1^{(1)} + \dot{C}_2 X_2^{(1)} + C_1 \dot{X}_1^{(1)} + C_2 \dot{X}_2^{(1)} \tag{D120}$$

and $$\ddot{X} = \dot{C}_1 \dot{X}_1^{(1)} + \dot{C}_2 \dot{X}_2^{(1)} + \ddot{C}_1 X_1^{(1)} + \ddot{C}_2 X_2^{(1)} + C_1 \ddot{X}_1^{(1)} + C_2 \ddot{X}_2^{(1)} \tag{D121}$$

and we require that $$\dot{C}_1 X_1^{(1)} + \dot{C}_2 X_2^{(1)} = 0 \tag{D122}$$

and $$\dot{C}_1 \dot{X}_1^{(1)} + \dot{C}_2 \dot{X}_2^{(1)} = \frac{F(t)}{m} \tag{D123}$$

Multiply (D123) by $\dot{X}_1^{(1)}$ to obtain (D124), and then (D121) by $X_1^{(1)}$ to obtain (D125), where (D124) and (D125) are as follows

$$\dot{C}_1 X_1^{(1)} \dot{X}_1^{(1)} + \dot{C}_2 X_2^{(1)} \dot{X}_1^{(1)} = 0 \tag{D124}$$

$$\dot{C}_1 \dot{X}_1^{(1)} X_1^{(1)} + \dot{C}_2 \dot{X}_2^{(1)} X_1^{(1)} = \frac{F(t)}{m} X_1^{(1)} \tag{D125}$$

Subtracting (D125) from (D124) gives the relation

$$\dot{C}_2 \left(\dot{X}_1^{(1)} X_2^{(1)} - \dot{X}_2^{(1)} X_1^{(1)} \right) = -\frac{F(t)}{m} X_1^{(1)} \tag{D126}$$

Carry out the same process again, only multiply (D120) by $\dot{X}_2^{(1)}$ and (D121) by $X_2^{(1)}$ and subtract the results to give

$$\dot{C}_1 \left(X_1^{(1)} \dot{X}_2^{(1)} - \dot{X}_1^{(1)} X_2^{(1)} \right) = -\frac{F(t)}{m} X_2^{(1)} \tag{D127}$$

From (D126) and (D127) the following relations are easily derived

$$\dot{C}_2.M = \frac{F(t)}{m} X_1^{(1)}$$
$$\dot{C}_1.M = -\frac{F(t)}{m} X_2^{(1)}$$

where
$$M = \frac{1}{m\omega_0} \tag{D128}$$

Direct integration of the set of equations in (D128) allows us to find expressions for the constants C_1 and C_2 as

$$C_1 = -\omega_0 \int_{t_0}^{t} X_2^{(1)}(t')F(t')dt' \tag{D129a}$$

And
$$C_2 = \omega_0 \int_{t_0}^{t} X_1^{(1)}(t')F(t')dt' \tag{D129b}$$

Substituting (D129a) and (D129b) into (D119) gives:

$$\begin{aligned} X &= \omega_0 \left(X_2^{(1)}(t) \int_{t_0}^{t} X_1^{(1)} F(t')dt' - X_1^{(1)}(t) \int_{t_0}^{t} X_2^{(1)} F(t')dt' \right) = \\ &= \omega_0 \left(\int_{t_0}^{t} (X_2^{(1)}(t) X_1^{(1)}(t') - X_1^{(1)}(t) X_2^{(1)}(t'))F(t')dt' \right) = \omega_0 \int_{t_0}^{t} g(t,t')dt' \end{aligned} \tag{D130}$$

This is the solution for **single** electron perturbed motion under the influence of an external force *F(t)*.

D2.4 Multiple Electrons Interacting with an Electromagnetic Field of a Linear Potential Well

The use of the term liner potential well, refers to the case in which the electrons oscillate in free space, interacting with the wave having a vector $k_z = \frac{\omega}{c}$. Considering the interaction of the electron beam with the quasi-synchronous wave, there are three stages:

1) Modulation of the beam by the wave: at this stage electrons situated in the accelerating phase of the wave increase and those in the decelerating phase decrease their velocity.
2) Bunching of electrons occurs, i.e. the uniformity of the beam is broken and it becomes density modulated, hence of RF current appears.
3) Deceleration (or acceleration) of the bunches, i.e. exchange of energy between the wave and the beam.

Now look at what happens with electrons at input of the interaction space that are uniformly distributed within one period of the synchronous wave, i.e. within one potential well.

- If the wave is exactly synchronous to the electron beam, the electrons driven by the RF field gather around the zero of the field, the resulting bunch cannot exchange energy with the EM wave.

- If the wave is slightly faster than the beam, the bunch due to velocity mismatch, becomes shifted to the accelerating phase of the RF field therefore takes energy from it. However if the bunch were in accelerating phase where the bunch would extract energy from the RF wave; therefore its density would decrease, giving the electrons a stronger velocity spread.

- If the wave is slightly slower than the beam the bunch becomes shifted to the decelerating phase of the RF electric field and gives a part of its energy to the electromagnetic wave, i.e. if the bunch is in decelerating phase it gives energy to the RF wave, it therefore becomes more dense and decelerates stronger.

The average position of an electron ensemble of different phases is given by:

$$\overline{\langle X \rangle}^{\varphi} = \frac{1}{2\pi}\int_0^{2\pi} X d\varphi_0 \tag{D131}$$

$$\text{where : } \overline{X}^{\varphi_0} = \frac{\omega}{2\pi}\int_{t_0}^{t}\int_0^{2\pi} g(t,t',\varphi_0)F(t')dt'd\varphi_0 = \frac{\omega}{2\pi}\int_{t_0}^{t} F(t')dt'\int_0^{2\pi} g(t,t',\varphi_0)dt'd\varphi_0$$

(D132)

and $\varphi_0 \in [0, 2\pi)$ is the initial phase of the electron.

This is the case for a single electron, and it is multiplied by an external force, then integrated over all phase and time to obtain an average position of the ensemble.

Recalling from (D114) that

$$X_1^{(1)} = \frac{\partial X_0}{\partial \varphi_0} \qquad\qquad X_2^{(1)} = \frac{\partial X_0}{\partial \psi}$$

where the phase of the ensemble is given by $\varphi(t,\varphi_0) = \omega_0(\psi)t + \varphi_0$. (D133)

Also due to the periodic motion, the position at time *t* may be given as

$$X(t) = \sum_n X_n(\psi)e^{-in\varphi(\varphi_0,t)} \tag{D134}$$

where *n* is any integer number.

If we now introduce the factors:

$$\begin{aligned} f &= X_n(\psi) & g &= e^{-in\varphi} \\ f' &= \frac{dX_n(\psi)}{d\psi} & g' &= -in\frac{d\varphi}{d\psi}e^{-in\varphi} \end{aligned} \tag{D135}$$

we can write $X_{1,2}^{(1)}(t)$ as

$$X_2^{(1)}(t) = \frac{dX^{(0)}}{d\psi} = \sum_n \left(\frac{dX_n}{d\psi}e^{-in\varphi} - X_n in\frac{d\varphi}{d\psi}e^{-in\varphi} \right) \tag{D136a}$$

$$X_1^{(1)}(t) = \frac{dX^{(0)}}{d\varphi_0} = \sum_n \left(-X_n ine^{-in\varphi} \right) \tag{D136b}$$

where X_n is a real function, let us note that $X_n = X_{-n} = X_n^*$, where X_n^* is the conjugate. Also to get $\overline{g(t,t',\varphi_0)}^{\varphi_0} \neq 0$, $n' = -n$ due to the fact that $\frac{d\varphi}{d\psi}$ does not depend on φ_0. Therefore using the identity

$$g(t,t',\varphi_0) = X_1^{(1)}(t')X_2^{(1)}(t) + X_1^{(1)}(t)X_2^{(1)}(t') \tag{D137}$$

the function representing the ensemble becomes

$$\overline{g(t,t',\varphi_0)}^{\varphi_0} = \sum_{n=-\infty}^{\infty} (-in)\frac{d}{d\psi}\left\{ \left| X_n^2 \right| e^{in(\varphi-\varphi')} \right\} \tag{D138}$$

Assuming now that the external force F is given by $F = eE_0e^{i\omega t}$, equation (D132) becomes

$$\overline{X}^{\varphi_0} = \frac{\omega}{2\pi}\int_{t_0}^{t} F(t')dt' \int_{0}^{2\pi} \overline{g(t,t'\varphi_0)}^{\varphi_0} dt' d\varphi_0$$
$$= e^{i\omega t}\int_{t_0}^{t} e^{-i(\omega-\omega_0 n)(t-t')}dt' = \frac{e^{i\omega t}}{-i(\omega-\omega_0 n)}\left[1-e^{-i(\omega-\omega_0 n)(t-t_0)}\right] \quad \text{(D139)}$$

therefore the average position of the ensemble may be given as

$$\overline{X}^{\varphi_0} = e^{i\omega t}\frac{\left[1-e^{-i(\omega-\omega_0 n)T}\right]}{-i(\omega-\omega_0 n)} \quad \text{(D140)}$$

This shows that electrons appear and disappear from the interaction space, where T is the time interval of an electron being inside the interaction space. Introducing the particle life time as τ, and the electron life expectancy function as

$$f = \upsilon e^{-\upsilon\tau} \quad \text{(D141a).}$$

It is a probability function therefore can be written as

$$\int_{0}^{\infty} f d\tau = 1 \quad \text{(D141b)}$$

with $\frac{1}{\upsilon} = \tau$. (D141c)

Substitution of (D141a) into (D141b) gives

$$\int_{0}^{\infty} \upsilon e^{-\upsilon\tau}\left(1-e^{-i(\omega-\omega_0 n)T}\right)d\tau = 1+\frac{i\upsilon}{(\omega-n\omega_0)-i\upsilon} = \frac{\omega-n\omega_0}{(\omega-n\omega_0)-i\upsilon} \quad \text{(D142)}$$

Hence the average position of the ensemble, taking into account the particle's life time is given by

$$\overline{X}^{\varphi_0\tau} = -eEe^{i\omega t}\omega_0 \sum_{n=-\infty}^{\infty} (-in)\frac{d}{d\psi}\left\{\left|X_n^2\right|\frac{1}{\upsilon + i(\omega - n\omega_0)}\right\} \tag{D143}$$

This is the solution which demonstrated the electron bunch dynamics under the influence of the monochromatic RF field.

D2.5 Multiple Electrons Interacting with an Electromagnetic Field of a Non-Linear Potential Well

In the previous section it was assumed that the electric and magnetic fields were in free space, with no material bodies present. In practice this is not often true. Let us now assume that the RF wave propagates in a dielectric. For a dielectric material, an applied electric field $\underline{E}$ causes the polarisation of the atoms or molecules of the material to create an electric dipole moment, which augments the total displacement flux $\underline{D}$. The additional polarisation vector is $\underline{P}_e$.

If we introduce the density of the dipole moment as

$$P = eN\overline{X}^{\varphi_0,\tau} \tag{D144}$$

where e is the electron charge and N is the particle density. Also introduce the displacement flux $\underline{D}$ as

$$\underline{D} = \varepsilon\underline{E} + 4\pi\underline{P}_e \tag{D145}$$

where ε is the dielectric constant (equal to one in a vacuum) and take into account that

$$\underline{P}_e = \varepsilon\chi_e\underline{E}, \tag{D146}$$

where χ_e is the electrical susceptibility, and may be complex. Equation D145 becomes

$$\underline{D} = \varepsilon\underline{E} + 4\pi\underline{P}_e = \varepsilon\left(1+\chi_e\right)\underline{E} = \tilde{\varepsilon}\underline{E}, \tag{D147}$$

where $\tilde{\varepsilon} = \varepsilon(1+\chi_e)$. This is the constitutive relation, it relates the vector fields $\underline{D}$ and $\underline{E}$

where the $\tilde{\varepsilon}$ can be written as

$$\tilde{\varepsilon} = \tilde{\varepsilon}' - i\tilde{\varepsilon}'' \tag{D148}$$

and is the complex permittivity/dielectric constant of the material. The imaginary part of $\tilde{\varepsilon}$ accounts for losses in the medium, such as heat.

Equation (D147) may be rearranged to obtain an expression for the dielectric constant where it is assumed that $\varepsilon = 1$.

$$\tilde{\varepsilon} = 1 - \frac{4\pi}{E} P \tag{D149}$$

Now consider the case of a plasma (collection of classical electrons) by substituting the expression for electron life expectancy into (D144) and allowing for no external force such that the particle moves with motion proportional to $e^{i\omega_0 t}$. Assume the well is parabolic, i.e. consider only $X_{\pm 1}$ and $X_n = 0$ for all $n \neq \pm 1$. This leads to an expression for the dielectric constant, (with substitution of equation (D143)), as

$$\tilde{\varepsilon} = 1 - 4\pi e^2 N \omega \left[\frac{d}{d\psi} \left(\frac{\left| X_1^2 \right|}{(\omega - \omega_0) - i\upsilon} - \frac{\left| X_1^2 \right|}{(\omega + \omega_0) - i\upsilon} \right) \right] \tag{D150}$$

where N is the particle density.

Taking into account that the energy ψ is given by

$$\psi = 2m\omega_0^2 \left| X_1 \right|^2 \tag{D151}$$

and if we also set the plasma to be collisionless such that $\upsilon \to 0$ hence $lifetime \to \infty$, then (D150) becomes

$$\tilde{\varepsilon} = 1 - \frac{4\pi e^2 N}{m} \frac{d}{d\psi}\left[\frac{\psi}{\omega^2 - \omega_0^2}\right] \tag{D152}$$

If there are no free oscillations ($\omega_0 \to 0$), then this becomes

$$\tilde{\varepsilon} = 1 - \frac{\omega_p^2}{\omega^2} \tag{D153}$$

where the plasma frequency is expressed as: $\omega_p^2 = \frac{4\pi e^2 N}{m}$. (D154)

In the general case for a plasma with collisions, the dielectric constant would be as stated in equation (D150) above.

Let us now assume that ($\omega \to \omega_0$), then the dielectric constant $\tilde{\varepsilon}$ becomes

$$\tilde{\varepsilon} = 1 - \frac{\Omega}{\omega - \omega_0 \pm i\upsilon} = 1 - \frac{\Omega(\omega - \omega_0)}{(\omega - \omega_0)^2 + i\upsilon^2} - i\frac{\Omega\upsilon}{(\omega - \omega_0)^2 + \upsilon^2} \tag{D155}$$

where $\Omega = \frac{\omega_p^2}{2\omega_0}$.

This illustrated that the dielectric constant has both real and imaginary parts and can be represented graphically as per Figure D2 which demonstrates that there is only absorption of EM field with zero emmitance as the imaginary component is always negative.

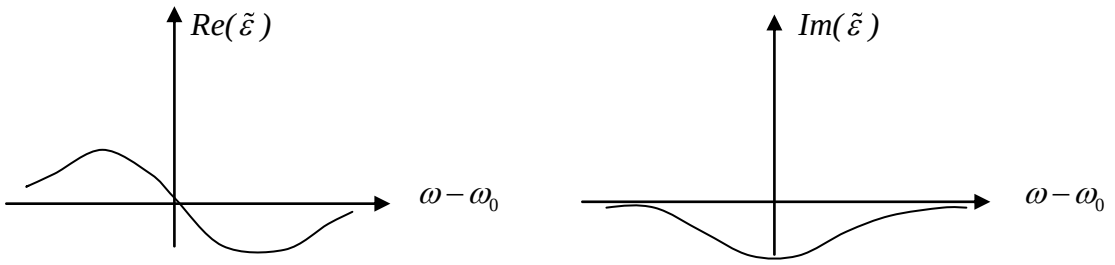

Figure D2: Graphical representation of the dielectric constant.

Now if the well is <u>*NOT*</u> parabolic there will exist an infinite number of harmonics, for which it can be assumed that $\upsilon \to 0$ therefore allowing the dielectric constant to become

$$\tilde{\varepsilon} = \sum_n \varepsilon_n \tag{D156a}$$

where

$$\tilde{\varepsilon}_n = 1 - \omega_p^2 m\omega_0 \frac{d}{d\psi}\left[\frac{n|X_n|^2}{\omega - n\omega_0 - i\upsilon}\right] = 1 + \Delta\mathcal{E}_1 + \Delta\mathcal{E}_2 \tag{D156b}$$

Let us consider $\tilde{\varepsilon}_n$ in this case, where

$$\Delta\tilde{\varepsilon}_1 = \frac{A_1}{\omega - n\omega_0 - i\upsilon} \qquad \text{and} \qquad \Delta\tilde{\varepsilon}_2 = \frac{A_2}{(\omega - n\omega_0 - i\upsilon)^2} \tag{D157}$$

and writing the constants A_1 and A_2

$$A_1 = -\omega_p^2 m\omega_0 n\frac{d|X_n|^2}{d\psi} \qquad \text{and} \qquad A_2 = -\omega_p^2 m\omega_0 n^2 |X_n|^2 \frac{d\omega_0}{d\psi} \tag{D158}$$

If the initial angular frequency is not a function of energy, i.e. $\omega_0 \neq \omega_0(\psi)$ then we have a linear oscillator therefore $A_2 = 0$ and $\Delta\tilde{\varepsilon}_2 = 0$. It is possible to change the sign of $\Delta\tilde{\varepsilon}_1$ by choosing $\frac{d\left|X_n\right|^2}{d\psi} < 0$ thus giving a negative conductivity and observed radiation emission. Assume for example that the rate of frequency change with energy is less than zero, i.e. $\frac{d\omega_0}{d\psi} < 0$, this is the case for cyclotron oscillations (ω_0 is the cyclotron frequency). This indicates that $A_2 > 0$ therefore

$$\Delta\tilde{\varepsilon}_2 = A_2 \frac{(\Delta\omega)^2 - \upsilon^2}{((\Delta\omega)^2 - \upsilon^2)^2} + 2iA_2 \frac{\upsilon\Delta\omega}{\left[\Delta\omega^2 + \upsilon^2\right]^2} \tag{D159}$$

where $\Delta\omega = \omega - n\omega_0$.

Conference Proceedings

36th International Conference on Plasma Science and 23rd Symposium on Fusion Engineering, May 31 – June 5 2009, San Diego, California.

'CHERENKOV MASER BASED ON A TWO-DIMENSIONAL PERIODIC LATTICE'

The National Vacuum Electronics Conference (NVEC), 9th September 2009, The Cockroft Institute, Daresbury.

'CHERENKOV MASER BASED ON A TWO-DIMENSIONAL PERIODIC LATTICE'

The IET European Pulsed Power Conference 2009, 21 – 25 September 2009, CERN, Geneva, Switzerland.

'HIGH POWER MASER BASED ON 2D PERIODIC STRUCTURE AND OPERATING IN THE W-BAND FREQUENCY RANGE'

35th IEEE International Conference on Plasma Science, June 15 - 19, 2008. Congress Center Karlsruhe, Germany.

'A High Power Maser based on a Two-Dimensional Periodic Lattice'

The International Conference on Infrared and Millimeter Waves/THz Electronics, September 15th – 18th 2008, California Institute of Technology, Pasedena.

'High Power Masers based on 2D periodic structures: from the GHz to THz frequency range'

The International Vacuum Electronics Conference, 22nd – 24th April 2008, Monterey, California.

'Design of a High Power W-Band Maser based on a Two Dimensional Periodic Structure'

The Joint 32nd International Conference on Infrared and Millimetre Waves and 15th International Conference on Terahertz Electronics, 2nd – 7th September 2007, Cardiff.

'Concept of a High Power W-band Maser based on a Two-Dimensional Structure'

49th American Physical Society Meeting of the Division of Plasma Physics, November 12-16th 2007, Orlando, Florida.

'A HIGH POWER HIGH FREQUENCY MASER BASED ON A TWO-DIMENSIONAL STRUCTURE'

The National Vacuum Electronics Conference, 2nd – 4th April 2007, Surrey Ion Beam Centre.

'A High Harmonic Gyrotron Based on a Two-Dimensional Structure'

The IEEE Pulsed Power and Plasma Science Conference, June 17 – 22 2007, Albuquerque, New Mexico.

'THE CONCEPT OF A HIGH-HARMONIC COAXIAL GYROTRON BASED ON TWO-DIMENSIONAL LATTICE.'

Wave propagation and tunneling through periodic structures

I. V. Konoplev,[a] P. MacInnes, A. W. Cross, A. D. R. Phelps, L. Fisher, and K. Ronald
Department of Physics, SUPA, University of Strathclyde, Glasgow G4 0NG, United Kingdom

(Received 2 October 2008; accepted 4 November 2008; published online 10 December 2008)

The phenomenon of tunneling manifests itself in nearly every field of physics. The ability to distinguish a wave tunneling through a barrier from one propagating is important for a number of applications. Here we explore the properties of the wave traveling through the band gap created by a lattice, either as a consequence of tunneling through the barrier or due to the presence of a pass band inside the gap. To observe the pass band for studying tunneling and propagating waves simultaneously, a localized lattice defect was introduced. The differences between the two phenomena are highlighted via waves' dispersion characteristics. © *2008 American Institute of Physics*. [DOI: 10.1063/1.3033826]

The study of properties of a wave tunneling through a band gap is one of the fundamental and divisive problems of physics.[1–3] The wave tunneling manifests itself in every field of physics including quantum computing, signal processing, optics, electronic, photonics, and condensed matter physics. In this paper we compare the properties of the electromagnetic waves tunneling and propagating through the band gap formed by a one-dimensional (1D) periodic lattice.[4] In previous works[3,5] attempts to measure the time required for a single photon or wave packets to tunnel across the 1D photonic band gap have been made and compared with the time required for a photon/wave packet to propagate through the same distance in free space. These studies triggered a number of questions and discussions.[1,2,6] Here we study the dispersions of the propagated and the tunneled waves to distinguish and compare their properties. We also demonstrate that tunneling and propagating photons can be distinguished via analysis of their dispersion properties.

To conduct the studies a pass band (associated with localized lattice defect eigenmode) inside the band gap was created[7,8] and the properties of the waves inside and outside the pass band were compared. By creating a periodic lattice with a specific defect it is possible to modify the properties of the lattice band gap and to control the pass band location.[8,9] As a result, 1D periodic lattices, with and without localized defects, are perfectly suited to study tunneling and propagating phenomena. In this letter, we demonstrate that if the 1D lattice has a finite length L, some of the photons having energy and momentum inside the band gap will pass through the barrier gaining a phase shift at the output $\Delta\varphi \equiv \varphi_{\text{out}} - \varphi_{\text{in}}$ proportional to L, where $\varphi_{\text{in,out}}$ are the photons' phases at the input and output of the structure. We show that an electromagnetic wave at the exact Bragg resonance has a phase change at the output of the structure equal to 0, i.e., $\Delta\varphi = 0$, which makes the waves at the input and output of the structure "indistinguishable," i.e., changing the phase of the photon at one side of barrier will result in the same change in the photon phase at another end of the barrier. We also show that a localized defect inside a periodic structure significantly alters the lattice dispersive properties. It is demonstrated that the gradient of the wave dispersion inside the pass band is the same as for a propagating wave in a conventional waveguide and significantly differs from one outside the pass band. The gradient difference observed was constant and did not depend on either the defect or the lattice parameters. This allows us to distinguish a "tunneled" wave from a wave that propagates through the barrier due to a lattice defect. We have also observed that a photon located at the pass band center gains zero phase change while passing through the barrier. The results observed are important for determining the lattice suitability for a number of applications including narrow band filters, mirrors, and specialized wave guiding. Also in spite of the fact that the system studied is a 1D periodic structure based on a cylindrical waveguide, the results observed are applicable for any particle/wave traveling or tunneling through a band gap.

The band gap formation due to the interaction between an electromagnetic wave and a 1D periodic structure takes place in the vicinity of the Bragg resonance defined as $\vec{\delta} = \vec{\vec{k}} - \vec{k}_i + \vec{k}_s$, where $\vec{k}_{i,s}$ are the wave vectors of the incident and scattered waves and $|\vec{k}_{i,s}| = 2\pi f/v$, v is the speed of light in the unperturbed medium and f is the wave frequency, $\vec{\vec{k}}$ is the lattice eigenvector $|\vec{\vec{k}}| = 2\pi/d$, d is the lattice period, and $\vec{\delta}$ is the detuning from the resonance condition $\vec{\vec{k}} = \vec{k}_i - \vec{k}_s$. In this letter, a low contrast 1D periodic lattice based on dielectric inserts, having a periodic refractive index [the variation in the refractive index Δn is small in comparison with the refractive index of the unperturbed dielectric n_0 $(\Delta n/n_0 \ll 1)$], inside a smooth cylindrical metal waveguide was studied (Fig. 1).[8] The annular inserts had inner and outer radii of 5.0 and 11.0 mm, respectively, with an unperturbed refractive index of ~1.87. The periodicity of the refractive index of the dielectric structure was achieved via a corrugation of the inner surface of the inserts (the period of corrugation is 10.0

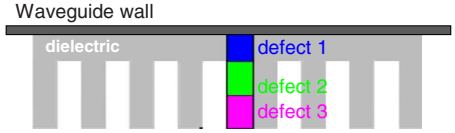

FIG. 1. (Color online) Schematic of the 1D periodic structures (side view) with corrugated dielectric insert (the air, dielectric, and waveguide walls are shown by the white, gray, and black colors) with localized "zero" length defects of the period. Defect 1 has a radius equal to the maximum radius of the corrugation; defect 2 has an intermediate radius; and defect 3 has a radius equal to the minimum corrugation radius.

[a]Author to whom correspondence should be addressed. Electronic mail: ivan.konoplev@strath.ac.uk. Tel.: +44-141-5484272. FAX: +44-141-5522891.

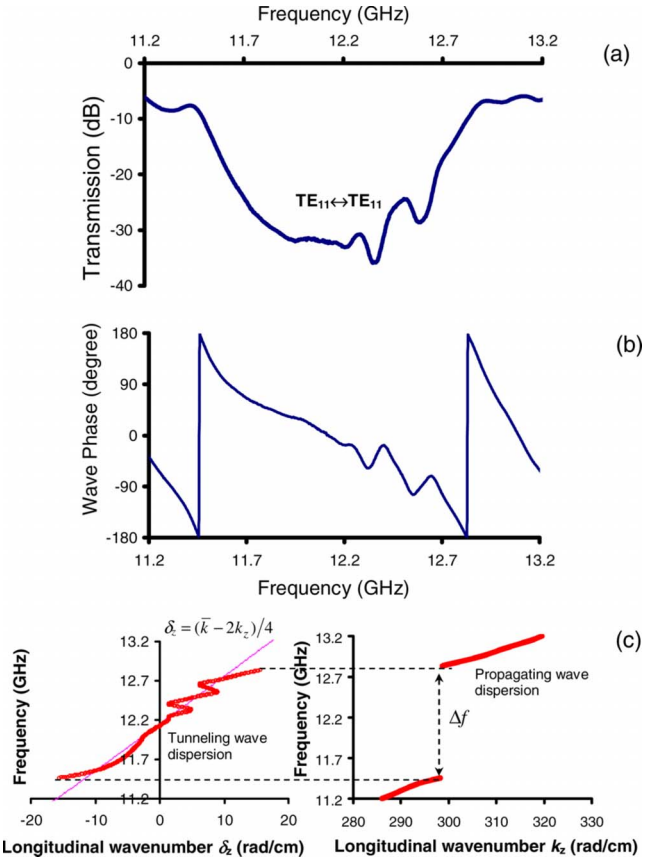

FIG. 2. (Color online) Experimental study of the regular 1D periodic structure. (a) Dependence of the transmission profile vs frequency. (b) Variation in the wave's phase at the output of the structure vs wave frequency. (c) The dispersion diagrams of the periodic structure in wave number ranges [−20;20] (left diagram) and [280, 330] (right diagram) evaluated from experimental data (bold line) and calculated (thin line).

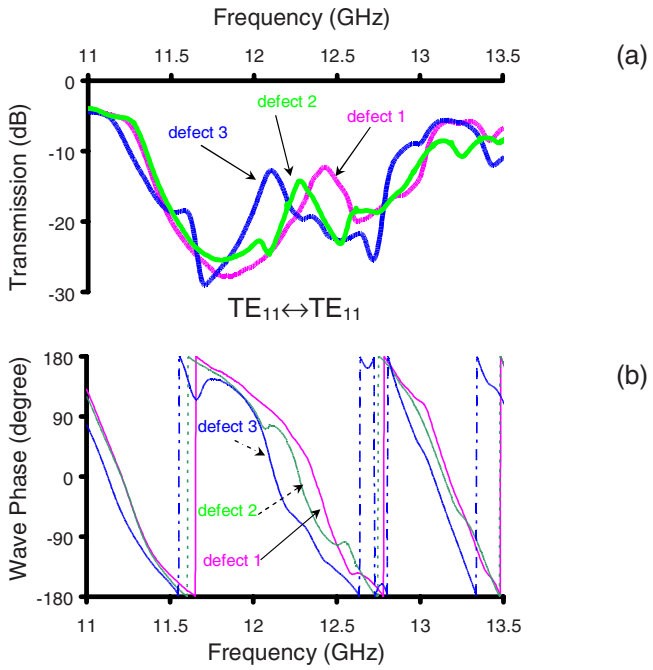

FIG. 3. (Color online) Results of the experimental studies of transmission through the 1D Bragg dielectric structures with zero length defects. (a) Dependence of the transmission through the structures with the defects. (b) Measured wave's phase variation with the frequency at the output of the structures.

mm and the corrugation depth is 4.0 mm). In the case of the periodic structure, with a lattice defect, the defect was made by inserting a dielectric ring between two regular periodic structures of equal length (Fig. 1). Figure 1 illustrates three periodic structures with localized defects having different refractive indices and used in the experiments. The experiments were carried out using a vector network analyzer capable of both wave amplitude and phase measurements. At the start the experimental apparatus was calibrated to reduce the background noise signal and to measure the relative wave's phase at the output of the lattice, i.e., to measure the phase difference between input and output waves. To conduct the experiments the fundamental TE_{11} mode (the photons having the smallest transverse momentum allowed in such a structure) of the cylindrical waveguide was used. The frequency-chirped electromagnetic wave was launched and the amplitude (transmission coefficient) and the phase of the signal at the output of the structure were measured in the frequency range from 11.0 to 13.5 GHz. In this frequency range the formation of the band gap (barrier) associated with $TE_{11} \leftrightarrow TE_{11}$ (11.5–12.8 GHz) wave scattering takes place.[8] In this case the expression for the detuning δ_z (δ_z is the projection of $\vec{\delta}$ on the longitudinal axis z) can be simplified $\delta_z = \bar{k} - 2k_z$, where $k_z = k_{sz,iz} = \sqrt{(2\pi f/v)^2 - k_{s\perp,i\perp}^2}$ and $k_{s\perp,i\perp}$ are the transverse wave numbers of the scattered and incident waves, respectively. In the first set of experiments a conventional 1D Bragg structure was investigated. In Figs. 2(a) and 2(b) the results observed from the measurement of the wave's transmission and phase versus frequency are shown. The phase data observed [Fig. 2(b)] were analyzed and the dispersion characteristic of the periodic structure was obtained [Fig. 2(c)]. The dispersion diagrams have been evaluated from phase data due to the direct link between the longitudinal wave number k_z and the phase of the transmitted signal ($\varphi = k_z L$, where L is the length of the structure[10]). To obtain the $(f;\delta_z)$ diagram (dispersion inside the band gap region), the Bragg resonance condition was taken into account. The band gap observed in Fig. 2(c) is indicated as Δf on the right hand side diagram and agreed well with the profile of the transmission coefficient in Fig. 2(a). The left hand figure shows the wave dispersion inside the frequency interval associated with the band gap (11.5–12.8 GHz). The straight line on the left graph (best fit line to the measured dispersion) is obtained using the following expression: $\delta_z \approx (\bar{k} - 2k_z)/g$, where g is a constant approximately equal to 4. Let us note that the dispersion relation for the propagating wave should be obtained from the definition of the detuning, i.e., $\delta_z \approx (\bar{k} - 2k_z)$, and it is clear that the gradient of the dispersion inside the band gap frequency range is larger as compared with the dispersion outside the band gap [see also the phase variation in Fig. 2(b)]. The gradient observed in the experiments was the same for different lattice parameters, i.e., parameter $g \sim 4$ observed here empirically was constant for all experiments. It is possible to assume that this parameter depends on material properties, for instance, a refractive index; however more experiments will be required to identify this dependence. One also notes that the only wave that tunneled through the band gap at the exact Bragg frequency gained no phase change. Therefore the wave phase velocity observed inside the band gap is large as compared with the phase velocity of the propagating wave but still has a finite value except for a single point associated with the exact

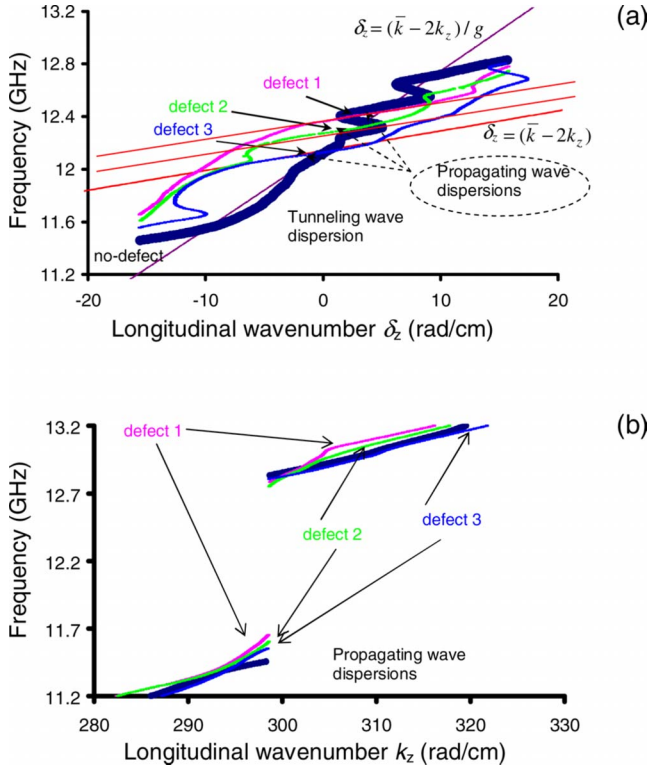

FIG. 4. (Color online) The comparison of the dispersion diagrams of the periodic structures with defects (thin lines) and without (bold lines) in the wave number ranges (a) [−20;20] and (b) [280, 330]. The straight red lines in (a) indicate the gradient of the dispersions associated with waves propagating through the band gap due to the presence of the pass band and the brown line indicates the gradient of the dispersion associated with the tunneled wave.

Bragg frequency. This indicates a change in the wave's properties during the tunneling through such a barrier unless it has a specific Bragg frequency defined by the lattice.

To compare the properties of the propagating and tunneling photons, a zero length defect inside the 1D periodic structure has been introduced and its influence on the band gap parameters has been studied in the 11.0–13.5 GHz frequency range. In Fig. 3 the transmission coefficients versus frequency [Fig. 3(a)] as well as the results of the phase measurements [Fig. 3(b)] are shown. The transmission profiles and the frequency dependence of the phase illustrate the presence of pass bands associated with the defect, as well as strong dependence of the pass band location on the value of the defect's refractive index. The variation in the defect refractive index results in a frequency shift in the pass band position [Fig. 3(a)] and alteration of the waves' dispersions [Fig. 4(a)]. Although the lines of the dispersions associated with the pass bands are frequency shifted, it is clear that the dispersions are parallel to each other [Fig. 4(a)]. Analyzing the data the difference between the waves propagating through the pass band and the waves tunneling through the barrier [Fig. 4(a) compared with Fig. 2(c)] can be observed. Indeed, the gradients of the dispersion characteristics [Fig. 4(a)] outside the pass bands coincide well with the gradient of the dispersion of the lattice without the defect [Fig. 2(c)], while the gradients of the dispersions inside the pass band (parallel and frequency shifted lines) are the same as the gradient of the dispersion of the wave propagating in a smooth waveguide. Let us note that to obtain the straight lines [Fig. 4(a)], which fit with the dispersion inside the pass band, the expression $\delta_z=(\bar{k}-2k_z)$ was used. In contrast $\delta_z=(\bar{k}-2k_z)/g$, where g is a constant approximately equal to 4, was used to observe the line that either fits with the dispersion inside the band gap [Fig. 2(c)] or is parallel (having the same gradient) in the case of the lattices with the localized defect [Fig. 4(a)]. Analyzing the dispersion diagrams the boundaries between the pass band and the band gap as well as the center of the pass band can be defined.

To conclude, 1D band gap structures were investigated, with the results of the experimental studies presented and discussed. We demonstrate that the dispersion of the wave tunneling through the barrier is different from the dispersion of the wave propagating through the lattice due to a pass band, allowing us to distinguish two different phenomena. It is demonstrated that the gradient of the dispersions associated with the wave that have tunneled through the band gap is larger as compared with the gradient of the dispersions associated with the wave propagating through the lattice due to the presence of the pass band and can be used to differentiate the waves. The analysis of the dispersion characteristics allows one to define the boundaries of the band gaps and pass bands as well as the position of the defect eigenmodes (pass band center). It is demonstrated that the dispersion diagrams provide information about lattice structure and can be used to identify the characteristics of lattice defects such as refractive index via analysis of pass band location, which strongly depends on the variation in the defect refractive index. We have to stress that we did not demonstrate superluminal behavior of wave tunneling through the band gap as the dispersion's gradient in this case cannot be considered as an energy propagation velocity.

The authors thank EPSRC, U.K., for their support.

[1]M. Büttiker and S. Washburn, Nature (London) **422**, 271 (2003).
[2]H. G. Winful, Proc. SPIE **6664**, 66640C (2007).
[3]S. Doiron, A. Hache, and H. G. Winful, Phys. Rev. A **76**, 023823 (2007).
[4]H. Kogelnik and C. V. Shank J. Appl. Phys. **43**, 2327 (1972); D. C. Flanders, H. Kogelnik, R. V. Schmidt, and C. V. Shank, Appl. Phys. Lett. **24**, 194 (1974); H. G. Winful, *ibid.* **46**, 527 (1985).
[5]A. M. Steinberg, P. G. Kwait, and R. Y. Chiao, Phys. Rev. Lett. **71**, 708 (1993); T. E. Hartman, J. Appl. Phys. **33**, 3427 (1962); M. Palomino-Ovando, H. A. Coyotecatl, R. Esquivel-Sirvent, and G. H. Cocoletzi, Phys. Lett. A **267**, 429 (2000); Ch. Spielmann, R. Szipöcs, A. Stingl, and F. Krausz, Phys. Rev. Lett. **73**, 2308 (1994); A. B. Shvartsburg, M. Marklund, G. Borodin, and L. Stenflo, Phys. Rev. E **78**, 016601 (2008).
[6]H. G. Winful, Phys. Rev. A **76**, 057803 (2007).
[7]S.-H. Kim and C. G. Fonstad, IEEE J. Quantum Electron. **QE-15**, 1405 (1979); R. D. Meade, K. D. Brommer, A. M. Rappe, and J. D. Joannopoulos, Phys. Rev. B **44**, 13772 (1991); L. I. Deych, A. Yamilov, and A. A. Lisyansky, Europhys. Lett. **46**, 524 (1999).
[8]I. V. Konoplev, P. McGrane, A. D. R. Phelps, A. W. Cross, and K. Ronald, Appl. Phys. Lett. **87**, 121104 (2005); I. V. Konoplev, P. McGrane, A. W. Cross, K. Ronald, and A. D. R. Phelps, J. Appl. Phys. **97**, 073101 (2005); I. V. Konoplev, G. Doherty, A. W. Cross, A. D. R. Phelps, and K. Ronald, Appl. Phys. Lett. **88**, 111108 (2006); I. V. Konoplev, P. MacInnes, A. W. Cross, A. D. R. Phelps, and K. Ronald, *ibid.* **91**, 171107 (2007).
[9]E. Yablonovitch, Phys. Rev. Lett. **58**, 2059 (1987); S. Lan, S. Nishikawa, Y. Sugimoto, N. Ikeda, K. Asakawa, and H. Ishikawa, Phys. Rev. B **65**, 165208 (2002); V. I. Kopp and A. Z. Genack, Phys. Rev. Lett. **89**, 033901 (2002); O. Painter, R. K. Lee, A. Scherer, A. Yariv, J. D. O'Brien, P. D. Dapkus, and I. Kim, Science **284**, 1819 (1999); O. Cohen, B. Freedman, J. W. Fleischer, M. Segev, and D. N. Christodoulides, Phys. Rev. Lett. **93**, 103902 (2004).
[10]G. Burt, S. V. Samsonov, K. Ronald, G. G. Denisov, A. R. Young, V. L. Bratman, A. D. R. Phelps, A. W. Cross, I. V. Konoplev, W. He, J. Thomson, and C. G. Whyte, Phys. Rev. E **70**, 046402 (2004).

Surface wave Cherenkov maser based on a periodic lattice

I. V. Konoplev,[a] L. Fisher, A. W. Cross, A. D. R. Phelps, K. Ronald, and C. W. Robertson
Department of Physics, SUPA, University of Strathclyde, Glasgow G4 0NG, United Kingdom

(Received 18 December 2009; accepted 12 April 2010; published online 28 June 2010)

The excitation of a surface wave cavity based on a two-dimensional periodic structure by an energy source, such as relativistic electrons, results in stimulated, single frequency coherent emission. A high-Q cavity has been achieved via a resonant coupling between surface waves and volume waves. The concept of a Cherenkov maser based on the surface wave cavity is discussed and results of numerical studies presented. Links between the model described and the concept of a surface plasmon amplifier, which has been recently introduced are described. © *2010 American Institute of Physics*. [doi:10.1063/1.3456618]

The intensive studies of periodic structures have resulted in the development of guiding materials, cavities, and active devices,[1–7] which operate in the gigahertz (GHz), terahertz (THz), and near-infrared frequency range. In 2003 a concept known as a "Spaser"[4] was introduced and later developed by Zheludev *et al.*[6] It was suggested that a periodic set of split-ring resonators should ensure spatial and temporal coherence of radiation, if driven by an external source of radiation via resonance coupling of surface and volume waves via induced electric currents. In our work this concept has been further developed and we propose using two-dimensional (2D) periodic corrugations instead of split-ring resonators to form the interaction region. In this case the single element of the corrugation (the elementary cell of the periodic surface) is a single mode cavity which can be described by either using a lumped element circuit (i.e., LCR-circuit) approximation, or a coupled-waves method. Such structures are compatible with a broad variety of active media, including relativistic electron beams and plasmas. It is expected that the external source will initially generate incoherent radiation at the noise level. However, the surface fields, defined by the periodic lattice and excited by the noise radiation are resonantly coupled with a near cut-off volume wave resulting in mode and frequency selection, energy storage inside the cavity and stimulation of the coherent emission from the active medium. We demonstrate that such a maser based on grating radiation[8–12] is capable of producing coherent high-power (megawatt) output radiation in the high-GHz (low-THz) frequency range, which is very attractive for a number of applications.[9] We show the possibility of scaling the device to the THz frequency range using the relation which links the cavity parameters, output radiation frequency and electron beam energy. The results of the study of the cavity based on a 2D periodic lattice[12–14] are discussed and we suggest that its implementation will improve the operation of the Cherenkov maser.

Let us consider a surface wave (SW) cavity defined by a 2D periodic lattice [Fig. 1(a)] created on the inner surface of a cylindrical waveguide. The lattice can be described as[12–14] $r=r_0+r_1 \cos \bar{k}_z z \cos \bar{m}\phi$, where r_0 is the mean radius of the waveguide, $\bar{k}_z=2\pi/d_z$, d_z is the structure's longitudinal period and $\bar{m}$ is the number of the structure's azimuthal variations. The cavity excitation and wave coupling on the corrugation takes place in the following stages: in the first stage the excitation of periodic surface currents around a single-cell cavity occurs due to the incident electromagnetic (EM) field [Fig. 1(a)]. In the second stage only the inductively coupled surface currents collectively interact with EM waves ensuring excitation of coherent localized SWs. Figure 1(a) demonstrates the excitation of surface currents $I_{n,x}$ (x-projection of the I_n, first figure), $I_{n,z}$ (z-projection of the I_n second figure) on the periodic lattice. The contour plots demonstrate the current distributions and polarity on the cavity C_j surface, while the arrows indicate the direction of current flow. The figures were obtained using the three-dimensional (3D) EM code Computer Simulation Technology (CST) Microwave Studio. The surface current flows [Fig. 1(a)] ensure the coupling between the cavities C_j (inductive coupling) and the localized SWs inside an individual cavity cell allowing coherent and collective interaction between the cavities similar to that observed in Refs. 5 and 6. In the third stage the energy stored in the resonantly coupled (via surface cur-

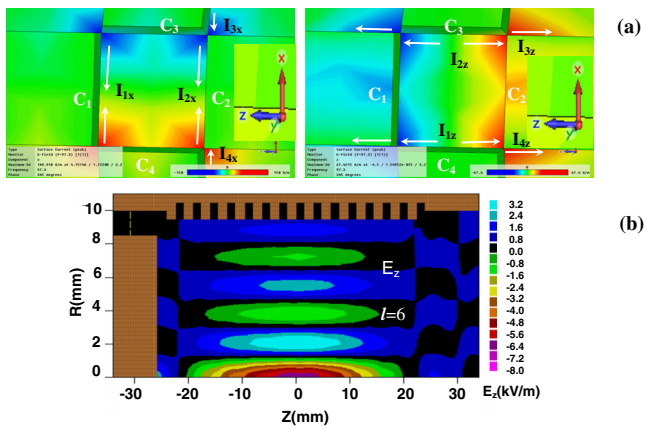

FIG. 1. (Color online) (a) Excitation of surface currents I_j ($j=1,2,\ldots$) on the periodic lattice surface which ensure the coupling between cavity cells C_j observed using the 3D code CST Microwave Studio. The figures are contour plots which demonstrate surface current flow projections on the x and z axes. (b) 2D contour plot of the E_z field component associated with the "volume" field of the cavity eigenmode having six radial variations and excited by a TEM wave pulse of the coaxial waveguide (the figure observed using 3D code MAGIC).

[a]Author to whom correspondence should be addressed. Electronic mail: ivan.konoplev@strath.ac.uk. Tel.: +44(0)-141-548-5818. FAX: +44-141-552-2891.

rents) surface and volume fields [Figs. 1(a) and 1(b)] is radiated from the cavity due to diffraction. In the previous models considered[5,6] the SWs coupled to the propagating wave result in direct scattering, i.e., energy loss into radiation. We suggest coupling the SWs to a near cut-off wave ensuring the energy storage in the cavity, while the parasitic modes will be scattered into propagating waves, which radiate from the large volume cavity. The cavity eigenmode (superposition of localized surface and near cut-off waves) stays in the cavity, thereby increasing its intensity and thus energy exchange between the EM fields and the active media resulting in stimulated radiation being observed.

To describe the transverse structure of the surface localized wave, the field inside a single local cell of the periodic structure can be represented as a superposition of E and H surface modes of the cylindrical waveguide. Taking into account the periodicity of the structure along the z coordinate the Fourier field decomposition can be applied

$$\begin{pmatrix} E_z \\ H_z \end{pmatrix} = J_{\bar{m}}(k_\perp r)\begin{pmatrix} \sin \bar{m}\varphi \\ \cos \bar{m}\varphi \end{pmatrix} \sum_{n=-\infty}^{\infty} \begin{pmatrix} E_n(z) \\ H_n(z) \end{pmatrix} e^{in\bar{k}_z z} e^{-i\omega t}, \quad (1)$$

where E_z and H_z are the longitudinal field components, n is the harmonic number, $k_\perp$ is the transverse wave number which can be imaginary, $J_m(x)$ is the Bessel function of order m, E_n and H_n are the amplitudes of the harmonics.

The resonant coupling between the surface and volume wave takes place if the Bragg resonance conditions $\vec{\bar{k}}=\vec{k}_s-\vec{k}_v$ are satisfied, where $\vec{\bar{k}}$ is the lattice reciprocal vector and $\vec{k}_{s,v}$ are the eigenvectors of the surface (subscript s) and volume (subscript v) waves. Considering these conditions one finds that an azimuthally symmetric volume wave with zero azimuthal variation and zero longitudinal wave vector ($k_{zv} \cong 0$) will be excited if $m=\bar{m}$ and $k_{zs}=\bar{k}_z$ where k_{zs} is the wave number of the cavity surface field first harmonic. This means that the volume field defined by $E_z=E_0J_0(k_{\perp v}r)$ have l radial variations such that $k_{\perp v}=\chi_l^v/r_0$, where χ_l^v is the l-th root of the Bessel function and $k_{\perp s}=k_{\perp v}$.

For the specific model used ($r_0=10$ mm, $r_1=0.5$ mm, and $\bar{m}=16$), the volume wave has the structure of a $TM_{0,6}$ mode of the cylindrical waveguide, while the SW is associated with the $EH_{16,1}$ wave. The structure's parameters were chosen to operate at around 90 GHz and to model the field evolution inside the cavity the 3D software package MAGIC was used. The cavity was excited via a coaxial coupler [Fig. 1(b)] using a frequency chirped pulse of 7 ns duration, having a flat spectrum from 80 to 100 GHz [Fig. 2(a)] and formed by the fundamental TEM wave of a coaxial waveguide. After a transition time of 3.5 ns, which allows nonresonant components to be radiated from the cavity, the field structure inside the cavity was analyzed. The frequency spectrum observed consisted of two spikes associated with the cavity eigenmodes as shown in Fig. 2(a). The two modes' separation was approximately 10 GHz, which is large enough to avoid any mode competition. Using the observed data the Q-factors of these modes were found to be around 2500. The contour plots of the E_z [Figs. 1(b) and 2(b)] and B_z [Fig. 2(c)] field components are shown. It is easy to see the 16 azimuthal variations of the SWs associated with the $EH_{16,1}$ mode and the six radial variations associated with the $TM_{0,6}$ wave.

The numerical modeling (Fig. 3) of the maser based on a

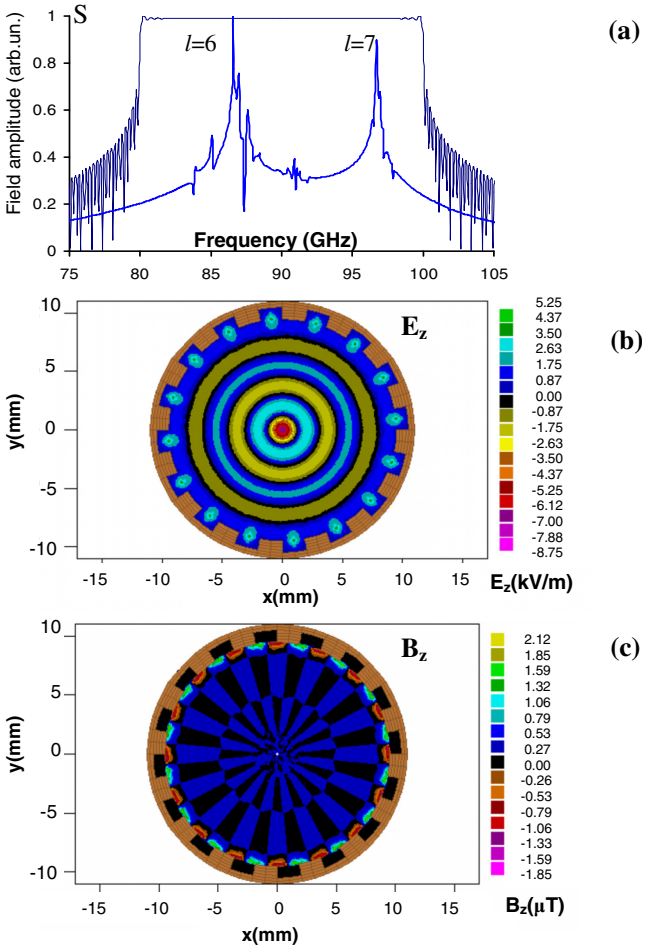

FIG. 2. (Color online) (a) The spectra of the 7 ns input pulse (thin line) and longitudinal electric field (solid line) measured on the cavity's axis in the time frame (10–30 ns) having length 4.8 cm. The spikes are the cavity eigenmodes having radial indices $l=6$ and $l=7$. The contour plots of the longitudinal (b) electric (E_z) and (c) magnetic (B_z) components of the field inside the cavity observed using the 3D code MAGIC.

SW cavity was carried out using the 3D PiC code MAGIC. To observe the lasing, the cavity has been driven by a relativistic (300 kV), high current (1.6 kA) electron beam of annular geometry[15] (mean radius-8.6 mm, radial thickness-1 mm). The electrons propagating in the vicinity of the lattice behaved as a set of oscillating dipoles having a frequency $\Omega_{\text{eff}}=2\pi v_z/d_z$ (v_z is the axial velocity of the electrons, d_z is the corrugation period). These dipoles excite an EH mode inside each single cavity cell of the lattice, resulting in a surface field having an azimuthal variation number equal to the number of lattice azimuthal variations (Smith–Purcell or grating radiation).[8–12] To observe a resonant interaction between the electron beam and the EM fields the synchronism condition $\omega-k_zv_z=n\Omega_{\text{eff}}$ has to be met, where ω is the angular frequency of the EM wave. Taking into account that $k_z \approx 0$ and $n=1$ the relations between the operating wavelength λ, the lattice parameter d_z and the electron beam accelerating voltage U_e can be derived: $U_e(\text{kV}) \approx 511(\text{kV}) \times [\sqrt{\lambda^2/(\lambda^2-d_z^2)}-1]$. A detuning of the period d_z from the optimum value defined by the relation above resulted in a reduction in the maser efficiency and no interaction was observed outside the region of effective wave coupling i.e., if d_z was strongly detuned from the resonance condition. This expression shows the possibility of tuning the device to operate at high frequencies. For instance if the desired operating fre-

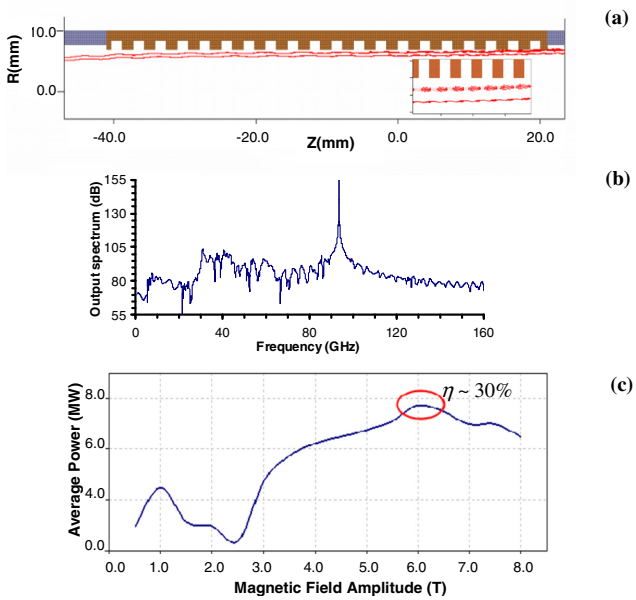

FIG. 3. (Color online) Results of numerical studies showing: (a) the relativistic electron beam trajectories with strong interaction between the electrons and SW manifesting itself in electron density wave formation (insets); (b) the output spectrum showing operation at ~97 GHz; and (c) the variation in average output power with magnetic field amplitude.

quency is 0.395 THz ($\lambda \sim 0.76$ mm), the electron beam has an accelerating voltage of ~51 kV and current of 40 A, then the structure parameters are as follows: diameter 10 mm, length ~14.4 mm, period $d_z \sim 0.32$ mm, number of azimuthal variations is 40. We note that the maser considered in this paper differs from devices studied in Refs. 3 and 8–12. Thus the beams[8,9] propagate through volume structures limiting the output power and the device lifetime, while in the model described here the beam propagates above the surface lattice allowing high-power output radiation to be produced. Also the structure's topology and beam's parameters are different. We note that the interaction region of the maser considered has some similarities with the gyrotron cavity,[16] while the maser interaction is driven by the Cherenkov instability.

At the beginning of the interaction the SWs ($EH_{16,1}$) are excited and couple with the $TM_{0,6}$ wave. The superposition of both fields forms the cavity eigenmode and ensures effective energy accumulation. The lasing takes place due to diffraction of the $TM_{0,6}$ wave while the $EH_{16,1}$ wave interacts with electrons and synchronizes the energy extraction from the different parts of the beam. Figure 3(a) shows the electron beam trajectory inside the interaction region indicating a dependence of the wave-beam coupling on the distance between the beam and the structure (see the inset). An interaction between the electron beam and the E_z component of the EM field manifests itself in the formation of the electron density wave which as expected increases along the interaction region. In Fig. 3(b) the spectrum of the output radiation is shown and a single mode operation at a single frequency of 97 GHz is demonstrated. The dependence of the output power on the guide magnetic field strength was also studied and the variation in the efficiency versus guide magnetic field is presented in Fig. 3(c). To observe an efficiency of 30% the guide field should be ~6 T, at a moderate strength of 2 T an efficiency of 15% was achieved.

The implementation of an oversized (in comparison with the operating wavelength) SW cavity based on a 2D surface lattice allows effective mode selection to be achieved along the longitudinal and the transverse indices resulting in a single mode, single frequency, and steady state operation of a high-power Cherenkov maser. The numerical simulations have shown that the resonant coupling of localized surface and volume waves allows the problems associated with mode and frequency purity common for such devices to be overcome. Mode selection and control along the radial and azimuthal indices has been achieved ensuring stable high-power maser operation. The application of a 2D periodic lattice allows oversized structures to be used to define the interaction region of masers operating in the high-GHz and THz frequency range, making manufacturing of such a structure, as well as beam transportation feasible and overcoming some of the challenges listed in Ref. 17. We also suggest that cylindrical lattices can form the interaction region of oscillators based on different active media.

The authors thank the EPSRC (Grant No. EP/E058868/1) for research support and the UK Faraday Partnership in High Power rf for providing the MAGIC code.

[1]A. Ishikawa, S. Zhang, D. A. Genov, G. Bartal, and X. Zhang, Phys. Rev. Lett. **102**, 043904 (2009).
[2]A. V. Zayats, I. I. Smolyaninov, and A. A. Maradudin, Phys. Rep. **408**, 131 (2005); W. L. Barnes, J. Opt. A, Pure Appl. Opt. **8**, S87 (2006); M. A. Shapiro, K. R. Samokhvalova, J. R. Sirigiri, R. J. Temkin, and G. Shvets, J. Appl. Phys. **104**, 103107 (2008); D. L. Mills and A. A. Maradudin, Phys. Rev. B **39**, 1569 (1989).
[3]V. L. Bratman, G. G. Denisov, M. M. Ofitserov, S. D. Korovin, S. D. Polevin, and V. V. Rostov, IEEE Trans. Plasma Sci. **15**, 2 (1987).
[4]D. J. Bergman and M. I. Stockman, Phys. Rev. Lett. **90**, 027402 (2003).
[5]V. A. Fedotov, M. Rose, S. L. Prosvirnin, N. Papasimakis, and N. I. Zheludev, Phys. Rev. Lett. **99**, 147401 (2007).
[6]N. I. Zheludev, S. L. Prosvirnin, N. Papasimakis, and V. A. Fedotov, Nat. Photonics **2**, 351 (2008).
[7]S. Kim, J. Jin, Y.-J. Kim, I.-Y. Park, Y. Kim, and S.-W. Kim, Nature (London) **453**, 757 (2008).
[8]F. S. Rusin and G. D. Bogomolov, Radiophys. Quantum Electron. **11**, 430 (1968).
[9]Yu. A. Grishin, M. R. Fuchs, A. Schnegg, A. A. Dubinskii, B. S. Dumesh, F. S. Rusin, V. L. Bratman, and K. Möbius, Rev. Sci. Instrum. **75**, 2926 (2004); V. L. Bratman, V. A. Gintsburg, Yu. A. Grishin, B. S. Dumesh, F. S. Rusin, and A. E. Fedotov, Radiophys. Quantum Electron. **49**, 866 (2006); V. L. Bratman, P. B. Makhalov, A. E. Fedotov, and I. M. Khaimovich, *ibid.* **50**, 780 (2007).
[10]G. S. Nusinovich, Phys. Plasmas **13**, 053107 (2006); G. S. Nusinovich and O. V. Sinitsyn, *ibid.* **13**, 123104 (2006).
[11]N. I. Zaitsev and N. F. Kovalev, Radiophys. Quantum Electron. **29**, 180 (1986); N. S. Ginzburg, N. A. Zavolskii, V. E. Zapevalov, M. A. Moiseev, and Yu. V. Novozhilova, Tech. Phys. **45**, 480 (2000).
[12]N. E. Glass, Phys. Rev. A **36**, 5235 (1987).
[13]I. V. Konoplev, P. McGrane, W. He, A. W. Cross, A. D. R. Phelps, C. G. Whyte, K. Ronald, and C. W. Robertson, Phys. Rev. Lett. **96**, 035002 (2006); I. V. Konoplev, A. W. Cross, A. D. R. Phelps, W. He, K. Ronald, C. G. Whyte, C. W. Robertson, P. MacInnes, N. S. Ginzburg, N. Yu. Peskov, A. S. Sergeev, V. Yu. Zaslavsky, and M. Thumm, Phys. Rev. E **76**, 056406 (2007).
[14]A. W. Cross, I. V. Konoplev, A. D. R. Phelps, and K. Ronald, J. Appl. Phys. **93**, 2208 (2003); I. V. Konoplev, A. D. R. Phelps, A. W. Cross, and K. Ronald, Phys. Rev. E **68**, 066613 (2003).
[15]I. V. Konoplev, A. W. Cross, P. MacInnes, W. He, C. G. Whyte, A. D. R. Phelps, C. W. Robertson, K. Ronald, and A. R. Young, Appl. Phys. Lett. **89**, 171503 (2006).
[16]N. F. Kovalev, Yu. V. Novazhilova, and M. I. Petelin, Radiophys. Quantum Electron. **50**, 794 (2007).
[17]J. H. Booske, Phys. Plasmas **15**, 055502 (2008).

Surface-field cavity based on a two-dimensional cylindrical lattice

I. V. Konoplev,[1,a)] L. Fisher,[1] K. Ronald,[1] A. W. Cross,[1] A. D. R. Phelps,[1] C. W. Robertson,[1] and M. Thumm[2]
[1]*Department of Physics, SUPA, University of Strathclyde, Glasgow G4 0NG, United Kingdom*
[2]*Institute for Pulsed Power and Microwave Technology (IHM) and Institute of High Frequency Techniques and Electronics (IHE), Karlsruhe Institute of Technology (KIT), Karlsruhe D-76131, Germany*

(Received 26 March 2010; accepted 21 April 2010; published online 9 June 2010)

The results of theoretical and experimental studies of a high-Q cavity based on a cylindrical, periodic lattice are presented. The coupling of localized surface and volume electromagnetic fields results in cavity mode selection over radial, azimuthal, and longitudinal indices and formation of a high-Q cavity eigenmode. Numerical analyses of the field evolution inside the cavity were carried out. Application of these two-dimensional periodic structures in the development of high-power terahertz masers is proposed. © *2010 American Institute of Physics*. [doi:10.1063/1.3428776]

Understanding the properties of electromagnetic fields within periodic structures that are oversized in comparison with the radiation wavelength is an important and challenging problem for modern science and such studies have already resulted in the development of breakthrough ideas.[1–8] For example in 2003 a concept of a surface plasmon amplifier was introduced and is an ongoing area of research.[7–11] Let us note that in the works[7–10] nanoshells and nanowires were used to form the interaction region, with localized fields tightly coupled to the surface of the particles. In our work we consider the "inverted model" of the structures studied in Refs. 7–10, i.e., surface fields inside the structure are investigated and are coupled to the corrugated inner surface of the cylindrical metal waveguide. The structure studied was made from an oversized (in comparison with an operating wavelength λ) cylindrical, copper waveguide with a two-dimensional (2D) corrugation of the inner wall. The corrugation supports localized surface fields mitigating the field bonding to the metal surface of the waveguide. The structure is a high-Q cavity in which excitation takes place in three stages. In the first stage the excitation of surface currents around an elementary cell of the periodic surface by the incident electromagnetic field occurs. Then the inductively coupled surface currents are interacting collectively ensuring excitation of a coherent surface field (decaying toward the center of the structure). In the third stage the energy stored in the surface fields is coupled into the propagating waves, which ensures mode selectivity due to scattering and diffraction allowing a high-Q cavity to be observed. In this paper the coupling between localized surface (having imaginary transverse wavenumber) and volume (having real transverse wavenumber) fields on the surface of the cylindrical 2D periodic lattice[12–15] is studied and the results observed are discussed. The coupling of the localized surface fields to a near cut-off wave is demonstrated and excitation of a high-Q cavity eigenmode due to such a coupling is investigated. We suggest that implementation of such a cavity will improve the efficiency and stability of masers operating in the terahertz (THz) frequency range. The limitations of such structures and ways to overcome these limits are discussed.

The surface wave cavity (Fig. 1) can be formed for instance from a cylindrical copper waveguide by machining small periodic perturbations on the inside of the wall ($\Delta r \ll \lambda$) such that: $r = r_0 + \Delta r \cos \bar{k}_z z \cos \bar{m}\phi$. Here, r_0 is the mean radius of the unperturbed waveguide, $\bar{k}_z = 2\pi/d_z$ is the longitudinal wave number of the structure, and $\bar{m}$ is the number of azimuthal variations around the structure. The structure was constructed using electrochemical copper deposition on an aluminum mandrel which was dissolved later in alkaline solution. Let us note that a large diameter structure such that $r_0 \gg d_z$ and $r_0 \gg \lambda$ is studied in the experiment allowing a "square wave," chessboard structure to be used in the numerical model as an approximation[12–15] of the lattice shown in Fig. 1. The field of the cavity eigenmode outside the periodic corrugation (i.e., $r \leq r_0 - \Delta r$) can be represented as a superposition of surface and volume (subscripts "*s*" and "*v*") partial fields the transverse structures of which coincide with the transverse structures of the eigenmodes of the unperturbed cylindrical waveguide.[12–15] The surface fields have imaginary transverse wavenumbers while the volume, near cut-off, fields have zero longitudinal and real transverse wavenumbers. The transverse structure of the surface fields can be described as a superposition of E and H

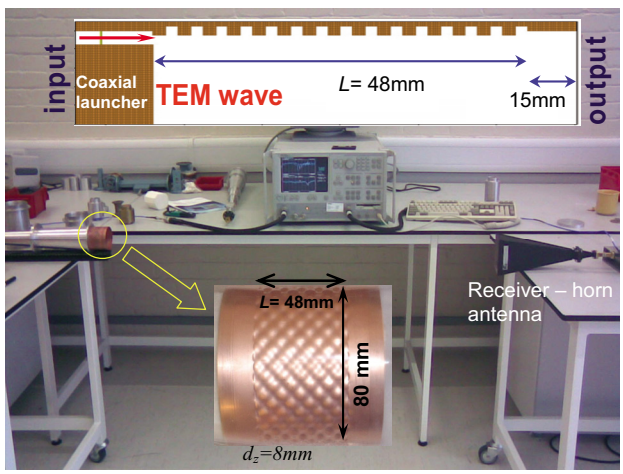

FIG. 1. (Color online) Photograph of the experimental setup and cylindrical 2D periodic structure (inset) which forms the cavity having diameter 80 mm, corrugation depth 1 mm, 28 azimuthal variations and longitudinal period of 8 mm.

[a)]Author to whom correspondence should be addressed. Electronic mail: ivan.konoplev@strath.ac.uk. Tel.: +44(0)-141-548-5818. FAX: +44-141-552-2891.

surface modes and taking into account the periodicity of the structure the Fourier field decomposition can be applied:

$$\begin{pmatrix} E_z \\ H_z \end{pmatrix} = I_{m_s}(k_{\perp s} r) \begin{pmatrix} \sin m_s \varphi \\ \cos m_s \varphi \end{pmatrix} \sum_{n=-\infty}^{\infty} \begin{pmatrix} E_n(z) \\ H_n(z) \end{pmatrix} e^{in\bar{k}_z z} \quad (1)$$

where E_z, H_z are the longitudinal field components, n is the harmonic number, $k_{\perp s}$ is the transverse wave number, $I_m(x)$ is the modified Bessel function of order m indicating field decay along x, and $E_n(z)$ and $H_n(z)$ are the slowly varying amplitudes of the field harmonics. The surface and volume field coupling takes place on the surface of the lattice allowing the approximate analysis of the cavity behavior, without the need for detailed analysis of the surface field inside the corrugation, which has a more complex structure and its study is outside the scope of this paper. The surface wave is coupled to the near cut-off TM_{0l} volume wave described by $E_z = J_0(k_{\perp v} r) \Sigma_{n=-\infty}^{\infty} E_n^v(z) e^{in\bar{k}_z z}$ where l is the number of radial variations, $k_{\perp v}$ is the transverse wavenumber, and $J_m(x)$ is the Bessel function of order m. The resonant coupling between partial fields takes place if the Bragg resonance condition $\vec{\bar{k}} = \vec{k}_s - \vec{k}_v$ is satisfied, where $\vec{\bar{k}}$ is the lattice reciprocal vector, and $\vec{k}_{s,v}$ are the surface "s" and volume "v" wave vectors. As a result one notes that a volume wave with zero azimuthal variation and zero longitudinal wave vector ($k_{zv} \cong 0$, near cut-off wave) will be excited, if $k_{zs} = \bar{k}_z$ (first harmonic) and the number of the surface field azimuthal variations is $m_s = \bar{m}$. The volume field will have l radial variations such that $k_{\perp v} = \chi_l^v / r_0$ where χ_l^v is the l^{th} root of the Bessel function of zero order and the frequency of the cavity eigenmodes ω_r having the highest Q-factor ($k_{zv} \cong 0$) can be estimated as $\omega_r = c k_{\perp v}$. Taking into account that $k_{\perp s} = i\sqrt{(\omega/c)^2 - k_{zs}^2}$ and $\bar{k}_z \geq \omega/c$ one notes that the first harmonic of the surface wave is decaying spatially from the periodic surface as $I_{\bar{m}}(k_{\perp s} r_0)$ demonstrating one of the conventional[2] surface structure's limitations to creating a large aperture ($k_{\perp s} r_0 \gg 1$) Cherenkov maser which is driven by an electron beam. The field decay results in a weak coupling between the field and the electron beam if $2k_{\perp s} r_0 \leq 1$ is not satisfied. To overcome this limit, relativistic electron beams are used in conventional devices[2] leading to $\bar{k}_z \to \omega/c$ and thus $k_{\perp s} r_0 \to 0$. In the structure investigated the coupling of the surface fields and near cut-off propagating wave allows electromagnetic energy accumulation[16] thus relaxing the condition on the beam-lattice proximity. To illustrate this one may introduce an effective surface at a radius, r_e, on which the impedances of the partial waves are matched and r_e can be defined by the equation:

$$k_{\perp s}[I_{\bar{m}}(k_{\perp s} r_e)/I'_{\bar{m}}(k_{\perp s} r_e)] = k_{\perp v}[J_0(k_{\perp v} r_e)/J'_0(k_{\perp v} r_e)], \quad (2)$$

where $I'_{\bar{m}}(x)$ and $J'_0(x)$ are the derivatives ($\partial/\partial x$) of the Bessel functions. The r_e defines the beam radius at which it is still interacting with the surface field harmonic. Assuming that $r_e/r_0 \sim 1$ and applying a Taylor expansion to Eq. (2) the condition under which the electron beam having a relativistic Lorentz factor $\gamma > 1.41$, propagating above the lattice can interact with the surface wave takes the form: $k_{\perp s} r_0 < \bar{m}$, instead of $2k_{\perp s} r_0 \leq 1$ for conventional structures.

The finite-difference time-domain (FDTD) three-dimensional (3D) code MAGIC has been used to calculate the fields in the cavity. In Fig. 2(a) the structures of the E_z and B_z field components associated with the cavity eigenmode having ten radial variations and located at the frequency $f_{28,10,1}$(~37.5 GHz) are shown. One notes that only the E_z component exists in both the surface and volume partial field while the B_z component vanishes toward the center. The spectrum of the cavity eigenmodes excited by a broadband pulse (29–44 GHz) launched in a transverse-electromagnetic (TEM) wave from a coaxial coupler shown in Fig. 1 and calculated using the code MAGIC, is shown in Fig. 2(b). The cavity mode frequencies $f_{m,l,j}$ (m, l, and j are the highest variation numbers of volume and surface partial fields along the φ, r, and z coordinates, respectively) are observed at the frequencies, $f_{28,8,1}$(~30 GHz), $f_{28,9,1}$(~33.8 GHz), $f_{28,10,1}$ (~37.5 GHz), and $f_{28,11,1}$(~41.2 GHz), indicating that increasing the operating frequency results in an increase in the eigenmode radial wavenumber.

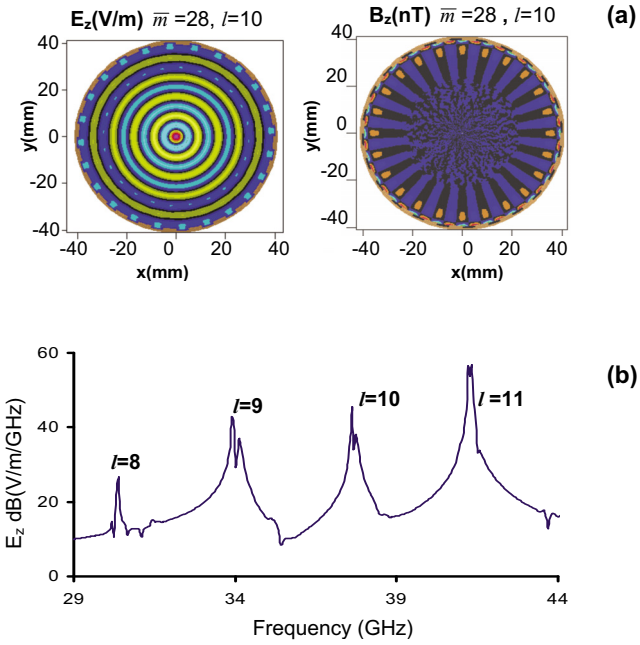

FIG. 2. (Color online) (a) The $r-\varphi$ contour plot of the E_z and B_z field components of the cavity eigenmode. The coupling between the surface and volume field can be seen on the first plot while the second plot shows the surface field decaying toward the cavity center (the plot observed using 3D code MAGIC). (b) Spectra of the cavity eigenmodes (with radial indices $l \in [8-11]$) excited by a broadband [29–44 GHz] pulse formed by the TEM wave.

To study the 2D surface wave cavity experimentally a set up similar to one used for studying coaxial structures[14] has been constructed. A photograph of the set up with an insert showing the structure studied is presented in Fig. 1. The periodic structure [inset to Fig. 1] made of copper has the following parameters: $r_0 = 40$ mm, lattice length 48 mm, $\bar{m} = 28$, $d_z = 8$ mm, and $\Delta r = 0.5$ mm. The experiments were carried out using a vector network analyzer (Fig. 1) with a receiving horn antenna positioned at ~1.2 m distance from the radiating structure. The results observed are shown in Fig. 3. First the receiving detector was positioned centrally (in front of the structure) in the far-field zone and a frequency scan [36–38.5 GHz] was conducted. In Fig. 3(a) the result observed (bold line) is shown in comparison to the same scan performed for a smooth cylindrical waveguide (thin line) of equal length and radius but having no corrugations on the inner surface. The deep minimum in the transmission spectrum is associated with the resonant scattering

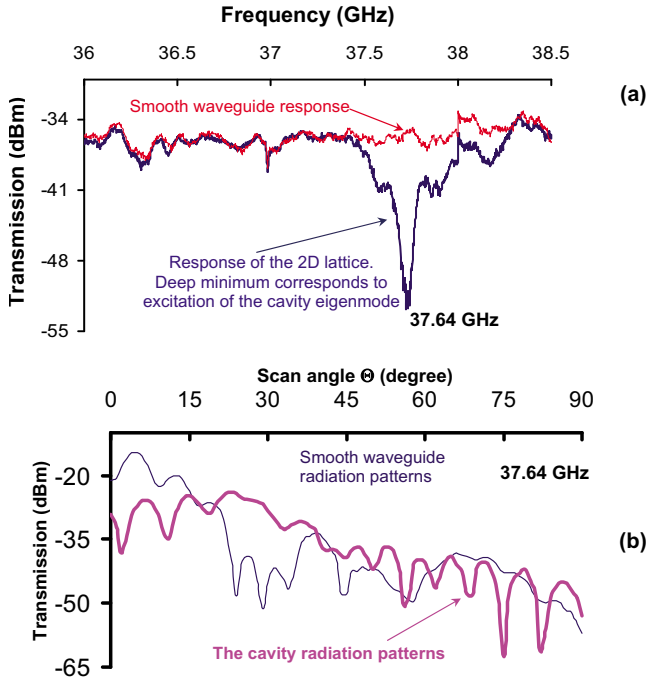

FIG. 3. (Color online) (a) Frequency dependence of the signal transmission through the smooth waveguide (thin line) and the surface field cavity (thick line) measured by the receiving horn antenna at 1.2 m distance from the output [see Fig. 1]. (b) The results of the radiation mode pattern measurements in the far field zone (~1.2 m) from the cavity (thick line) and cylindrical waveguide (thin line).

of the incident wave into surface waves and a near cut-off mode, i.e., excitation of the cavity eigenmode. The results presented resemble those demonstrated in the work of Seymour *et al.*[17] and Zayats *et al.*,[18] where a similar feature in the reflection versus incident angle was reported when surface waves were excited on the metal-dielectric interface. In the case studied in this paper due to a fixed value of the transverse wavenumber (for a specific mode) the frequency variation is similar to the variation in the wave incident angle and the transmission is synonymous with the reflection from the metal-dielectric interface. The excitation of the cavity eigenmode has been also confirmed by analyzing the radiation mode pattern. To conduct the mode pattern scan the horn used in the previous experiments was substituted with a waveguide pick-up probe (to improve the angular resolution). The results of the experimental measurements are shown in Fig. 3(b) (thick line) and compared with the scan when the lattice is substituted with a smooth cylindrical waveguide (thin line). The thin line shows that the radiation from the smooth waveguide consists mainly of low order modes (most of the energy is inside a small solid angle) with a small presence of high order modes. The cavity radiation mode patterns indicate the strong presence of the near cut-off, high-order mode manifesting itself as periodic variations (periodicity ~6°) of the field intensity for observation angles above 45° and much smaller radiation intensity at observation angles below 45°.

In this letter the inverted model of the interaction regions considered in earlier work[7–10] has been studied. The application of the 2D cylindrical lattice allows mode selection along the radial and azimuthal coordinates, as well as energy storage in the combined fields of the volume and surface waves. This allows an interaction region to be formed having a transverse dimension (aperture) much larger than the operating wavelength. We have shown numerically, using the 3D code MAGIC, that the resonant coupling between surface waves and near cut-off waves takes place on the periodic structure surface. The full 3D model was used to allow excitation and evolution of the azimuthally symmetric and nonsymmetric fields to be simulated. The cavity excitation and the mode structure were analyzed. Experimental studies of the structure have been conducted and the measurements agree well with the numerical simulations. The radiation mode pattern has been studied and incident wave resonant scattering on the periodic lattice has been demonstrated. A cavity of this nature is compatible with a broad variety of active media, including relativistic electron beams[19] and plasmas and can be used to ensure the stable operation of high-power terahertz masers. The results obtained provide a strong basis for the concept and design of a high power maser operating in the THz and infrared frequency ranges using a 2D periodic lattice.

One of the authors, L. Fisher, thanks the EPSRC for supporting her PhD studentship. The UK Faraday Partnership in High Power rf provided the MAGIC license.

[1]E. Yablonovitch, Phys. Rev. Lett. **58**, 2059 (1987).
[2]V. L. Bratman, G. G. Denisov, M. M. Ofitserov, S. D. Korovin, S. D. Polevin, and V. V. Rostov, IEEE Trans. Plasma Sci. **15**, 2 (1987).
[3]I. V. Konoplev, P. McGrane, A. D. R. Phelps, A. W. Cross, and K. Ronald, Appl. Phys. Lett. **87**, 121104 (2005); I. V. Konoplev, P. McGrane, A. W. Cross, K. Ronald, and A. D. R. Phelps, J. Appl. Phys. **97**, 073101 (2005).
[4]I. V. Konoplev, A. W. Cross, P. MacInnes, W. He, A. D. R. Phelps, C. G. Whyte, K. Ronald, and C. W. Robertson, Appl. Phys. Lett. **92**, 211501 (2008).
[5]J. B. Pendry, L. Martin-Moreno, and F. J. Garcia-Vidal, Science **305**, 847 (2004).
[6]I. V. Konoplev, A. W. Cross, A. D. R. Phelps, W. He, K. Ronald, C. G. Whyte, C. W. Robertson, P. MacInnes, N. S. Ginzburg, N. Y. Peskov, A. S. Sergeev, V. Y. Zaslavsky, and M. Thumm, Phys. Rev. E **76**, 056406 (2007).
[7]D. J. Bergman and M. I. Stockman, Phys. Rev. Lett. **90**, 027402 (2003).
[8]M. I. Stockman, Nat. Photonics **2**, 327 (2008).
[9]S. A. Maier, S. R. Andrews, L. Martin-Moreno, and F. J. Garcia-Vidal, Phys. Rev. Lett. **97**, 176805 (2006).
[10]D. E. Chang, A. S. Sorensen, P. R. Hemmer, and M. D. Lukin, Phys. Rev. B **76**, 035420 (2007).
[11]N. I. Zheludev, S. L. Prosvirnin, N. Papasimakis, and V. A. Fedotov, Nat. Photonics **2**, 351 (2008).
[12]A. W. Cross, I. V. Konoplev, K. Ronald, A. D. R. Phelps, W. He, C. G. Whyte, N. S. Ginzburg, N. Y. Peskov, and A. S. Sergeev, Appl. Phys. Lett. **80**, 1517 (2002).
[13]N. S. Ginzburg, N. Y. Peskov, A. S. Sergeev, I. V. Konoplev, A. W. Cross, A. D. R. Phelps, G. R. M. Robb, K. Ronald, W. He, and C. G. Whyte, J. Appl. Phys. **92**, 1619 (2002); N. S. Ginzburg, N. Y. Peskov, A. S. Sergeev, A. D. R. Phelps, A. W. Cross, and I. V. Konoplev, Phys. Plasmas **9**, 2798 (2002).
[14]A. W. Cross, I. V. Konoplev, A. D. R. Phelps, and K. Ronald, J. Appl. Phys. **93**, 2208 (2003).
[15]I. V. Konoplev, P. McGrane, W. He, A. W. Cross, A. D. R. Phelps, C. G. Whyte, K. Ronald, and C. W. Robertson, Phys. Rev. Lett. **96**, 035002 (2006).
[16]I. V. Konoplev, L. Fisher, A. W. Cross, A. D. R. Phelps, and K. Ronald, I.E.T. Conference on High Power RF Technologies (Issues CP548), London, 2009.
[17]R. J. Seymour, J. J. Krupczak, and G. I. Stegeman, Appl. Phys. Lett. **44**, 373 (1984).
[18]A. V. Zayats, I. I. Smolyaninov, and A. A. Maradudin, Phys. Rep. **408**, 131 (2005).
[19]I. V. Konoplev, A. W. Cross, P. MacInnes, W. He, C. G. Whyte, A. D. R. Phelps, C. W. Robertson, K. Ronald, and A. R. Young, Appl. Phys. Lett. **89**, 171503 (2006).

High-Current Electron Beams for High-Power Free-Electron Masers Based on Two-Dimensional Periodic Lattices

Ivan V. Konoplev, Philip MacInnes, Adrian W. Cross, Lorna Fisher, Alan D. R. Phelps, Wenlong He, Kevin Ronald, Colin G. Whyte, and Craig W. Robertson

***Abstract*—High-power gigawatt-level radiation can be generated by the interaction of an electromagnetic wave and an annular electron beam with a transverse dimension much larger than the operating wavelength. The use of such a large-circumference annular beam allows the generation of high beam currents while also maintaining low space charge and RF power densities inside the interaction region. This circumvents the problems associated with potential depression in the beam channel and RF breakdown inside the oscillator. In this paper, we present the studies of high-current magnetically confined annular electron beams and discuss their production and transportation through a coaxial beam channel which formed the interaction region of a free-electron maser (FEM). The results from numerical simulations, using the software packages KARAT and MAGIC, are compared with the experimental measurements. The operation of a FEM, driven by a high-current annular electron beam, is presented, and the tunability of the maser, inside a frequency range defined by an input 2-D Bragg mirror, is demonstrated.**

***Index Terms*—Distributed feedback laser, free-electron maser (FEM), high-current electron beam, surface periodic lattice.**

I. Introduction

IT IS WELL known that different devices (such as high-power masers operating in the frequency range from 30 to 300 GHz, masers operating in the terahertz frequency range, and conventional high-Q cavities of linear accelerators) are affected by the common problems of breakdown, associated with the high electromagnetic (EM) field power density, overheating, and electron beam disruption [1]. To overcome these problems, the application of 1-D and two-dimensional (2-D) periodic lattices, either to form an entire high-Q cavity or simply a part of the interaction region, has been considered as a possible solution [2]–[7] for masers and accelerators, although one should note that the solution of these issues for one group of devices may, in turn, lead to breakthroughs in the design in other groups. As a result, interest in devices based on periodic lattices and operating in the frequency range from 30 to 300 GHz has significantly increased in recent years [2]–[9]. The use of 2-D periodic structures in which 2-D distributed feedback can be realized was proposed [6], [7] for application in gigawatt-power-level free-electron masers (FEMs), operating at millimeter wavelengths, to circumvent the problems associated with the high EM power densities present in the interaction regions. This is achieved by ensuring spatiotemporal coherence of the output radiation across a large-size electron beam [6], [7], [11]–[13], where such a beam propagates inside a cavity which has a large transverse dimension with respect to the wavelength of operation. The formation and transportation of a large-size electron beam are an interesting and challenging problem in its own right [14]–[20], due to the necessity of addressing simultaneously the scientific and technological challenges associated with high-energy electron beam production, confinement, and transportation. Let us note that the original and groundbreaking theoretical research [21]–[24] conducted by Prof. N. S. Ginzburg's group at the IAP of the Russian Academy of Sciences laid the basis for theoretical and experimental studies of the application of such Bragg structures in high-power FEMs operating at millimeter wavelength.

In this paper, we discuss an electron beam accelerating system which was used to generate high-current (1.5 kA, 3.5 kA) magnetically confined thin annular electron beams with a circumference of $\sim$220 mm and a wall thickness of $\sim$2 mm. We present the design of an electron beam guiding system which allowed for beam formation and transportation through a 2-m coaxial beam channel, with inner and outer radii of 30 and 40 mm, respectively. The surrounding facilities required to produce such a beam are discussed, and their design is presented, namely, for the high-pulse-power generator, high-current accelerator (HCA), and FEM. The results of the experimental studies of the FEM are discussed with experimental data compared to numerical simulation. It will be shown that, as the electron beam current increased, without adjustment of the FEM cavity parameters, the transition time was reduced as anticipated, although a decrease in FEM efficiency and alteration to the output microwave pulse shape was noted. We demonstrate that a frequency shift in the output radiation spectrum can be achieved by tuning the amplitude of the magnetic field of the undulator.

In Section II, the designs of the pulse power supply, including the Marx generator (MG), the pulse-forming transmission line,

Manuscript received August 11, 2009; revised October 1, 2009, October 13, 2009, and November 16, 2009. First published January 26, 2010; current version published April 9, 2010. This work was supported in part by QinetiQ and in part by EPSRC, U.K.

The authors are with SUPA, Department of Physics, University of Strathclyde, G4 0NG Glasgow, U.K. (e-mail: acp96115@strath.ac.uk; philip.macinnes@strath.ac.uk; a.w.cross@strath.ac.uk; lfisher14@hotmail.com; w.he@strath.ac.uk; k.ronald@strath.ac.uk; c.g.whyte@strath.ac.uk; c.w.robertson@strath.ac.uk).

Color versions of one or more of the figures in this paper are available online at http://ieeexplore.ieee.org.

Digital Object Identifier 10.1109/TPS.2009.2038161

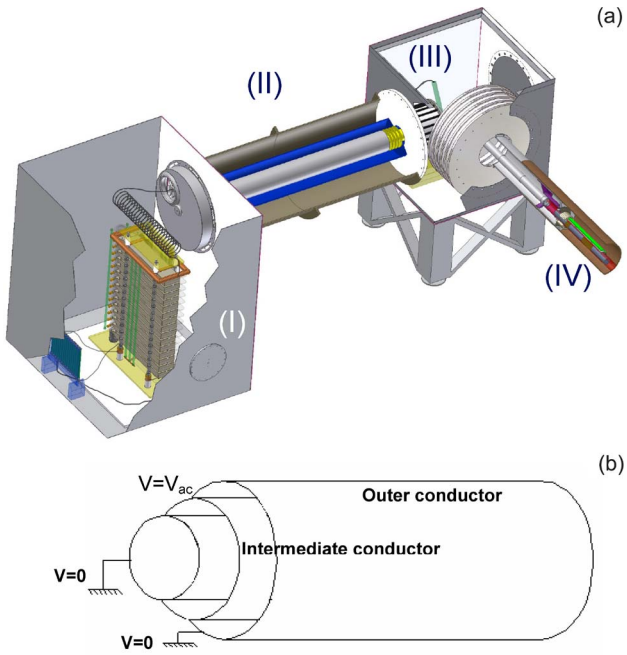

Fig. 1. (a) Schematic diagram of the FEM experimental setup showing (I) MG PPS, (II) deionized-water-filled transmission line, (III) oil tank hosting the spark gap and the HCA, and (IV) cross section of the FEM and guide solenoid. (b) Double-fold transmission line.

and the high-current spark gap, are presented. The dependence of the voltage pulse amplitude on the system parameters of the pulse power supply and components is reported. In Section III, the design of the HCA is shown, and results of the HCA experimental studies are presented. The data observed are compared with numerical simulations conducted using the particle-in-cell (PiC) code KARAT. Section IV is dedicated to the numerical modeling of FEMs based on 2-D distributed feedback. These models were designed and studied using the 3-D PiC code MAGIC. Using the numerical model developed, the particle dynamics are analyzed, and the electron beam evolution inside the interaction region is discussed. The field distribution inside different parts of the interaction region is also studied and compared with the analytical models developed in [6], [7], [12], and [25]. The FEM operating regimes observed in the simulations are discussed, and it is shown that, by varying the cavity and beam parameters, it is possible to observe single-mode, as well as multimode, oscillations. The design of the FEM cavities to realize single-mode steady-state operation and high efficiency is discussed. In Section V, experimental data, observed from studies of FEMs driven by 1.5- and 3.5-kA electron beams, are presented. A shift in the FEM operating frequency with variation of undulator parameters is shown. We demonstrate that increasing the electron beam current, while keeping the cavity parameters constant, results in a decrease in the FEM efficiency and a deterioration of the output pulse shape [25]. The frequency of the output radiation was also analyzed, first using cutoff filters and then more accurately using a heterodyne frequency diagnostic. Measurements of the output signal spectrum are shown and discussed. In the last section, conclusions are presented, and future work and development of the experiment are discussed.

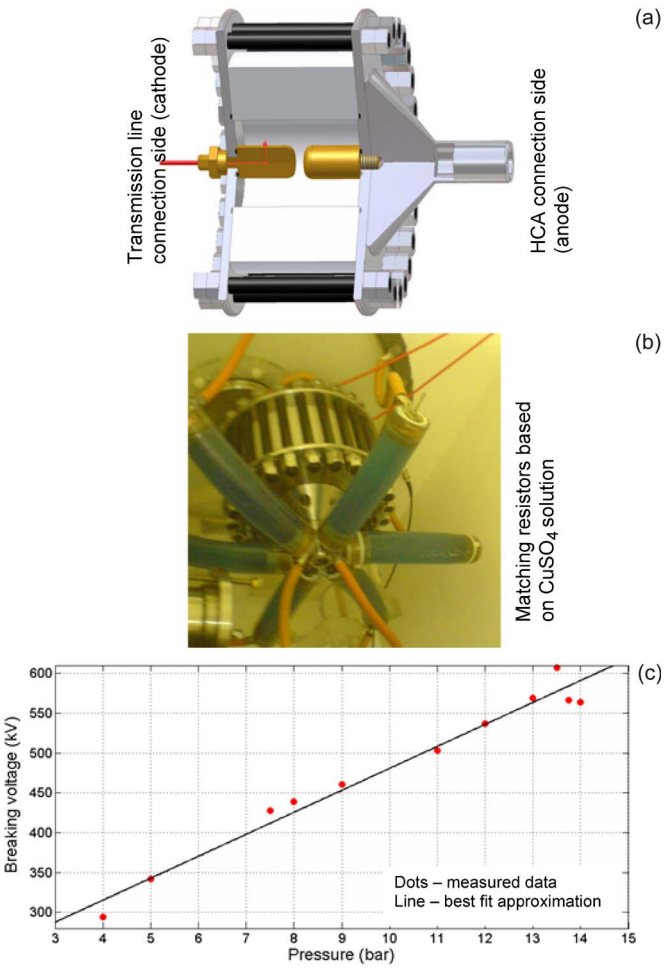

Fig. 2. (a) Schematic diagram and (b) photograph of the high-pressure spark gap. The arrow indicates the gas line. (c) Dependence of the self-breaking voltage on the nitrogen gas pressure inside the gap.

II. Design of the High-Voltage Pulse Power Generator

A high-voltage (up to 1 MV) pulse (250 ns) power generator has been designed and constructed to drive an HCA used in the Strathclyde FEM experiments. In Fig. 1(a), a schematic diagram of the FEM experimental setup is shown. The experiment was located in an L-shaped laboratory, determining the location and configuration of the pulsed power supply (PPS) and the FEM experiment. The PPS is based on a 1.5-MV MG which is located inside an insulator oil-filled tank (I). It is connected via a transmission line (II) and a high-pressure spark gap to a plasma flare emission electron gun (III). The oil tank used to host the MG has the following dimensions: $1.2\ \text{m} \times 1.6\ \text{m} \times 1.8\ \text{m}$ $(l \times w \times h)$. The MG is elevated above the tank floor by 150 mm using corrugated nylon supports. The oil used to insulate the MG had a breakdown strength of $\sim$120 kV/cm, which is sufficient to prevent air and surface breakdown during charging/discharging of the MG. The MG consisted of 15 "General Atomic" capacitors with individual capacitances of $\sim 0.3\ \mu$F. The capacitors are charged in parallel (up to 100 kV each) and discharged in series using an externally triggered spark gap, multiplying the output voltage by a factor of 15. The transmission line, connected to the MG,

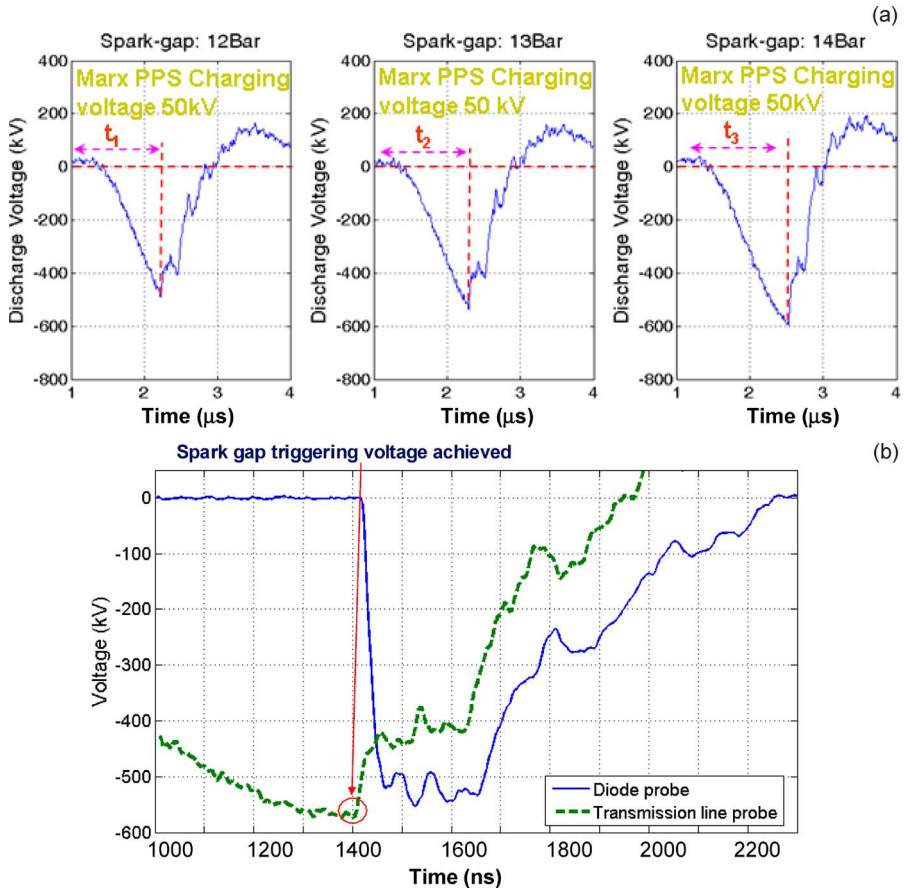

Fig. 3. Traces of the (a) transmission line output voltage pulse for the set of different pressures inside the spark gap for the same MG charging voltage. (b) Voltage pulses from the (dashed line) transmission line and the spark gap. The arrow indicates the time when self-breakdown of the pressurized spark gap takes place.

has a "folded" configuration. It is a triple-conductor coaxial line [Fig. 1(b)] with the intermediate conductor charged to the operating voltage and the inner and outer conductors at the ground potential. This setup effectively doubles the length of the standard transmission line, resulting in a factor of two reduction in the length required for a long-pulse ($\sim$250 ns) operation. The length of each conductor of the transmission line was 2 m with an outer conductor diameter of 70 cm and a ratio of 2 : 1 between successive conductor diameters. The line was filled with deionized ($\sim$14 MΩ/cm) water with a characteristic impedance of 4.7 Ω and a total capacitance of 25 nF. The conductors are well aligned and supported to minimize variation in the voltage pulse amplitude with time, e.g., through parasitic reflections. The intermediate electrode of the transmission line can be charged up to 1 MV through a 50-μH inductor which is located $\sim$40 cm above the MG field-relieving electrode. The transmission line was switched into the load via a high-pressure (12–14 bar) nitrogen-filled spark gap [Fig. 2(a)]. To match the impedances of the transmission line and the HCA, 6×100 Ω copper sulfate matching resistors were used [see photograph shown in Fig. 2(b)]. In Fig. 2(a) and (b), a technical drawing and a photograph of the spark gap, connected to the transmission line and matching resistors, are shown. On the technical drawing of the spark gap, the arrowed line indicates the gas pipe used to pressurize the switch. The performance of the spark gap was studied, and a graph showing the dependence of the gap breakdown voltage on the applied gas pressure is shown in Fig. 2(c). The spark gap was used to rectify the transmission line output voltage pulse, producing a flattop pulse of up to 250-ns duration at the input of the load. In Fig. 3, typical traces of the voltage pulses from the transmission line and voltage pulse after the spark gap are shown. The voltage pulses observed at the end of the transmission line have the conventional shape of the pulses formed by the charging and discharging LRC circuit with an $\sim$1.5-μs time constant. The set of diagrams [Fig. 3(a)] demonstrates the dependence of the output voltages on the pressure inside the spark gap. By changing the spark gap pressure, one effectively changes the impedance of the circuit, thus changing the LRC circuit time constant. In the cases shown, the pressure inside the spark gap was varied from 12 to 14 bar, while the MG charging voltage was kept constant (50 kV). In this experiment, the amplitude variation of the output pulse due to the pressure difference was around 10%, with maximum amplitude and optimum pulse shape achieved at the highest pressure. In Fig. 3(b), the time correlation between the input and output pulses from the spark gap is shown with the dashed line associated with the transmission line output pulse, and the solid line shows the output pulse from the spark gap. Further increase of the pressure inside the switch resulted in termination of the high-voltage pulse as the operating voltage was not enough to allow the gap to breakdown. For instance, increasing the pressure in the switch

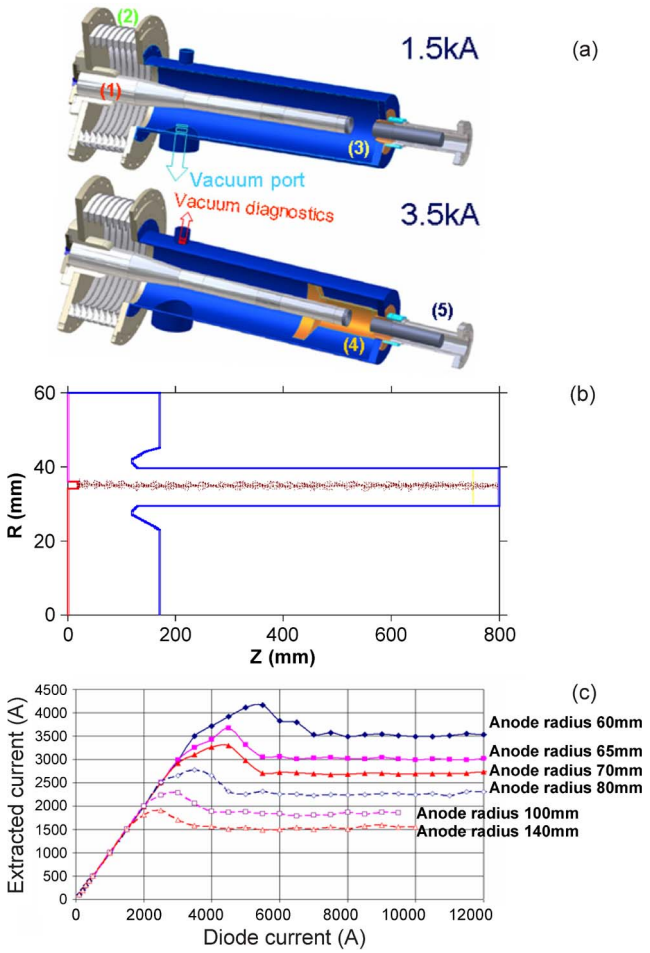

Fig. 4. (a) HCA cross sections showing (1) the aluminum cathode support with electron-emitting graphite ring, (2) the high-voltage insulator between the anode and cathode plates, (3) the anode–cathode gap, (4) the anode insert to increase SCL electron beam current, and (5) the coaxial electron beam channel. (b) Numerical model of the diode used in the PiC KARAT to optimize the HCA design and (c) the dependence of the extracted one into the coaxial channel electron beam current versus the diode current observed for a range of anode–cathode radial distances $r_{\mathrm{anode}} \in [60\ \mathrm{mm}; 140\ \mathrm{mm}]$.

beyond 14 bar, for the given voltage (∼500 kV), results in failure of the switch to close, as insufficient electrical stress is applied across the spark-gap electrodes. Independent (active) triggering of this circuit is a potential improvement for the PPS, although, with proper calibration, passive triggering has shown exceptional reproducibility between experimental runs.

III. Design and Operation of HCA

The flattop voltage pulse from the spark gap is applied to the cathode–anode gap of the HCA, producing an annular electron beam. The HCA has a cylindrical diode configuration [Fig. 4(a)] with a variable cathode–anode axial separation [20]. One notes that, while the FEM interaction region is formed by a coaxial drift tube, it is the cylindrical geometry of the HCA which defines the maximum electron beam current, governed by the relativistic Child–Langmuir law for cylindrical waveguide [16]–[20]

$$I = I_0 \left(\gamma_0^{2/3} - 1\right)^{3/2} / \left(1 - f + 2\ln(R/b)\right) \qquad (1)$$

where $I_0 = mc^3/e$, γ_0 is the relativistic mass factor, R is the anode radius, b is the outer radius of the beam, and f is a function that is dependent only on the beam inner and outer radii which tends to one if the beam thickness is small in comparison with the beam outer radius and zero for a solid beam.

In the experiments conducted, the electron beam current was varied from 1.5 to 3.5 kA. This was achieved by adjusting the radial distance [see (1)] between the anode and the cathode [Fig. 4(a)], via variation of the anode radius. In Fig. 4(a), the drawings of the HCA designs to produce 1.5- and 3.5-kA electron beams are shown. Taking into account the geometrical parameters of the system, such as the outer radius of the emitting surface at 36 mm, the beam wall thickness of 2 mm, and the accelerating voltage of 450 kV, the anode radii required to produce 1.5- and 3.5-kA electron beams were calculated to be 150 and 60 mm, respectively.

The goal of the HCA design was to minimize spread in the electron beam velocity and energy and to ensure beam propagation through the interaction region. For this purpose, the 2.5-D PiC code KARAT was used. The final geometry of the cathode has been optimized to reduce electron beam velocity spread to below 7%. An $r-z$ cross section of the 2.5-D model of the simulated HCA and the electron beam trajectory is shown in Fig. 4(b), while in Fig. 4(c), the results of the simulations of the HCA having the different anode radii are demonstrated. The diode currents in Fig. 4(c) correspond to the maximum available beam currents set in the KARAT code, with the steady-state regions, for each anode radius, taken as synonymous with the space-charge-limited (SCL) emission current. It was observed that the analytical first estimations of the electron beam currents (1) matched well with those given in the steady-state regions in Fig. 4(c); however, an overestimate results when the available diode current is set too low (for example, within 20% of the expected SCL value). To ensure electron beam propagation through the beam channel, with minimum losses, the HCA was immersed in a uniform magnetic field [13], [20]. During the numerical studies, it was found that, to meet this criterion, the magnetic field must be above some critical value (in our case, 0.4 T), i.e., at $B > 0.4$ T, the beam trajectory is well confined, and no beam loss is observed at the anode aperture. As a result, a single-layer, pulsed, guide solenoid having the following parameters was designed: length of 2.5 m, diameter of 0.33 m, and maximum guide field amplitude of 1 T.

To obtain the required amplitude of the magnetic field for the FEM experiment (up to 0.8 T), a solenoid pulsed power system, consisting of ten 250-μF capacitors connected in parallel, was used. The capacitors were charged and discharged at voltages of up to 18 kV to provide a current through the solenoid of up to 3 kA. The capacitors were connected to the power supply via current-limiting charging resistors and high-voltage diodes, while the solenoid itself was connected to the capacitors via a single ignitron switch, and matching resistors were used to slightly overdamp the LRC circuit. The resistors used, as well as the high-voltage diode, ensure the absence of current feedback into the dc power supply during the capacitors' discharge. The duration of the magnetic field pulse [1 ms, Fig. 5(a)] significantly exceeds the electron beam

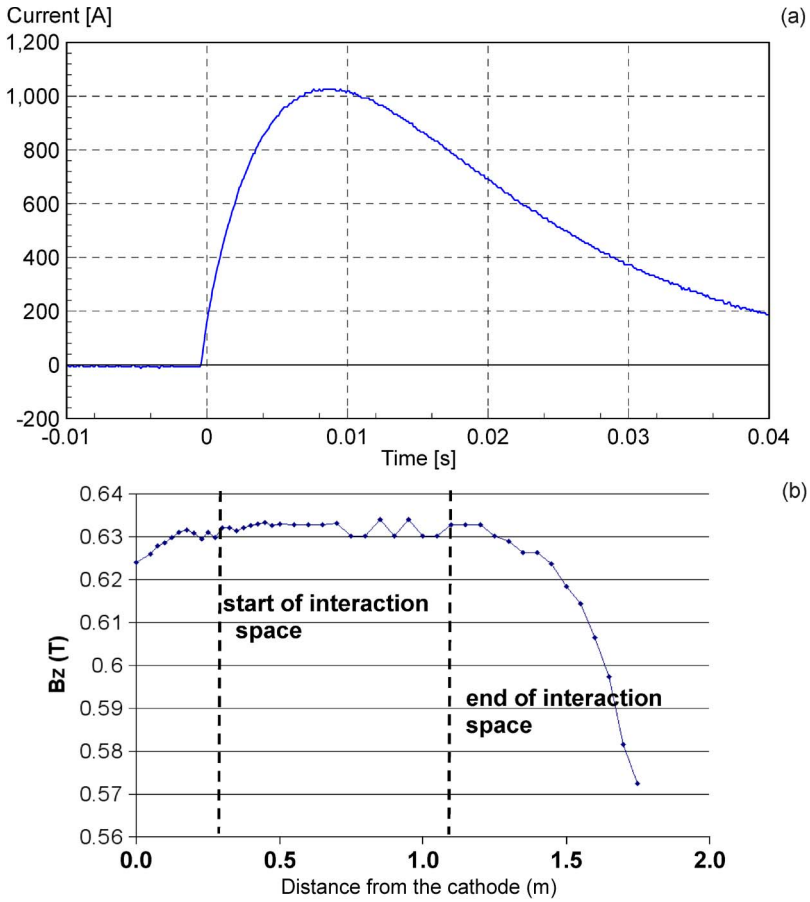

Fig. 5. (a) Time evolution of the drive current to the guide solenoid. (b) Dependence of the amplitude of the guide solenoid magnetic field on the longitudinal coordinate.

current pulse duration ($\sim$200 ns), simplifying the design of the FEM triggering units and minimizing the magnetic field exclusion. In Fig. 5(b), the guide field profile is shown indicating that the perturbations of the guide field observed do not exceed 5% of the unperturbed value. In accordance with the simulations and measurements that have been conducted, the perturbations observed did not significantly affect the quality of the electron beam and, therefore, the operation of the high-power FEM.

To study the electron beam current, a Rogowski coil was used. The dielectric core (Perspex) Rogowski coil had the following parameters: inner and outer radii of 50 and 80 mm, respectively, thickness of 20 mm, and number of copper wire turns of 200. The results of the beam current measurements are shown in Fig. 6. The visible oscillations on the top of the current pulse [thin line in Fig. 6(a)] were associated with the noise signal produced by the PPS. The possibility of current oscillations due to the transverse beam instabilities [14], [15] was also considered; however, the numerical simulations indicate that such type of instabilities would require significantly higher current densities in order to develop. It is important to note that, in spite of the high currents, the electron beam current densities (current per unit area) are rather low ($\sim$300 A/cm^2 and $\sim$1 kA/cm^2 for the 1.5- and 3.5-kA electron beams, respectively). To filter out the noise signal, the following technique was used. First, the signal from the Rogowski coil was measured without the electron beam [dashed line in Fig. 6(a)], which was achieved by switching off the guide magnetic field. Then, the signal with the electron beam passing through the interaction region was measured (thin line), and from this signal, the noise signal (dashed line) was subtracted [Fig. 6(a), bold line]. In Fig. 6(b) and (c), the results of the electron beam current measurements as compared with the typical trace of the voltage pulse are shown for the case of a 1.5- and a 3.5-kA electron beam, respectively. The correlations between the typical voltage pulse and the electron beam currents are rather clear. In both cases, slow electrons extracted from the plasma cloud and accelerated by the voltage pulse tail were observed.

IV. Numerical Modeling of FEM Based on Two-Dimensional Distributed Feedback

Analytical studies of a FEM based on 2-D distributed feedback have been recently conducted, and the results observed can be found in the following works: [6], [7], [13], and [21]–[32]. In this section, we will discuss the numerical model, developed by using the 3-D PiC code MAGIC. Let us note that the coaxial FEM considered in this paper is based on a two-mirror cavity formed by a 2-D periodic lattice [4], [12], [29] (an input 2-D Bragg mirror) and a 1-D periodic lattice (an output 1-D Bragg mirror), i.e., a 2-D–1-D Bragg cavity [22], [27], [30]–[32]. The mirrors were obtained by introducing shallow

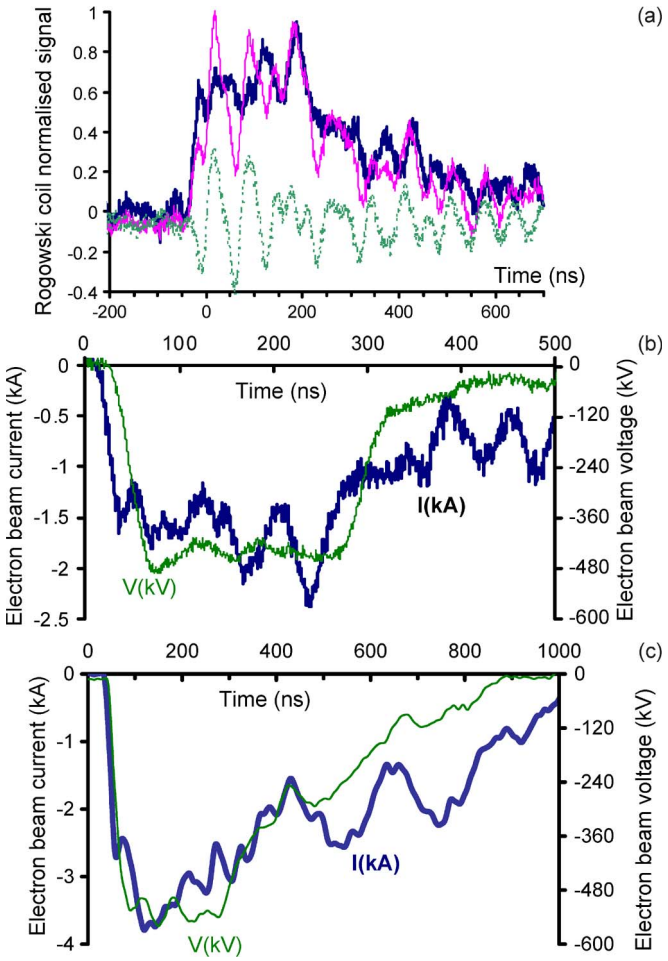

Fig. 6. Results of the electron beam current measurements: (a) Trace of the (bold line) electron beam current after the noise reduction procedure via extraction of the (dashed line) noise signal from the (thin line) measured signal; (b) trace of the (bold line) 1.5-kA electron beam current produced when the spark gap pressure was 13 bar and trace of a (thin line) typical voltage pulse; (c) trace of the (bold line) 3.5-kA electron beam current when the spark gap pressure was 14 bar and trace of the (thin line) typical voltage pulse.

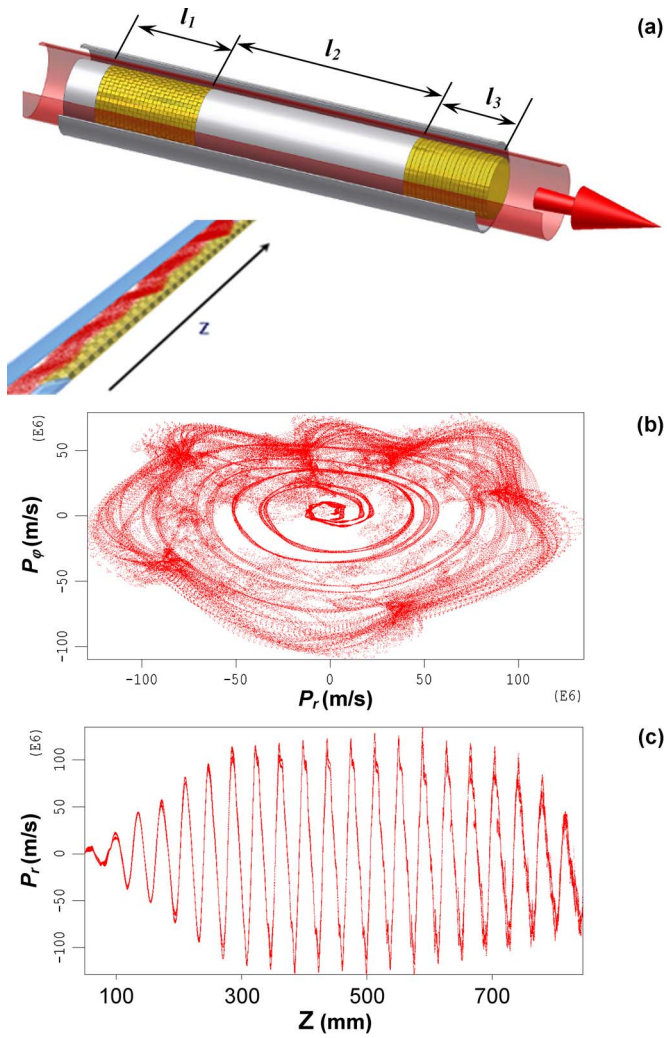

Fig. 7. (a) Schematic of the FEM interaction region showing the 2-D Bragg input (l_1) and 1-D Bragg output (l_3) mirrors separated by a regular coaxial line (l_2) and an electron beam propagating between inner and outer conductors. The insert shows the electron beam observed from the 3-D numerical model developed using the 3-D PiC code MAGIC, showing the electron beam propagating in the region of the input mirror in the combined fields of the undulator and the guide solenoid. (b) Evolution of the transverse momenta inside the interaction region, i.e., the particle momentum evolution in $(P_r; P_\varphi)$ phase space. (c) Radial momentum evolution along the interaction region.

"square-wave" corrugations on the surface of the inner conductor [12], [29]

$$r = r_{\text{in}} + a_2 \text{sign}\left(\cos(\bar{k}_{z2} z)\right) \text{sign}\left(\cos(\bar{m}\varphi)\right) \tag{2a}$$

in the case of the 2-D Bragg mirror and

$$r = r_{\text{in}} + a_1 \text{sign}\left(\cos(\bar{k}_{z1} z)\right) \tag{2b}$$

in the case of the 1-D Bragg mirror [2], [3], [33]–[35]. Here, $\text{sign}(x)$ is a step function that is equal to 1 if $x > 0$ and -1 if $x < 0$, r_{in} is the radius of the inner conductor, $a_{1,2}$ are the amplitude of the 1-D and 2-D periodic perturbations, $\bar{k}_{z1,2} = 2\pi/d_{z1,2}$, $d_{z1,2}$ are the axial periodicities of the perturbations, and $\bar{m}$ is the number of azimuthal variations of the 2-D Bragg mirror. A 3-D schematic of the interaction region, with the electron beam propagating between the inner and outer conductors, is shown in Fig. 7(a). In this figure, $l_{1,2,3}$ are the lengths of the input mirror, the intermediate section, and the output mirror, respectively. The insert in Fig. 7(a) shows the 3-D particle motion inside the input mirror in the combined fields of the guide solenoid and the undulator. Taking into account the results of previous analytical studies [11]–[13], [21]–[31], which demonstrated that, in the frequency region of interest, only coupling between the TEM and $\text{TE}_{24,1}$ waves takes place, the symmetry of the model allows one to consider in the simulations only a single section $\varphi \in [-\pi/\bar{m}; \pi/\bar{m}]$ (where φ is the azimuthal coordinate) of the interaction region, with periodic boundary conditions applied at $\varphi = -\pi/\bar{m}$ and $\varphi = \pi/\bar{m}$. This allows the computational run time to be reduced to an acceptable level (15 days) at a computational speed of up to 10 ns/day. A time interval of 150 ns has to be simulated in order to see the evolution of FEM operation from the transient stage to the steady-state regime of oscillations. Let us note that, during the numerical studies, it was observed that the change of the number of azimuthal periods used in the simulations (in one simulation up to eight periods, i.e., $\varphi \in [-8\pi/\bar{m}; 8\pi/\bar{m}]$ were used) did not affect the mode purity or the output mode structure. This allows us to assume that the numerical modeling

produced evidence of mode selection inside the 3-D structure based on the surface (2-D) periodic lattice along the longitudinal and azimuthal indexes supporting independently the results predicted by the 2-D analytical theory [6], [7], [11], [12], [25]–[28]. We note that the numerical modeling took into account the full 3-D geometry of the system (i.e., radial dimension included), as well as the complex geometry of the lattice, which consisted of a superposition of two "square" waves [12]. This strongly supports the results of analytical studies which were based on the set of self-consistent 2-D coupled wave equations, observed using the slow-envelop variation approximation under the assumption of four-wave coupling on the ideal periodic corrugation [6], [7], [11], [12], [21]–[28].

To avoid numerical instabilities, the dimensions of the individual mesh cells were varied inside the interaction region. However, the degree of mesh cell variation along the chosen coordinate was relatively small with the ratio between maximum and minimum mesh cell dimensions not exceeding two. The smallest mesh cell dimensions $(\partial z; \partial r; \partial \varphi)$, along the coordinates (z, r, φ), were chosen to accommodate the smallest features of the periodic lattice and had the following dimensions: $\partial z = d_{z2}/10; \partial r = a_2/2; \partial \varphi = 2\pi/12\bar{m}$. The electron beam trajectories in the particle phase space $(P_r; P_\varphi)$, where P_r and P_φ are the radial and azimuthal electron momenta, respectively, are shown in Fig. 7(b). In Fig. 7(c), the dependence of the radial momentum on the longitudinal coordinate z is shown. These plots show three different regions of electron beam trajectories: first, the spiral trajectories of electrons inside part of the interaction region, where the undulator field is adiabatically increased; second, the uniform circular trajectories, when the interaction between the electron beam and the EM field is weak and it does not affect the beam motion; and third, the trajectories when strong interaction between the electrons and the field takes place, resulting in electron beam bunching. Let us note that the 2-D results demonstrated were observed from 3-D simulation of electron beam propagation inside the interaction region.

In the model developed, it was assumed that the electron beam enters the interaction region from the left "port" having an accelerating voltage of 450 kV, a radius of 3.5 cm, and a wall thickness of 2 mm. To "launch" the electron beam, the "BEAM" command defined in the PiC code MAGIC was used. The electron beam was confined by a guide magnetic field of 0.63 T and propagated in the combined fields of the undulator and the guide solenoid. The periodic magnetic field used to pump the electron beam transverse velocity was created by a large-radius (45 mm) undulator consisting of 60 single coils each of length 20 mm (30 periods of 40-mm length). The undulator field required was estimated analytically to be $\sim$0.06 T, which agreed well with the optimized undulator field strength (0.063 T) of the numerical simulations.

The parameters of the two-mirror cavities were optimized to observe a single-mode steady-state FEM operation. It was found that, for a 1.5-kA electron beam, the cavity parameters should be $l_1 = 140$ mm, $l_2 = 400$ mm, and $l_3 = 70$ mm, while in the case of the 3.5-kA electron beam, the distance between the input and output mirrors should be reduced to $l_2 = 200$ mm. The particle dynamics and trajectories were also analyzed during the numerical modeling, with the observed results shown in Figs. 7 and 8. The results presented are observed for the case when the FEM is driven by a 1.5-kA electron beam, and single-mode steady-state operation was achieved. Fig. 8(a) shows the particle energy evolution, with inserts to the figure showing a closer detail of the particles entering and exiting the interaction region. First, quasi-monoenergetic electron particles enter into the interaction region; then, after passing through it (second insert), the particles become trapped in potential "buckets" with most of the particles having their mean energy reduced from 450 to $\sim$400 keV. In Fig. 8(b), the longitudinal spatial bunching of the particles is also shown. The figures show that a uniform beam enters the interaction region, while at the exit, i.e., after the interaction with the EM field, a strongly bunched electron beam emerges.

The distributions of the EM field components E_r and B_z, associated with the partial waves (TEM and $TE_{24,1}$) coupled inside the 2-D periodic lattice and participating in the beam–wave interaction, are shown in Fig. 9. The field structures are also observed for the steady-state part of the FEM operation. As predicted by the theory developed in previous works [6], [7], [11]–[13], [21]–[28], the coupling between the near-cutoff $TE_{24,1}$ wave [B_z field component, Fig. 9(a)] and a propagating TEM wave [E_r field component, Fig. 9(b)] takes place inside the 2-D Bragg mirror. Indeed, as shown in Fig. 9(a), the B_z component exists only inside the 2-D periodic structure, and its longitudinal wavenumber is very small $\sim 1/l_1$. Let us also note that the field inside the 2-D mirror synchronizes radiation of the electron beam and influences the output signal spectral characteristic. In Fig. 10, the spectra of the E_r field component, of the output radiation associated with the TEM operating mode, are shown for driving currents of 1.5 (1) and 3.5 kA (2 and 3). The rest of the field components were also observed in the output radiation, but in the operating frequency range, their amplitude is negligible (at least 20 dB lower). The satellites observed in spectrum 1 in Fig. 10 correspond to the spectral components associated with the number of the longitudinal variation of the near-cutoff partial wave $TE_{24,1}$. It was found that the variation of the mirror length affected the distance between the satellite modes and also resulted in detuning of the operating frequency inside the 2-D mirror band gap. An increase of the electron beam current up to 3.5 kA without changing the cavity parameters resulted in the appearance of a high noise signal (spectrum 2 in Fig. 10). However, single-mode operation was observed for this increased beam current when the length of the intermediate section (smooth waveguide) between the mirrors was decreased from 400 to 200 mm (Fig. 10).

V. Experimental Studies of FEM Based on Two-Dimensional Distributed Feedback

In the previous experiments conducted with the coaxial FEM based on 2-D distributed feedback, a two-mirror high-Q cavity was formed by 2-D Bragg structures [13], [36]. The high Q factor of the cavity restricted the efficiency to 6% while, due to features specific to the 2-D structures as detailed in [12], [23]–[27], and [37], the power losses inside the output mirror were high. To overcome these problems, the use of a coaxial

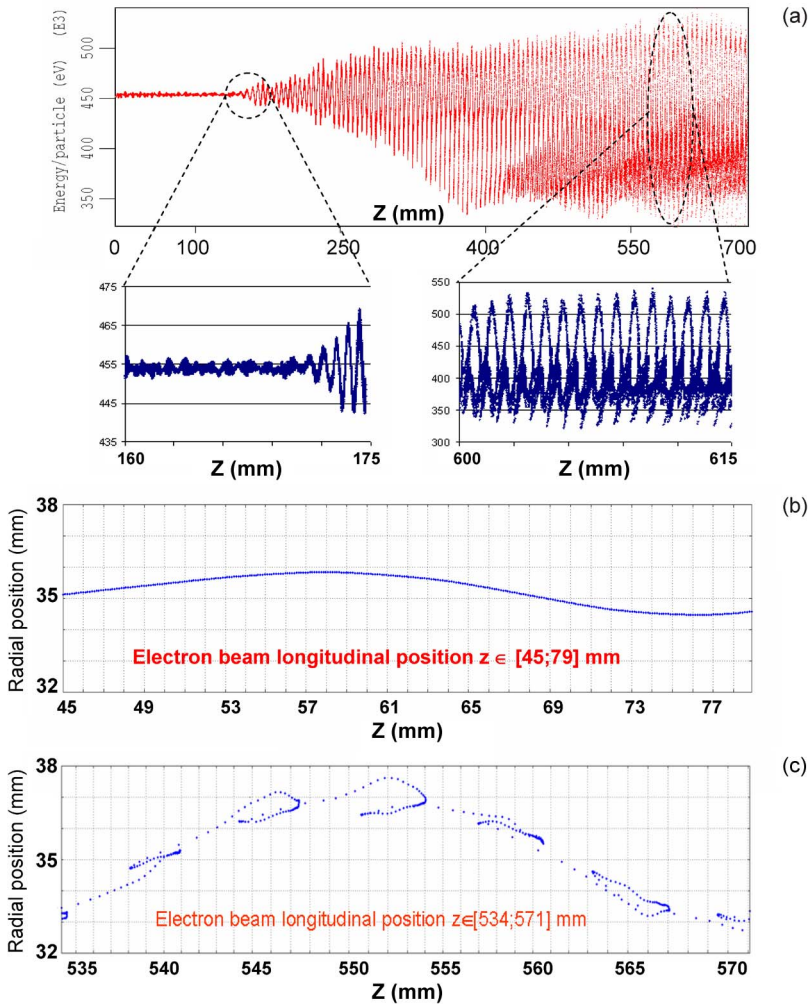

Fig. 8. (a) Dependence of the electron beam macroparticles' energy on the position inside the interaction region. The inserts show the zoom ins of the aforementioned graph at the (left insert) entrance and the (right insert) exit from the interaction space. (b) Illustration of the electron beam evolution, i.e., (first figure) a uniform beam entering into the interaction region and (second figure) a strongly bunched electron beam near the exit.

1-D Bragg structure as an output reflector was suggested [23], [24], [27]. A two-mirror cavity was formed using 2-D–1-D periodic structures as input and output mirrors, respectively, separated by a length of regular coaxial waveguide. The closed feedback loop inside such a cavity was observed via EM wave reflection from the input (2-D) and output (1-D) mirrors, which can only be achieved if the band gaps of the input and output mirrors are overlapping not only in terms of frequency but also in terms of wavenumbers [12], [13]. The operation of the FEM, demonstrated in this paper, is an experimental proof of the broad concept that the 2-D distributed feedback formed inside a part of the interaction space (for instance, inside the input mirror) is sufficient to synchronize the radiation from different parts of the electron beam. The 2-D and 1-D periodic structures used in the experiment to define the two-mirror cavity are designed and constructed to ensure that the overlap between the mirrors' band gaps takes place only for the fundamental TEM mode of the cavity. The periodic structures have the following parameters: The 2-D lattice (input mirror) has an axial periodicity of 8 mm and shows 24 periodic variations across the azimuth, with a corrugation amplitude of 0.8 mm; the 1-D lattice (output mirror) has an axial periodicity of 4 mm and a corrugation amplitude of 0.4 mm.

To ensure the start-up of FEM oscillations, the cavity used in the experiment had a longer interaction region as compared with that designed using numerical methods. The experimental cavity was formed by input (2-D) and output (1-D) mirrors of lengths $l_1 = 112$ mm and $l_3 = 100$ mm, respectively, with the length of the smooth coaxial waveguide between them set at $l_2 = 600$ mm. Such alterations to the cavity were carried out as a consequence of the fact that the numerical model developed did not take into consideration some technical solutions realized in the experiment, such as the inner conductor supports, increased EM field losses due to surface roughness of the machined components, etc., which ultimately result in a drop of the driving current, a decrease of the cavity Q factor, and, thus, an increase of the transition time. The electron beam current pulse duration is $\sim$200 ns, and therefore, it was important to ensure that the transition time did not exceed 100 ns. The requirement for the minimum transition time also means that the minimum electron beam current required to drive the FEM should be above 1 kA. This led to the alterations made, to

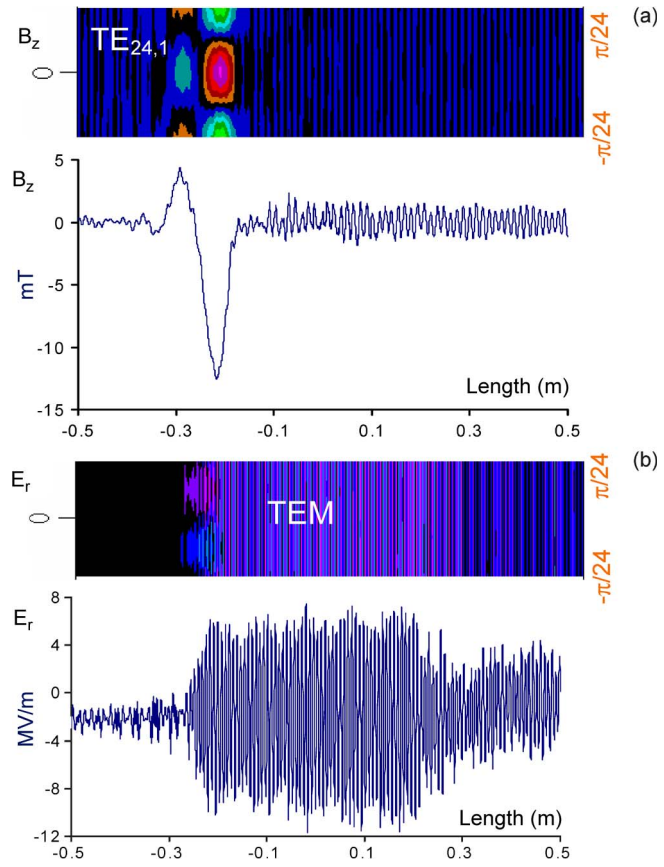

Fig. 9. Contour plots and graphs showing the dependences of the amplitude of the (a) longitudinal magnetic field and the (b) radial electric field associated with the $TE_{24,1}$ and TEM partial waves, the superposition of which defines the fundamental eigenmode of the cavity.

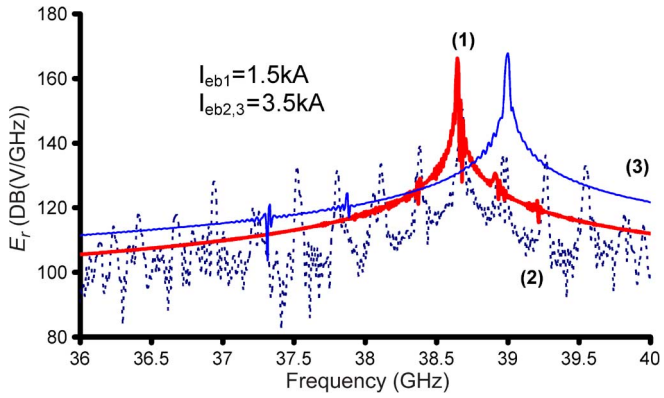

Fig. 10. Spectra of the FEM output radiation associated with the E_r field component and observed from the numerical studies of the FEM having $a_2 = 0.4$ mm, $a_1 = 0.2$ mm, and the following: (Curve (1), solid line) $l_1 = 140$ mm, $l_2 = 400$ mm, and $l_3 = 70$ mm and driven by a 1.5-kA electron beam; (curve (2), dotted line) $l_1 = 140$ mm, $l_2 = 400$ mm, and $l_3 = 70$ mm and driven by a 3.5-kA electron beam; and (curve (3), thin line) $l_1 = 140$ mm, $l_2 = 200$ mm, $l_3 = 70$ mm and driven by a 3.5-kA electron beam.

the cavity design based on numerical simulations. However, it is our intention to study a FEM based on a cavity having parameters close to optimum values in future experiments.

The two-mirror cavity was located inside the uniform part of the large-diameter azimuthally symmetric 30-period undulator with a single period of length 40 mm ($k_u = 2\pi/d_u, d_u =$

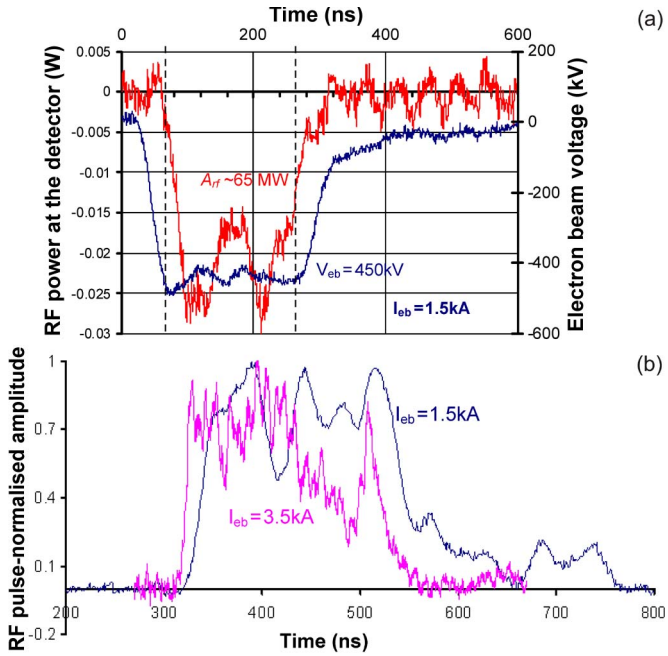

Fig. 11. (a) Measured microwave output pulse and electron beam voltage observed during experimental studies of the FEM when driven by a 1.5-kA electron beam. (b) Comparison of the microwave output pulses' shapes observed from the FEM when driven by 1.5- and 3.5-kA electron beams.

40 mm). To minimize parasitic cyclotron oscillations, the undulator field was slowly up tapered over the initial six periods, ensuring an adiabatic entrance of the electron beam inside the interaction space. During the experiments, the amplitude of the undulator was varied from 0 to 0.07 T, while the amplitude of the guide magnetic field was tuned between 0.5 and 0.7 T. In Fig. 11(a), the time correlation between the traces of the electron beam accelerating voltage and microwave output pulse, obtained using a driving current of 1.5 kA, is shown. The transition period takes place during the first ~100 ns [Fig. 11(a)], which indirectly confirms the estimation of the cavity Q factor and the electron beam current. A comparison of the microwave output pulses observed from the FEM driven by 1.5- and 3.5-kA electron beams is shown in Fig. 11(b). The increase of the current to 3.5 kA resulted in a decrease of the transition time [Fig. 11(b)]; however, the pulse shape and the FEM efficiency were strongly affected. It was estimated that the efficiency dropped from ~10% in the case of the FEM driven by a 1.5-kA electron beam to ~5% when the FEM was driven by a 3.5-kA electron beam.

The frequency of the output radiation was measured using both the following: cutoff filters [Fig. 12(a)] and a heterodyne technique [Fig. 12(b) and (c)]. Using a set of cutoff filters, it was established that the 2-D Bragg FEM operated within the 33- to 40-GHz frequency region [Fig. 12(a)]. To study the output spectrum in more detail, the frequency of the output radiation was measured using a heterodyne frequency diagnostic. For this purpose, the microwave radiation from the FEM was mixed in a dc-biased Farran Technology waveguide balanced mixer (BMC-28B). The comparison between the traces of the mixed signal and the FEM output microwave signal is shown in Fig. 12(b). Calibration of the mixer was confirmed in the

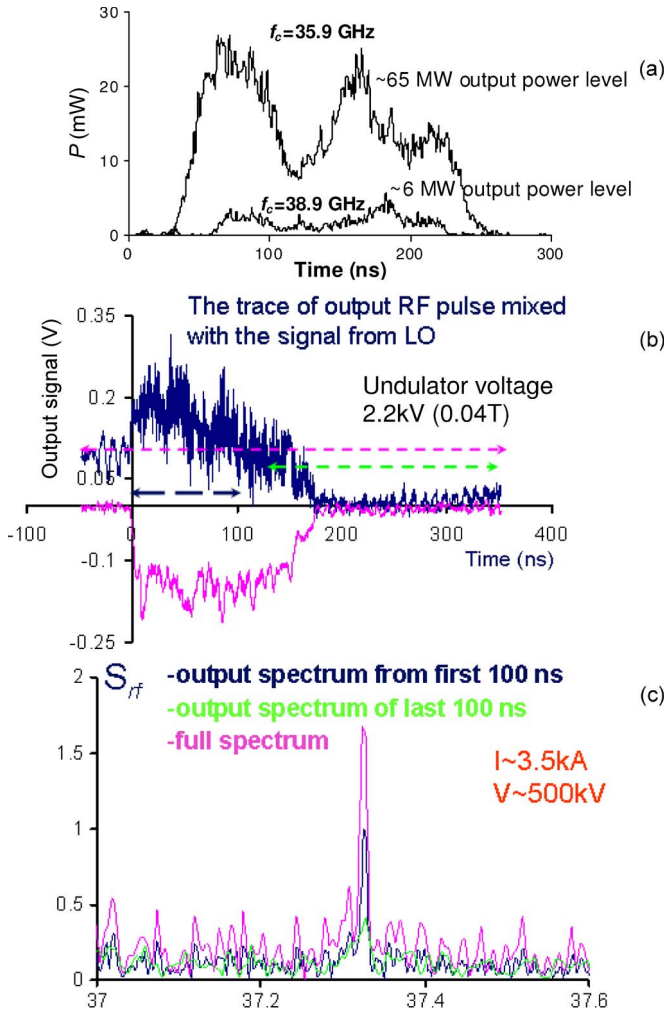

Fig. 12. Results of the study of the output pulse spectra using (a) 35.9- and 38.9-GHz cutoff filters. (b) Traces of the microwave output pulse and mix of the microwave pulse and signal from the LO. (c) Spectra of the microwave pulse shown above sampled in different time intervals, as shown in (b).

frequency range 26.5–40 GHz in cold microwave measurements, using a 40-GHz HP synthesized sweeper acting as the local oscillator (LO) and an Anritsu pulsed sweeper acting as the FEM source to be measured. The Anritsu sweeper could produce 100-ns-duration millimeter-wave pulses in the frequency range 0.01–50 GHz. In the FEM experiments, the Anritsu swept source was replaced with the output signal from the FEM. The resultant intermediate frequency was captured using a 12-GHz Tektronix TDS6124C real-time digital storage oscilloscope and analyzed using a conventional FFT algorithm. Knowing the frequency of the LO and ensuring that the signal to be measured was located within a frequency of ± 6 GHz (digitizing bandwidth of the oscilloscope) from the LO, measurement of the resultant intermediate frequency enabled the output frequency of the FEM to be determined. In Fig. 12(c), the spectra observed from the mixed signal [see Fig. 12(b)] are presented. The dashed lines in Fig. 12(b) indicate the time intervals which were analyzed to observe the spectra shown in Fig. 12(c).

Oscillations in two frequency regions around 36.7 and 37.3 GHz were observed (Fig. 13). In Fig. 13, the dependence of the microwave output pulse, the mixed signal, and the spectra of the output signal are shown (note here that the dc bias on the mixed signal has been removed, with no detrimental effect shown on the resulting spectral content). It was found that, in the vicinity of the resonance values of the undulator field, suppression of the low-frequency parasitic mode located around 36.7 GHz occurred and that the excitation of the main operating mode at 37.3 GHz of the FEM was observed. The tunability of the operating mode when the FEM was driven by a 3.5-kA electron beam was also studied. The microwave radiation and spectra measured at two different undulator fields are shown in Fig. 14. Analyzing the spectrum of the output radiation, it was found that, for a high amplitude of the undulator field, the operating mode was excited at a frequency of 37.3 GHz, and for a slightly lower field amplitude, the operating frequency was up shifted to 37.4 GHz [Fig. 14(b)].

The output radiation pattern measured was similar to that observed in [13] and [36] and confirmed the excitation of the fundamental mode. In the case of a 1.5-kA driving electron beam, the output power measured at the detector was integrated over the radiation pattern, resulting in a FEM output power of 65 MW, which corresponded to $\sim$10% efficiency. For a microwave pulse duration of 150 ns, the energy stored inside the pulse was calculated to be $\sim$10 J. To demonstrate the output pulse power intensity, a neon bulb panel was placed $\sim$0.2 m from the output window. The excitation of the neon bulb panel by the output radiation pulse is visible in Fig. 15(b), and its pattern corresponds well with the mode pattern [Fig. 15(a)] measured by scanning a millimeter-wave detector horizontally in front of the output window. Let us note that the relative uncertainty of the FEM output power measured did not exceed $\sim$10%.

VI. Conclusion

In this paper, the FEM experiments conducted at the University of Strathclyde were discussed, and the results achieved at each step were reported. The experimental setup, including the designs of the pulse power supply and the HCA, was presented, and the results of experimental studies of the PPS and HCA and measurements conducted were discussed. We demonstrated the results of the numerical modeling and experimental studies of the HCA used to power a FEM based on 2-D distributed feedback.

It was shown that the application of 2-D distributed feedback in a part of the interaction region is sufficient to synchronize the radiation of an oversized electron beam. In the experiments conducted, a mode pattern associated with a radiating TEM wave from the coaxial output horn was measured, and it was demonstrated that the microwave peak power from the FEM was large enough to excite a neon bulb panel at the output. The effect of increasing the electron beam current (from 1.5 to 3.5 kA) without adjustment of the cavity parameters on the performance of the FEM was studied. It was demonstrated that such an increase in beam current resulted in a decrease of the transition time and a deterioration in the output microwave pulse shape and in the FEM efficiency. The excitation of parasitic modes was also observed when the FEM was driven by a 3.5-kA electron beam. Numerical simulations indicate that, to improve

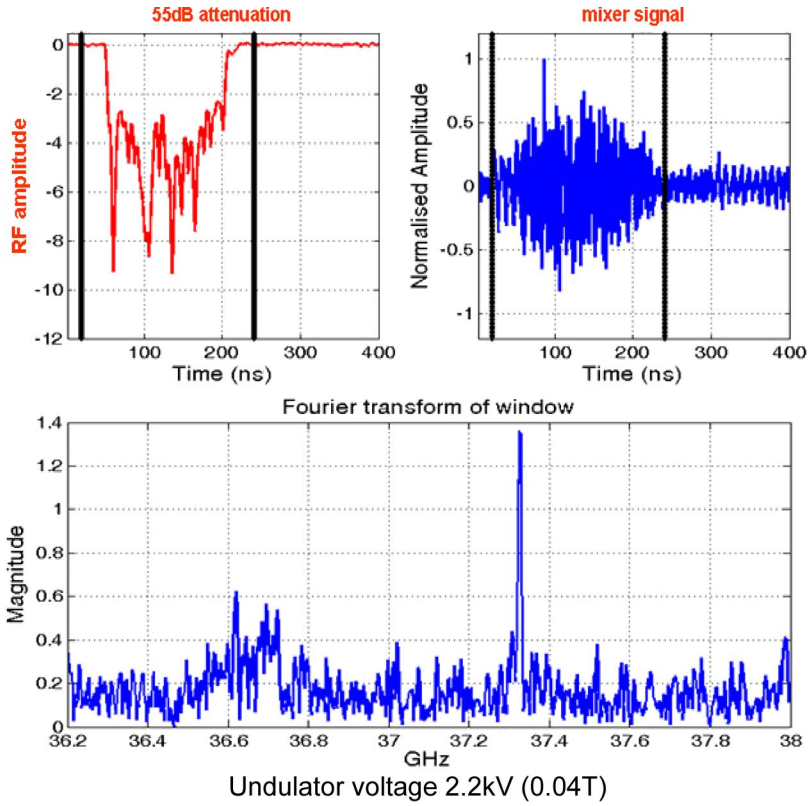

Fig. 13. Results of the experimental study of the microwave output pulse from the FEM driven by a 3.5-kA electron beam when the amplitude of the undulator field was equal to 0.04 T.

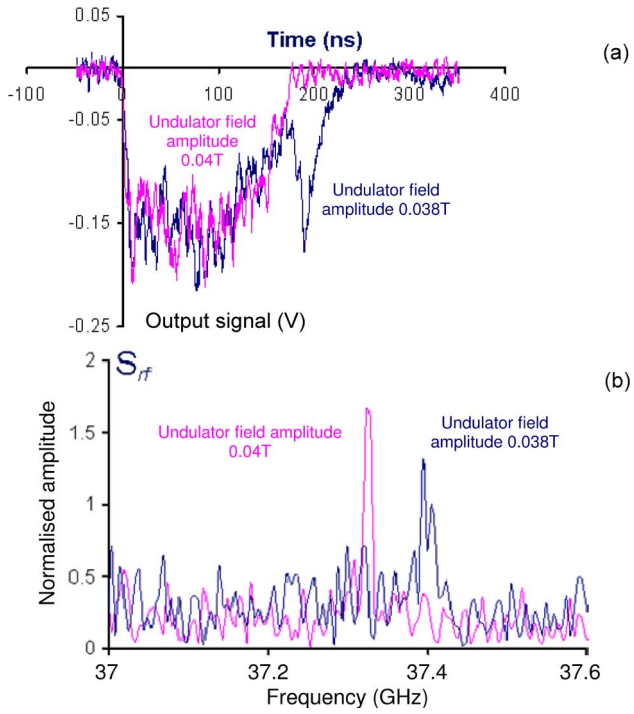

Fig. 14. (a) Measured microwave pulses from the FEM driven by a 3.5-kA electron beam when the undulator field was 0.038 and 0.04 T. (b) Spectra of the output pulses shown above.

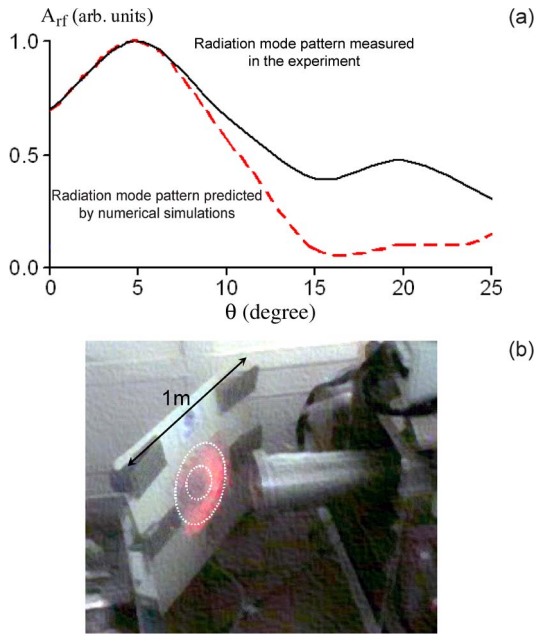

Fig. 15. (a) Mode pattern of the output signal from the coaxial horn (bold line) measured in the experiment and (dashed line) predicted by the 3-D code MAGIC. (b) Excitation of the neon bulb panel by the output microwave pulse.

the FEM operation when driven by a high-current (3.5 kA) electron beam, the length of the cavity (between mirrors) should be reduced from 600 (used in the experiments) to 200 mm.

Using the results of the theoretical studies and data from measurements, a new two-mirror cavity has been designed and constructed having the parameters close to the one used in numerical simulations. Application of this cavity should result in an increase in efficiency and FEM operation stability; however,

it is anticipated that the transition time may be increased. The detailed spectral analysis of the output radiation from the FEM driven by a 1.5-kA electron beam will be the next goal of the future experiments.

ACKNOWLEDGMENT

The authors would like to thank Prof. N. S. Ginzburg, Dr. N. Y. Peskov, Prof. M. Thumm, and B. A. Kerr for stimulating and useful scientific discussions. P. MacInnes would like to thank PPARC/STFC and the University of Strathclyde for the support of his Ph.D.

REFERENCES

[1] J. H. Booske, "Plasma physics and related challenges of millimeter-wave-to-terahertz and high power microwave generation," *Phys. Plasmas*, vol. 15, no. 5, p. 055502, Feb. 2008.

[2] C. K. Chong, D. B. McDermott, M. M. Razeghi, N. C. Luhmann, J. Pretterebner, D. Wagner, M. Thumm, M. Caplan, and B. Kulke, "Bragg reflectors," *IEEE Trans. Plasma Sci.*, vol. 20, no. 3, pp. 393–402, Jun. 1992.

[3] M. C. Wang, V. L. Granatstein, and R. A. Kehs, "Design of a Bragg cavity for a millimeter wave free-electron laser," *Appl. Phys. Lett.*, vol. 48, no. 13, pp. 817–819, Mar. 1986.

[4] N. E. Glass, "Enhanced Smith–Purcell radiation from a bigrating surface through multiplasmon excitation," *Phys. Rev. A, Gen. Phys.*, vol. 36, no. 11, pp. 5235–5250, Dec. 1987.

[5] E. I. Smirnova, A. S. Kesar, I. Mastovsky, M. A. Shapiro, and R. J. Temkin, "Demonstration of a 17-GHz, high-gradient accelerator with a photonic-band-gap structure," *Phys. Rev. Lett.*, vol. 95, no. 7, p. 074801, Aug. 2005.

[6] N. S. Ginzburg, N. Y. Peskov, and A. S. Sergeev, "Two-dimensional double-periodic Bragg resonators for free electron lasers," *Opt. Commun.*, vol. 96, no. 4–6, pp. 254–258, Feb. 1993.

[7] N. S. Ginzburg, N. Y. Peskov, A. S. Sergeev, A. D. R. Phelps, I. V. Konoplev, G. R. M. Robb, A. W. Cross, A. V. Arzhannikov, and S. L. Sinitsky, "Theory and design of a free-electron maser with two-dimensional feedback driven by a sheet electron beam," *Phys. Rev. E, Stat. Phys. Plasmas Fluids Relat. Interdiscip. Top.*, vol. 60, no. 1, pp. 935–945, Jul. 1999.

[8] A. S. Kesar, M. Hess, S. E. Korbly, and R. J. Temkin, "Time- and frequency-domain models for Smith–Purcell radiation from a two-dimensional charge moving above a finite length grating," *Phys. Rev. E, Stat. Phys. Plasmas Fluids Relat. Interdiscip. Top.*, vol. 71, no. 1, p. 016501, Jan. 2005.

[9] Y. A. Grishin, M. R. Fuchs, A. Schnegg, A. A. Dubinskii, B. S. Dumesh, F. S. Rusin, V. L. Bratman, and K. Möbius, "Pulsed orotron—A new microwave source for submillimeter pulse high-field electron paramagnetic resonance spectroscopy," *Rev. Sci. Instrum.*, vol. 75, no. 9, pp. 2926–2936, Sep. 2004.

[10] G. S. Nusinovich, "Analytical nonlinear theory of the orotron," *Phys. Plasmas*, vol. 13, no. 5, p. 053107, May 2006.

[11] N. S. Ginzburg, A. S. Sergeev, N. Y. Peskov, G. R. M. Robb, and A. D. R. Phelps, "Mode competition and control in free electron lasers with one- and two-dimensional Bragg resonators," *IEEE Trans. Plasma Sci.*, vol. 24, no. 3, pp. 770–780, Jun. 1996.

[12] A. W. Cross, I. V. Konoplev, A. D. R. Phelps, and K. Ronald, "Studies of surface two-dimensional photonic band-gap structures," *J. Appl. Phys.*, vol. 93, no. 4, pp. 2208–2218, Feb. 2003.

[13] I. V. Konoplev, A. W. Cross, A. D. R. Phelps, W. He, K. Ronald, C. G. Whyte, C. W. Robertson, P. MacInnes, N. S. Ginzburg, N. Y. Peskov, A. S. Sergeev, V. Y. Zaslavsky, and M. Thumm, "Experimental and theoretical studies of a coaxial free-electron maser based on two-dimensional distributed feedback," *Phys. Rev. E, Stat. Phys. Plasmas Fluids Relat. Interdiscip. Top.*, vol. 76, no. 5, p. 056406, Nov. 2007.

[14] C. C. Cutler, "Instability in hollow and strip electron beams," *J. Appl. Phys.*, vol. 27, no. 9, pp. 1028–1029, Sep. 1956.

[15] H. F. Webster, "Some additional observations of the vortex instability in electron beams," *Phys. Plasmas*, vol. 7, no. 1, pp. 84–88, Jan. 2000.

[16] R. B. Miller, K. R. Prestwich, J. W. Poukey, and S. L. Shope, "Production of annular electron beams by foilless diodes," *J. Appl. Phys.*, vol. 51, no. 7, pp. 3506–3515, Jul. 1980.

[17] M. Friedman, "Propagation of an intense relativistic electron beam in an annular channel," *J. Appl. Phys.*, vol. 80, no. 3, pp. 1263–1267, Aug. 1996.

[18] A. V. Arzhannikov, V. S. Nikolaev, S. L. Sinitsky, A. V. Smirnov, M. V. Yushkov, and R. P. Zotkin, "Generation and transport of 140 kJ ribbon electron beam," *J. Appl. Phys.*, vol. 72, no. 4, pp. 1657–1659, Aug. 1992.

[19] A. N. Bastrikov, S. P. Bugaev, I. N. Kiselev, V. I. Koshelev, and K. N. Sukhushin, "Formation of hollow microsecond electron beams at megavolt diode voltages," *Sov. Phys. Tech. Phys.*, vol. 33, p. 291, 1988.

[20] I. V. Konoplev, A. W. Cross, P. MacInnes, W. He, C. G. Whyte, A. D. R. Phelps, C. W. Robertson, K. Ronald, and A. R. Young, "High-current oversized annular electron beam formation for high-power microwave research," *Appl. Phys. Lett.*, vol. 89, no. 17, p. 171 503, Oct. 2006.

[21] N. S. Ginzburg, N. Y. Peskov, A. S. Sergeev, A. V. Arzhannikov, and S. L. Sinitsky, "Planar free-electron lasers with combined 1D/2D Bragg mirror resonators: A theoretical study," *Tech. Phys. Lett.*, vol. 26, p. 701, 2000.

[22] N. S. Ginzburg, N. Y. Peskov, and A. S. Sergeev, "Spatially coherent radiation from a coaxial free-electron laser with a resonator composed of one-dimensional and two-dimensional Bragg mirrors," *Tech. Phys.*, vol. 46, p. 1009, 2001.

[23] N. S. Ginzburg, N. Y. Peskov, and A. S. Sergeev, "Dynamics of free-electron lasers with two-dimensional distributed feedback," *Opt. Commun.*, vol. 112, no. 3/4, pp. 151–156, Nov. 1994.

[24] N. S. Ginzburg, I. V. Konoplev, and A. S. Sergeev, "Application of 2-dimensional distributed feedback for emission synchronization in FEL with large-diameter piped REB," *Tech. Phys.*, vol. 66, p. 108, 1996.

[25] N. S. Ginzburg, N. Y. Peskov, A. S. Sergeev, I. V. Konoplev, A. W. Cross, A. D. R. Phelps, G. R. M. Robb, K. Ronald, W. He, and C. G. Whyte, "Theory of free-electron maser with two-dimensional distributed feedback driven by an annular electron beam," *J. Appl. Phys.*, vol. 92, no. 3, p. 1619, Aug. 2002.

[26] N. S. Ginzburg, N. Y. Peskov, A. S. Sergeev, I. V. Konoplev, G. R. M. Robb, and A. D. R. Phelps, "Mode competition and control in free electron lasers with one and two dimensional Bragg resonators," *Nucl. Instrum. Methods Phys. Res. A, Accel. Spectrom. Detect. Assoc. Equip.*, vol. 375, p. 202, 1996.

[27] N. S. Ginzburg, N. Y. Peskov, A. S. Sergeev, A. D. R. Phelps, A. W. Cross, and I. V. Konoplev, "The use of a hybrid resonator consisting of one-dimensional and two-dimensional Bragg reflectors for generation of spatially coherent radiation in a coaxial free-electron laser," *Phys. Plasmas*, vol. 9, no. 6, p. 2798, Jun. 2002.

[28] N. S. Ginzburg, N. Y. Peskov, A. S. Sergeev, V. Y. Zaslavsly, I. V. Konoplev, L. Fisher, K. Ronald, A. D. R. Phelps, A. W. Cross, and M. Thumm, "Mechanism of azimuthal mode selection in two-dimensional coaxial Bragg resonators," *J. Appl. Phys.*, vol. 105, no. 12, p. 124 519, Jun. 2009.

[29] A. W. Cross, I. V. Konoplev, K. Ronald, A. D. R. Phelps, W. He, C. G. Whyte, N. S. Ginzburg, N. Y. Peskov, and A. S. Sergeev, "Experimental studies of two-dimensional coaxial Bragg structures for a high-power free-electron maser," *Appl. Phys. Lett.*, vol. 80, no. 9, p. 1517, Mar. 2002.

[30] A. V. Arzhannikov, N. S. Ginzburg, V. Y. Zaslavskii, V. G. Ivanenko, I. A. Ivanov, P. V. Kalinin, A. S. Sergeev, S. L. Sinitskii, and V. D. Stepanov, "Generation of spatially coherent radiation in free-electron masers with two-dimensional distributed feedback," *JETP Lett.*, vol. 87, p. 618, 2008.

[31] A. V. Arzhannikov, A. W. Cross, N. S. Ginzburg, W. He, P. V. Kalinin, I. V. Konoplev, S. A. Kyznetsov, N. Y. Peskov, A. D. R. Phelps, C. W. Robertson, K. Ronald, A. S. Sergeev, S. L. Sinitsky, V. D. Stepanov, M. Thumm, C. G. Whyte, and V. Y. Zaslavsky, "Production of powerful spatially coherent radiation in planar and coaxial FEM exploiting two-dimensional distributed feedback," *IEEE Trans. Plasma Sci.*, vol. 37, no. 9, pp. 1792–1800, Sep. 2009.

[32] I. V. Konoplev, A. W. Cross, P. MacInnes, W. He, A. D. R. Phelps, C. G. Whyte, K. Ronald, and C. W. Robertson, "Free-electron maser based on a cavity with two- and one-dimensional distributed feedback," *Appl. Phys. Lett.*, vol. 92, no. 21, p. 211 501, May 2008.

[33] N. F. Kovalev, I. M. Orlova, and M. I. Petelin, "Mode transformation in multimode corrugated waveguide," *Izv. VUZov-Radiofizika*, vol. 11, p. 783, 1968, (translated from Russian).

[34] G. G. Denisov and M. G. Reznikov, "Corrugated cylindrical resonators for short-wave relativistic VHF generators," *Izv. VUZov-Radiofizika*, vol. 25, p. 562, 1982.

[35] V. L. Bratman, G. G. Denisov, N. S. Ginzburg, and M. I. Petelin, "FEL's with Bragg reflection resonators: Cyclotron autoresonance masers versus

ubitrons," *IEEE J. Quantum Electron.*, vol. QE-19, no. 3, pp. 282–296, Mar. 1983.
[36] I. V. Konoplev, P. McGrane, W. He, A. W. Cross, A. D. R. Phelps, C. G. Whyte, K. Ronald, and C. W. Robertson, "Experimental study of coaxial free-electron maser based on two-dimensional distributed feedback," *Phys. Rev. Lett.*, vol. 96, no. 3, p. 035002, Jan. 2006.
[37] I. V. Konoplev, A. D. R. Phelps, A. W. Cross, and K. Ronald, "Experimental studies of the influence of distributed power losses on the transparency of two-dimensional surface photonic band-gap structures," *Phys. Rev. E, Stat. Phys. Plasmas Fluids Relat. Interdiscip. Top.*, vol. 68, no. 6, p. 066613, Dec. 2003.

Ivan V. Konoplev was born in USSR in 1973. He received the B.Sc. and M.Sc. degrees in physics from N. I. Lobachevsky State University of Nizhny Novgorod, Nizhny Novgorod, Russia, in 1994 and 1996, respectively, and the M.Phil. and Ph.D. degrees in physics from the University of Strathclyde, Glasgow, U.K., in 1997 and 2001, respectively.

He worked for a short period of time as a Junior Member of the research staff with the Institute of Applied Physics, Nizhny Novgorod, until 1997. Since 1997, he has been with the Atoms, Beams and Plasmas Group, Department of Physics, University of Strathclyde, where he is currently a Senior Research Fellow and is also with SUPA. He has been involved in various aspects of research on free-electron lasers, cyclotron autoresonance masers, superradiant sources, and high-current accelerators. More recently, he has primarily been concerned with research on submillimeter radiation sources based on periodic lattices and application of periodic lattices for imaging and information technology.

Philip MacInnes was born in Glasgow, U.K. He received the M.Sci. degree (with honor) in physics and the M.Sc. degree in high power RF from the University of Strathclyde, Glasgow, in 2004 and 2005, respectively, where he is currently working toward the Ph.D. degree in physics in the ABP Group.

He is also currently with SUPA, University of Strathclyde.

Adrian W. Cross received the B.Sc. degree (with honor) in physics and the Ph.D. degree from the University of Strathclyde, Glasgow, U.K., in 1989 and 1993, respectively.

In 1993, he joined the Atoms, Beams and Plasmas Group, University of Strathclyde, as a Research Fellow, where he became a Lecturer in 2000 and a Senior Lecturer in 2005 and is currently a Reader with the Department of Physics and also with SUPA. He has been involved in various aspects of research on gyrotrons, cyclotron autoresonance masers, free-electron lasers, superradiant sources, and plasma applications. More recently, he has primarily been concerned with research on radiation sources for use in accelerators and pseudospark physics.

Lorna Fisher was born in Glasgow, U.K., in 1983. She received the B.Sc. (Hons.) degree in physics and the M.Sc. degree in high power RF science and engineering from the University of Strathclyde, Glasgow, in 2005 and 2006, respectively, where she is currently working toward the Ph.D. degree in millimeter-wave resonator design in the Department of Physics.

She is also currently with SUPA, University of Strathclyde. Her research interests include electron beam devices and photonic band-gap structures in addition to high-power/frequency microwave sources.

Alan D. R. Phelps was born in U.K. in 1944. He received the B.A. degree (with honor) in physics and the M.A. degree from Cambridge University, Cambridge, U.K., in 1966 and 1970, respectively, and the Dr.Phil. degree for plasma research from the University of Oxford, Oxford, U.K., in 1970.

In 1978, he founded a research group at the University of Strathclyde, Glasgow, U.K., where he became a Full Professor in 1993. He is currently with the Department of Physics, University of Strathclyde, where he was the Head of the Department of Physics from 1998 to 2001 and is also currently with SUPA. His research interests include high-power free-electron radiation sources and plasmas.

Prof. Phelps is a Fellow of the Institute of Physics and of the Royal Society of Edinburgh.

Wenlong He received the B.Sc. degree in physics from Soochow University, Suzhou, China, in 1983, the M.Sc. degree in accelerator physics from the China Academy of Engineering Physics, Chengdu, China, in 1988, and the Ph.D. degree in relativistic electron beams and masers from the Department of Physics, University of Strathclyde, Glasgow, U.K., in 1995.

He is currently a Senior Research Fellow with the Department of Physics, University of Strathclyde, where he is also with SUPA. His main research interests include relativistic electron beams, CARMs, FELs, gyro-TWT/BWOs, and other high-power microwave devices.

Kevin Ronald was born in Glasgow, U.K. He received the B.Sc. (with honor) and Ph.D. degrees in physics from the University of Strathclyde, Glasgow, in 1992 and 1997, respectively.

He is currently a Lecturer with the Department of Physics, University of Strathclyde, where he is also currently with SUPA. His research career commenced with his investigations into the operation of plasma flare cathodes. Recently, his research has included the scaling of corrugated waveguides to the millimeter-wave band with the development of a 95-GHz BWO, the creation of an experiment to reproduce critical aspects of the complex cyclotron resonant electrodynamics of the Earth's auroral magnetosphere, and the development of surface lattices to guarantee highly selective mode control and reflection in grossly oversized resonators.

Colin G. Whyte was born in Selkirk, U.K., in 1969. He received the B.Sc. degree in physics from the University of Glasgow, Glasgow, U.K., in 1991 and the M.Sc. degree in laser physics and pulsed power technology and the Ph.D. degree in physics from the University of St Andrews, St Andrews, U.K., in 1992 and 1996, respectively.

Since 1996, he has been with the ABP Group, Department of Physics, University of Strathclyde, Glasgow, where he is also currently with SUPA. His research interests include the design and experimental investigation of high-power broadband microwave amplifiers and oscillators, including novel helical gyro-TWT devices and reverse-guide-field free-electron lasers. He also designs and builds high-voltage pulsed power supplies.

Craig W. Robertson was born in Ayrshire, U.K., in 1977. He received the B.Sc. (Hons.) degree in physics and the Ph.D. degree from the University of Strathclyde, Glasgow, U.K., in 1999 and 2004, respectively.

He is currently with SUPA, Department of Physics, University of Strathclyde. His interests include low-temperature plasma production and diagnostics, as well as high-power microwave sources.

Excitation of surface field cavity and coherence of electromagnetic field scattering on two-dimensional cylindrical lattice

I. V. Konoplev,[1,a] L. Fisher,[1] A. W. Cross,[1] A. D. R. Phelps,[1] K. Ronald,[1] and M. Thumm[2]
[1]*Department of Physics, SUPA, University of Strathclyde, Glasgow G4 0NG, United Kingdom*
[2]*Karlsruhe Institute of Technology (KIT), Institute for Pulsed Power and Microwave Technology (IHM) and Institute of High Frequency Techniques and Electronics (IHE), Karlsruhe D-76131, Germany*

(Received 13 August 2010; accepted 30 November 2010; published online 28 December 2010)

The excitation of a surface field cavity based on a large area two-dimensional cylindrical lattice and surface field scattering within the cavity are investigated. It is shown that the interaction between surface and volume fields via distributed scatterers becomes coherent and the cavity excitation takes place only when it is irradiated with a near cut-off transverse-magnetic polarized field. The coherence of the radiation observed from the surface field scattering is investigated. © *2010 American Institute of Physics*. [doi:10.1063/1.3529953]

The evolution of electromagnetic (EM) fields inside and on the surface of structures based on periodic lattices is an important problem.[1–15] The lattice provides an interface where nonlinear and nonstationary phenomena, associated with an interaction between active media and EM fields take place.[1,3–7] The understanding of the EM field evolution inside and on the surface of a periodic lattice will result in the realization of many concepts and ideas such as surface plasmon amplifiers,[1] signal transformations,[2] particle acceleration,[6] and cloaking devices.[8] It will lead to the realization of compact, oscillators operating in the high-gigahertz, terahertz,[3–5] and x-ray[7] frequency ranges. Already nanoparticles and nanowires have been suggested to form the interaction regions, with localized surface fields tightly coupled to the surface, allowing an interaction with the surrounding active media.[1,9] The size of the particles (less than the operating wavelength λ) ensures individual emitters/scatterers are synchronized, resulting in a coherent emission. Here we consider an "inverted model," i.e., a hollow copper cylinder with circumference much larger than λ and the scatterers arranged in a two-dimensional (2D) periodic lattice on the cylinder's inner wall (2D corrugation of the metal cylinder inner surface[4,10,11]). The coupling of the surface field (SF) to the structure's wall is mitigated by this 2D periodic lattice[9,12,13] which supports localized SFs bounded to and decaying from the lattice toward the cavity center and provides coupling between the localized surface and volume EM fields. The single element of the corrugation has dimensions less than λ and plays the role of a scatterer. The coupling between surface and volume fields takes place inside the frequency range defined by the Bragg resonance conditions[2,9–15] and we show that within the cylindrical lattice it depends on the incident wave polarization and modal structure. We demonstrate that the eigenmode excitation takes place if the incident wave is a near cut-off transverse-magnetic (TM) wave, which ensures the synchronization of radiation from an individual scatterer. It is shown that only in this case the SF coherent scattering from a large area (in comparison with λ^2) 2D lattice can be observed. It is also shown that if coupling between the SFs and the set of propagating waveguide modes takes place on the lattice, either partially coherent or incoherent radiation is observed.

The structure studied in this letter was made by electroforming a copper tube[2] with a 2D corrugation of the inner wall [Fig. 1(a)]. This produces an open, SF cavity. The 2D periodic corrugation on the surface of the cylindrical waveguide is defined as: $r=r_0+\Delta r \cos \bar{k}_z z \cos \bar{m}\phi$.[3,4,11,14] Here, Δr is the corrugation amplitude ($\Delta r \ll \lambda$), r_0 is the waveguide mean radius ($r_0 \gg d_z$, $r_0 \gg \lambda$), $\bar{k}_z=2\pi/d_z$, $d_z \leq \lambda$ is the lattice longitudinal period, and $\bar{m}$ is the lattice azimuthal number. The photograph [Fig. 1(a)] and schematic [Fig. 1(b)] of the experiments are shown. The forward transmission depen-

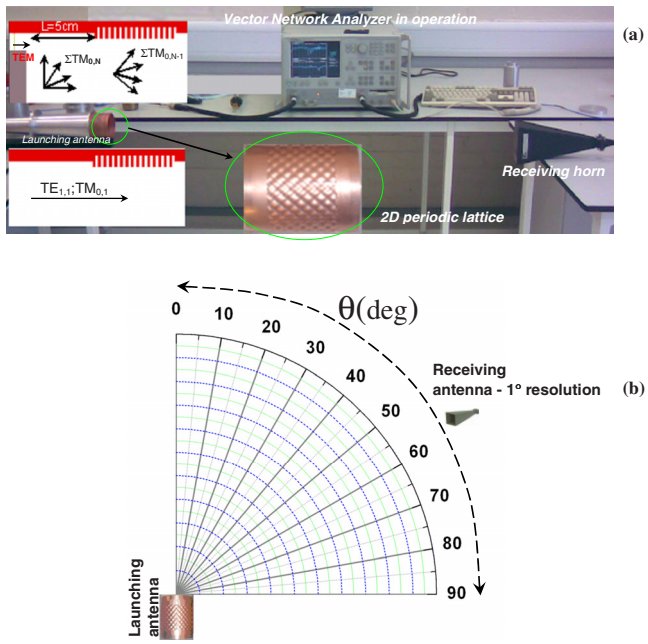

FIG. 1. (Color online) (a) Photographs of experimental setups constructed to study the cylindrical 2D periodic structure (diameter 80 mm, corrugation depth 1 mm, 28 azimuthal variations, longitudinal period 8 mm, and length 48 mm) and based on coaxial (top inset) and cylindrical (bottom inset) signal launches. The insets are schematics of the setups with arrows illustrating the waves' propagations. The smooth section of length $L=5$ cm separating the lattice from the launcher is a cut-off wave filter. (b) Schematic of the experiment to study the radiation mode patterns from the SF and SCW cavities.

[a]Author to whom correspondence should be addressed. Electronic mail: ivan.konoplev@strath.ac.uk. Tel.: +44(0)-141-548-5818. FAX: +44-141-552-2891.

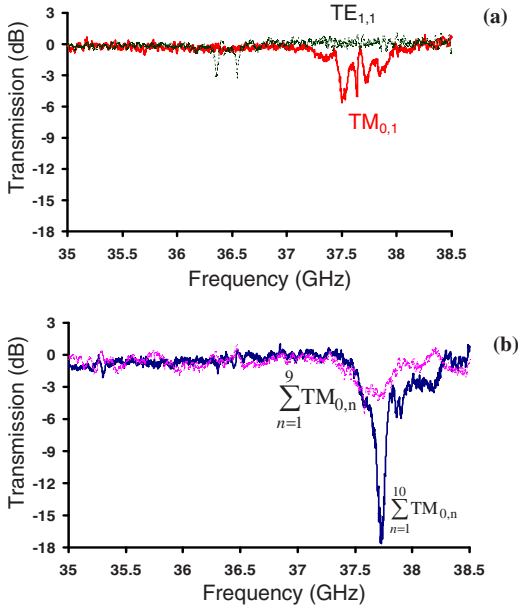

FIG. 2. (Color online) (a) The dependence of the transmission through the SF cavity on the frequency, if the input wave-beam is formed by $TE_{1,1}$ (dotted line) and $TM_{0,1}$ (solid line) modes of cylindrical waveguide. (b) The dependence of the transmission through the SF cavity on the frequency if the input wave-beam is formed by the set of propagating $TM_{0,n}$ (excluding the cut-off wave) waves (dotted line) and by the set of all $TM_{0,n}$ (including the cut-off wave) (solid line) waves of the cylindrical waveguide.

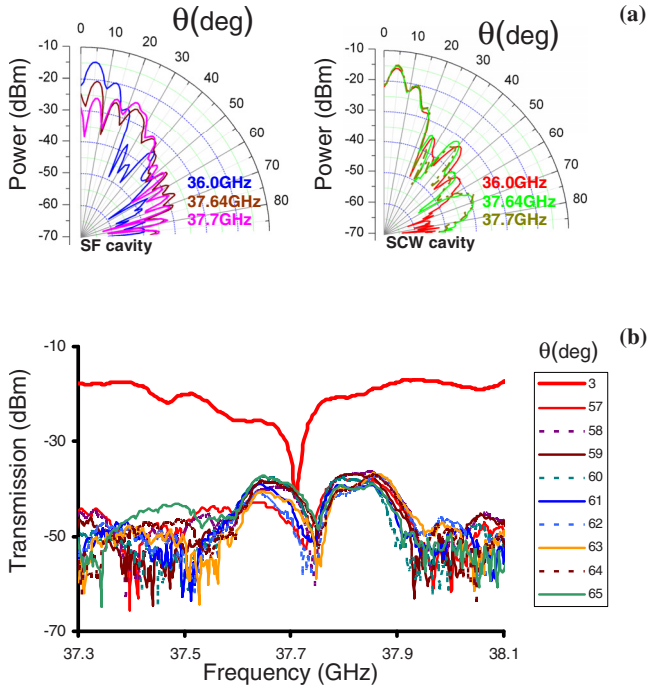

FIG. 3. (Color online) (a) The diagram illustrating the output radiation patterns vs receiving antenna angular position observed from SF (graph 1) and SCW (graph 2) cavities for the set of frequencies (36, 37.64, and 37.7 GHz). (b) Dependence of the signal transmission through the SF cavity observed for the set of angular positions of the receiving antenna.

dence of the electromagnetic (EM) radiation on the frequency [Fig. 1(a)] and the frequency dependence of the output power for the set of receiving antenna angles [Fig. 1(b)] have been studied. The results observed are calibrated and compared against the data obtained from the measurements of a smooth cylindrical waveguide (SCW) cavity of similar dimensions. To excite the cavity eigenmode, the structure[4] was irradiated via a conical horn using the EM wave-beams formed by the $TE_{1,1}$, $TM_{0,1}$, and $\Sigma TM_{0,n}$ modes [Fig. 1(a)] of cylindrical waveguide (the subscripts indicate the numbers of modes' azimuthal and radial variations, respectively). To observe the modes a transmission line operating in the frequency-band (33–40 GHz) was constructed.[11] The smooth waveguide, of length 5 cm, [top inset to Fig. 1(a)], was located between the coaxial launcher and the SF cavity in order to filter the cut-off $TM_{0,10}$ mode, as illustrated in the top inset to Fig. 1(a). The pick-up horn to receive the transmitted signals was located ~1.2 m away from the structure being studied. In the first set of experiments, a frequency sweep from 35 to 40 GHz was conducted and the spectral analysis of the transmitted signals was performed. The SF cavity was irradiated with the signal formed by the $TE_{1,1}$ and $TM_{0,1}$ modes of circular waveguide having $k_\perp \ll k_z$ [bottom inset, Fig. 1(a)]. The results calibrated against the data from the SCW cavity measurements are shown in Fig. 2(a). If the signal is formed by a $TE_{1,1}$ (s-polarized) wave, the coupling between the surface and volume fields (a scattering of the incident wave) was not observed and the transmission was not affected (dotted lines). This indicates that the SF is not excited, which agrees well with previous observations.[9,12,13,15] If however, the cavity is radiated with the $TM_{0,1}$ (p-polarized) wave [Fig. 2(a), solid line] a transmission gap in the frequency region between 37.5 and 38 GHz (as expected from the Bragg condition) is present. The gap observed in this frequency band is relatively small (~−5 dB) and has an irregular shape. This is indicative of weak coupling between the SF and the propagating wave ($k_\perp \ll k_z$). The single scatterers which form the lattice are not synchronized as the propagating wave freely radiates from the structure, leading to an incoherent scattering of the EM fields on the lattice and the "weak response" observed. Then the cylindrical launcher was substituted with the coaxial transmission line so only the transverse-electromagnetic wave can be excited.[11] The line was terminated before the periodic structure resulting in excitation of the set of $TM_{0,n}$ waves of the cylindrical waveguide where $n \in [1,10]$ and $n=10$ corresponds to the cut-off number of the radial variations. The intermediate section of the smooth waveguide [top inset Fig. 1(a), $L=5$ cm] filters out the cut-off wave ($n=10$) resulting in SF cavity excitation only by the propagating waves, i.e., $\Sigma_{n=1}^{9} TM_{0,n}$. The gap observed [Fig. 2(b), dotted line] has approximately the same amplitude and bandwidth as before (~−5 dB, ~0.5 GHz) but a more regular shape. This indicates, as in the previous case, that incoherent scattering takes place (small amplitude, wide gap) and a high-Q eigenmode is not formed inside the cavity. The presence of a number of propagating waves having different modal structures ensures a more regular (smoother) shape of the gap. Removing the regular waveguide section allows excitation of the SF cavity with the full set of waves including the cut-off wave $TM_{0,10}$. In this case a strong and narrow gap (≈−15 dB, 80 MHz) in the transmitted signal spectrum was observed [Fig. 2(b), solid line] indicating the excitation of the cavity and coherent scattering of the EM fields on the corrugation. To study the coherence of the scattered field, the angular (θ) dependence of the power of the output radiation was investigated [Fig. 1(b)] using small area (better then 1° angular resolution) horn antenna. The results are presented in Fig. 3(a) showing the output radiation patterns for θ

$\in[0°-90°]$ (graph 1 corresponds to the SF cavity, graph 2 corresponds to the SCW cavity). The measurements were conducted for the following frequencies: 36 GHz (far from the gap center), 37.64 GHz, and 37.7 GHz (in the vicinity of the gap center). Comparing the results one notes that the radiation patterns are the same at 36 GHz, however, tuning the signal frequency toward the gap center the amplitude of the central lobe $\theta\in[0°-20°]$ (SF cavity) is decreased, while it is constant over the whole frequency range in the case of the SCW cavity. Let us look at the regions of graph 1 associated with the angles $\theta\in[20°;40°]$ and $\theta\in[50°;90°]$ where increase (up to 15 dB) in the field amplitude has been observed at the frequencies 37.64 and 37.7 GHz. The region $\theta\in[20°;40°]$ (small scattering angle) is associated with the incoherent scattering of the EM fields (i.e., coupling between SFs and propagating waves on the lattice), while the region $\theta\in[50°;90°]$ (large scattering angle) is associated with cavity excitation and coherent scattering of the EM fields (coupling of the SF and near cut-off wave). The amplitude increase is also observed in the region $\theta\in[60°;90°]$ of graph 2 and is due to input signal coupling to the near cut-off wave of the cylindrical waveguide. Comparing the graphs one notes that the radiation lobe at $\theta\in[60°;90°]$ (graph 2) is smooth (single source radiation, no interference patterns) as the lobe in the region $\theta\in[20°;40°]$ (graph 1) (incoherent scattering, no interference observed), while the radiation patterns at $\theta\in[50°;90°]$ (graph 1) have a fine periodic ($\sim6°$) structure with the contrast (difference between peaks and trough) increasing as the signal frequency is tuned from 37.64 to the 37.7 GHz. The fine structures and variation of the contrast (graph 1) resemble diffraction patterns and illustrate the behavior of coherent radiation (strong contrast) and partially coherent radiation (weak contrast) scattering and interference. Taking into account that the SF is bound to the lattice, the set of oscillators (individual scatterers) can be approximated by a narrow annular ring, allowing the periodicity of the fine structures observed to be estimated by using the "obscured Airy disc" model.[16] Assuming that the diameters of the aperture and obscuring disk are close to each other, the minima locations are at $\sim(48°, 54°, 60°, 66°, 72°, 79°, 86°)$ which agrees well with the experimental data. In Fig. 3(b) the frequency dependencies of signal transmissions through the SF cavity (not calibrated against SCW cavity) for the set of receiving antenna angles $\theta\in[3°,57°-65°]$ are shown. The large signal (~10 dB above the noise level) in the frequency region (37.65–37.85 GHz) has been observed at the angles of the receiving antenna $\theta\in[57°-65°]$, illustrating the coupling between near cut-off waves and the SF. The minima in the signal transmission traces are due to the destructive interference of the waves originating from the different scatterers. The results [Fig. 3(b)] show the excitation of the cavity eigenmode at the center of the pass band minimum (~37.7 GHz), while the frequency interval, in which the deviations of the pass band minimum were observed , defines the eigenmode Q-factor (~700).

In this letter we considered a cylindrical SF cavity based on discrete scatterers arranged in a 2D lattice on the cylindrical waveguide wall. The SF, supported by the lattice, is bound to the metal waveguide and coupled to the near cut-off mode of the waveguide. We demonstrated the experimental setup required to excite such a structure and the results of the experimental studies. It is shown that the coherence of the fields scattering on the lattice and the cavity excitation depend on the incident wave polarization, frequency, and modal structure. It has been demonstrated that the excitation of the SF cavity's eigenmode and coherent scattering take place only if the input is a TM polarized, near cut-off wave. We have shown that the coupling of the SFs to the near cut-off wave of the waveguide led to synchronization of the SFs and "switching" the system into a "coherent state" associated with the cavity high-Q-eigenmode excitation. It has been shown that the SFs can also be excited by propagating waves, however, the radiation observed due to such scattering was either partially coherent or incoherent. The diffraction patterns have been measured and analyzed. The SF cavity Q-factor has been estimated and result agrees with numerical predictions. It is worthwhile noting that a SF cavity studied can be compatible with a broad variety of active media, including electron beams and plasmas.[2–7,10,11] The topology of the structure allows it to be applied as a vessel for vacuum, gas, plasmas, and to form a high-Q cavity.[4,14] The structures have a notable resemblance to the nanoparticles doped fibers, light wells, and graphene nanotubes.

[1] D. J. Bergman and M. I. Stockman, Phys. Rev. Lett. **90**, 027402 (2003).
[2] G. Burt, S. V. Samsonov, K. Ronald, G. G. Denisov, A. R. Young, V. L. Bratman, A. D. R. Phelps, A. W. Cross, I. V. Konoplev, W. He, J. Thomson, and C. G. Whyte, Phys. Rev. E **70**, 046402 (2004); I. V. Konoplev, P. MacInnes, A. W. Cross, A. D. R. Phelps, L. Fisher, and K. Ronald, Appl. Phys. Lett. **93**, 231110 (2008); I. V. Konoplev, P. McGrane, A. D. R. Phelps, A. W. Cross, and K. Ronald, *ibid.* **87**, 121104 (2005).
[3] I. V. Konoplev, A. W. Cross, A. D. R. Phelps, W. He, K. Ronald, C. G. Whyte, C. W. Robertson, P. MacInnes, N. S. Ginzburg, N. Y. Peskov, A. S. Sergeev, V. Y. Zaslavsky, and M. Thumm, Phys. Rev. E **76**, 056406 (2007).
[4] I. V. Konoplev, L. Fisher, K. Ronald, A. W. Cross, A. D. R. Phelps, C. W. Robertson, and M. Thumm, Appl. Phys. Lett. **96**, 231111 (2010); I. V. Konoplev, L. Fisher, A. W. Cross, K. Ronald, A. D. R. Phelps, and C. W. Robertson, *ibid.* **96**, 261101 (2010).
[5] Yu. A. Grishin, M. R. Fuchs, A. Schnegg, A. A. Dubinskii, B. S. Dumesh, F. S. Rusin, V. L. Bratman, and K. Möbius, Rev. Sci. Instrum. **75**, 2926 (2004).
[6] E. I. Smirnova, A. S. Kesar, I. Mastovsky, M. A. Shapiro, and R. J. Temkin, Phys. Rev. Lett. **95**, 074801 (2005)..
[7] V. Karagodsky, D. Schieber, and L. Schächter, Phys. Rev. Lett. **104**, 024801 (2010).
[8] J. B. Pendry, L. Martin-Moreno, and F. J. Garcia-Vidal, Science **305**, 847 (2004).
[9] S. A. Maier, S. R. Andrews, L. Martin-Moreno, and F. J. Garcia-Vidal, Phys. Rev. Lett. **97**, 176805 (2006).
[10] N. E. Glass, Phys. Rev. A **36**, 5235 (1987).
[11] A. W. Cross, W. He, I. V. Konoplev, A. D. R. Phelps, K. Ronald, G. R. M. Robb, C. G. Whyte, N. S. Ginzburg, N. Y. Peskov, and A. S. Sergeev, Nucl. Instrum. Methods Phys. Res. A **475**, 164 (2001); I. V. Konoplev, A. D. R. Phelps, A. W. Cross, and K. Ronald, Phys. Rev. E **68**, 066613 (2003).
[12] J. M. Pitarke, J. E. Inglesfield, and N. Giannakis, Phys. Rev. B **75**, 165415 (2007).
[13] G. Gaborit, D. Armand, J.-L. Coutaz, M. Nazarov, and A. Shkurinov, Appl. Phys. Lett. **94**, 231108 (2009).
[14] N. S. Ginzburg, I. V. Konoplev, and A. S. Sergeev, Tech. Phys. **41**, 465 (1996); I. V. Konoplev, A. W. Cross, P. MacInnes, W. He, C. G. Whyte, A. D. R. Phelps, C. W. Robertson, K. Ronald, and A. R. Young, Appl. Phys. Lett. **89**, 171503 (2006); I. V. Konoplev, A. W. Cross, P. MacInnes, W. He, A. D. R. Phelps, C. G. Whyte, K. Ronald, and C. W. Robertson, *ibid.* **92**, 211501 (2008).
[15] A. V. Zayats, I. I. Smolyaninov, and A. A. Maradudin, Phys. Rep. **408**, 131 (2005); R. J. Seymour, J. J. Krupczak, and G. I. Stegeman, Appl. Phys. Lett. **44**, 373 (1984).
[16] C. Rivolta, Appl. Opt. **25**, 2404 (1986).

Mechanism of azimuthal mode selection in two-dimensional coaxial Bragg resonators

N. S. Ginzburg,[1] N. Yu. Peskov,[1,a)] A. S. Sergeev,[1] V. Yu. Zaslavsky,[1] I. V. Konoplev,[2] L. Fisher,[2] K. Ronald,[2] A. D. R. Phelps,[2] A. W. Cross,[2] and M. Thumm[3]
[1]*Institute of Applied Physics, RAS, Nizhny Novgorod 603950, Russia*
[2]*Department of Physics, SUPA, University of Strathclyde, Glasgow G4 0NG, United Kingdom*
[3]*Forschungszentrum Karlsruhe, IHM, Karlsruhe 76021, Germany*

(Received 24 September 2008; accepted 5 May 2009; published online 25 June 2009)

The analysis of electrodynamic properties of two-dimensional (2D) Bragg resonators of coaxial geometry realizing 2D distributed feedback was carried out using a quasioptical approach of coupled-wave theory and three-dimensional (3D) simulations. It is shown that the high selectivity of a 2D Bragg resonator over the azimuthal index originates from the topological difference in the dispersion diagrams of the normal symmetrical and nonsymmetrical waves near the Bragg resonance frequency in a double-periodic corrugated unbounded waveguide. For a symmetrical mode near the Bragg frequency it was found that the group velocity tends to zero as well as its first derivative. This peculiarity of the dispersion characteristic provides the conditions for the formation of an eigenmode with a Q-factor essentially exceeding the Q-factors of other modes. The results of the theoretical analysis coincide well with results of 3D simulations using the CST code "MICROWAVE STUDIO" and confirm the high azimuthal selectivity of the system. © *2009 American Institute of Physics*. [DOI: 10.1063/1.3143019]

I. INTRODUCTION

The use of two-dimensional (2D) distributed feedback has been proposed[1,2] as a method of producing spatially coherent radiation from either sheet or annular high-current relativistic electron beams with the transverse size greatly exceeding the wavelength. The 2D distributed feedback can be realized in planar and coaxial 2D Bragg cavities with a double-periodic corrugation of the walls. On this corrugation mutual scattering of the electromagnetic energy fluxes propagating in the forward, backward, and transverse directions (relative to the direction of the electron beam propagation) takes place. These transverse waves can act to synchronize radiation from different parts of a large size electron beam. Experimental studies of free electron masers (FEMs) exploiting this novel feedback mechanism have demonstrated effective transverse (azimuthal) mode selection both in planar[3] and coaxial[4,5] schemes.

In support of the FEM experiments detailed studies of the mechanism of mode selection in 2D Bragg resonators is required. The present paper is devoted to the analysis of the electrodynamic properties of 2D Bragg cavities of coaxial geometry with the diffraction effects taken into account. In Sec. II the basic model and equations describing the scattering of the four partial electromagnetic waves propagating in the longitudinal and azimuthal directions are presented. In Sec. III dispersion properties of the normal waves propagating in an unbound double-periodic corrugated waveguide of coaxial geometry are studied. It is shown that the symmetrical and nonsymmetrical normal waves demonstrated totally different behavior near the Bragg resonance frequency. This results in a high selectivity of the coaxial 2D Bragg resonators over the azimuthal mode indices. Such resonators, which are formed from double-periodic coaxial waveguide sections of finite length are considered in Sec. IV. The results of this theoretical analysis are corroborated by three-dimensional (3D) modeling, which was performed using the code CST "MICROWAVE STUDIO" and is described in Sec. V.

II. MODEL AND BASIC EQUATIONS

A coaxial 2D Bragg structure (Fig. 1) consists of two conductors of radii r_{in} and r_{out} having a small depth corrugation which is a superposition of two helical corrugations with opposite rotations:

$$a = \frac{a_1}{2}\cos(\bar{h}_z z)\cos(\bar{M}\varphi) = \frac{a_1}{4}[\cos(\bar{h}_z z - \bar{M}\varphi) + \cos(\bar{h}_z z + \bar{M}\varphi)], \quad (1)$$

where a_1 is the corrugation depth, $\bar{h}_z = 2\pi/d_z$, d_z is the period of the corrugation along the z-coordinate, $\bar{M}$ is the number of variations along the corrugation over the azimuthal coordinate, z and φ are the longitudinal and azimuthal coordinates, respectively. We assume small curvature of the resonator surface, i.e., that the waveguide mean radius $r_0 = (r_{in} + r_{out})/2$ greatly exceeds the distance between the conductors $a_0 = r_{out} - r_{in}$ and the radiation wavelength λ:

$$r_0 \gg a_0, \quad r_0 \gg \lambda. \quad (2)$$

In this approximation the dispersion equation for the eigenwaves of a coaxial waveguide can be reduced to the form[6,7] which is similar to the case of a planar waveguide:

a)Electronic mail: peskov@appl.sci-nnov.ru.

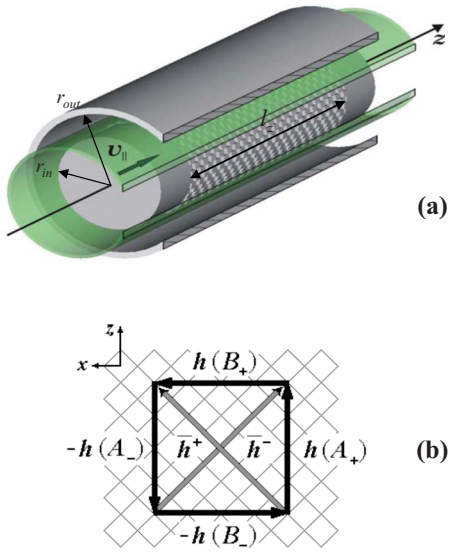

FIG. 1. (Color online) (a) Schematic diagram of FEM with coaxial 2D Bragg resonator and annular electron beam moving in the $+z$ direction. (b) Diagram illustrating the scattering of partial waves on the 2D Bragg grating ($\vec{h}_1$ and $\vec{h}_2$ are the wave vectors of the partial waves $A_\pm$ and $B_\pm$, respectively, and $\vec{\bar{H}}_\pm = \bar{h}_x\vec{x}^0 \pm \bar{h}_z\vec{z}^0$ are the grating vectors).

$$\frac{\omega^2}{c^2} \approx h_z^2 + h_x^2 + \kappa_p^2, \tag{3}$$

where h_z is the longitudinal wavenumber, $h_x = M/r_0$ is the transverse (azimuthal) wavenumber, $\kappa_p \approx p\pi/a_0$ is the radial wavenumber, M and p are the azimuthal and the radial mode index, respectively. Thus, we can adopt the planar model and introduce the transverse coordinate $x = r_0\varphi$ over the azimuth of the system.

Under assumption (2) together with the assumption of a shallow corrugation: $\bar{h}_{x,z}a_1 \ll 1$, we present the electromagnetic field inside the structure in the form of four partial wave beams propagating in the $\pm z$ and $\pm x$ directions:

$$\vec{E} = \mathrm{Re}[(A_+\vec{E}_1^0 e^{-ih_1 z} + A_-\vec{E}_1^0 e^{ih_1 z} + B_+\vec{E}_2^0 e^{-ih_2 x} + B_-\vec{E}_2^0 e^{ih_2 x})e^{i\omega t}], \tag{4}$$

where $A_\pm(x,z)$, $B_\pm(x,z)$ are slow functions of the longitudinal and transverse (azimuthal) coordinates and the functions $\vec{E}_{1,2}^0(r)$ describe radial distributions of the waves and coincide with one of the modes of a coaxial waveguide. The four partial waves with the wavenumbers $h_{1,2}$ undergo coupling on the double-periodic structure (1) if the Bragg resonance conditions are satisfied [see. Fig. 1(b)]:

$$h_1 \approx \bar{h}_z, \quad h_2 \approx \bar{h}_x, \tag{5}$$

where $\bar{h}_x = \bar{M}/r_0$. Under condition $2\pi/d_z = \bar{M}/r_0$ we have $\bar{h}_x = \bar{h}_z = \bar{h}$ and according to Eq. (5) all the four partial waves possess the same wavenumber $h_1 = h_2 = h$ and have the same number of field variations over the radius. For simplicity we consider coupling of the lowest waves having zero variation of the field over the radius $p=0$. This corresponds to longitudinally propagating partial wave-beam ($A_\pm$) consisting of a number of $\mathrm{TE}_{M,0}$-type modes of a coaxial waveguide with low azimuthal indices ($M = 0, 1, 2, \ldots$) including the fundamental TEM-mode ($M=0$) and transversely propagating wave beams ($B_\pm$) consisting of $\mathrm{TE}_{M,0}$-modes (whispering gallery modes) with high azimuthal indices ($M \approx \bar{M} \gg 1$). It is important to note that the radial structure of the $\mathrm{TE}_{M,0}$-type modes is also close to a TEM-type wave when conditions (2) are fulfilled. As a manifestation of this fact the dispersion equation of the partial waves reduces to form (3).

The process of the partial waves scattering on corrugation (1) may be described by the set of coupled-wave equations (compare with Refs. 2 and 8):

$$\pm\frac{\partial A_\pm}{\partial z} + i\delta A_\pm + i\alpha(B_+ + B_-) = 0, \tag{6a}$$

$$\frac{i}{2\bar{h}}\frac{\partial^2 B_\pm}{\partial z^2} \pm \frac{\partial B_\pm}{\partial x} + i\delta B_\pm + i\alpha(A_+ + A_-) = 0, \tag{6b}$$

where $\delta = (\omega - \bar{\omega})/c$ is the frequency mismatch from the Bragg resonance $\bar{\omega} = \bar{h}c$ and α is the wave coupling coefficient, which for the considered case of coupling between TEM and $\mathrm{TE}_{M,0}$-modes when both conductors are corrugated equals

$$\alpha = \frac{a_1\bar{h}}{8a_0}. \tag{7}$$

Note that for azimuthally propagating waves $B_\pm$ we have the parabolic type Eq. (6b) which includes diffraction effects (these transverse waves would be locked inside the resonator if the diffraction is neglected). At the same time for longitudinally propagating waves $A_\pm$ diffraction effects are not so important and have no significant influence on the properties of the system.

Due to the coaxial geometry of the cavity the wave-beam amplitudes should satisfy the cyclic boundary conditions:

$$B_\pm(x + l_x, z) = B_\pm(x,z), \quad A_\pm(x + l_x, z) = A_\pm(x,z), \tag{8}$$

where $l_x = 2\pi r_0$ is the resonator perimeter. Conditions (8) allow a solution of Eq. (6) to be presented in a Fourier series:

$$A_\pm(x,z) = \sum_{m=-\infty}^{\infty} A_\pm^m(z)e^{2\pi imx/l_x}, \quad B_\pm(x,z) = \sum_{m=-\infty}^{\infty} B_\pm^m(z)e^{2\pi imx/l_x}. \tag{9}$$

Each Fourier term in Eq. (9) with its own index m may be considered as a normal wave. Substituting Eq. (9) in Eq. (6) for the normal wave amplitude we get

$$\pm\frac{dA_\pm^m}{dz} + i\delta A_\pm^m + i\alpha(B_+^m + B_-^m) = 0, \tag{10a}$$

$$\frac{1}{2\bar{h}}\frac{d^2B_\pm^m}{dz^2} + \left(\delta \pm \frac{2\pi m}{l_x}\right)B_\pm^m + \alpha(A_+^m + A_-^m) = 0. \tag{10b}$$

Note that in correspondence with relations (3) and (4) for the transversely propagating partial waves $B_\pm$ the index m must be considered in addition to the azimuthal index $\bar{M}$ (it is

assumed $m \ll \bar{M}$). Thus, to clarify the nomenclature of the normal waves of a corrugated coaxial waveguide, the normal wave with index $m=0$, which is called a symmetrical wave, consists of both the longitudinal partial waves $A_{\pm}$, which only possess an azimuthally symmetrical structure, and transversely propagating partial waves $B_{\pm}$ with high azimuthal index $\bar{M}$. In the general case, the normal wave with index m is a set of four coupled partial waves $A_{\pm}$ and $B_{\pm}$, which are characterized by azimuthal indices m and $M = \bar{M} \pm m$, respectively.

III. DISPERSION PROPERTIES OF THE NORMAL WAVES IN DOUBLE-PERIODIC CORRUGATED COAXIAL WAVEGUIDES

Let us consider normal waves propagating in an unbounded coaxial waveguide having a double-periodic corrugation of the walls (1). Looking for solution of Eq. (10) in the form $A_{\pm}^{m} = a_{\pm}^{m} e^{i\Gamma z}$, $B_{\pm}^{m} = b_{\pm}^{m} e^{i\Gamma z}$ we get the dispersion equation for the normal waves

$$\left(2\bar{h}\delta - 2\bar{h}\frac{2\pi m}{l_x} - \Gamma^2\right)\left(2\bar{h}\delta + 2\bar{h}\frac{2\pi m}{l_x} - \Gamma^2\right)(\delta^2 - \Gamma^2) = 8\alpha^2\bar{h}\delta(2\bar{h}\delta - \Gamma^2). \tag{11}$$

Obviously dispersion Eq. (11) describes coupling of the four partial waves given by Eq. (4). At $\alpha=0$ this equation reduces to four separate equations: two equations describing both longitudinally propagating waves $A_{\pm}$

$$\delta = \pm\Gamma \tag{12a}$$

and two equations describing dispersion of the transversely propagating waves $B_{\pm}$

$$2\bar{h}\delta = \pm 2\bar{h}\frac{2\pi m}{l_x} + \Gamma^2. \tag{12b}$$

For $\alpha \neq 0$ the dispersion diagrams for normal waves with $m=0$ and $m=\pm 1$ are shown in Fig. 2. From comparison with the asymptotes given by Eq. (12) and shown on the same diagrams by thin lines one can conclude that the branches "1" and "2" originate from the partial waves $A_{\pm}$ while the branches "3" and "4" originated from the quasi-cut-off partial waves $B_{\pm}$. In general, the main difference in the diagrams presented as compared to traditional one-dimensional (1D) Bragg structures is the existence of a dispersion curve near the Bragg frequency $\omega \approx \bar{\omega}$ (i.e., $\delta \approx 0$). This peculiarity is obviously related with the participation in the scattering process of the quasi-cut-off partial waves $B_{\pm}$.

Even more important is the fact that the dispersion diagrams have totally different behavior in the case of azimuthally symmetric ($m=0$) and nonsymmetric normal waves. When $m=0$ for the quasi-cut-off partial waves $B_{\pm}$ the convergence of the unperturbed dispersion curves (12b) takes place and in this case the coupling of waves at $\alpha \neq 0$ result in a dispersion equation in the form

$$(2\bar{h}\delta - \Gamma^2)(\delta^2 - \Gamma^2) = 8\alpha^2\bar{h}\delta. \tag{13}$$

It follows from Eq. (13) that near the Bragg frequency instead of the traditional parabolic dependence of frequency on the wave number (which is realized, in particular, near the Bragg reflection zone in the case of the traditional resonators with a 1D corrugation[9–12]) we get the fourth order dependence[13]

$$\Gamma^4 \approx 8\alpha^2\bar{h}\delta. \tag{14}$$

Thus, near the Bragg frequency (i.e., $\delta \to 0$) not only does the group velocity of the normal wave tend to zero but its first derivative as well. This peculiarity of the dispersion characteristic of the normal wave $m=0$ near the Bragg frequency provides the conditions for the formation of an eigenmode with a Q-factor essentially exceeding the Q-factors of other modes. Indeed the dispersion diagrams for other normal waves with $m \neq 0$ have topologically different behavior [compare Figs. 2(a) and 2(b)] near $\delta \approx 0$ as well as the traditional square dependence of the frequency on the wave number at the extremes of the dispersion curves.

Let us consider now the geometrical-optical approach, which was used in previous works (see, for example, Refs. 2 and 14) for the analysis of the FEM based on coaxial 2D Bragg resonators. In the frame of Eq. (10) it corresponds to a limit $\bar{h} \to \infty$. In this case it is possible in Eq. (10) to neglect the term $\sim d^2 B_{\pm}^{m}/dz^2$, which is responsible for the diffraction of the waves $B_{\pm}$. As a result, the dispersion Eq. (11) can be reduced to

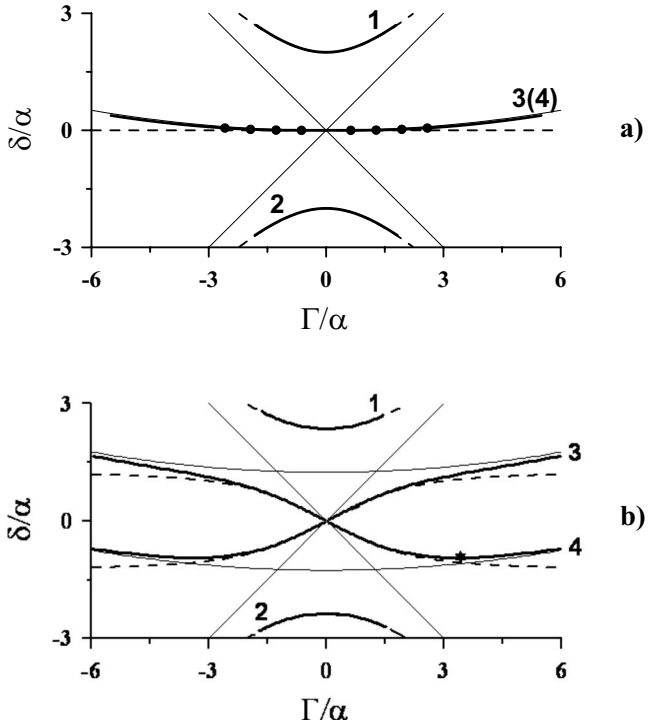

FIG. 2. Dispersion diagrams of the normal waves in the coaxial 2D Bragg structure unbounded in the longitudinal direction when $\bar{h}/\alpha = 35$: (a) symmetrical waves $m=0$ and (b) nonsymmetrical waves $m=\pm 1$ (these waves are classified by the azimuthal structure of the longitudinally propagating partial waves). Thin lines correspond to the dispersion curve of the partial waves, dashed lines show dispersion diagrams of the normal waves obtained using the geometrical-optical approach. Positions of a few symmetrical modes with the lowest longitudinal indices n are shown in (a) by circles, position of the nonsymmetrical mode having the maximum-Q in the family is shown in (b) by the asterisk.

$$\left(\delta - \frac{2\pi m}{l_x}\right)\left(\delta + \frac{2\pi m}{l_x}\right)(\delta^2 - \Gamma^2) = 4\alpha^2\delta^2. \tag{15}$$

Dispersion diagrams corresponding to Eq. (15) are shown in Fig. 2 by dashed lines. It is seen that in the region of small wavenumbers $\Gamma \leq \alpha$ these dispersion diagrams approximate well with the dispersions obtained using the full Eq. (11). The most important fact even when the geometrical-optical approach is used is that the dispersion curves demonstrate totally different behavior for the case of symmetrical ($m=0$) and nonsymmetrical ($m \neq 0$) waves, which finally results in high selectivity of the system over the azimuthal index. At the same time, the dispersion curves $\langle\langle 3\rangle\rangle$ and $\langle\langle 4\rangle\rangle$ in the case $m=0$ are transformed into a straight line: $\delta \equiv 0$. In fact, in the geometrical-optical approach the azimuthally symmetric modes are degenerate over the longitudinal index n. All these modes for any indices n have the same frequency which coincides with the Bragg resonance frequency $\bar{\omega}$ ($\delta \equiv 0$) and the same Q-factor which tends to infinity. So in this approximation these modes have no diffraction losses. However, as it was shown in Ref. 13, this degeneration can be removed when diffraction is taken into account and the dispersion curve transforms to the form given by Eq. (14). Nevertheless the use of the geometrical-optical approach in nonlinear theory is justified by the fact that the interaction with the electron beam resolves this mode degeneration (see, in particular, Refs. 2 and 14). The Q-factor of these modes would be finite when Ohmic losses are taken into consideration.

IV. MODE SELECTION IN 2D BRAGG RESONATORS OF COAXIAL GEOMETRY

To find eigenmodes of the 2D Bragg cavity having a double-periodic corrugation of finite length l_z in the longitudinal direction we should apply boundary conditions at the cavity ends at $z=0$ and $z=l_z$. We assume here an ideally matched system which could provide in the definite frequency band zero reflections for all partial waves from the ends of the corrugations. Thus, in the assumption that the partial waves do not reflect from the ends of the corrugated surface and EM fluxes from outside of the resonator are absent, the boundary conditions for Eq. (10) for the longitudinally propagating waves take the form

$$A_+(x, z=0) = 0, \quad A_-(x, z=l_z) = 0. \tag{16}$$

From Eq. (10b) for the transverse propagating wave fluxes $B_{\pm}^m$ outside the resonator $z<0$ and $z>l_z$, where the corrugation is absent $\alpha=0$, we get

$$\frac{d^2 B_{\pm}^m}{dz^2} + 2\bar{h}\left(\delta \pm \frac{2\pi m}{l_x}\right)B_{\pm}^m = 0. \tag{17}$$

General solution of Eq. (17) is

$$B_{\pm}^m = C_1^{\pm} e^{i\Lambda z} + C_2^{\pm} e^{-i\Lambda z}, \tag{18}$$

where $\Lambda = \sqrt{2\bar{h}(\delta \pm 2\pi m/l_x)}$, $C_{1,2}^{\pm}$ are the arbitrary constants. At $z<0$ only the radiated wave propagating away from the resonator edge should be presented. Thus, in Eq. (18) we should put $C_2^{\pm} \equiv 0$ and get $B_{\pm}^m = C_1^{\pm} e^{i\Lambda z}$. From the continuity of the fields $B_{\pm}^m$ and their derivatives $dB_{\pm}^m/dz$ at $z=0$ (which follows from the continuity of the electrical field and magnetic field at the resonator edge correspondingly) we get the following boundary conditions:

$$\left[\frac{dB_{\pm}^m}{dz} - i\sqrt{2\bar{h}\left(\delta \pm \frac{2\pi m}{l_x}\right)}B_{\pm}^m\right]\Bigg|_{z=0} = 0. \tag{19a}$$

In the same way, at $z=l_z$ we have

$$\left[\frac{dB_{\pm}^m}{dz} + i\sqrt{2\bar{h}\left(\delta \pm \frac{2\pi m}{l_x}\right)}B_{\pm}^m\right]\Bigg|_{z=l_z} = 0. \tag{19b}$$

Eigenfrequencies and Q-factors for the resonator modes are given by

$$\omega_{m,n} = \bar{\omega} + c\ \mathrm{Re}(\delta_{m,n}), \tag{20a}$$

$$Q_{m,n} \approx \frac{\bar{\omega}}{2c\ \mathrm{Im}(\delta_{m,n})}, \tag{20b}$$

where $\delta_{m,n}$ is the complex frequency mismatch from the Bragg resonance for the mode with the indices $\{m;\ n\}$, $n=1,2,3,\ldots$ is the longitudinal index of the modes. In the case of the azimuthally symmetric modes $m=0$ near the Bragg frequency, where we have the dispersion Eq. (14), the analytical solution for the complex eigenfrequencies can be presented in the form (see Ref. 8 for details)

$$\delta_{0,n} = \frac{\pi^4 n^4}{8\bar{h}\alpha^2 l_z^4} + i\frac{\pi^4 n^4}{4\bar{h}\alpha^3 l_z^5}. \tag{21}$$

It follows from relations (20) and (21) that the highest Q-factor (lowest diffraction losses) is realized for the mode with one longitudinal variation $n=1$. The analytical solutions (21) coincide well with the results of numerical simulation of the full characteristic equation, which can be written based on dispersion Eq. (11) and boundary conditions (16) and (19). In Fig. 3 the real and imaginary parts of δ are shown for longitudinal modes $n=1$ as a function of αl_z and demonstrate good agreement with the results of numerical simulation of this characteristic equation for $\alpha l_z \geq 3$.

The longitudinal profile of the partial waves for the fundamental eigenmode ($m=0; n=1$) for $\alpha l_x = \alpha l_z = 5$ is shown in Fig. 4(a). With the increase of the longitudinal mode indices the diffraction losses increase as $\sim n^4$. Note, that in the case of a traditional 1D Bragg resonator in the form of a single corrugated section having the same coaxial geometry and coupling coefficient, for the diffraction losses we get[9,12]

$$\mathrm{Im}(\delta_n) \approx \frac{\pi^2 n^2}{\alpha^2 l_z^3}. \tag{22}$$

Thus, we can conclude that fundamental modes in a 2D Bragg resonator have much higher Q-factors as compared to a 1D Bragg resonator. Moreover, a 2D Bragg resonator has more efficient selectivity even over the longitudinal indices as compared to a traditional 1D Bragg cavity of the same geometry.

Note, that together with the symmetrical modes positioned near $\delta \approx 0$ there are high-Q azimuthally symmetrical modes with frequencies located near $\delta \approx \pm 2\alpha$ [see Fig.

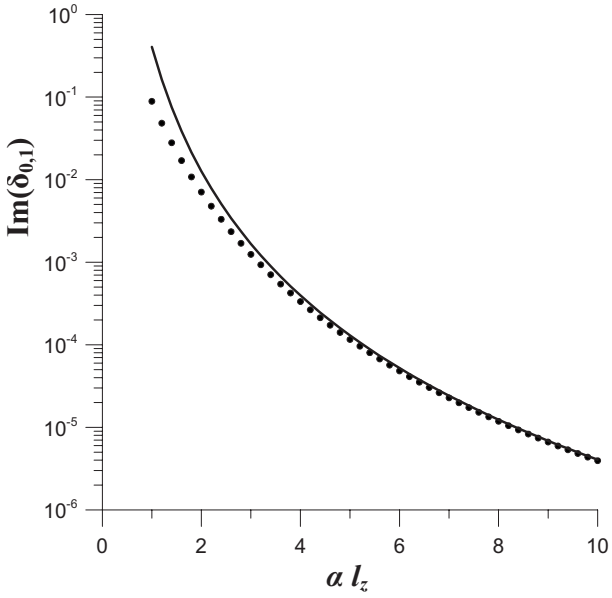

FIG. 3. Comparison of analytical (solid line) and numerical (dashed line) solutions of the characteristic equation for diffraction loss $\mathrm{Im}(\delta_{0,1})$ for the fundamental symmetrical mode ($m=0$; $n=1$): $\bar{h}/\alpha=60$, $\alpha l_x=2.5$.

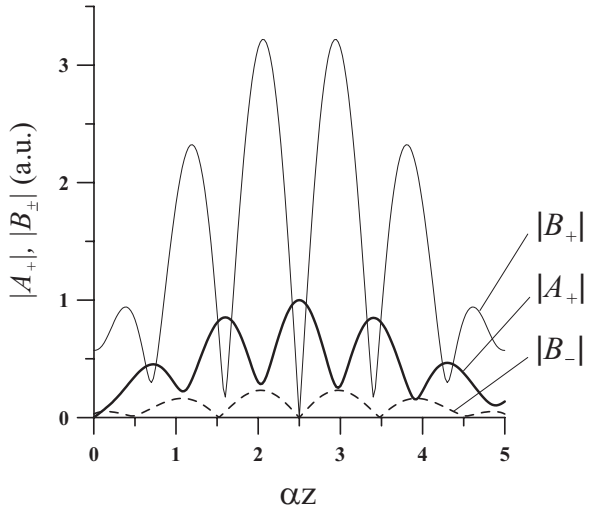

FIG. 5. Longitudinal profiles of the partial waves A_+ and $B_\pm$ for nonsymmetrical wave ($m=1$; $n=6$) having the maximum-Q in the family [in Fig. 2(b) position of this mode is shown by the asterisk]; $\bar{h}/\alpha=35$, $\alpha l_x=\alpha l_z=5$.

4(b)], i.e., near the extremes of the dispersion curves for the normal waves. Evidently, at these extremes the group velocity tends to zero as well. However the difference with the dispersion curve "3" ("4") passing through the exact Bragg frequency is that the second derivation for branches "1" and "2" is not zero and this results in significantly lower Q-factors as compared to the modes located at $\delta\approx 0$.

For nonsymmetrical waves $m\neq 0$ the complex eigenfrequencies were found by numerical solution of the characteristic equations. The profiles of the partial waves for the high-Q nonsymmetrical $m=1$ eigenmode are shown in Fig. 5. According to the simulations for the nonsymmetrical modes the maximum-Q factor is realized when the mode eigenfrequency is positioned near the minimums on the dispersion curves 3 and 4 [position of one such mode is shown in Fig. 2(b) by the asterisk], i.e., occurs near the point where the group velocity tends to zero. However similar to the case of the symmetrical modes with the eigenfrequencies located near $\delta\approx\pm 2\alpha$ we have a nonzero second derivative here as well. As a result, all these modes also have significantly

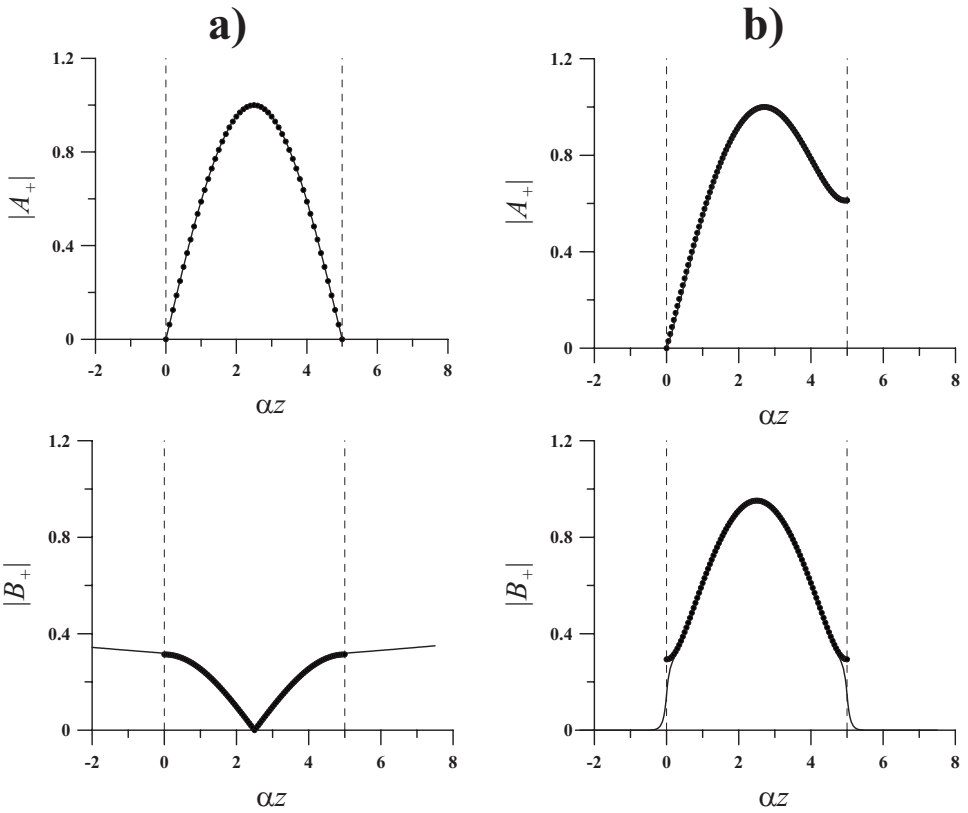

FIG. 4. Longitudinal profiles of the partial waves A_+ and B_+ for symmetrical eigenmodes ($m=0$; $n=1$) with the frequencies located near $\delta\approx 0$ (left column) and near $\delta\approx -2\alpha$ (right column): $\bar{h}/\alpha=35$, $\alpha l_x=\alpha l_z=5$. The profiles of waves found for the same resonator in the frame of the geometrical-optical approach are represented by dots.

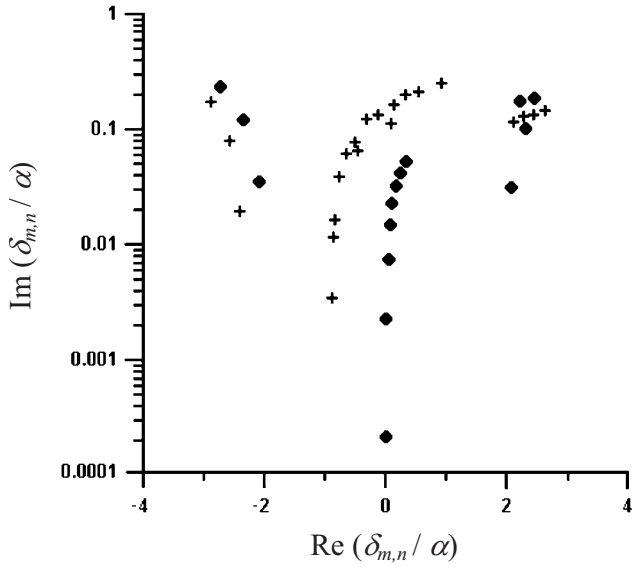

FIG. 6. The eigenmode spectrum: diffraction losses Im($\delta_{m,n}$) of the modes vs their eigenfrequencies Re($\delta_{m,n}$). Symmetrical modes $m=0$ are shown by the dots, nonsymmetrical modes $m=1$—by the crests ($\bar{h}/\alpha=35$, $\alpha l_x=\alpha l_z=5$).

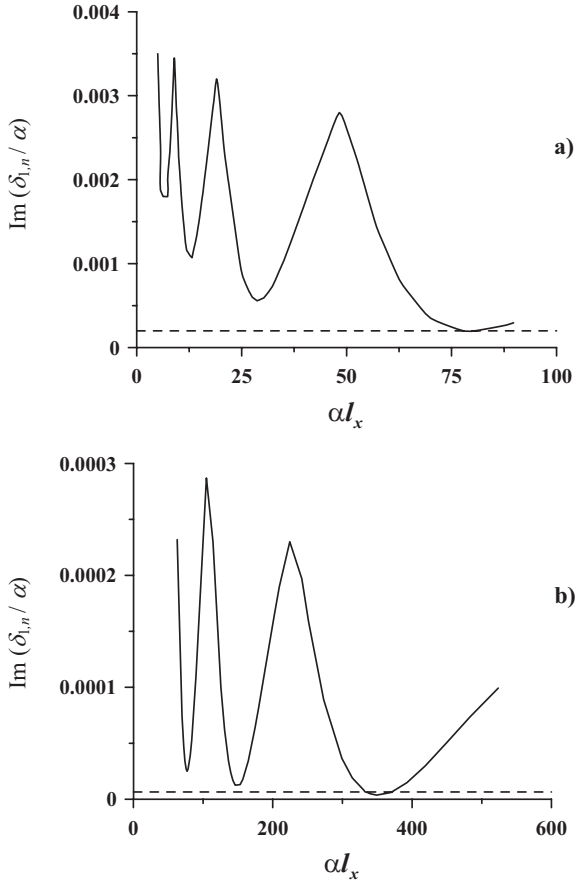

FIG. 7. Dependence of the diffraction losses Im($\delta_{1,n}$) on the normalized perimeter αl_x for nonsymmetrical mode $m=1$ having the maximum-Q (number of the longitudinal variations n of this mode varies with the change in the perimeter): $\bar{h}/\alpha=35$ and (a) $\alpha l_z=5$, (b) $\alpha l_z=10$. The dashed lines are the diffraction losses for the fundamental symmetrical mode ($m=0$; $n=1$).

lower Q-factors as compared to the fundamental symmetrical mode.

Thus, by considering all of the above, 2D Bragg resonators possess high selectivity when the perimeter is of the same order as the length of resonator $l_x \approx l_z$ and both greatly exceed the radiation wavelength $l_{x,z} \gg \lambda$. For the resonator geometry $\alpha l_x=\alpha l_z=5$ the spectrum of the eigenmodes presented in Fig. 6 shows that the diffraction losses for the fundamental mode are about an order of magnitude lower than the lowest losses of higher order modes. Note also, that the high-Q nonsymmetrical modes possess a large number of longitudinal variations of the field as well as a relatively low amplitude of the longitudinally propagating partial waves in comparison with the transversely propagating waves $A_+^{\max}/B_+^{\max} \ll 1$ (compare Figs. 4 and 5). Therefore, some additional mechanisms of so-called electronic selection exist for these modes when interacting with the electron beam [we have assumed that in the FEM the electrons only interact with the forward propagating partial wave A_+ (Refs. 2, 5, and 14)]. The electronic selection should lead to the additional discrimination of the excitation of the nonsymmetrical modes due to two factors—first, the fast longitudinal variation of field amplitude results in violating the synchronism condition, and second the low amplitude of the partial operating wave results in small coupling with the beam.

With the increase in the resonator perimeter l_x for fixed coupling parameter α and length l_z the selective properties of the resonator deteriorates. Obviously, with increasing perimeter l_x the dispersion curves 3 and 4 for the nonsymmetrical waves ($m \neq 0$) become more and more flat and in the limit $l_x \to \infty$ [see Eq. (11)] tends to the dispersion curve of the symmetrical wave, which does not depend on the perimeter. Nevertheless this implies that restrictions on the system perimeter are not severe. In Fig. 7(a) for the nonsymmetrical mode $|m|=1$ with the maximum-Q factor the dependence of the diffraction losses on the resonator perimeter is shown together with the losses of the fundamental symmetrical mode, which is shown by the dotted line. It is seen that for the given cavity length $\alpha l_z=5$ the losses of the nonsymmetrical mode approaches the losses of the fundamental symmetrical mode only when the system perimeter exceeds $\alpha l_x \geq 70$. Note that the irregularities in the dependence of the losses on the perimeter shown in Fig. 7 are caused by the change in number of the longitudinal variations n of the nonsymmetrical mode, which possesses the highest-Q factor. For example, when $\alpha l_x=5$ the highest Q-factor in the family of nonsymmetrical modes with $m=1$ is realized at the mode with $n=6$ (see Fig. 5).

It is important to note, that if the resonator length l_z increases, then the Q-factor of the fundamental symmetrical mode in accordance with Eq. (20b), Eq. (21) will grow as l_z^5 and, therefore, the selective properties of the resonator can be maintained even for larger perimeters l_x. This is confirmed by Fig. 7(b) where the dependence of the minimum diffraction losses for the nonsymmetrical modes $m=1$ on the resonator perimeter is shown for $\alpha l_z=10$. Doubling the length of the resonator will result in a significant increase in the perimeter of up to $\alpha l_x \leq 300$ [compare Figs. 7(a) and 7(b)] while still permitting high selectivity.

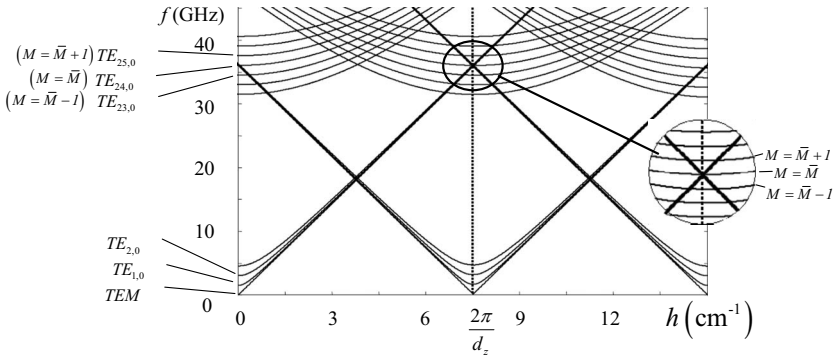

FIG. 8. Dispersion diagrams of the partial waves in a coaxial waveguide, which undergo coupling on the 2D Bragg corrugation (r_0=3.5 cm, d_z=0.8 cm, $\bar{M}$=24). The zone of effective 2D Bragg scattering is marked and shown in the large scale. Corresponding dispersion diagrams of the normal waves in this zone are presented in Fig. 2.

As can be seen from the dispersion Eq. (11) increase in the azimuthal index of the modes m is equivalent to a decrease in the effective perimeter as $l_x^{\mathrm{eff}}=l_x/m$. Thus, following from Fig. 7 an increase in the azimuthal index in general does not lead to an increase in the Q-factor of the nonsymmetrical modes. Note also, that due to the dependence of the Q-factors of the modes on the dimensionless scale parameter $\alpha l_{x,z}$, there is an additional potential ability to maintain selectivity when increasing the perimeter l_x by simultaneously decreasing the coupling coefficient α (for example, by decreasing the corrugation depth) while still keeping the normalized parameter αl_x constant. Obviously, the resonator length l_z should be increased proportionally to the perimeter.

Let us compare the results obtained using the above quasioptical approach with the geometrical-optical approach. The longitudinal profiles of the partial waves for the symmetrical eigenmodes $(m=0;n=1)$ with frequencies located near $\delta\approx 0$ and $\delta\approx -2\alpha$ which are plotted inside the resonator using the geometrical-optical approach are represented in Fig. 4 by the dots. It can be seen, that except for the zone near the boundary of the corrugation both the quasioptical and geometrical-optical approaches give similar wave profiles for the partial waves. Therefore, the partial wave amplitudes found in the frame of the geometrical-optics approach can be used to correctly calculate the energy extraction when modeling the interaction with the electron beam.

It should be noted that if one takes into account Ohmic losses the realistic situation arises where for the fundamental mode the diffraction Q-factor given by Eq. (20b), Eq. (21) strongly exceeds its Ohmic Q-factor. At the same time for all other modes the Ohmic Q-factor is higher than the diffraction Q-factor and, thus, their Q-factors are still governed by the diffraction losses. Under such conditions in the frame of the geometric-optical approach[2,14] we can consider that the Q-factor of the fundamental symmetric mode is defined exclusively by the Ohmic losses while other modes possess diffraction losses. This assumption was used in self-consistent theory of FEMs with a 2D Bragg resonator.[2,13,14]

Note that the parameters of the resonator taken here for the modeling are close to the parameters of an experiment studying a coaxial FEM with 2D distributed feedback based on a high-current accelerator at the University of Strathclyde.[4,5] In these experiments the cavity with diameters of the inner and outer conductors of 3 and 4 cm, respectively ($l_x\approx 25$ cm) was made to ensure transportation of a large-size annular electron beam through the system.[15] The 2D Bragg structures were designed to operate around 37.5 GHz via coupling of TEM and $TE_{24,1}$—type waveguide modes with the wave coupling coefficient $\alpha\sim 0.2$ cm^{-1}. The theoretical analysis presented in this paper demonstrates the ability of the 2D Bragg resonator of $l_z\sim l_x$ to provide high azimuthal mode selection that coincides well with the results of the experiments.[4,5]

V. 3D SIMULATIONS OF THE COAXIAL 2D BRAGG CAVITY

To prove the theoretical analysis described above additional studies of coaxial 2D Bragg resonators has been conducted using the 3D electrodynamic code CST "MICROWAVE STUDIO."[16] Temporal evolution of the rf-field and formation of a fundamental symmetrical mode inside the 2D Bragg cavity were investigated. The most important questions, which should be clarified from the 3D simulations with respect to the models described in Sec. IV, is the existence of the high-Q eigenmodes in the vicinity of the Bragg resonance frequency as well as demonstration of azimuthal mode selection.

The cavity parameters were chosen to be close to the parameters of the Strathclyde 2D Bragg FEM experiment.[4,5] Similar to the Bragg resonator designed for the experiment, the 2D corrugation was only considered to be on the inner conductor. The perimeter was taken to be l_x=20 cm ($\sim 25\lambda$), length l_z=11.8 cm ($\sim 15\lambda$) and the gap a_0=0.2 cm (0.25λ), i.e., parameters satisfy conditions (2). Note that the gap between the conductors was decreased in the simulations (as compared to the experimental realization described Sec. IV) to reduce the running time while still keeping in this frequency band all the radial and azimuthal modes required for 3D analysis. Thus, the difference in the gap should not affect the goal of the paper to demonstrate the ability of the 2D Bragg resonator to provide high azimuthal mode selection. The corrugation profile was in the form of the so-called chessboard pattern which approximates well to the "ideal" sinusoidal 2D corrugation (1) but is much more simple to manufacture in practice (and to depict in numerical simulations). Thus, it is used in the experimental studies of the FEM with this novel feedback mechanism. The corrugation depth was 0.32 mm which was equivalent to a sinusoidal corrugation depth of $a_1\approx 0.5$ mm. The corrugation was made with 24 variations along the azimuthal coordinate and had a longitudinal period of 0.83 cm. Following the Bragg resonance conditions (5) and the exact dispersion relation for

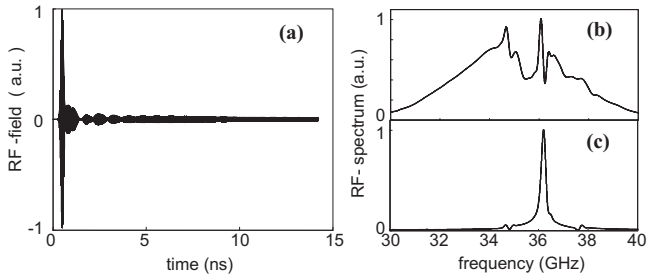

FIG. 9. 3D simulations of excitation of 2D Bragg resonator by incident short e.m. pulse, which is a superposition of the modes with azimuthal indices $m=0$ and $m=\pm 1$: (a) time dependence of the rf-field amplitude at the observation point, (b) rf-spectrum at the initial stage $0 \leq t \leq 7$ ns and (c) at the final stage of evolution $7 \leq t \leq 15$ ns.

waves of a coaxial waveguide (Fig. 8), this corrugation should provide, at a frequency near 36.3 GHz, mutual scattering of the four partial waves: two longitudinally propagating TEM-type waves ($A_{\pm}$) and two azimuthally propagating ($B_{\pm}$) near cutoff $TE_{24,0}$-type waves. These waves form the fundamental symmetrical normal wave (following the classification considered in the previous sections). Note also that several other longitudinally propagating partial waves with $m \neq 0$ and the corresponding azimuthally propagating modes which undergo coupling on the same grating are also presented in Fig. 8. The coupling coefficient for mutual scattering of all these waves was calculated to be $\alpha \approx 0.13$ cm^{-1}.

To find eigenmodes the simulations were carried out by excitation of the resonator by launching a short (in comparison with observation time) external rf-pulse from the edge at $z=0$ which was composed from eigenwaves of regular coaxial waveguide. The duration of the rf-pulse was taken to be $\Delta t \approx 0.15$ ns and provided a frequency sweep in the region of $\Delta f \approx 7$ GHz around the carrier frequency of 36 GHz. Temporal evolution of the rf-field inside the resonator was analyzed. After a few passes of the wave over the structure the eigenmodes are formed and the positions of these modes can be found from the maxima in the rf-field spectrum.

To demonstrate selectivity of the resonator over the azimuthal index the incident rf-pulse contains a set of three eigenwaves of a coaxial waveguide with equal amplitudes and azimuthal indices $m=0$ and $m=\pm 1$. Temporal evolution of the rf-field at the point $z=0$ is shown in Fig. 9(a). It is seen, that at the transient stage $t \leq 7$ ns the modes with different azimuthal indices are presented in the rf-spectrum [Fig. 9(b)]. From comparison with the theoretical analysis given above we can conclude that the fundamental azimuthally symmetrical mode $m=0$ is positioned at the Bragg frequency of 36.3 GHz and the spectral maxima at the frequencies of 34.8 and 37.8 GHz correspond to the modes having azimuthal indices $M=\bar{M} \pm 1$ respectively (Fig. 8). The Q-factor of the azimuthally symmetrical mode exceeds the Q-factors of all other modes and, thus, at the final stage the fundamental mode $m=0$ is the only mode present in the spectrum [Fig. 9(c)]. Correspondingly, at the final stage the azimuthal and longitudinal field structure is close to the structure of the azimuthally symmetrical mode, which was found in the frame of analytical consideration [see Figs. 10 and Figs. 11(a) and 11(b)]. The ratio between the amplitudes

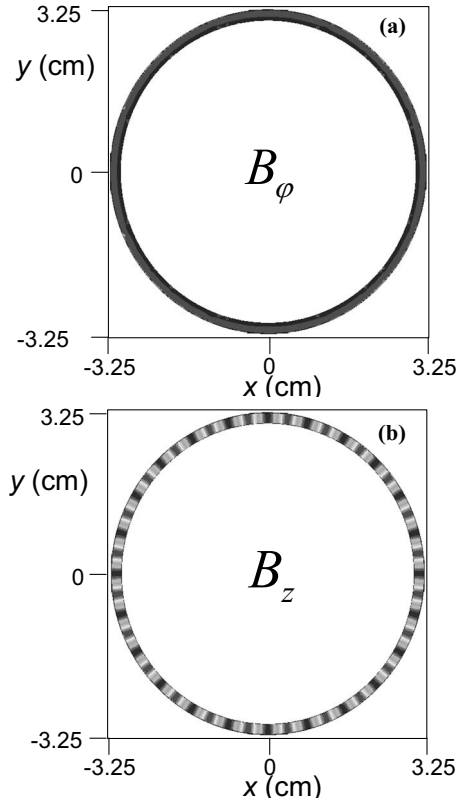

Fig.10

FIG. 10. The 3D simulation snapshots of the structure of (a) B_{φ} and (b) B_z field components in radial cross section when the fundamental azimuthally symmetrical mode is established. These structures correspond to superposition of symmetrical TEM partial wave A_+ (components E_r, B_{φ}) and the two counterpropagating partial waves $B_{\pm}$ forming $TE_{24,0}$ mode (components E_r, B_z).

of the partial waves $A_{\pm}$ and $B_{\pm}$ also coincides well with the coupled-wave model. Good agreement between the longitudinal mode structure found in the 3D simulation and an analytical solution exploiting radiation boundary conditions (16), Eq. (17) proves the adequacy of the model consisting of a resonator with matched edges. Let us note, that the resonator was excited also by a dipole positioned inside the cavity which radiated for a short time. In this case at the initial stage simultaneous excitation of the modes with different azimuthal indices $m=0,1,2,\ldots$ took place. However, at the final stage only the fundamental (azimuthally symmetric) mode survived.

To define the ratio between the Q-factors of modes with different azimuthal indices, symmetrical $m=0$ and nonsymmetrical modes $m=1$ were excited in the resonator separately. Due to radiation losses, after the incident wave was switched off, the eigenmodes were dissipated exponentially $F \sim F_0 e^{-\omega t/2Q}$ with the decay time depending on the Q-factor. Thus, the Q-factor of eigenmodes may be evaluated from the simple expression

$$Q_{m,n} = \pi f_{m,n} \tau_{m,n}^{\mathrm{dec}}, \tag{23}$$

where $\tau_{m,n}^{\mathrm{dec}}$ is the decay time required for an e-fold decrease in field amplitude.

Simulations demonstrated that for the resonator of length $l_z=11.8$ cm $\approx 15\lambda$ and perimeter $l_x=20$ cm $\approx 25\lambda$ the

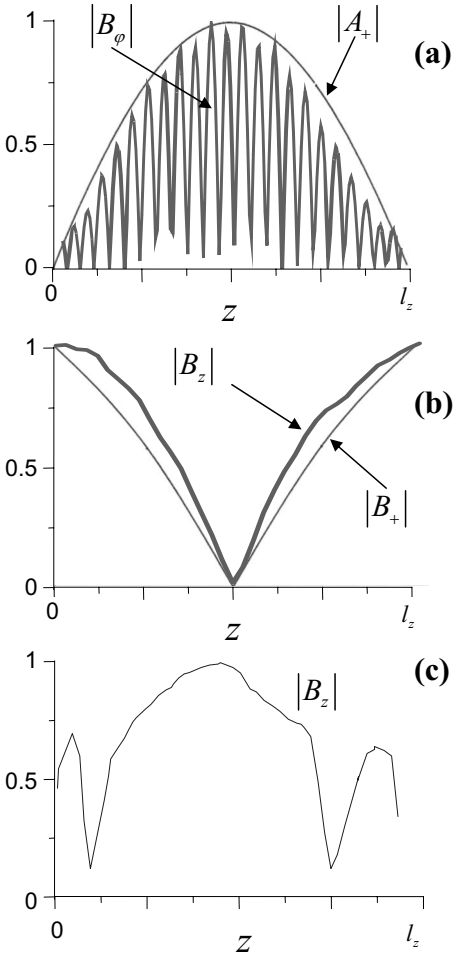

FIG. 11. Longitudinal structure of (a) B_φ and (b) B_z field components for the fundamental symmetrical mode ($m=0$; $n=1$) found in 3D simulations (thick lines) in comparison with structure of the partial waves A_+ and B_+ in the frame of the coupling wave approach (thin lines). (c) The B_z-component for nonsymmetrical mode $m=1$ having the maximal Q-factor ($\bar{h}/\alpha=60$, $\alpha l_x=2.5$; $\alpha l_z=1.5$).

Q-factor of the fundamental azimuthally symmetrical mode exceeds the Q-factor of the nonsymmetrical modes $|m|=1$ by about three times [see Fig. 12(b)]. The analysis carried out in the frame of the coupled-wave method shows that the selectivity of the 2D Bragg resonator is enhanced by increasing its length. The Q-factors versus the resonator length for the fundamental symmetrical as well as for the nonsymmetrical modes $m=1$, which were found in the 3D simulations, are presented in Fig. 13. For the fundamental symmetrical mode these dependences are in good agreement with the numerical solution of the Eqs. (10), (16), and (19), which is represented by the dotted line. The level of the Ohmic losses is also shown by the gray line for the resonator made from copper. It is seen, that in the realistic situation the diffraction Q-factor of the fundamental symmetrical mode is substantially higher than its Q-factor associated with Ohmic losses. Thus, for the fundamental mode the Q-factor can be taken as approximately equal to the Ohmic Q-factor. In contrast, for all other modes the diffraction losses play a principal role and define their Q-factors. Thus direct numerical simulations justify assumptions that have been used in the modeling of the nonlinear dynamics of the coaxial FEM with 2D distributed feedback presented in previous works.[5,13,14]

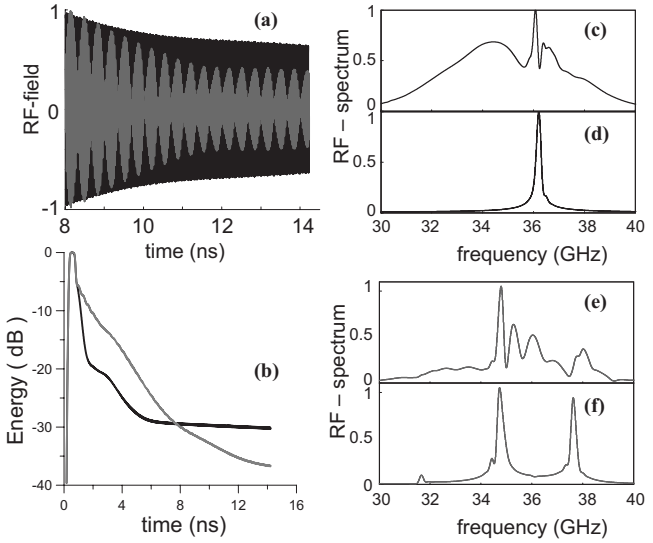

FIG. 12. 3D simulations of separate excitation of 2D Bragg resonator by incident e.m. pulse with azimuthally symmetrical ($m=0$, black line) and nonsymmetrical ($m=\pm 1$, gray line) structures: (a) time dependence of the rf-field amplitude at the observation point, (b) rf-energy decay on time, [(c) and (e)] rf-spectra at the initial stage $0\leq t\leq 7$ ns and [(d) and (f)] at the final stage of evolution $7\leq t\leq 15$ ns.

Note in conclusion 3D simulations of the dependence of the Q-factors of the fundamental and other modes on the resonator perimeter were not studied in detail in contrast to the coupled-wave model. However in a few variants, the resonator perimeter was increased up to $l_x=30$ cm$\approx 40\lambda$ with the number of the azimuthal corrugation variations $\bar{M}=36$ for the same length $l_z=11.8$ cm. In this case the Q-factor of the fundamental azimuthally symmetrical mode exceeds the Q-factor of the other modes not less than twice. Note also that simulations have demonstrated that for a perimeter $l_x=20$ cm the resonator keeps its selectivity when the gap between the conductors is increased up to 4 mm.

VI. CONCLUSION

The analysis of electrodynamic properties of 2D Bragg resonators of coaxial geometry realizing 2D distributed feedback was carried out in the frame of a quasi-optical approach

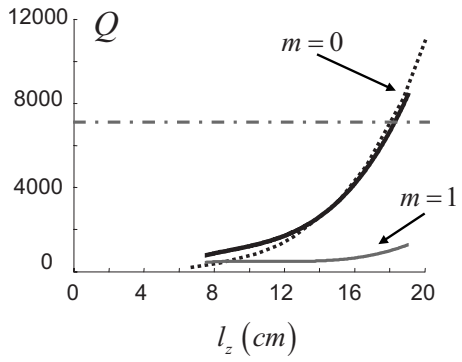

FIG. 13. Dependence of the Q-factor of the fundamental symmetrical $m=0$ (solid black line) and nonsymmetrical $m=1$ (solid gray line) modes on the resonator length found in 3D simulations. The Q-factor of the fundamental symmetrical mode obtained using the coupling wave approach is shown by the dotted line. The dashed-and-dotted line is the Ohmic Q factor for a resonator made from copper.

of coupled-wave theory as well as by carrying out 3D simulations. Both approaches demonstrate the high selectivity of coaxial 2D Bragg resonators over the azimuthal indices. It is shown that the high selectivity of 2D Bragg resonators can be explained by the different behavior of the normal symmetrical and nonsymmetrical waves near the Bragg resonance in a double corrugated unbound waveguide. As in the case of 2D Bragg structures of planar geometry[17] existence of such modes without any defects of periodicity strongly distinguish 2D Bragg structures from traditional 1D structures.[9–12]

[1]A. V. Arzhannikov, N. S. Ginzburg, V. S. Nikolaev, N. Yu. Peskov, A. S. Sergeev, S. L. Sinitsky, R. P. Zotkin, and M. V. Yushkov, *Abstracts of the 14th International* FEL Conference, Kobe, Japan, 1992, p. 214.
[2]N. S. Ginzburg, N. Yu. Peskov, and A. S. Sergeev, Opt. Commun. **112**, 151 (1994).
[3]N. V. Agarin, A. V. Arzhannikov, V. B. Bobylev, N. S. Ginzburg, V. G. Ivanenko, P. V. Kalinin, S. A. Kuznetsov, N. Yu. Peskov, A. S. Sergeev, S. L. Sinitsky, and V. D. Stepanov, Nucl. Instrum. Methods Phys. Res. A **445**, 222 (2000).
[4]I. V. Konoplev, P. McGrane, W. He, A. W. Cross, A. D. R. Phelps, C. G. Whyte, K. Ronald, and C. W. Robertson, Phys. Rev. Lett. **96**, 035002 (2006).
[5]I. V. Konoplev, A. W. Cross, A. D. R. Phelps, W. He, K. Ronald, C. G. Whyte, C. W. Robertson, N. S. Ginzburg, N. Yu. Peskov, A. S. Sergeev, and M. Thumm, Phys. Rev. E **76**, 056406 (2007).
[6]L. A. Vainshtein, *Electromagnetic Waves* (Soviet Radio, Moscow, 1957) (in Russian).
[7]A. F. Harvey, *Microwave Engineering* (Academic, New York, 1963).
[8]N. S. Ginzburg, N. Yu. Peskov, and A. S. Sergeev, Tech. Phys. Journal **73**, 54 (2003).
[9]A. Yariv, *Quantum Electronics* (Wiley, New York, 1975).
[10]H. Kogelnik and C. V. Shank, J. Appl. Phys. **43**, 2327 (1972).
[11]N. F. Kovalev, M. I. Petelin, and M. G. Reznikov, Resonator: USSR Authors Certificate No. 720592, bulletin No. 9 (1980).
[12]V. L. Bratman, G. G. Denisov, N. S. Ginzburg, and M. I. Petelin, IEEE J. Quantum Electron. **19**, 282 (1983).
[13]N. S. Ginzburg, A. S. Sergeev, and I. V. Konoplev, Tech. Phys. Journal **66**, 108 (1996).
[14]N. S. Ginzburg, N. Yu. Peskov, A. S. Sergeev, I. V. Konoplev, A. W. Cross, A. D. R. Phelps, G. R. M. Robb, K. Ronald, W. He, and C. G. Whyte, J. Appl. Phys. **92**, 1619 (2002).
[15]I. V. Konoplev, A. W. Cross, P. MacInnes, W. He, C. G. Whyte, A. D. R. Phelps, C. W. Robertson, K. Ronald, and A. R. Young, Appl. Phys. Lett. **89**, 171503 (2006).
[16]CST Microwave Studio User Manual—Advanced Topics, Computer Simulation Technology, Wellesley Hills, MA.
[17]N. S. Ginzburg, N. Yu. Peskov, A. S. Sergeev, G. G. Denisov, S. V. Kuzikov, V. Yu. Zaslavsky, A. V. Arzhannikov, P. V. Kalinin, S. L. Sinitsky, and M. Thumm, Appl. Phys. Lett. **92**, 103512 (2008).